UC Berkeley
UC Berkeley Electronic Theses and Dissertations

Title
Mechanistic Studies of Catalysis and Molecular Recognition by Synthetic Supramolecular Enzyme Mimics

Permalink
https://escholarship.org/uc/item/38n5b781

Author
Kaphan, David Melvin

Publication Date
2016

Peer reviewed|Thesis/dissertation

eScholarship.org Powered by the California Digital Library
University of California

Mechanistic Studies of Catalysis and Molecular Recognition by Synthetic Supramolecular Enzyme Mimics

By

David Melvin Kaphan

A dissertation submitted in partial satisfaction of the

requirements for the degree of

Doctor of Philosophy

in

Chemistry

in the

Graduate Division

of the

University of California, Berkeley

Committee in charge:

Professor F. Dean Toste, Co-Chair
Professor Kenneth N. Raymond, Co-Chair
Professor Alexander Katz

Fall 2016

Abstract

Mechanistic Studies of Catalysis and Molecular Recognition by Synthetic Supramolecular Enzyme Mimics

by

David Melvin Kaphan

Doctor of Philosophy in Chemistry

University of California, Berkeley

Professor F. Dean Toste, Co-Chair

Professor Kenneth N. Raymond, Co-Chair

Chapter 1 – A summary and overview of the application of self-assembled synthetic microenvironment catalysts is presented. The various clusters for which catalytic applications have been reported are introduced together, grouped by mechanism of self-assembly (i.e. hydrogen bond network or metal ligand coordination). The examples of catalysis are then discussed in the context of the nature of charge buildup in the transition state, with neutral reactions presented first, followed by reactions that develop anionic charge in the transition state, and finally reactions that develop cationic charge in the transition state.

Chapter 2 – The tetrahedral $[Ga_4L_6]^{12-}$ supramolecular assembly developed in the Raymond group is shown to catalyze a bimolecular aza-Prins cyclization featuring an unexpected transannular 1,5-hydride transfer. This reaction pathway is promoted by the constrictive binding of the interior microenvironment of the cluster, and is kinetically inaccessible in bulk solution. A thorough investigation of the mechanism of this process is presented, including isotope labeling studies and kinetic analysis, indicating that the rate limiting step of the process is encapsulation of a transiently formed iminium ion and supports the proposed 1,5-hydride transfer pathway. This work represents a striking example of the enzyme-like ability of synthetic microenvironment catalysts to selectively modulate kinetic barriers in order to promote otherwise inaccessible selectivity.

Chapter 3 – Catalysis of alkyl-alkyl reductive elimination from high valent transition metal complexes [such as gold(III) and platinum(IV)] by the $[Ga_4L_6]^{12-}$ Raymond cluster is described. Kinetic experiments delineate an enzyme-like Michaelis-Menten mechanism, with rate accelerations (kcat/kuncat) up to 1.9×10^7. Indirect evidence for the intermediacy of a coordinatively unsaturated encapsulated species is garnered from the observation of several persistent donor-arrested inclusion complexes, including a crystallographically characterized gold(III) cation. The catalysis of reductive elimination is further incorporated into a dual-catalytic cross coupling for which the presence of the supramolecular cluster is necessary in

order to achieve efficient turnover, and the full catalytic cycle of this process is elucidated through a series of stoichiometric experiments.

Chapter 4 – A novel supramolecular assembly of M_4L_4 stoichiometry is reported for which the addition of a guest effects an increase from S_4- to *T*-symmetry. A mechanistic investigation of this guest-induced host isomerization revealed that the guest binding occurs by a mechanism similar to the conformational selection model for ligand binding in proteins. A comprehensive study of this simple system provides insight into analogous behavior in biophysics and enzymology, as well as important information to support future efforts in the design of more efficient self-assembled microenvironment catalysts.

Acknowledgements

My time in Berkeley has been a privilege. In particular, I have been put in a position to pursue research questions that I found genuinely interesting, and have been supported in that pursuit by all those around me. While working in the Toste and Raymond groups, I have had the opportunity to make discoveries on my own and as part of a team, and I have been able to share those discoveries with community. There is a unique element of wonder in basic research, and I am grateful to those have enabled me to get to this point, and to have had these experiences. Some have simply pointed me in the right direction, while others have dragged me to where I needed to go as I went boneless in protest. I have been supported by a diverse set of individuals throughout my life, from family, to friends, to mentors, many of whom I cannot individually acknowledge here, but to each I am greatly indebted.

My family is a loving one. At times, we have confusing ways of showing it to one another. My parents have always been loving and supportive. I am particularly thankful for my parents' patience with me as I slowly matured through my most troublesome phases, and for their support and encouragement after I found some direction through chemistry. I would not be who I am today without my siblings, and I look forward to the continued evolution of our relationships.

I took a non-traditional route to the Toste and Raymond groups, and I will always be thankful to Ken and Dean for giving me this opportunity. Advisors like Ken and Dean, who have a real interest in the growth and wellbeing of their students, are few and far between, and I am grateful for their mentorship and support. While Ken and Dean are quite different in many ways, their ability foster creativity and excitement about chemistry is identical. I was also fortunate to have benefited from the mentorship of Bob Bergman as an advisor on the supramolecular collaboration. Bob's physorg class was an academically formative experience, and his influence from the class, as well as at BobTalk, has inspired a great deal of my graduate studies.

My lab mates and friends in the Toste and Raymond groups have made graduate school an extraordinary experience. The most important characteristic of our group is the constant excitement about chemistry and the ability to talk to anyone about your work. The insights that I gained from wandering around the lab and talking chemistry are invaluable. I would like to particularly acknowledge Matt Winston, Billy Hart-Cooper, and Andrew Neel (when he wasn't grumpy) for their mentorship and advice. The second most important characteristic of our group is that people are almost always down for some serious hoodrat stuff. Toste Salad taking home the trophy, an experiment in flow from the 6th floor to 5th floor balcony, wingpocalypse, the royal rumble (before the big freeze) and many other shenanigans. I have made too many friends to address everyone individually, but I think that all of you are awesome and I hope we continue to cross paths over the years. Dickthorn, Dewgong, Beehive, and New Steve, you're all cool and have cool nicknames. I would also like to thank my lab mates in 611 and 511 for putting up with whistling, singing and miscellaneous animal noises over the years.

I have had the pleasure of participating in two fruitful collaborations over the last couple of years of gradschool. Two minds working on a problem are always greater than the sum of their parts. Having a coworker and friend to share the excitement of success and the disappointment of failure is a special experience that not many graduate students get to have. Mark has been a close friend and collaborator since freshman organic chemistry lab at the University of Rochester. We have come a long way from late night lab reports in the POA, to holding office hours together senior year, to many evenings of kinetics runs in the NMR room. Cindy is a newer friend and a newer collaborator, but we make a great team nonetheless. Also, she does more serious hoodrat Cindy stuff than anyone else in the lab by a long shot.

Lastly, Leah. Your confidence in me and your support have been unwavering, even during the toughest moments here at Berkeley. You are the most loving person that I know and I have a lot of fun hanging out with you. No feelings of crippling regret yet, so, so far so good. Thank you for your love and your support. I look forward to the next chapter of our lives.

Dedicated to the reader in the hopes that he or she finds something interesting within

And to Leah

Mechanistic Studies of Catalysis and Molecular Recognition by Synthetic Supramolecular Enzyme Mimics

TABLE OF CONTENTS

Chapter 1

Self-assembled Supramolecular Microenvironments as Catalysts

1.1 Preface

This chapter is intended to introduce and summarize the field of supramolecular catalysis, focusing on the application of self-assembled architectures. The included examples provide a context for the work discussed in chapters 2, 3 and 4. Research in the areas of catalysis by covalent architectures, stoichiometric transformations within self-assembled clusters, and catalysis by metal centers encapsulated within host molecules is beyond the scope of this introduction, but has been reviewed extensively in the literature.[1–3] In this chapter, self-assembled hosts that have been successfully applied to catalysis are introduced, followed by a summary of their catalytic activity, as categorized by the positive, negative or neutral charge development in the reaction's transition state.

1.2 Introduction

The field of synthetic chemistry has traditionally relied on covalent interactions in order to influence the reactivity and physical properties of molecules. Covalent catalysis has grown into a mature field, with an ever-growing array of reactivity that supports our industrial synthetic needs from complex pharmaceutical synthesis to commodity chemical production.[4–6] However, the formation and cleavage of covalent bonds represents only a subset of how molecules interact. Indeed, a whole suite of noncovalent supramolecular interactions are crucial to the course of any molecular interaction, in the context of catalysis or otherwise. In fact, efficient catalysts can also be achieved purely through non-covalent interactions.[7–9] An abundance of compelling examples of purely supramolecular catalysis are found in the study of Nature's enzymes.

Enzymes function as catalytic microenvironments that are specifically tailored toward the selective and specific recognition and stabilization of the transition state of a desired transformation, in order to accelerate that overall process.[10] This acceleration is generally achieved by the enzymatic microenvironment through a series of additive supramolecular interactions, individually insignificant, but together capable of drastically lowing kinetic barriers otherwise insurmountable under physiological conditions.[11,12] This strategy of enzymatic microenvironment catalysis is so effective that enzymatic rate accelerations between 10^5 fold and 10^{12} fold are regularly observed, as well as accelerations up to 10^{17} fold in some extreme examples, such as in the case of Orotidine 5'-Posphate Decarboxylase (Table 1.1).[13]

Enzyme	Rate acceleration (k_{cat}/k_{uncat})
Cyclophilin	4.6×10^5
Carbonic anhydrase	7.7×10^6
Chymotrypsin	10^7
Triosephosphate Isomerase	3×10^9
Fumarase	10^{11}
Urease	10^{14}
Orotidine 5'-Phosphate Decarboxylase	1.4×10^{17}

Table 1.1. Representative rate accelerations for various enzymes

Beyond their dramatic rate accelerations, enzymes have an additional feature that allows them to effect transformations that are beyond the purview of traditional synthetic catalysts. The enzyme, by virtue of its complete encapsulation of the substrate, is capable of defining the local microenvironment for the entirety of its substrate molecule, as opposed to a small molecule catalyst, which controls only the functional groups with which it makes direct contact. As a result, the enzymatic catalytic microenvironment is capable of the selective stabilization of one specific reaction pathway, in the midst of many competing potential deleterious transformations.[14–17] One beautiful example of such a selective enzymatic transformation is the conversion of geranylgeranyl diphosphate to taxadiene en route to the biosynthesis of the natural product taxol (Scheme 1.1).[18]

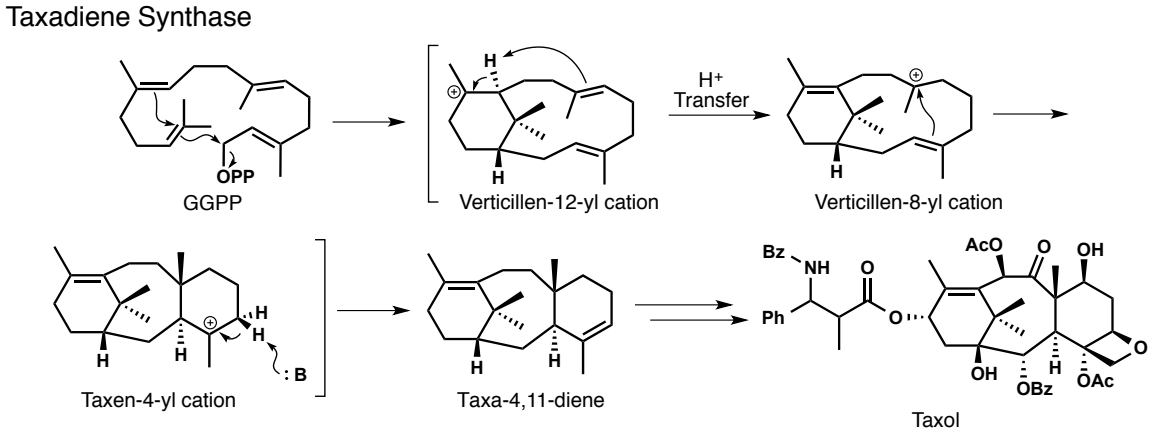

Scheme 1.1. Taxadiene Synthase mediated cyclization of geranylgeranyl diphosphate.

Inspired by the powerful host-guest chemistry displayed in a biological context, synthetic chemists were led into the field of supramolecular chemistry by Charles Pedersen in his synthesis of crown ethers for the recognition and binding of alkali metal cations in 1967.[19] Central to this work was the recognition that preorganization was crucial to lowering the entropic cost of chelation. Pederson's report of crown ethers was soon followed by Jean-Marie Lehn's investigation of cryptands[20] and Donald Cram's investigation of spherands and carcerands,[21] for which the three shared the 1987 Nobel Prize in recognition of their seminal contributions to supramolecular chemistry. Other early macrocyclic supramolecular host complexes include cyclodextrins (cyclic carbohydrate oligomers which bear a hydrophobic internal cavity), calixarenes (goblet-like macrocyclic oligomers formed from the condensation of electron rich arenes and formaldehyde), and cucurbiturils (macrocylic oligomers formed from the condensation of glycoluril and formaldehyde) (Figure 1.1).[22]

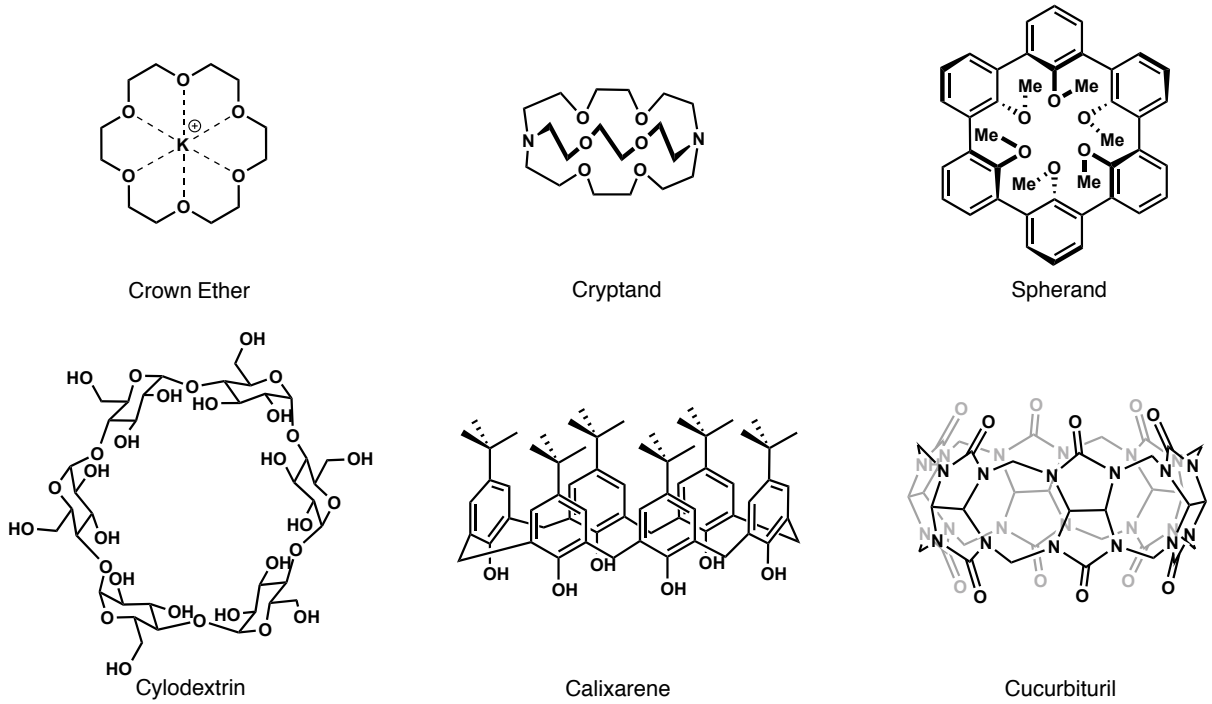

Figure 1.1. Important examples of early covalent macrocyclic host molecules.

While many important lessons can be learned from covalent macrocyclic hosts, they are inherently limited by synthetic difficulty and a lack of structural diversity. Novel covalent macrocyclic host structures were largely discovered serendipitously, and the synthesis of modified or rationally designed covalent hosts can be arduous to the point of impracticality. This makes modification of host size and electronic properties nearly impossible, thus limiting the scope of synthetic microenvironments available for application to molecular recognition and catalysis.

More recently, a complementary approach for the synthesis of controlled host microenvironment has emerged through the self-assembly of simple molecular building blocks in order to generate more complex three-dimensional architectures. These self-assembled supramolecular architectures are generally composed of rigid or semi-rigid building blocks that are stitched together through some dynamic coordination mode, typically in the form of metal-ligand coordination or hydrogen bonding networks.

1.3 Catalytically Relevant Self-assembled Architectures

While a large number of self-assembled clusters showing guest recognition behavior have been described in the literature,[23–25] their properties as catalytic microenvironments have been explored only in a handful of examples.[26,3] The main supramolecular clusters for which catalytic activity has been demonstrated are described below.

1.3.1 Hydrogen Bond Assemblies

Hydrogen bonding is a critical driving force for the formation of secondary structure in proteins.[11] In a similar manner, a molecule designed in such a way that it is self-

complementary with respect to its organization of hydrogen bond donors and acceptors can have a strong driving force for aggregation in solution. These interactions can lead to binary capsule formation, or in some cases, higher order structures are preferred.

The Rebek group has studied a variety of hydrogen bond based assemblies,[27–29] which frequently display encapsulation behavior, as well as some stoichiometric reactivity; however, only a small number of catalytic applications have been achieved. One example of this self-assembly is observed in the homodimerization of **1**, such that when the concave faces of two molecules approach one another, a series of 16 complementary hydrogen bonds form a large, roughly spherical internal cavity (Figure 1.2).[30]

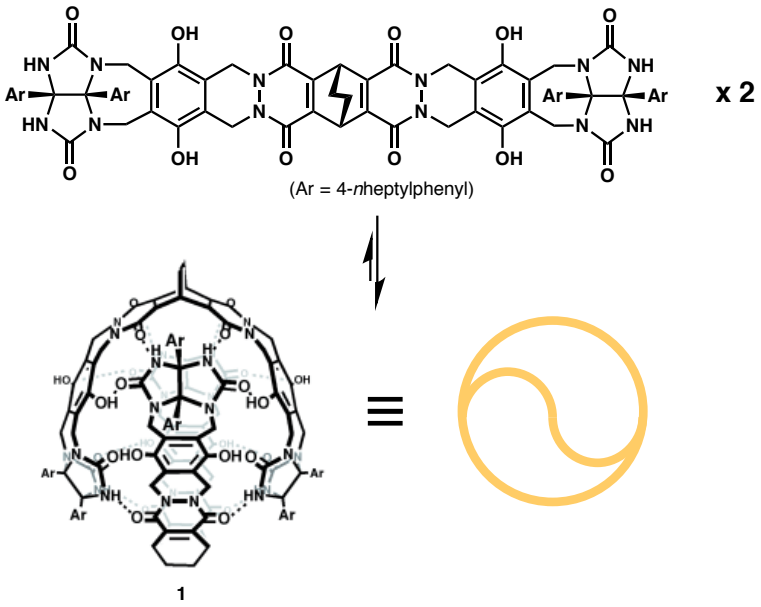

Figure 1.2. Self-assembly of hydrogen bond based tennis ball of Rebek and coworkers. Figure adapted from reference 23.

Another important hydrogen bond based assembly is formed by the hexameric aggregation of resorcinarene (**2**) in wet organic solvents (Figure 1.3). This capsule (**3**) was first characterized by Atwood[31]; however, its application as a catalyst for Brønsted acid mediated transformations was discovered and explored by Tiefenbacher[32] (*vide infra*). In addition to the six resorcinarene units, the Atwood cluster incorporates eight water molecules, one on each face of the octahedral assembly, which completes a network of 36 intermolecular hydrogen bond. Assembly **3** features an internal cavity of approximately 1400 Å^3, which is among the largest characterized hydrogen bond capsules. Furthermore, **3** encapsulates a variety of cationic and neutral guests, including tetraethyl ammonium, triethylamine and 3-ethylpentane.

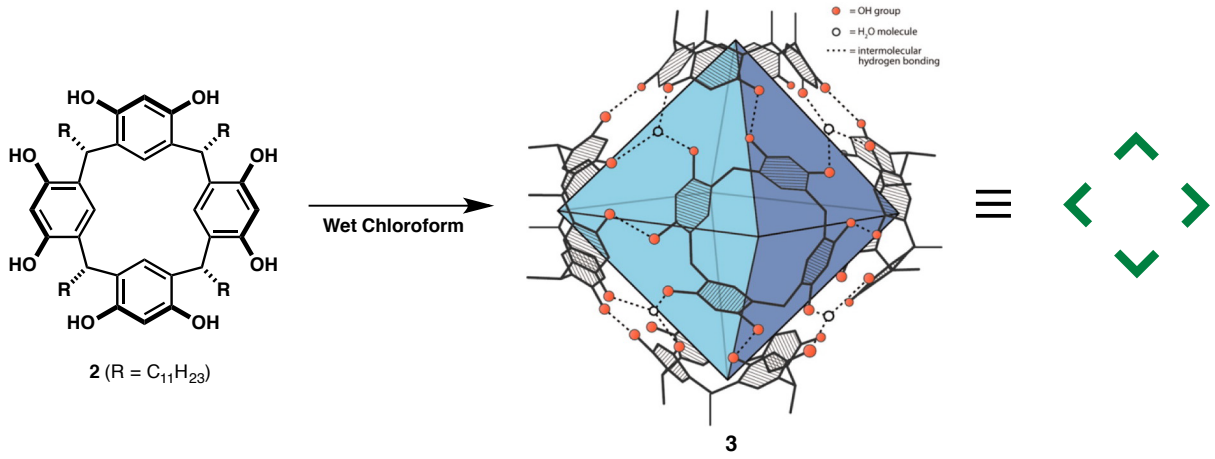

Figure 1.3. Hexameric self-assembly of resorcinarene (**2**) to form cluster **3**. Figure adapted from reference 30.

1.3.2 Metal-Ligand Coordination Assemblies

Metal coordination chemistry provides a convenient mechanism for the assembly of supramolecular architectures. The assembly of supramolecular architectures by metal-ligand coordination chemistry has many benefits, including modularity, dynamicity and directionality. The modularity of metal-ligand coordination allows many structural analogues with varying properties to be rapidly constructed by substitution of the bridging ligand or metal cation with similar elements, homologues or geometries. The dynamic nature of coordination for many metal-ligand combinations is crucial in order to allow the self-assembly to converge on a global thermodynamic minimum. Finally, the directionality of metal ligand coordination enables the rigid three-dimensional architecture necessary to generate a defined microenvironment.

The Fujita research group has developed a number of assemblies of various geometries, predominantly through the combination of bi- and tridentate pyridyl ligands and square planar ethylenediamine palladium or platinum capping groups with two open *cis*-coordination sites in order to enforce a 90º ligand approach.[33–36] The majority of the studies focusing on chemistry in a confined microenvironment from the Fujita group implement octahedral M_6L_4 cage **4**,[37] however, the open-faced bowl structure **5**[38] is necessary in some cases to avoid product inhibition and achieve catalysis (Figure 1.4). Both **4** and **5** bear an overall dodecacationic charge, rendering them water soluble, and are ideally suited for encapsulation of hydrophobic and aromatic guests.

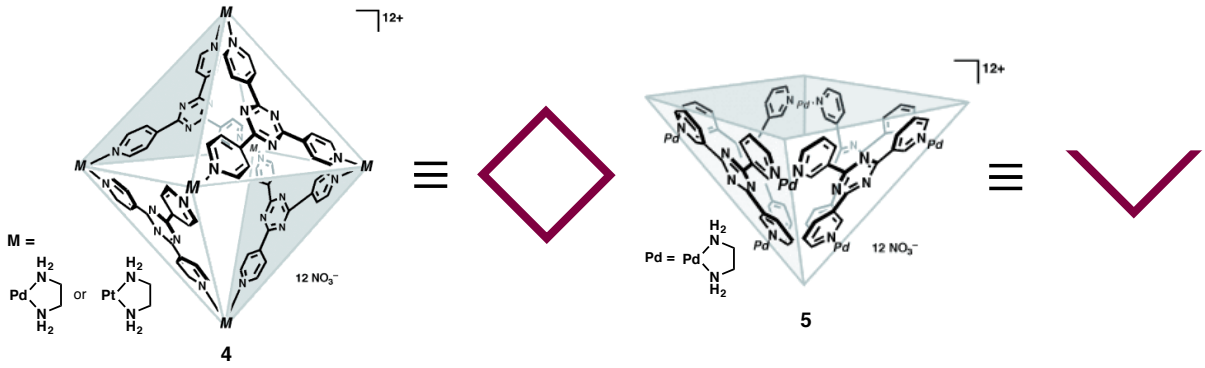

Figure 1.4. Cage and bowl assemblies **4** and **5** developed in the Fujita group. Figure adapted from reference 23.

Inspired by earlier observations by Saalfrank et al.[39] that bis-bidentate ligands and octahedral metal centers could self-assemble into M_4L_6 tetrahedra, the Raymond group designed tetrahedral cluster **6**, which is composed of six C_2-symmetric bis-catecholamide ligands and four octahedral gallium(III) metal centers, with an overall dodecaanionic charge (Figure 1.5).[40] As measured by single crystal X-ray diffraction, the internal cavity of **6** ranges from about 250 to 400 Å^3, as a function of the size of the encapsulated guest. Due to mechanical coupling through the ligand, the four gallium metal centers are rendered homochiral, and **6** is isolated as a racemic mixture of ΔΔΔΔ and ΛΛΛΛ enantiomers. Additionally, analogues of **6** have been synthesized with a variety of octahedral metal ions, including iron(III), aluminium(III), indium(III), titanium(IV) and germanium(IV).[41] Cluster **6** encapsulates a variety of neutral and cationic guests. Encapsulation within **6** can be considered to be a two-part process, involving an enthalpically driven external association intermediate, followed by an entropically driven internal encapsulation.[42–44] The major contribution to the enthalpy of external association is likely Coulombic in nature. Internal association is entropically favored due to the liberation of the guest solvation shell, as well as the solvent molecules confined to the interior of the cluster. Guest ingress and egress from **6** has been shown to proceed by an aperture dilation mechanism, as opposed to ligand dissociation, as evidenced by a series of kinetic experiments, which are supported by computational work.[45] Cluster **6** can also be enantioenriched by resolution with a chiral guest.[46] More recently, a terephthalamide-derived analogue of the cluster (**7**) bearing a peripheral chiral amide moiety was synthesized, which assembles into an enantiopure cluster without the necessity of a resolution, and is more thermally and oxidatively stable.[47]

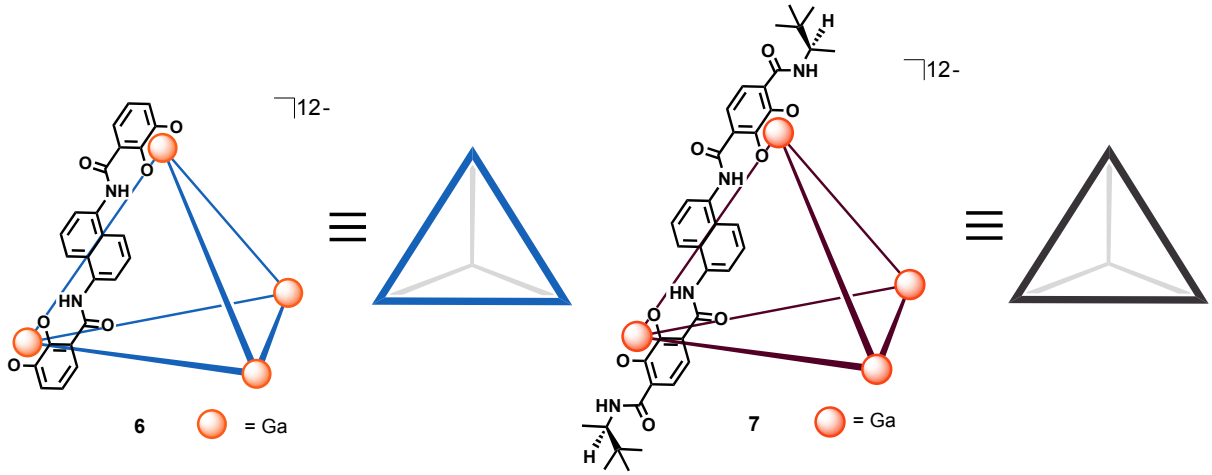

Figure 1.5. Tetrahedral M_4L_6 supramolecular assemblies developed in the Toste and Raymond groups.

Ward and coworkers have extensively studied the self-assembly of bis-bidentate pyrazolyl-pyridine ligands with divalent cobalt, nickel and cadmium octahedral metal centers. Similar to the Raymond clusters, the Ward group has reported that this class of bis-bidentate ligands with octahedral metal centers will reliably form clusters with 2M:3L stoichiometry, however, due to the increased flexibility of Ward's ligands, subtle geometric variation has resulted in the isolation of M_4L_6 tetrahedra;[48] M_8L_{12} cubes,[49] $M_{12}L_{18}$ truncated tetrahedra,[50] and $M_{16}L_{24}$ tetra-capped truncated tetrahedra,[51] however, only M_8L_{12} cube **8** has been demonstrated as a microenvironment catalyst (Figure 1.6). Cluster **8** has an overall charge of 16^+, and preferentially encapsulates neutral guest molecules with association constants of up to 10^8 M^{-1}.

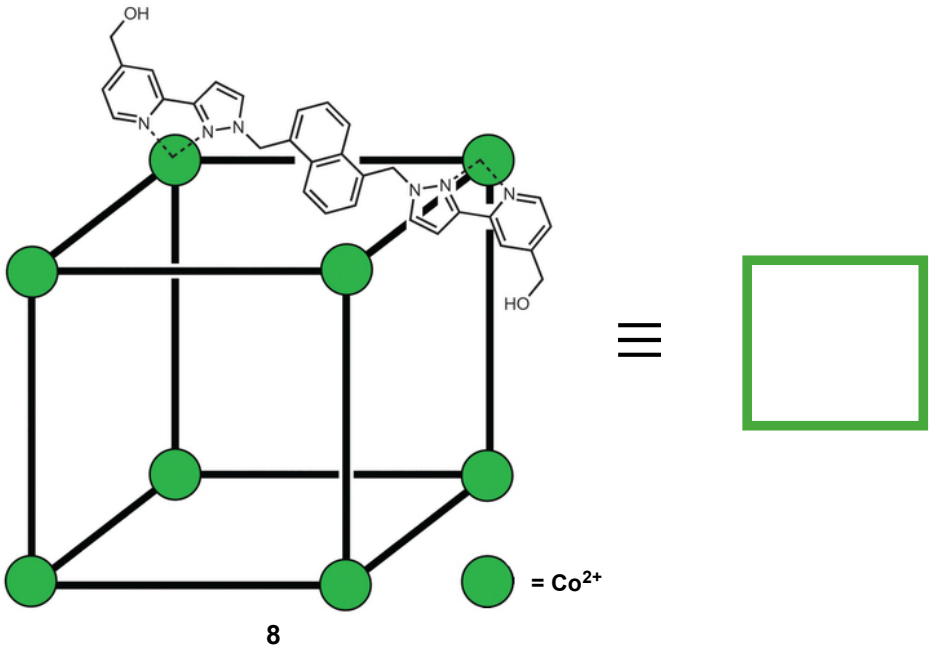

Figure 1.6. Cubic Co_8L_{12} cluster developed by Ward and coworkers. Figure adapted from reference 63.

Nitschke and co-workers have taken advantage of a similar bis-N,N-bidentate ligand class in order to prepare a variety of assemblies in M2:L3 stoichiometry. The Nitschke ligands are formed through in situ condensation of 2-formylpyridine and a C_2 symmetric dianiline. In particular, iron based cluster **9** undergoes self-assembly to form an enantiopure tetrahedral Fe_4L_6 cluster with an overall charge of 8^+ (Figure 1.7).[52] This assembly is rendered water-soluble by its overall charge and decoration with hydrophilic hydroxyl groups, and it has been shown to encapsulate a variety of neutral aliphatic and aromatic guest molecules.

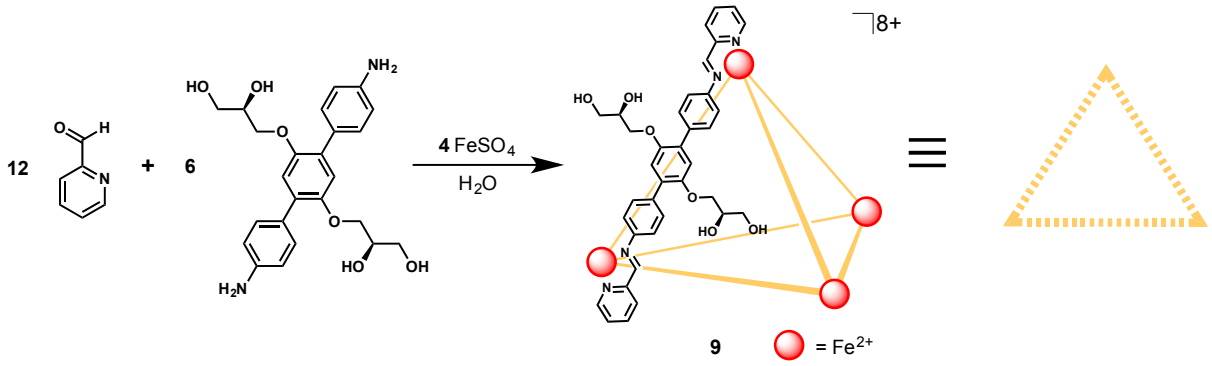

Figure 1.7. Tetrahedral M_4L_6 cluster developed by Nitschke and coworkers.

1.4 Supramolecular Catalysis

Just as enzymes act as microenvironment catalysts in a biological context, so too can synthetic hosts act as microenvironment catalysts if they are capable of the recognition and stabilization of a reaction transition state relative to the ground state of that system. Much of the early work in supramolecular catalysis focused largely on the application of covalent macrocyclic hosts as enzyme mimics, with rate accelerations (k_{cat} / k_{uncat}) generally very modest in magnitude ($\leq 10^2$ fold). Nonetheless, an important early demonstration of the power of supramolecular catalysis came in the form of a cucurbituril catalyzed alkyne-azide cycloaddition, which proceeded with a much more significant rate acceleration of 5.5 x 10^4 fold, while providing complete control of the regiochemical outcome of reaction.[53] In contrast, the study of self-assembly has been a boon in the development of hosts capable of acting as microenvironment catalysts (*vide supra*).

When considering the scope of transformations catalyzed by self-assembled supramolecular microenvironment catalysts, one natural and convenient classification is the nature of charge buildup in the transition state of the reaction. In many ways, the innate electronic properties of a given host render that host predisposed to the stabilization of complimentarily charged transition states. Hosts that bear a large negative charge and/or feature highly electron rich aromatic walls tend to recognize the transition states for reactions where a positive charge develops between the grounds state and the transition state of the reaction. Likewise, positively charged / electron poor hosts complement transition states that build up negative charge in the transition state. In reactions that undergo no change in charge between the ground state and transition state, conformational restriction and non-electrostatic thermodynamic considerations dominate the relative energetics of the reaction, and the electronic nature of the host is less relevant. The remainder of this introduction will focus on a

summary of reactions facilitated by self-assembled microenvironment catalysts, grouped by the nature of charge buildup in the transition state.

1.4.1 Supramolecular Catalysis Involving Neutral Transition States

Pericyclic reactions have proven amenable to microenvironment catalysis, and each of the three notable examples of electroneutral microenvironment catalyzed transformations described below are pericyclic in nature. In microenvironment catalysis of reactions where there is no buildup of charge in the transition state relative to the ground state, entropic gains from substrate preorganization are often a dominant source of transition state stabilization. Two main effects contribute to lowering the entropic barrier of a reaction upon encapsulation within a supramolecular host. In a unimolecular reaction such as a cyclization, encapsulation of a substrate typically forces the distal reactive sites on the molecule into a close proximity, eliminating the entropic cost associated with their approach. (This entropic gain is conceptually similar to a the Thorpe-Ingold effect.) Alternatively, in a bimolecular reaction, selective co-encapsulation of the two substrates effectively renders the reaction unimolecular, since the entropic cost of the random substrate encounter is paid upon encapsulation. In addition to entropic effects, microenvironment catalysts might potentially stabilize the transition state for a pericyclic reaction by a variety of secondary intramolecular effects. In particular, HOMO-LUMO modulation by π-π interactions with the capsule walls, effecting more favorable orbital overlap, may be a relevant factor in some cases.

The first example of a neutral pericyclic reaction catalyzed by a self-assembled supramolecular cluster was a Diels-Alder cycloaddition within capsule **1**, reported by Rebek and co-workers in 1998.[54] Previous reports from the Rebek group described the stoichiometric acceleration of the Diels-Alder reaction between *p*-quinone (**10**) and 1,3-cyclohexadiene (**11**), forming Diels-Alder adduct **12**, which was 170 fold faster in the presence of **1** than in the background reaction (Scheme 1.2A).[55,56] This acceleration is explained by the increased effective concentration of the two reactants when co-encapsulated within **1**. However, product **12** was strongly bound within the cavity of **1**, resulting in complete product inhibition. Product inhibition proves to be a systemic issue in supramolecular catalysis. In particular, two-component couplings are prone to product inhibition since the ternary inclusion complex of the starting materials (**10•11⊂1**) is more entropically disfavored than the binary inclusion complex of the product (**12⊂1)**. Serendipitously, the Rebek group found that if the diene is replaced with thiophene dioxide derivative **13**, then the resulting Diels-Alder adduct (**14**) is less strongly bound by **1**, and catalytic turnover can occur (Figure 1.2B).

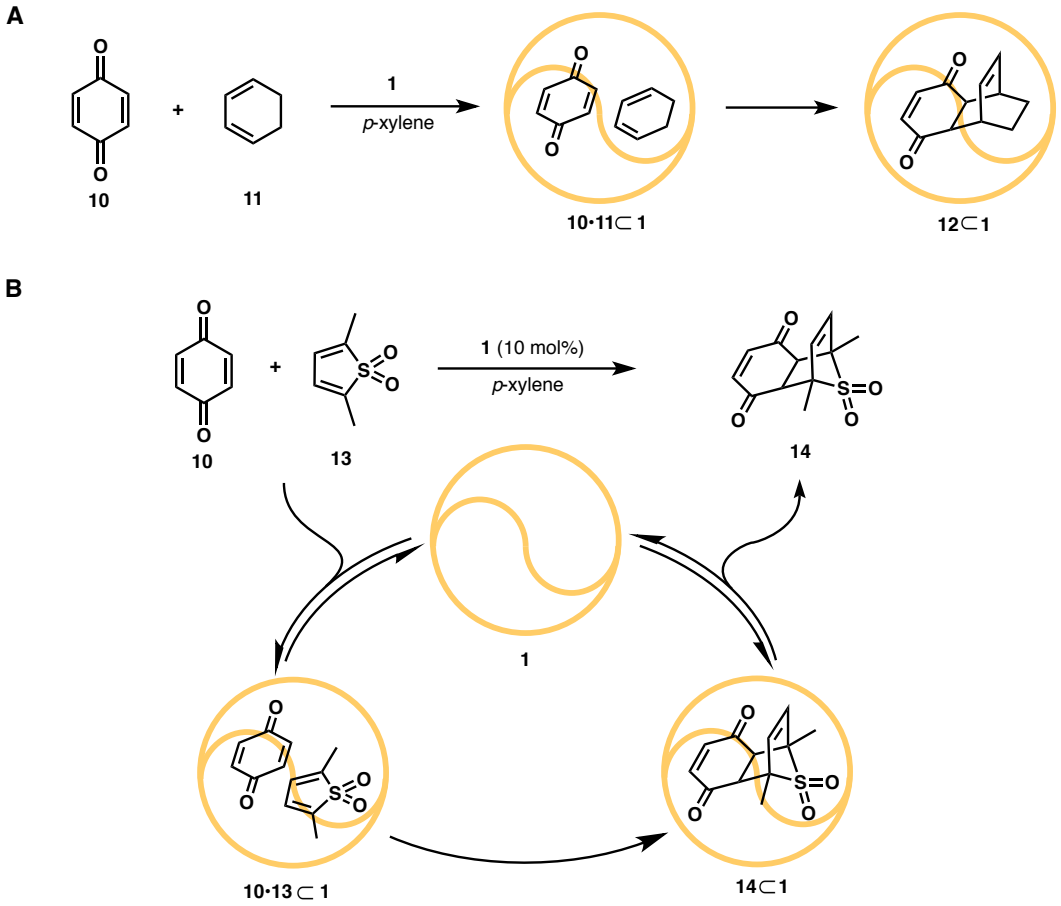

Scheme 1.2. (A) Stoichiometric acceleration of a Diels-Alder cycloaddition by capsule **1**. (B) Catalytic acceleration of a Diels-Alder cycloaddition by capsule **1**.

Fujita and coworkers obtained similar results employing capsule **4** and bowl **5** as catalysts. A variety of stoichiometric Diels-Alder reactions could be dramatically accelerated within **4**.[57–59] Interestingly, the Fujita group was able to show that stoichiometric encapsulation within **4** enabled transformations that would be inaccessible outside of the assembly. Of particular importance was the demonstration that co-encapsulation of 9-substituted anthracene molecules such as **15** and bulky maleimides such as **16** selectively promoted cycloaddition at the 1,4- position to form Diels-Alder adduct **17**, with none of the 9,10-substituted product (**18**) detectable after extraction of the reaction mixture (Scheme 1.3A). In the absence of **4**, only 9,10-substituted product **18** is observed. Unfortunately, as Rebek and coworkers had previously observed, the association constant for encapsulation of the Diels-Alder adduct was a sufficiently large that product inhibition was dominant and no catalytic turnover was feasible. In order to circumvent this, the Fujita group employed open-faced assembly **5**, hypothesizing that partial encapsulation would decrease the strength of product encapsulation, thus enabling turnover (Scheme 1.3B). Indeed, at 10 mole percent loading, **5** promoted rapid consumption of coupling partners **15** and **16**, however, the native regiochemical outcome of the reaction was observed, affording adduct **18**. The authors suggest that the decrease in planarity of **18** relative to the anthracenyl precursor interrupts the high surface area π-π interaction with host **5**, contributing to its decreased affinity for the host.

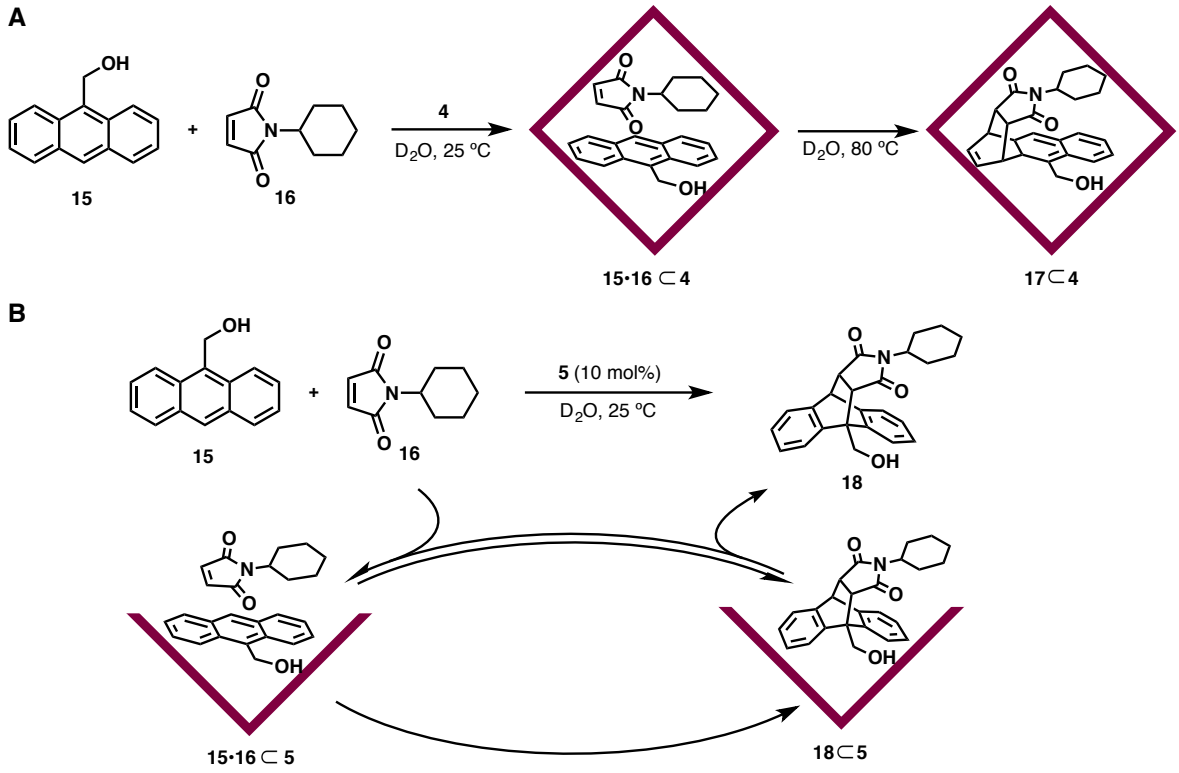

Scheme 1.3. (A) Stoichiometric Diels-Alder reaction between **15** and **16** accelerated by cluster **4** with an unusual regiochemical outcome. (B) Diels-Alder reaction between **15** and **16** catalyzed by host **5**.

An additional neutral pericyclic reaction catalyzed by a supramolecular microenvironment catalyst comes from the Bergman and Raymond groups, where Ga_4L_6 tetrahedron **6** was shown to catalyze the cationic aza-Cope rearrangement of ammonium ions such as **19** (Scheme 1.4).[60] While the substrate for this reaction is cationic, this reaction is classified as a "neutral" transformation because there is no buildup or change in charge between the ground state of the system and the transition state. In this catalytic process, ammonium **19** is encapsulated by **6**, followed by a [3,3]-sigmatropic rearrangement to afford encapsulated iminium ion **20⊂6**. Iminium ion **20** then egresses from **6** and is hydrolyzed either while externally associated to the host or in bulk solution, depending on the concentration of hydroxide and the presence of other tetraalkylammonium ions to compete for external association.[61] Rate accelerations (k_{cat} / k_{uncat}) ranged from 5 fold to 854 fold (for substrate **19**), with the degree of acceleration strongly correlated to the steric bulk on the allyl fragment. Ammonium ion **19** adopts a folded conformation upon encapsulation as determined by 2D NOESY NMR spectroscopy at -10 ºC. This chairlike conformation resembles the transition state for the aza-Cope rearrangement, and as such, upon encapsulation the substrate is advanced along the reaction coordinate. Further evidence for this effect is found in the comparison of the activation parameters for rearrangement for **19** in bulk solution compared to **19** encapsulated by **6**. While the enthalpy of activation remains essentially unchanged ($\Delta H^{\ddagger}$ = 23.6(3) vs. 22.6(9) kcal/mol), the rearrangement is entropically disfavored in bulk solution, while being roughly entropically neutral upon encapsulation ($\Delta S^{\ddagger}$ = -10(1) vs. -1(2) cal/molK). It was further demonstrated that substrates where the allyl fragment is replaced with a

propargyl group are competent to undergo rearrangement catalyzed by **6** to form a corresponding allenyl aldehyde.[62] Finally, by employing the enantiomerically resolved ΔΔΔΔ-**6**, rearranged products could be isolated with enantiomeric excesses of up to 78%.[63]

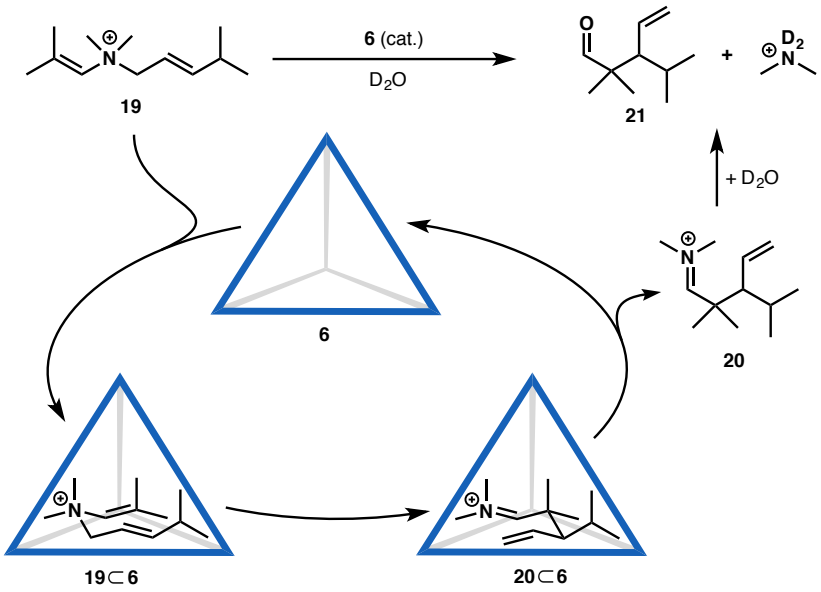

Scheme 1.4. Cationic aza-Cope rearrangement of **19** catalyzed by cluster **6**.

1.4.2 Supramolecular Catalysis Involving Anionic Transition States

While microenvironment catalyzed neutral pericyclic reactions described above were promoted by a diverse array of assemblies (neutral hydrogen bond based, as well as both polyanionic and cationic metal ligand clusters), the three examples of microenvironment catalyzed reactions that develop anionic charge in the transition state are uniformly catalyzed by polycationic metal ligand assemblies. These include octacationic Fe_4L_6 tetrahedron **9** from the Nitschke group, dodecacationic Pd_6L_4 octahedron **4** from the Fujita group, and hexadecacationic Co_8L_{12} cube **8** from the Ward group. This trend highlights the importance of coulombic considerations in supramolecular catalysis. While electron deficient aromatic walls could be beneficial for the stabilization of transition states that accumulate significant negative charge, this is inconsistent among **4**, **8**, and **9**. Cluster **4** is composed of highly electron poor trispyradyl-triazine ligands, while cluster **9** is composed of electron-rich heteroatom-substituted aromatic ligands. Further study of derivatives of **4**, **8**, and **9**, as well as the development of new bespoke catalysts, is necessary to determine the role of the electronic character of the ligands in the stabilization of anionic transition states.

In 2011 Fujita and coworkers reported the first application of a self-assembled microenvironment catalyst for a reaction proceeding through an anionic transition state. Octahedral cluster **4** was shown to catalyze the Knoevenagel condensation of naphthaldehyde **22** (and derivatives thereof) and Meldrom's acid **23** to afford olefinic condensation product **24** under neutral conditions in water (Scheme 1.5).[64] After six hours at room temperature in the presence of only 1 mole percent of cluster **4**, product **24** was isolated in 96 percent yield, as compared to only 4 percent in the absence of **4**. The authors suggest that negatively charged intermediates **A** and **B** (and by extension their adjacent transition states) are stabilized by

close proximity to the dicationic Pd metal centers that decorate the apertures of cluster **4**. In support of this hypothesis, the authors show that while open faced assembly **5** undergoes association to **22**, no substantial catalysis is observed after the addition of nucleophile **23**, presumably due to the inaccessibility of the cationic metal centers which are no longer situated around the host aperture. After elimination of water from intermediate **B⊂4**, the encapsulated product, **24** ⊂**4** is too sterically encumbered to be efficiently encapsulated, and **24** is easily ejected to regenerate the active catalyst, empty cluster **4**.

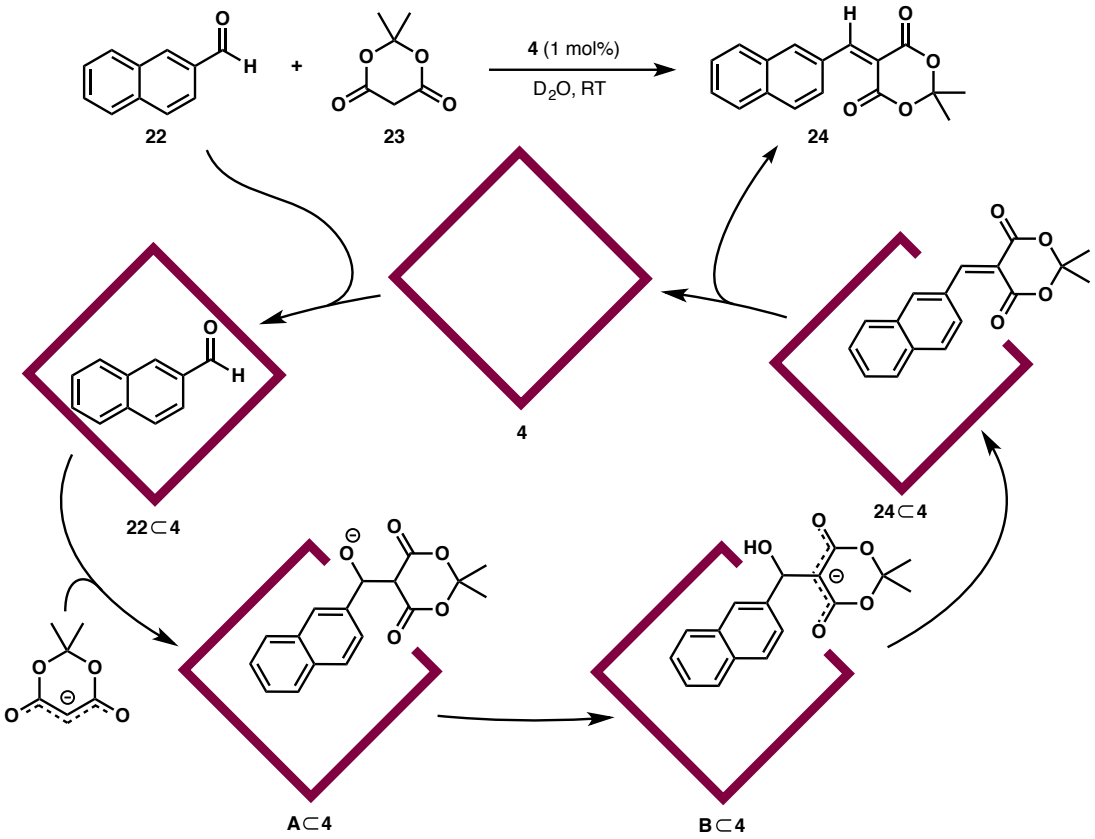

Scheme 1.5. Knoeveagel condensation of **22** and **23** catalyzed by cluster **4**.

Nitchke and coworkers demonstrated that $Fe_4L_6^{8+}$ tetrahedron **9** was capable of catalyzing the hydrolysis of the pesticide and chemical weapon simulant dichlorvos (**25**).[52] The alkyl phosphate undergoes an accelerated hydrolysis in the presence of 1 mole percent of **9** to form dimethylphosphoric acid, **26**, as the major product, and dichlorovinylmethylphosphoric acid, **27**, as the minor product (Scheme 1.6). The degree of acceleration, which is not quantified in the original report, is modest, certainly not exceeding an order of magnitude. However, control experiments in the presence of the individual components of self-assembly for **9**, or **9** in the presence of a strongly bound guest, clearly show that the cavity of **9** is integral to the observed acceleration. The authors suggest that, in addition to Coulombic stabilization of the developing negative charge, the pendant hydroxyl groups on the ligand may play a role in the catalysis.

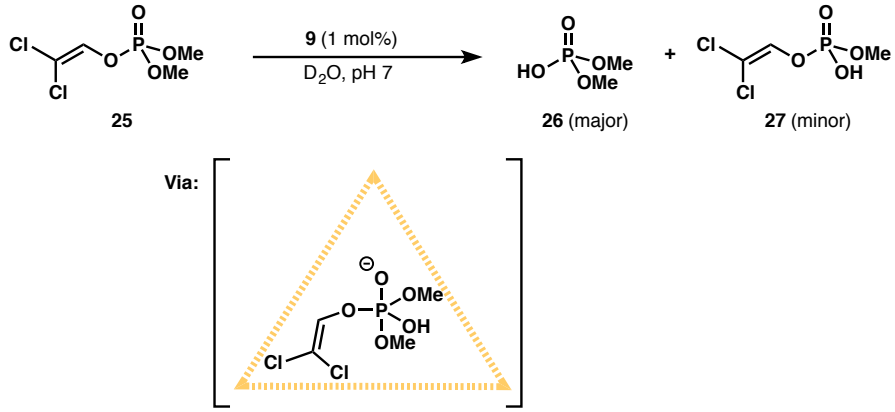

Scheme 1.6. Solvolysis of alkyl phosphate **25** accelerated by cluster **9**.

Ward and coworkers reported the implementation of $Co_8L_{12}^{16+}$ cube **8** as a catalyst for the acceleration of the Kemp elimination of benzoxazole (**28**), to afford the phenoxide **29** (Scheme 1.7).[65] Assembly **8** has been shown to preferentially bind neutral guests, not only relative to cationic species, but also relative to anionic species. This is attributed to the increased enthalpy of solvation for potential anionic guests such as benzoates. As such, anionic ring opened product **29** is rapidly expelled from the cavity of **8**, preventing product inhibition from hampering conversion, and facilitating turnover numbers in excess of 100. Interestingly, the rate of the Kemp elimination catalyzed by **8** is independent of pH, while the elimination in bulk solution is first order in hydroxide concentration. The authors suggest this phenomenon is explained by a high local concentration of hydroxide around the apertures of the cluster. This is supported by the observation that catalysis is completely inhibited when a large excess of chloride ion is added to the system in order to displace ion-paired hydroxide from the cluster. (More recently, the Ward group reported that cluster **8** is also capable of catalyzing the same hydrolysis reaction of alkyl phosphate **25** that was previously demonstrated by the Nitschke group.[66])

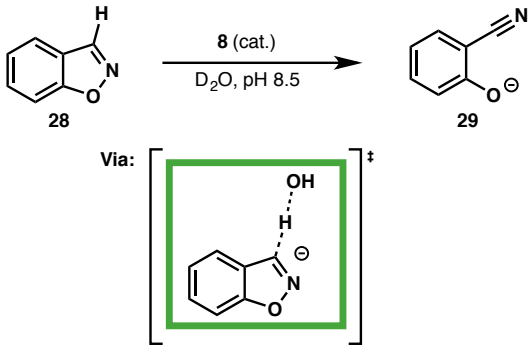

Scheme 1.7. Kemp elimination of **28** catalyzed by assembly **8**.

1.4.3 Supramolecular Catalysis Involving Cationic Transition States

Self-assembled microenvironment catalysis of reactions that develop positive charge in their transition state has been studied most extensively, particularly through collaborative work among the Raymond, Toste and Bergman groups, as well as by the Tiefenbacher group. While the transformations achieved by the Raymond and Tiefenbacher groups are similar

(*vide infra*), the assemblies which effect this catalysis (metal ligand cluster **6** from the Raymond group and hexameric resorcinarene capsule **3** from the Tiefenbacher group) differ in their mechanism of self assembly and their host properties. The dodecaanionic charge of cluster **6** begets solubility in water and other highly polar solvents. As such, the solvophobic effects play an important role in the thermodynamics of encapsulation within **6**. Furthermore, coulombic stabilization plays a significant role in the interactions between **6** and positively charged species. In contrast, capsule **3** is neutral upon assembly, and is therefore soluble in organic solvents such as chloroform. The hydrogen bond network around the seams of **3** renders it a fairly strong phenolic Brønsted acid, with the negative charge on the conjugate base highly delocalized around the capsule due to proton shuttling. On the other hand, highly electron rich aromatic rings compose the cavity walls for both **6** and **3**, which is ideal for cation recognition through cation-π interaction.

Following the observation that amines and phosphines underwent a basic pKa shift of up to 4.5 units upon encapsulation within **6**,[67] the Raymond and Bergman groups sought to demonstrate that transient protonation within **6** of more weakly basic molecules could be applied towards catalysis. This was first realized in the hydrolysis of trialkyl orthoformates in basic water, catalyzed by **6** (Scheme 1.8).[68] Size exclusion was observed in this system, with no observed acceleration in the hydrolysis of *n*-pentyl- or phenylorthophormate. This process proceeds by a Michaelis-Menten like mechanism, with rate accelerations of up to 3900 fold when R = *n*-butyl.[69] Furthermore, the authors favor a mechanism involving a rate determining protonation of the encapsulated orthoformate, whereas proton catalyzed orthorformate hydrolysis in bulk solution is expected to proceed by reversible protonation followed by rate limiting expulsion of one alkoxy group. This is supported by the observation of a negative entropy of activation ($\Delta S^{\ddagger}$ = -5 cal/mol*K), as well as a solvent isotope effect of 1.6, both inconsistent with the canonical bulk solution hydrolysis mechanism. This work was further extended to the catalytic hydrolysis of ketals and acetals by **6**.[70,71]

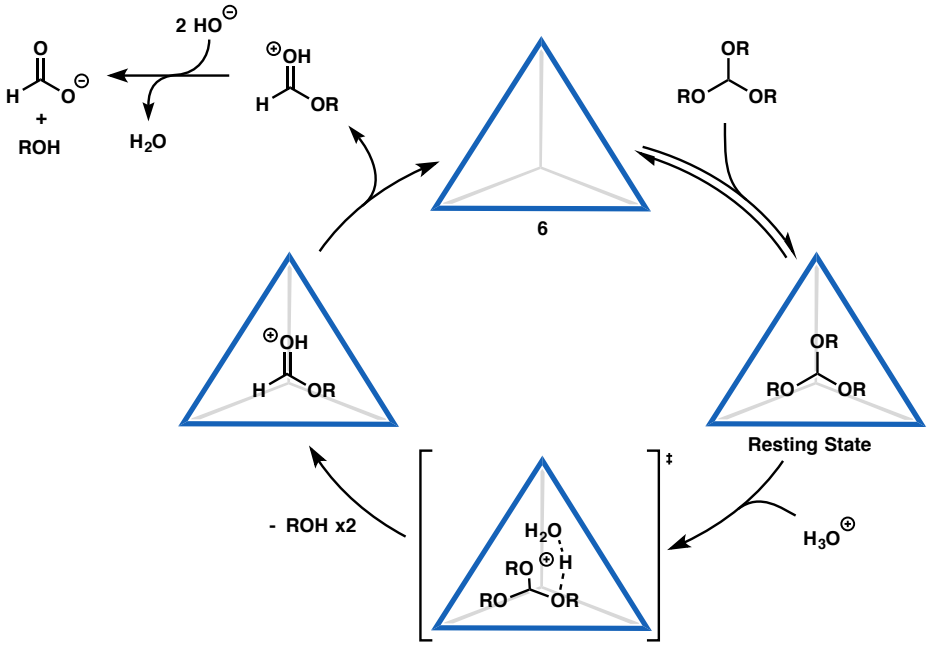

Scheme 1.8. Hydrolysis of orthoformates catalyzed by **6**.

Brønsted acid hydrolysis is also catalyzed by capsule **3**. While the bulk of the application of **3** as a microenvironment catalyst has been carried out by the Tiefenbacher group, **3** was first applied as a catalyst in 2013 by Strukul and coworkers, in the hydrolysis of isonitriles to afford alkyl formamides (Scheme 1.9A).[72] Later in the same year, Tiefenbacher reported the application of **3** as a catalyst for acetal hydrolysis (Scheme 1.9B).[32] Interestingly, hydrolysis of acetals by **3** was found to be highly selective for the hydrolysis of short chain aliphatic acetals, with 1,1-diethoxyethane (**30**) hydrolyzed selectively over 1,1-diethoxydodecane (**31**) to form aldehydes (**32** and **33** respectively) in a 98:2 ratio, despite the fact that both guests are easily accommodated within the cavity of **3**.

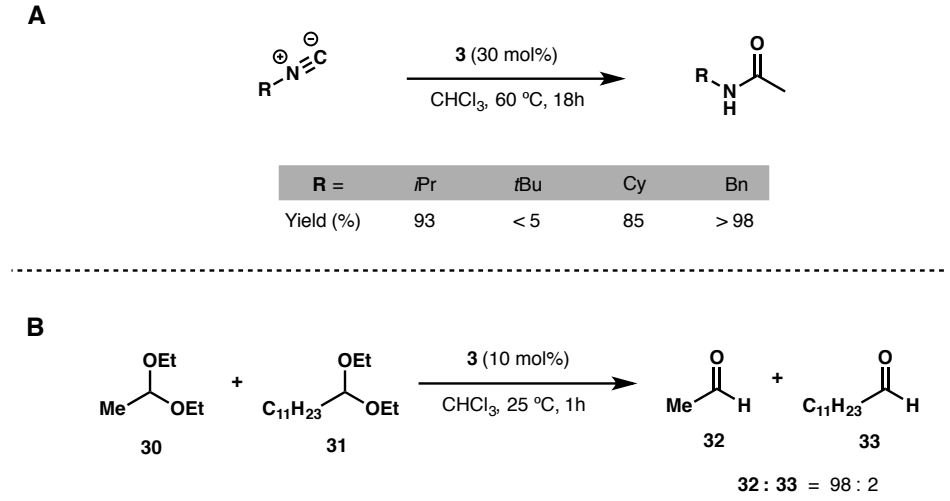

Scheme 1.9. (A) Hydrolysis of isonitriles promoted by **3**. (B) Hydrolysis of acetals promoted by **3**.

Having demonstrated a proof of principle for Brønsted acid catalysis within **6**, the Raymond and Bergman groups set out to apply this modality to a more synthetically relevant transformation. It was hypothesized that an acid promoted cyclization reaction would combine the elements contributing to cation stabilization from the orthoformate hydrolysis and the reduction of the entropic barrier to cyclization observed in the aza-Cope cyclization (*vide supra*). In accordance with this hypothesis, the targeted transformation was the Nazarov-like cyclization of divinyl alcohol **34** to afford pentamethylcyclopentadiene **35**, which would occur through protonation and ionization of the hydroxyl group, followed by 4π-conrotatory ring closure and elimination (Scheme 1.10A).[73] In the presence of a catalytic amount of cluster **6**, **35** was rapidly formed, however, it was found to be strongly encapsulated by **6**, and thus product inhibition hampered efficient catalyst turnover. In order to overcome this, an equivalent of maleimide was added to the reaction, which underwent a rapid Diels-Alder cycloaddition with **35** to afford adduct **36**, which is not encapsulated by **6**. Impressively, for substrate ***Z,Z*-34**, an enzyme-like rate acceleration of 2.1×10^6 was measured, representing the largest rate acceleration of the synthetic microenvironment catalyst at the time of its publication. Further study revealed that under milder conditions (unbuffered D_2O at 25 ºC), the kinetic product of elimination for substrates ***E,E*-34** and ***Z,Z*-34** was diene **37**, derived from selective deprotonation of the methyl group while inside the cluster (Scheme 1.10B).[74] This kinetic product could not be detected upon reaction in bulk solution. Subjecting **37** to the

original reaction conditions afforded rapid isomerization to **35**, which explains how it eluded detection in the initial report.

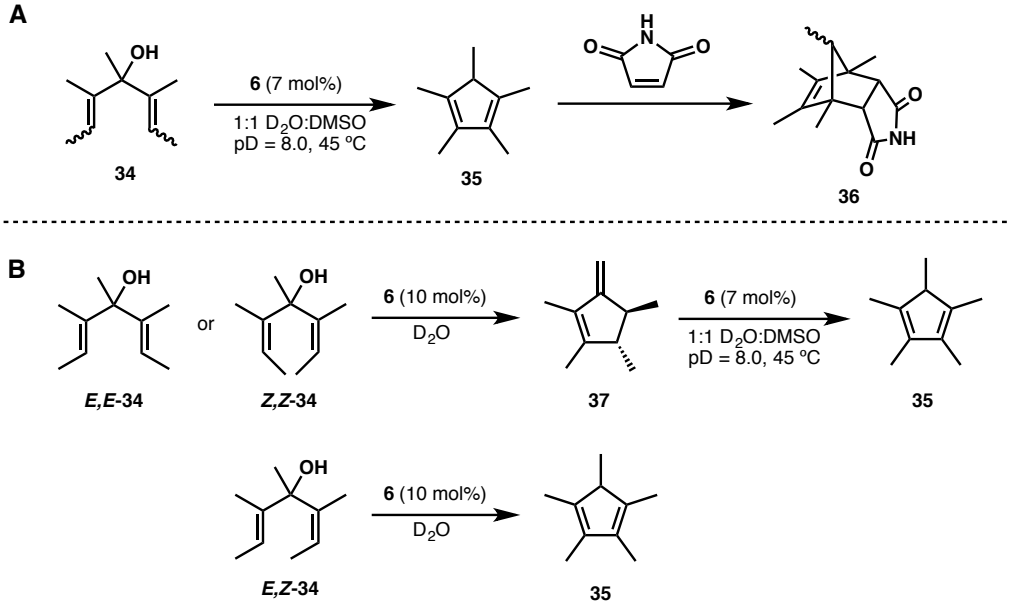

Scheme 1.10. (A) Nazarov-like cyclization of **34** catalyzed by cluster **6**. (B) Identification of the kinetic product of elimination for each isomer of **34**.

The Tiefenbacher group was also able to extend their Brønsted acid mediated hydrolysis within **3** to an acid mediated cyclization reaction. It was found that appropriately basic olefins baring a pendant alcohol group, such as **38**, could undergo protonation at the double bond to generate a tertiary carbocation, which would then be trapped by the hydroxyl group to form a cyclic ether (**39**) (Scheme 1.11).[75] The system was tolerant to some substitution, with most substrates proceeding to around 90% conversion in the presence of **3**, with less than 10% conversion in the background reaction for all substrates.

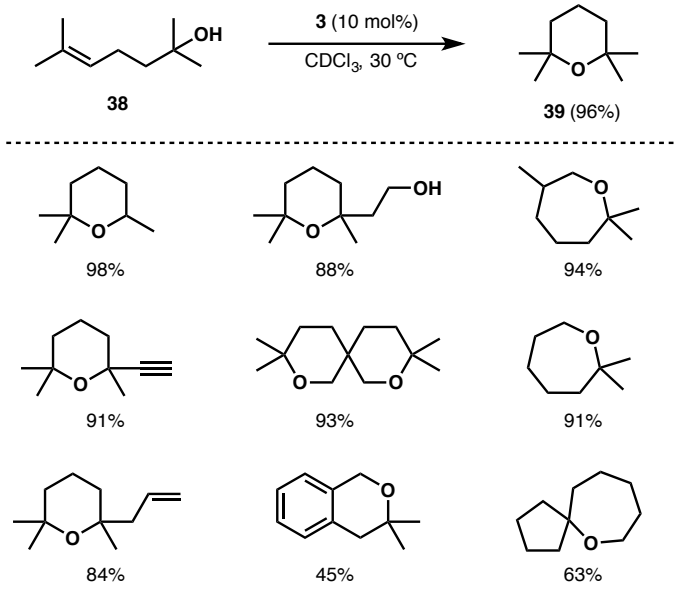

Scheme 1.11. Hydroalkoxylative cyclization catalyzed by assembly **3**.

The Raymond and Bergman groups, in collaboration with the Toste group, were further able to demonstrate that cluster **6** was capable of the activating carbonyl groups for nucleophilic attack, in the form of a Prins cyclization of terpene **40** (Scheme 1.12).[76] After reversible encapsulation and protonation, the activated carbonyl group undergoes nucleophilic attack from the pendant double bond, to generate a carbocationic intermediate, which is then quenched by elimination within the cluster to afford cyclized product **41**. Notably, this process is highly selective for elimination inside of the cluster (97%), presumably due to water exclusion from the hydrophobic interior of the cluster cavity. In contrast, when aldehyde **40** is subjected to phosphoric acid catalyzed cyclization in bulk solution, diol **42** is obtained from hydration of the carbocationic intermediate with 92% selectivity. Rate accelerations of up to 1.9 x 10^5 fold have been observed when related enantioenriched cluster ΔΔΔΔ-**7** is matched with (*R*)-**40**.[77]

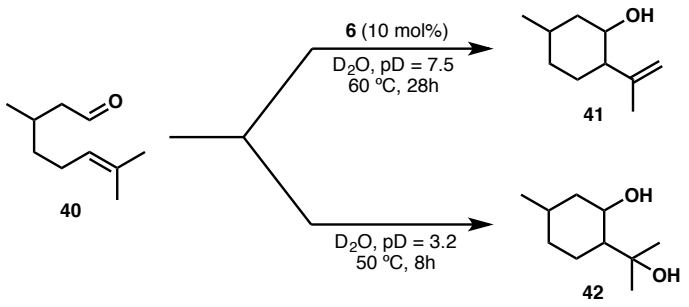

Scheme 1.12. Prins cyclization of aldehyde **40** catalyzed by **6**.

The Tiefenbacher group was able to demonstrate that assembly **3** was also capable of catalyzing the cyclization of terpenoid molecules.[78] While geraniol, nerol, and linalool could be cyclized by catalytic amounts of assembly **3**, these cyclizations were hampered by significant water trapping due to the equivalent of water liberated upon ionization of the starting material. Their corresponding acetyl esters (**43**, **45**, and **46** respectively) underwent cyclization with decreased byproducts from water trapping. The major product for the catalyzed cyclization of geranyl acetate **43** was α-terpinene (**44**), derived from ionization, cyclization and a 1,2-hydride shift, followed by elimination to form the conjugated diene (Scheme 1.13A). In contrast, both linalyl acetate (**45**) and neryl acetate (**46**) afforded predominantly terpinolene (**47**) at early reaction times, with an increasing proportion of α-terpinene (**44**) at extended reaction time (Scheme 1.13B). The authors suggest that this difference in reactivity can be explained by the fact that **45** and **46** can both undergo a concerted cyclization (by S_N2 or S_N2'), while the olefin geometry of **43** results in the necessity for a two step ionization/isomerization to occur before cyclization can take place. The authors further hypothesize that the relatively long-lived allylic cation intermediate in the cyclization of **43** allows the basic acetate to diffuse from the intermediate, and thus after cyclization there is ample time for the hydride migration to occur before deprotonation. In contrast, after direct concerted cyclization for substrates **45** and **46**, the acetate leaving group is in close proximity to the unstabilized carbocationic intermediate and thus direct elimination outcompetes the hydride migration pathway.

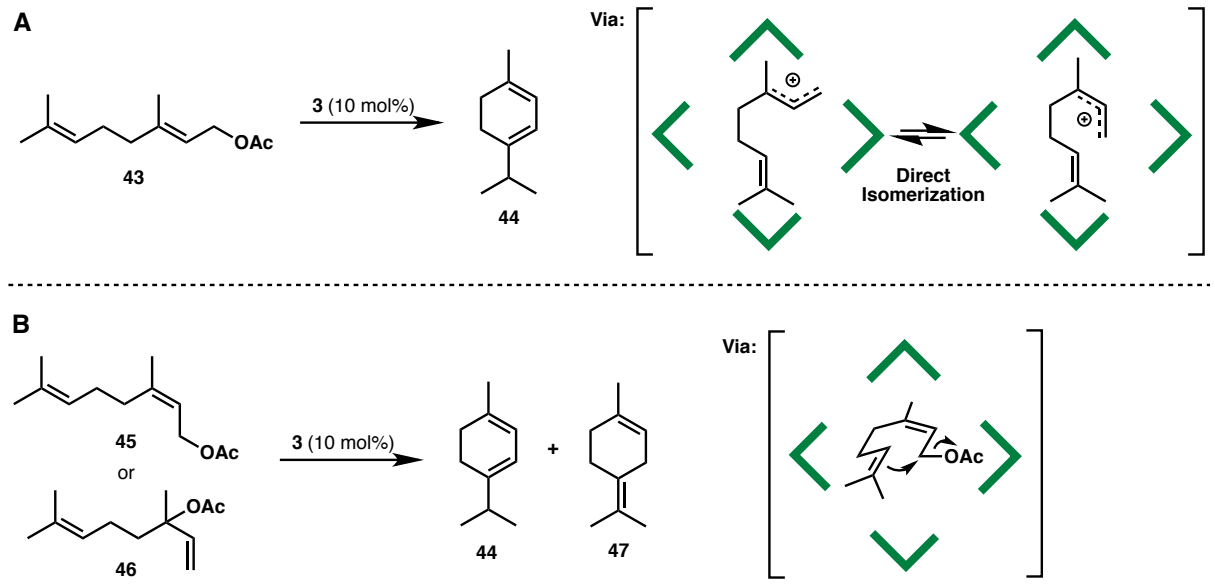

Scheme 1.13. (A) Cyclization of geranyl acetate (**43**) catalyzed by **3**. (B) Cyclization of linalyl acetate (**45**) and neryl acetate (**46**) catalyzed by **3**.

A final intriguing example of microenvironment catalysis of reactions proceeding through cationic transition states was the observation that clusters **5** and **6** accelerated the solvolysis of activated benzylic alcohols and benzyl halides with retention of stereochemistry (Scheme 1.14).[79] In particular, when enantioenriched trichloroacetimidate (*S*)-**48** was subjected to cluster **6** with loadings as low as 2.5 mol%, methanolysis product **49** could be isolated with 74 percent retention of stereochemistry. In contrast, bulk-solution methanolysis of **48** afforded **49** with 84 percent inversion of stereochemistry. It was proposed that the retention of stereochemistry within the cavity of the supramolecular cluster is the result of a strong interaction between the nascent carbocationic intermediate and the naphthalene walls of the supramolecular cluster, preventing approach from the opposite face.

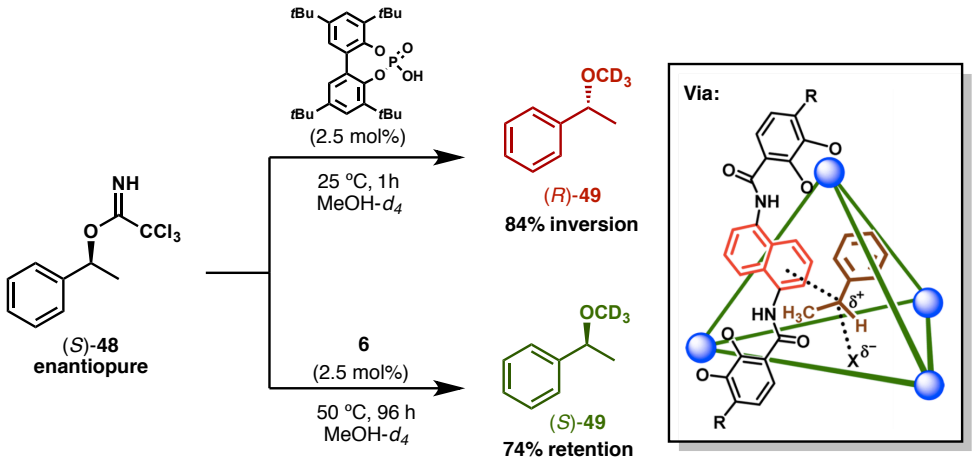

Scheme 1.14. Methanolysis of **48** with retention of stereochemistry, catalyzed by cluster **6**.

1.5 Conclusions and Outlook

Supramolecular microenvironment catalysis offers an intriguing opportunity to gain insight into the effects of subtle intermolecular interactions in reaction transition states. Further study in this field will continue to provide insight by analogy to similar phenomena in the biological context of enzymatic catalysis, and will contribute to the construction of novel catalyst platforms. The advent of self-assembled supramolecular architectures has led to a dramatic expansion in the quantity and diversity of transformations effected by supramolecular microenvironment catalysts. The marked increase in the complexity of catalyzed reactions over the past two decades highlights the rapid maturation of the field, and this trend shows no indications of deceleration.

As new research groups enter this area of research, and the number of examples of catalysis continue to increase, it is essential to take a retrospective look at the common threads that can be drawn among the body of published work, and to apply these lessons to direct catalyst design and identify potential new transformations. It is clear that the electronic properties of the supramolecular host are intimately tied to the nature of the developing charge in the transition states for the reactions that they are capable of accelerating. Overall assembly charge is likely to play an important role in charge stabilization. The electronics of the cavity walls are also likely to be a key factor in the stabilization of complementary electron rich or electron poor reaction intermediates. As new assemblies are designed with catalysis in mind, these features are sure to be accentuated and rigorously evaluated.

1.6 References

(1) Raynal, M.; Ballester, P.; Vidal-Ferran, A.; Leeuwen, P. W. N. M. van. *Chem. Soc. Rev.* **2014**, *43* (5), 1734.
(2) Kirby, A. J. *Angew. Chem. Int. Ed. Engl.* **1996**, *35* (7), 706.
(3) Brown, C. J.; Toste, F. D.; Bergman, R. G.; Raymond, K. N. *Chem. Rev.* **2015**, *115* (9), 3012.
(4) De Vries, J. G.; Jackson, S. D. *Catal. Sci. Technol.* **2012**, *2* (10), 2009.
(5) Nugent, W. A.; RajanBabu, T. V.; Burk, M. J. *Science* **1993**, *259* (5094), 479.
(6) Crawley, M. L.; Trost, B. M. *Applications of Transition Metal Catalysis in Drug Discovery and Development: An Industrial Perspective*; John Wiley & Sons, 2012.
(7) Zhao, Y.; Cotelle, Y.; Sakai, N.; Matile, S. *J. Am. Chem. Soc.* **2016**, *138* (13), 4270.
(8) Wiester, M. J.; Ulmann, P. A.; Mirkin, C. A. *Angew. Chem. Int. Ed.* **2011**, *50* (1), 114.
(9) Knowles, R. R.; Jacobsen, E. N. *Proc. Natl. Acad. Sci.* **2010**, *107* (48), 20678.
(10) Pauling, L. *Nature* **1948**, *161*, 707.
(11) Nelson, D. L.; Lehninger, A. L.; Cox, M. M. *Lehninger Principles of Biochemistry*; Macmillan, 2008.
(12) Berg, J. M.; Tymoczko, J. L.; Stryer, L. *Biochemistry*; W. H. Freeman, 2010.
(13) Silverman, R. B. *The Organic Chemistry of Enzyme-catalyzed Reactions*; Academic Press, 2002.
(14) Cunningham, F. X.; Gantt, E. *Proc. Natl. Acad. Sci.* **2001**, *98* (5), 2905.
(15) Degenhardt, J.; Köllner, T. G.; Gershenzon, J. *Phytochemistry* **2009**, *70* (15–16), 1621.
(16) Köksal, M.; Hu, H.; Coates, R. M.; Peters, R. J.; Christianson, D. W. *Nat. Chem. Biol.* **2011**, *7* (7), 431.
(17) Christianson, D. W. *Chem. Rev.* **2006**, *106* (8), 3412.
(18) Köksal, M.; Jin, Y.; Coates, R. M.; Croteau, R.; Christianson, D. W. *Nature* **2011**, *469* (7328), 116.
(19) Pedersen, C. J. *Angew. Chem. Int. Ed. Engl.* **1988**, *27* (8), 1021.
(20) Lehn, J.-M. *Angew. Chem. Int. Ed. Engl.* **1988**, *27* (1), 89.
(21) Cram, D. J. *Angew. Chem. Int. Ed. Engl.* **1988**, *27* (8), 1009.
(22) Steed, J. W.; Atwood, J. L. *Supramolecular Chemistry*; Wiley, 2009.
(23) Leininger, S.; Olenyuk, B.; Stang, P. J. *Chem. Rev.* **2000**, *100* (3), 853.
(24) Swiegers, G. F.; Malefetse, T. J. *Coord. Chem. Rev.* **2002**, *225* (1–2), 91.
(25) Seidel, S. R.; Stang, P. J. *Acc. Chem. Res.* **2002**, *35* (11), 972.
(26) Yoshizawa, M.; Klosterman, J. K.; Fujita, M. *Angew. Chem. Int. Ed.* **2009**, *48* (19), 3418.
(27) Shivanyuk, A.; Rebek, J. *Proc. Natl. Acad. Sci.* **2001**, *98* (14), 7662.
(28) Heinz, T.; Rudkevich, D. M.; Rebek, J. *Nature* **1998**, *394* (6695), 764.
(29) Rudkevich, D. M.; Hilmersson, G.; Rebek, J. *J. Am. Chem. Soc.* **1997**, *119* (41), 9911.
(30) Kang, J.; Rebek, J. *Nature* **1996**, *382* (6588), 239.
(31) MacGillibray, L.; Atwood, J. *Nature* **1997**, *389*, 469.
(32) Zhang, Q.; Tiefenbacher, K. *J. Am. Chem. Soc.* **2013**, *135* (43), 16213.
(33) Fujita, M.; Yazaki, J.; Ogura, K. *J. Am. Chem. Soc.* **1990**, *112* (14), 5645.
(34) Takeda, N.; Umemoto, K.; Yamaguchi, K.; Fujita, M. *Nature* **1999**, *398* (6730), 794.
(35) Fujita, N.; Biradha, K.; Fujita, M.; Sakamoto, S.; Yamaguchi, K. *Angew. Chem. Int. Ed.* **2001**, *40* (9), 1718.

(36) Kumazawa, K.; Biradha, K.; Kusukawa, T.; Okano, T.; Fujita, M. *Angew. Chem. Int. Ed.* **2003**, *42* (33), 3909.
(37) Fujita, M.; Oguro, D.; Miyazawa, M.; Oka, H.; Yamaguchi, K.; Ogura, K. *Nature* **1995**, *378* (6556), 469.
(38) Fujita, M.; Yu, S.-Y.; Kusukawa, T.; Funaki, H.; Ogura, K.; Yamaguchi, K. *Angew. Chem. Int. Ed.* **1998**, *37* (15), 2082.
(39) Saalfrank, R. W.; Stark, A.; Peters, K.; von Schnering, H. G. *Angew. Chem. Int. Ed. Engl.* **1988**, *27* (6), 851.
(40) Caulder, D. L.; Powers, R. E.; Parac, T. N.; Raymond, K. N. *Angew. Chem. Int. Ed.* **1998**, *37* (13-14), 1840.
(41) Caulder, D. L.; Brückner, C.; Powers, R. E.; König, S.; Parac, T. N.; Leary, J. A.; Raymond, K. N. *J. Am. Chem. Soc.* **2001**, *123* (37), 8923.
(42) Sgarlata, C.; Mugridge, J. S.; Pluth, M. D.; Tiedemann, B. E. F.; Zito, V.; Arena, G.; Raymond, K. N. *J. Am. Chem. Soc.* **2010**, *132* (3), 1005.
(43) Davis, A.; Fiedler, D.; Seeber, G.; Zahl, A.; van Eldik, R.; Raymond, K. N. *J. Am. Chem. Soc.* **2006**, *128*, 1324.
(44) Leung, D. H.; Bergman, R. G.; Raymond, K. N. *J. Am. Chem. Soc.* **2008**, *130* (9), 2798.
(45) Davis, A. V.; Raymond, K. N. *J. Am. Chem. Soc.* **2005**, *127* (21), 7912.
(46) Terpin, A. J.; Ziegler, M.; Johnson, D. W.; Raymond, K. N. *Angew. Chem. Int. Ed.* **2001**, *40* (1), 157.
(47) Zhao, C.; Sun, Q.-F.; Hart-Cooper, W. M.; DiPasquale, A. G.; Toste, F. D.; Bergman, R. G.; Raymond, K. N. *J. Am. Chem. Soc.* **2013**, *135* (50), 18802.
(48) Paul, R. L.; Bell, Z. R.; Jeffery, J. C.; McCleverty, J. A.; Ward, M. D. *Proc. Natl. Acad. Sci.* **2002**, *99* (8), 4883.
(49) Tidmarsh, I. S.; Faust, T. B.; Adams, H.; Harding, L. P.; Russo, L.; Clegg, W.; Ward, M. D. *J. Am. Chem. Soc.* **2008**, *130* (45), 15167.
(50) Bell, Z. R.; Jeffery, J. C.; McCleverty, J. A.; Ward, M. D. *Angew. Chem. Int. Ed.* **2002**, *41* (14), 2515.
(51) Argent, S. P.; Adams, H.; Riis-Johannessen, T.; Jeffery, J. C.; Harding, L. P.; Ward, M. D. *J. Am. Chem. Soc.* **2006**, *128* (1), 72.
(52) Bolliger, J. L.; Belenguer, A. M.; Nitschke, J. R. *Angew. Chem. Int. Ed.* **2013**, *52* (31), 7958.
(53) Mock, W. L.; Irra, T. A.; Wepsiec, J. P.; Manimaran, T. L. *J. Org. Chem.* **1983**, *48* (20), 3619.
(54) Kang, J.; Santamaría, J.; Hilmersson, G.; Rebek, J. *J. Am. Chem. Soc.* **1998**, *120* (29), 7389.
(55) Kang, J.; Rebek, J. *Nature* **1997**, *385* (6611), 50.
(56) Kang, J.; Hilmersson, G.; Santamaría, J.; Rebek, Jr., J. *J. Am. Chem. Soc.* **1998**, *120*, 3650.
(57) Kusukawa, T.; Nakai, T.; Okano, T.; Fujita, M. *Chem. Lett.* **2003**, *32* (3), 284.
(58) Yoshizawa, M.; Tamura, M.; Fujita, M. *Science* **2006**, *312* (5771), 251.
(59) Murase, T.; Horiuchi, S.; Fujita, M. *J. Am. Chem. Soc.* **2010**, *132* (9), 2866.
(60) Fiedler, D.; Bergman, R. G.; Raymond, K. N. *Angew. Chem.* **2004**, *116* (48), 6916.
(61) Fiedler, D.; van Halbeek, H.; Bergman, R. G.; Raymond, K. N. *J. Am. Chem. Soc.* **2006**, *128* (31), 10240.

(62) Hastings, C. J.; Fiedler, D.; Bergman, R. G.; Raymond, K. N. *J. Am. Chem. Soc.* **2008**, *130* (33), 10977.
(63) Brown, C. J.; Bergman, R. G.; Raymond, K. N. *J. Am. Chem. Soc.* **2009**, *131* (48), 17530.
(64) Murase, T.; Nishijima, Y.; Fujita, M. *J. Am. Chem. Soc.* **2012**, *134* (1), 162.
(65) Cullen, W.; Misuraca, M. C.; Hunter, C. A.; Williams, N. H.; Ward, M. D. *Nat. Chem.* **2016**, *8* (3), 231.
(66) Taylor, C. G. P.; Piper, J. R.; Ward, M. D. *Chem Commun* **2016**, *52* (37), 6225.
(67) Pluth, M. D.; Bergman, R. G.; Raymond, K. N. *J. Am. Chem. Soc.* **2007**, *129* (37), 11459.
(68) Pluth, M. D.; Bergman, R. G.; Raymond, K. N. *Science* **2007**, *316* (5821), 85.
(69) Pluth, M. D.; Bergman, R. G.; Raymond, K. N. *J. Am. Chem. Soc.* **2008**, *130* (34), 11423.
(70) Pluth, M. D.; Bergman, R. G.; Raymond, K. N. *Angew. Chem. Int. Ed.* **2007**, *46* (45), 8587.
(71) Pluth, M. D.; Bergman, R. G.; Raymond, K. N. *J. Org. Chem.* **2009**, *74* (1), 58.
(72) Bianchini, G.; Sorella, G. L.; Canever, N.; Scarso, A.; Strukul, G. *Chem. Commun.* **2013**, *49* (46), 5322.
(73) Hastings, C. J.; Pluth, M. D.; Bergman, R. G.; Raymond, K. N. *J. Am. Chem. Soc.* **2010**, *132* (20), 6938.
(74) Hastings, C. J.; Backlund, M. P.; Bergman, R. G.; Raymond, K. N. *Angew. Chem.* **2011**, *123* (45), 10758.
(75) Catti, L.; Tiefenbacher, K. *Chem Commun* **2015**, *51* (5), 892.
(76) Hart-Cooper, W. M.; Clary, K. N.; Toste, F. D.; Bergman, R. G.; Raymond, K. N. *J. Am. Chem. Soc.* **2012**, *134* (43), 17873.
(77) Hart-Cooper, W.; Zhao, C.; Triano, R.; Yaghoubi, P.; Ozores, H. L.; Burford, K.; Toste, F. D.; Bergman, R. G.; Raymond, K. *Chem. Sci.* **2014**.
(78) Zhang, Q.; Tiefenbacher, K. *Nat. Chem.* **2015**, *advance online publication*.
(79) Zhao, C.; Toste, F. D.; Raymond, K. N.; Bergman, R. G. *J. Am. Chem. Soc.* **2014**, *136* (41), 14409.

Chapter 2

Enabling New Modes of Reactivity via Constrictive Binding in a Microenvironment Catalyzed Aza-Prins Cyclization

Portions of this chapter have been previously published in:

Kaphan, D. M.; Toste, F. D.; Bergman, R. G.; Raymond, K. N. *J. Am. Chem. Soc.* **2015**, *137*, 9202-9205.

2.1 Preface

This chapter details the discovery and mechanistic investigation of a supramolecular microenvironment catalyzed aza-Prins cyclization. The cluster catalyzed cyclization features a reaction pathway that is divergent from that observed in bulk solution. This is achieved within the supramolecular cluster by modulating the conformation of a reactive intermediate, which results in an emergent transannular 1,5-hydride transfer event. This highlights the power of the supramolecular catalyst to modulate the entire microenvironment of a reaction, and enable reaction pathways that would be otherwise inaccessible under traditional catalytic conditions. Furthermore, this work represents a major extension of the motifs recognized as catalytic intermediates by the Raymond supramolecular cluster from Brønsted acid generated oxonium ions to iminium ions generated from *in situ* condensation.

2.2 Introduction

Synthetic supramolecular microenvironment catalysts share functional and mechanistic similarities to many naturally occurring enzymatic catalysts. Enzymes are capable of promoting reactivity with product selectivity, substrate specificity and rate acceleration that is often beyond the means of the synthetic chemist. In the enzymatic assembly and rearrangement of complex natural product carbon skeletons, the binding pocket of the enzyme is able to control the reactivity of high energy intermediates through a series of cooperative noncovalent interactions and substrate preorganization in order to selectively form molecules that would be difficult to access in bulk solution.[1] The cavity of a supramolecular capsule bears strong resemblance to many hydrophobic enzymatic active sites.[1g,h] The properties of such capsules can be investigated in order to shed light on the nature of analogous enzymatic catalysis, as well as to develop highly selective and specific synthetic catalysts.[2]

Synthetic microenvironment catalysts emulate the enzymatic strategy of transition state recognition within complementary solvent excluded cavities by cumulative noncovalent interactions. Many self-assembled supramolecular architectures have shown high levels of catalytic activity. In particular, specially designed molecular capsules have been shown to accelerate reactions such as Diels-Alder cyclizations, condensations, and sigmatropic rearrangements, among other transformations.[3,4] Despite these accomplishments, complete divergence of reactivity by selective stabilization of reaction pathways too high in energy to be observed in bulk solution is rare in catalytic supramolecular systems.[5]

The Raymond group has developed a metal ligand capsule of M_4L_6 stoichiometry (**1**).[6] Previous studies have illustrated the unique chemical microenvironment of the cluster's interior cavity. For example, amines and phosphines exhibit an increase in effective basicity of up to 4.5 pKa units upon encapsulation.[7] Moreover, constrictive binding within the cluster cavity lowers the entropic barrier to reactions with constrained transition state conformations and enthalpically disfavors less compact transition state conformations.[8] These synergistic effects have been shown to promote a variety of acid-catalyzed, as well as pericyclic, transformations. Notably, the cluster catalyzes a Nazarov-like cyclization with up to 10^6 fold rate acceleration, as well as the Prins cyclization of citronellal and related derivates.[4,9] Cluster **1** is also capable of stabilizing a number of high- energy species within its cavity (e.g. quantitative iminium ion formation can be observed within the cluster in aqueous media).[10]

2.3 Results and Discussion

2.3.1 Initial Observation of Divergent Reactivity

Given the propensity of cluster **1** to effect cyclizative reactivity and stabilize transient carbocations, combined with its ability to perturb the equilibrium of iminium ion formation within its cavity, it was hypothesized that **1** might also be an effective catalyst for the aza-Prins cyclization. In this transformation, an amino group tethered to a nucleophilic double bond undergos condensation with an aldehyde or ketone, followed by cyclization and elimination or hydration of the resulting carbocation. Unexpectedly, treatment of amine **2** with formaldehyde in the presence of cluster **1** at ambient temperature afforded substituted piperidine **3** as the main product, wherein demethylation at nitrogen and reduction of the putative carbenium generated by the cyclization of **2** had occurred (Figure 2.1). This stands in stark juxtaposition to the aza-Prins cyclization of **2** in bulk solution, which required heating to reflux in neat formic acid and afforded alcohol **4** as the product.

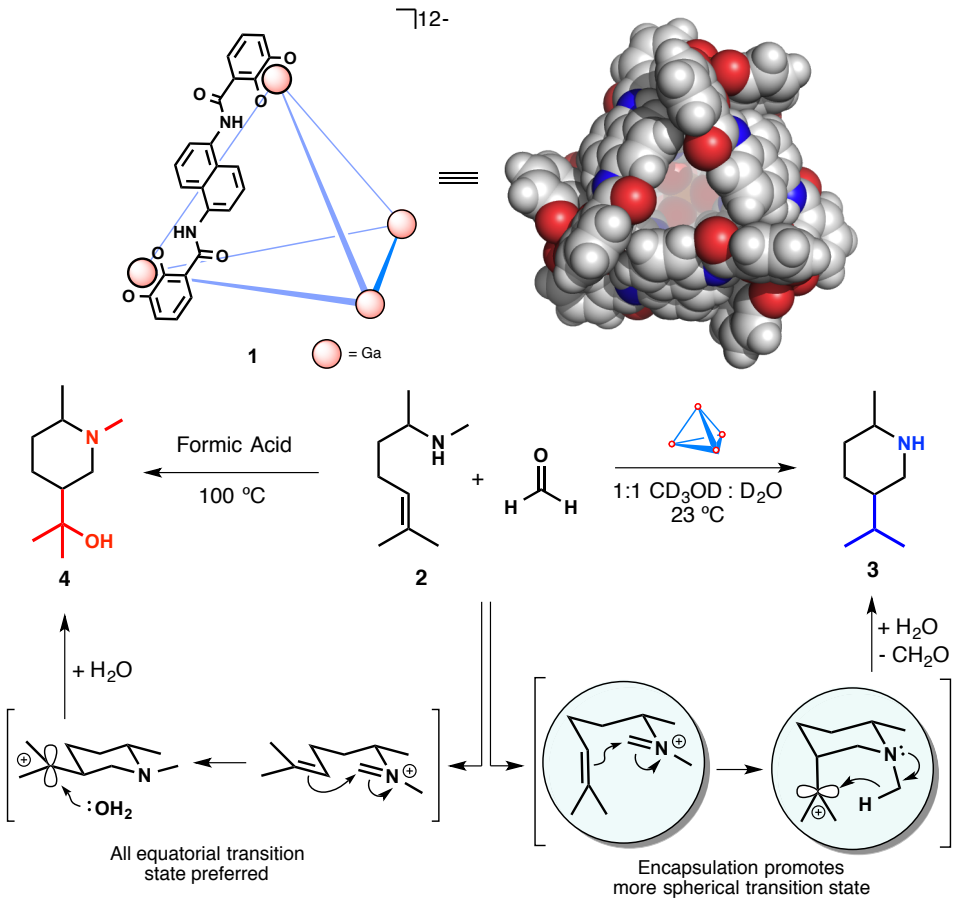

Figure 2.1. Divergent selectivity of cluster catalyzed aza-Prins cyclization.

2.3.2 Mechanistic Insights into the Formation of 3

In order to understand this unusual result, an isotopically enriched analogue of the starting material, **2**-d_3, was prepared in an effort to elucidate the origin of the hydrogen of the isopropyl methine in product **3**. **2**-d_3 was subjected to the cluster catalyzed aza-Prins

cyclization conditions, followed by treatment with *p*-nitrobenzenesulfonyl chloride in order to facilitate isolation and purification. The resulting sulfonamide, **5**-d_1, exhibited complete deuterium incorporation at the isopropyl methine (Scheme 2.1). Conversely, reaction of unlabeled amine **2** under otherwise identical conditions furnished nosylated product **5**, which did not incorporate any deuterium at the isopropyl methine (i.e., deuterium exchange with the solvent mixture does not account for the formation of **5**-d_1).

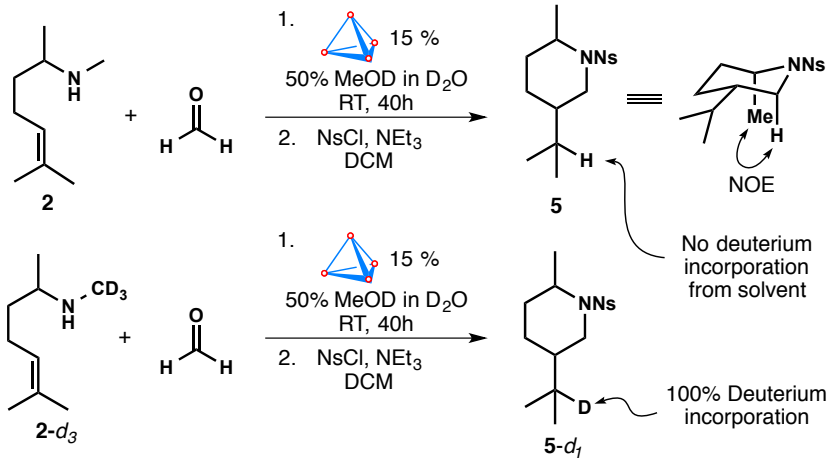

Scheme 2.1. Deuterium labeling study

Another observation that shed light on the mechanism of the divergent reactivity of **2** came from the exposure of the *N*-benzyl analogue of the starting material (**2i**) to the cluster cyclization conditions (Scheme 2.2). Importantly, the identical dealkylated amine product (**3**) was observed in conjunction with the appearance of benzaldehyde, suggesting the intermediacy of an iminium species resulting from hydride abstraction alpha to nitrogen, which undergoes hydrolysis.

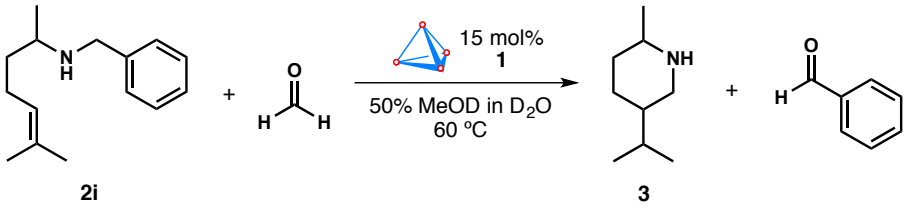

Scheme 2.2. Observation of benzaldehyde from the cyclization of **2i**, supporting an oxidative dealkylation mechanism.

The observation of quantitative deuterium incorporation from the cyclization of amine **2**-d_3, in addition to the appearance of benzaldehyde in the cyclization of **2i**, is consistent with a mechanism involving an aza-Prins cyclization with subsequent transannular 1,5-hydride transfer from the *N*-methyl group to the nascent tertiary carbocation (Figure 2.1). This divergent reactivity is hypothesized to be the result of the constrictive binding of the cluster cavity, which favors more compact transition states. This constrictive binding selects for the more compact axial orientation of the double bond in the transition state of the cyclization. Consequently, after cyclization, the carbocation in the intermediate is preorganized in close proximity to the *N*-methyl C-H bonds, facilitating a 1,5 through-space hydride transfer.

Hydrolysis of the resulting iminium ion in bulk solution affords **3**.[11] The relative configuration of product **5**—with the backbone methyl group in the axial position as determined by 1,3-diaxial NOE interactions—supports this hypothesis (Figure 2.2). This diastereomer likely reflects a transition state conformation that places the methyl group in an equatorial position and the double bond in an axial position, followed by a ring flip of the product to place the more sterically demanding isopropyl group in the equatorial position. In the absence of the unique cavity environment (i.e., in bulk solution), the enthalpically favored equatorial olefin orientation in the transition state should predominate. As the carbocation resulting from cyclization in bulk solution lacks the proximity to the *N*-methyl group and solvent exclusion necessary for hydride transfer to occur, it is rapidly sequestered by water to form alcohol **4**. This emergent mechanistic pathway is notable due to the fact that it is too high in energy to be observed in the absence of the constrictive microenvironment of the cluster's interior binding pocket.

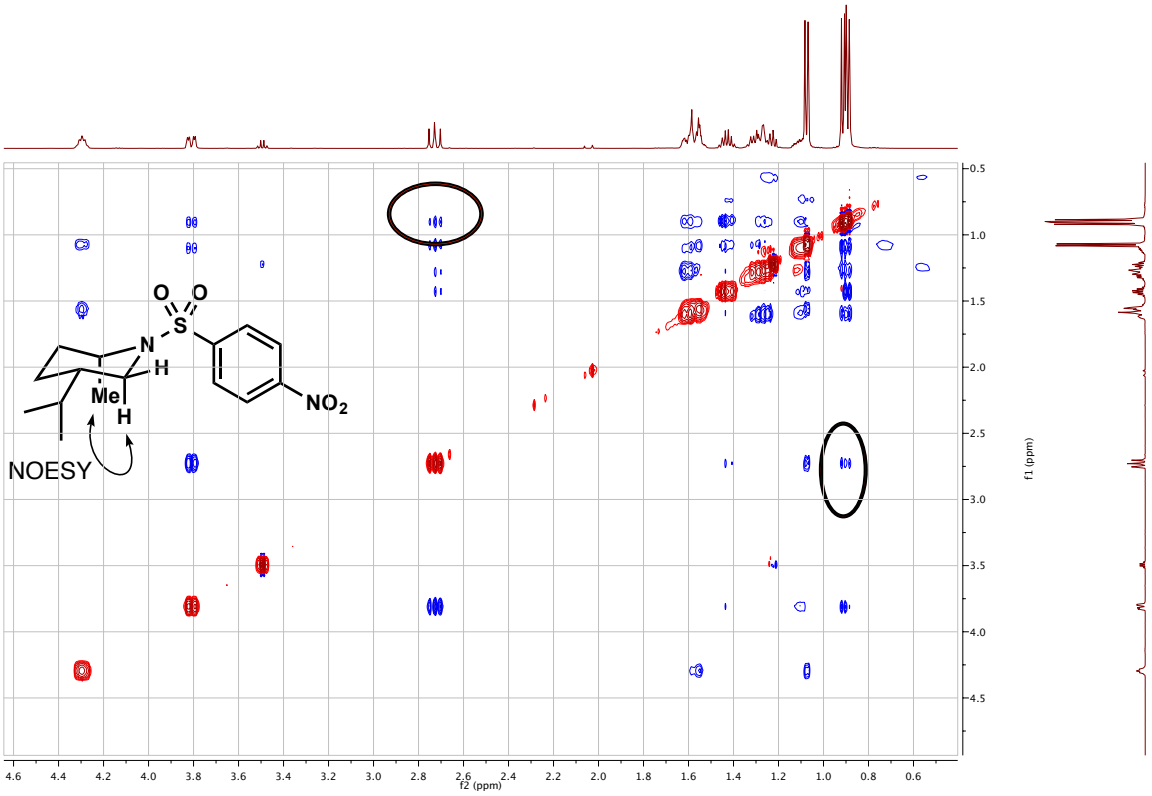

Figure 2.2. NOESY spectrum of **5** showing transannular interaction to determine relative stereochemistry

2.3.3 Substitutional Effects as a Mechanistic Probe

Having proposed a mechanism for the formation of **3** consistent with the experimental observations, the substitution at nitrogen was explored in order to gain further insight (Table 2.1). The parent *N*-methyl substrate **2a** underwent full conversion with three equivalents of formaldehyde and 20 mole percent cluster in a 25% MeOD in D_2O solvent mixture at room temperature in 40 hours. Increasing the chain length of *N*-alkyl substitution led to a sharp decrease in conversion: *N*-ethyl, -propyl and -butyl substrates proceeded to 53, 43 and 9 percent conversion, respectively. These data are consistent with size exclusion imposed by the

congested interior of the cluster. Branching alpha to the amine inhibited reactivity completely for *N*-isopropyl and *N*-cyclohexyl substrates **2f** and **2g**, even at elevated temperatures (entries 6 and 7); however, removal of the methyl group on the carbon backbone partially restored reactivity for the *N*-isopropyl substrate **2h** (entry 8). One possible explanation for this phenomenon is that doubly α-branched substrates are simply too bulky to undergo the condensation with formaldehyde to form the initial iminium ion, which precludes further reaction. *N*-benzylamine **2i** (entry 9) showed only trace reactivity, but by warming the reaction mixture to 60 ºC, 51 percent conversion was achieved after 40 hours. In contrast, 2-methoxybenzylamine **2j** (entry 10) did not react, even at elevated temperatures. This observation is again consistent with substrate specificity through size exclusion from the cluster cavity. Unexpectedly, *N*-trifluoroethyl substitution (entry 11) led to complete consumption of the starting material, however no hydride transfer was observed. Instead, elimination product **6** was observed exclusively.[12] This is most likely due to decreased hydricity alpha to the nitrogen because of the inductively electron withdrawing effect of the $-CF_3$ group.

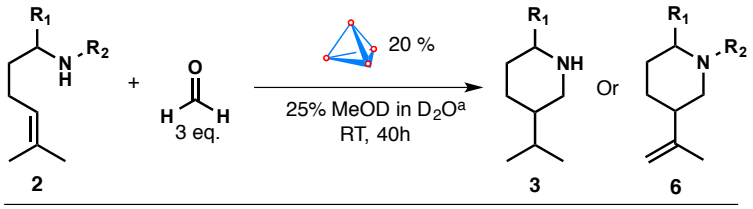

2 **3** **6**

Entry	R_1	R_2	Product	% Conversion[b]
1 (**2a**)	Me	Me	**3**	100
2 (**2b**)	H	Me	**3**	100
3 (**2c**)	Me	Et	**3**	53
4 (**2d**)	Me	*n*-Pr	**3**	43
5 (**2e**)	Me	*n*-Bu	**3**	9
6 (**2f**)	Me	*i*-Pr	*n/a*	0[c]
7 (**2g**)	Me	Cy	*n/a*	0[c]
8 (**2h**)	H	*i*-Pr	**3**	25
9 (**2i**)	Me	Bn	**3**	51[c]
10 (**2j**)	Me	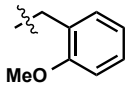	*n/a*	0
11 (**2k**)	Me		**6**	100

[a] pD = 8.0, $[PO_4^{3-}]$ = 100 mM [b]Calcluated by ratio of extracted product to starting material by ^{1}H-NMR spectroscopy [c] Conversion at 60 ºC

Table 2.1. Effect of N-substitution on reactivity.

2.3.4 Elucidation of the Overall Mechanism of Supramolecular Catalysis

A series of competition experiments were then conducted to determine the deuterium kinetic isotope effect associated with the 1,5 hydride shift (Scheme 2.3). First, the intermolecular isotope effect was assessed using a single vessel rate comparison of amine **2** and its trideuteromethyl labeled analogue **2**-d_3. In this experiment, the intermolecular kinetic

isotope effect was found to be 1.06 ± 0.03. The intramolecular isotope effect was then measured by preparing monodeuteromethylamine **2**-d_1 and subjecting it to the standard cluster catalyzed cyclization conditions. The intramolecular isotope effect was found to be 2.1 ± 0.4. The absence of an intermolecular isotope effect, while an intramolecular isotope effect was observed, indicates that the hydride transfer event occurs after rate limiting step of the catalytic cycle.

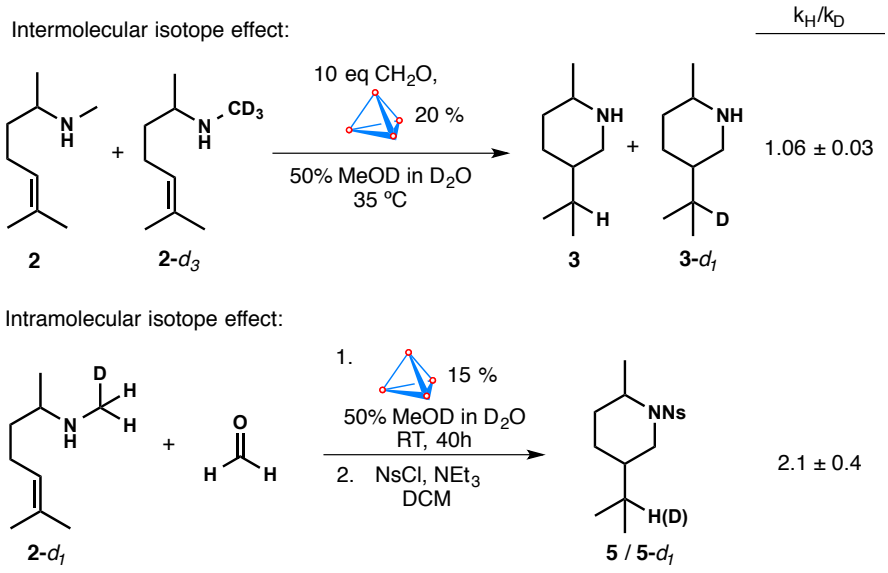

Scheme 2.3. Deuterium kinetic isotope experiments

Further kinetic analysis of the reaction was conducted with trifluoroethylamine **2k** as the substrate, given its convenient ^{19}F-NMR handle. Although **2k** undergoes elimination to form product **6**, it should follow a kinetic profile similar to that of **2a** due to the kinetic invisibility of the 1,5 hydride transfer in the transformation of **2a** to **3** (*vide supra*). When **2k** was exposed to formaldehyde in either the presence or absence of the cluster, a new peak was observed in the ^{19}F-NMR spectrum in addition to that of **2k**, which was assigned as hemiaminal **X**, the adduct of the amine and formaldehyde. This is supported by two major pieces of evidence. First, the minor species grows concomitantly with the addition of formaldehyde to the solution (Figure 2.3). Additionally, the ratio of the two starting material peaks is constant throughout the course of the cluster-catalyzed reaction (Figure 2.4). This suggests that the two species are in rapid equilibrium that is maintained over the course of the reaction. The consumption of the starting material [**2k** + **X**] displayed pseudo first order kinetic behavior with 10 or greater equivalents of formaldehyde.[13] Despite the tendency for tertiary amines to have a higher affinity for cluster **1**,[14] the product (**6**) was not strongly encapsulated, and therefore no product inhibition was observed. However, due to heterogeneity at the late stages of the reaction, the technique of initial rates was implemented.

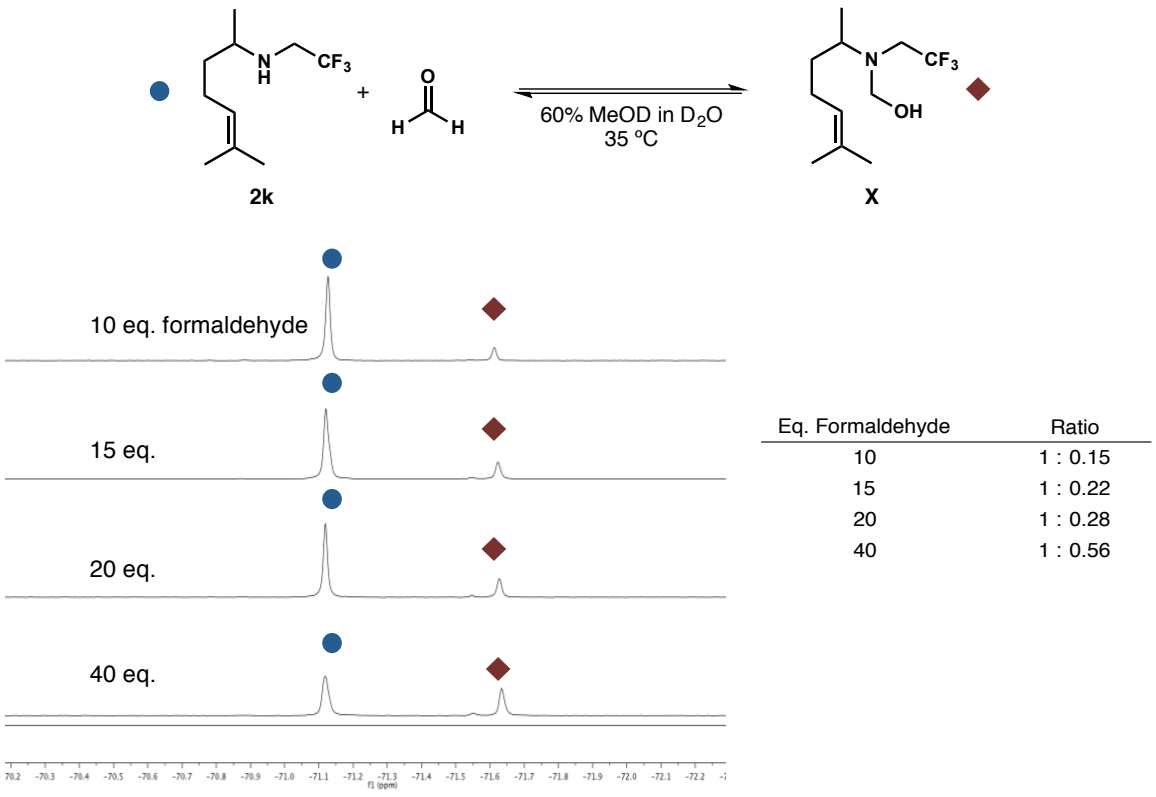

Eq. Formaldehyde	Ratio
10	1 : 0.15
15	1 : 0.22
20	1 : 0.28
40	1 : 0.56

Figure 2.3. Growth of an additional peak with addition of excess formaldehyde

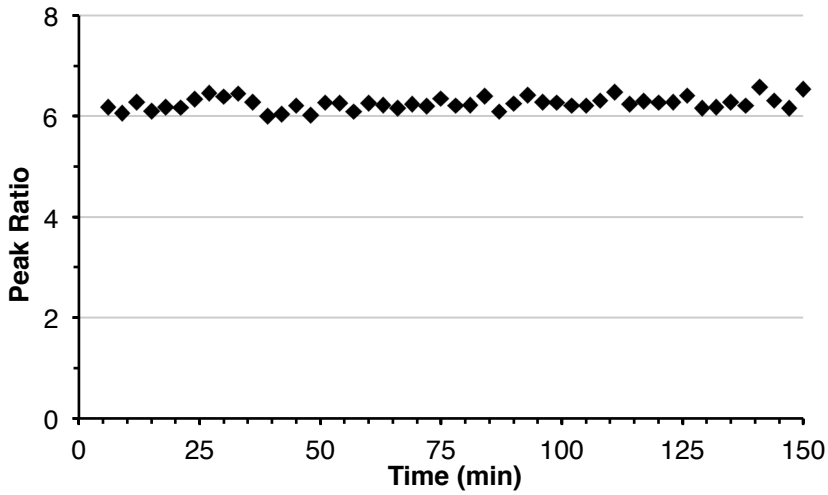

Figure 2.4. Constant peak ratio between **2k** and **X** over the course of the reaction.

The order of the reaction in cluster (**1**), substrate (**2k**) and formaldehyde was examined. The reaction was found to be first order in **2k**, however, the low solubility of the substrate precluded probing of the high concentration regime (Figure 2.5). The dependence of the rate on formaldehyde concentration[15] was also found to be first order over a range of 0.15 M to 0.6 M (10 to 40 equiv.; Figure 2.6). Intriguingly, variation of the concentration of the supramolecular catalyst did not result in a linear first-order rate dependence. Instead, a roughly first order regime was observed at low cluster concentrations, which transitioned into

a zero order region at larger cluster concentrations (Figure 2.7). Furthermore, these data could be linearized by plotting the double reciprocal of rate and cluster concentration (Figure 2.8). One explanation that is consistent with the observed saturation behavior is that a high-energy, steady state intermediate, iminium ion **Y**, is formed in bulk solution, which undergoes a rate determining encapsulation event with the cluster. The saturation behavior of cluster concentration corresponds to a transition in the rate limiting step of the reaction. At low cluster concentration, encapsulation of iminium ion **Y** (k_3) is rate limiting, while at higher cluster concentrations, the formation of **Y** (k_2) becomes rate limiting, and cluster is no longer involved in the rate limiting step (see proposed catalytic cycle in Scheme 2.4 below).[16,17]

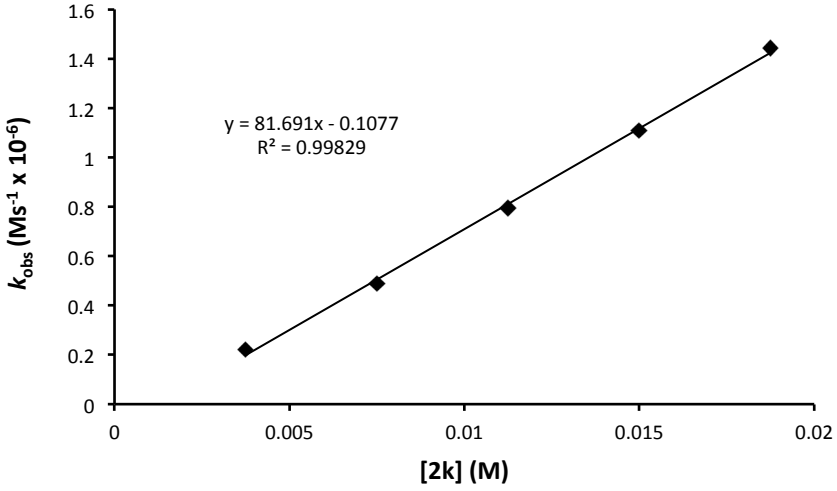

Figure 2.5. Rate dependence on amine concentration.

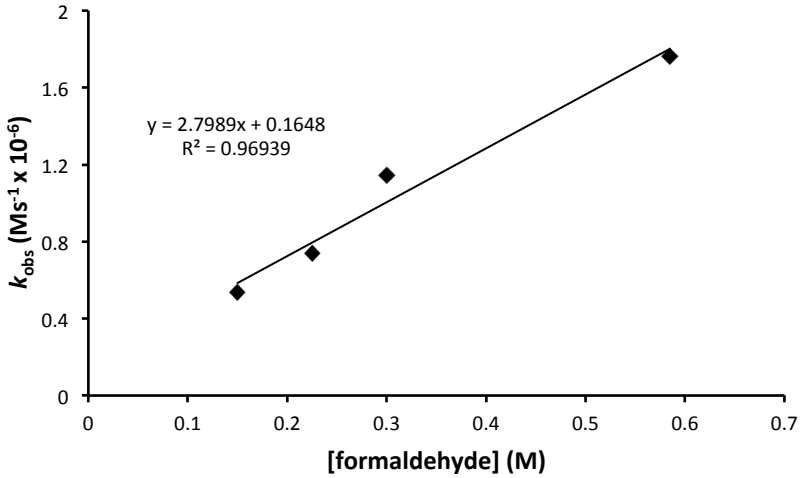

Figure 2.6. Rate dependence on formaldehyde concentration

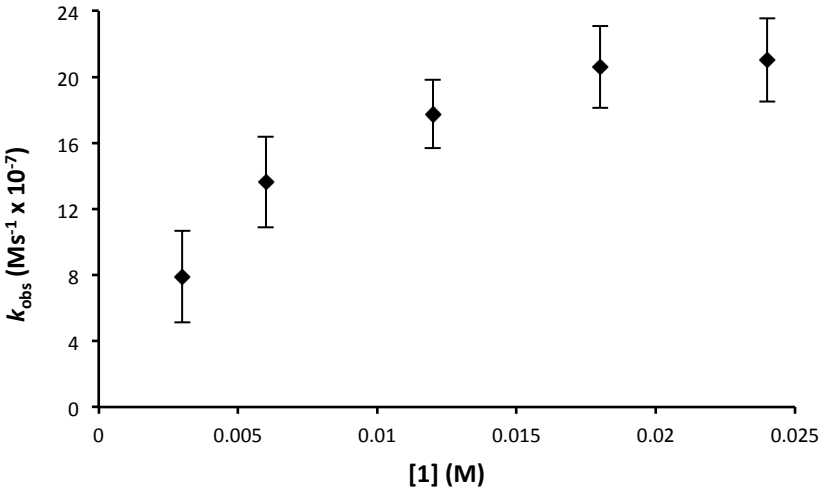

Figure 2.7. Dependence of initial rate on cluster concentration

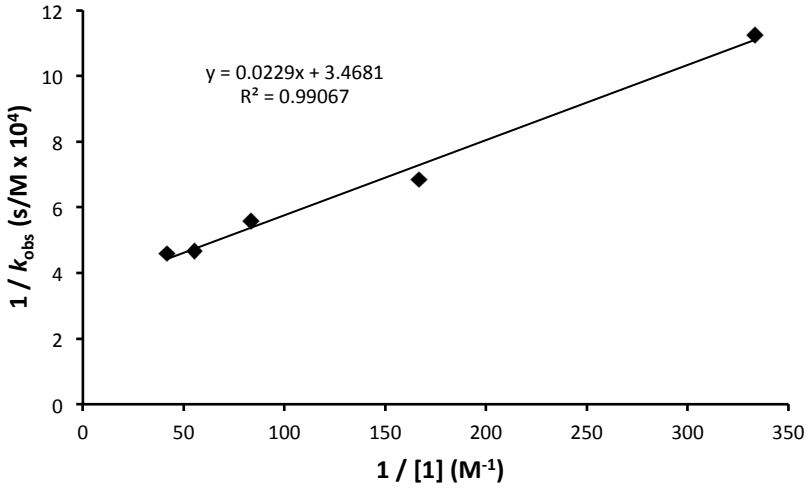

Figure 2.8. Double reciprocal plot for rate dependence on cluster concentration

From the information obtained in the above experiments, a catalytic cycle can be proposed for the cluster catalyzed aza-Prins cyclization (Scheme 2.4). Trifluoroethylamine **2k** is in rapid pre-equilibrium with the formaldehyde hemiaminal. The hemiaminal leads to the iminium ion as a high-energy, steady state intermediate, which is not directly detectable. The iminium ion is then intercepted in a rate limiting encapsulation event with the empty cluster (which is the cluster resting state, as observed by ^{1}H-NMR spectroscopy). The encapsulated iminium ion then undergoes rapid cyclization, and the nascent carbocation in this cyclized intermediate is quenched by elimination (or hydride transfer in the case of substrates **2a-j**). Finally, the product of the reaction is expelled from the cluster cavity, thus regenerating the empty cluster resting state.

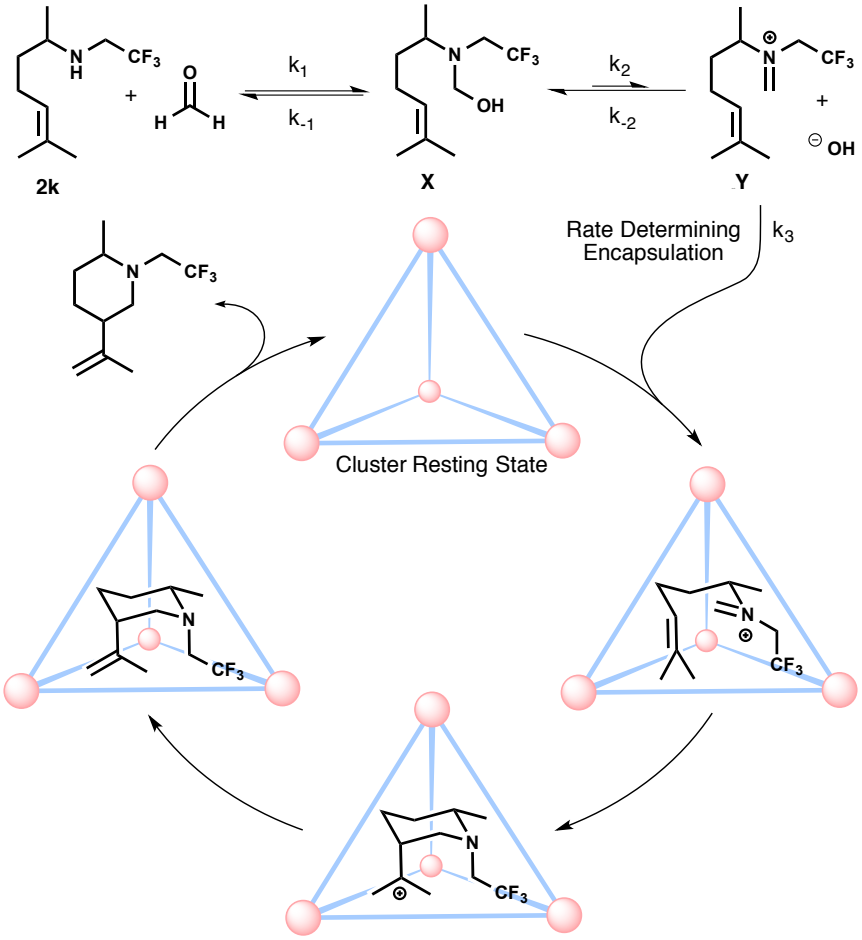

Scheme 2.4. Proposed catalytic cycle for the supramolecular cluster catalyzed aza-Prins cyclization

Steady state analysis of this catalytic pathway affords the rate law shown in Equation 1.1. This rate law accounts for the first order behavior in amine and formaldehyde, as well as the observed saturation behavior in cluster concentration. This mechanistic conclusion is quite significant, as supramolecular catalysts typically form Michaelis-type complexes, with the transformation of the substrate-catalyst complex constituting the rate determining step.[2]

$$\frac{\partial[P]}{\partial t} = \frac{K_1 k_2 k_3 [2k][CH_2O][1]}{k_{-2} + k_3[1]} \qquad (1.1)$$

While the observed saturation behavior in cluster concentration is consistent with the mechanism detailed above, two other possible explanations for the observation of rate saturation with respect to cluster concentration—strong internal encapsulation and strong external association—must be discounted. Both of these scenarios could conceivably lead to similar saturation-like behavior, since the addition of superstoichiometric cluster would not affect the rate if there is a quantitative 1:1 pre-association of substrate and cluster at the beginning of the reaction. Strong internal encapsulation of the substrate can be discounted because, in the saturation regime, there are no resonances in the characteristic upfield shifted

"encapsulation region" of the ^{1}H-NMR spectrum (0 to -2 ppm) (Figure 2.9). If strong external association were responsible for the saturation behavior, then it might be expected that the introduction of additional blocked cluster, as an additive to the typical reaction mixture, would inhibit the reaction by competitive external association to the inactive blocked cluster. In order to test this, a batch of cluster was quantitatively blocked with tetraethylphosphonium iodide, and this blocked cluster was added to the reaction; however, no inhibition of the reaction was observed (Figure 2.10). Additionally, if external association were responsible for the observed saturation behavior, then one would expect to observe a binding isotherm on the titration of **2k** into a solution of cluster **1**, however, no such isotherm is observed (Figure 2.11).

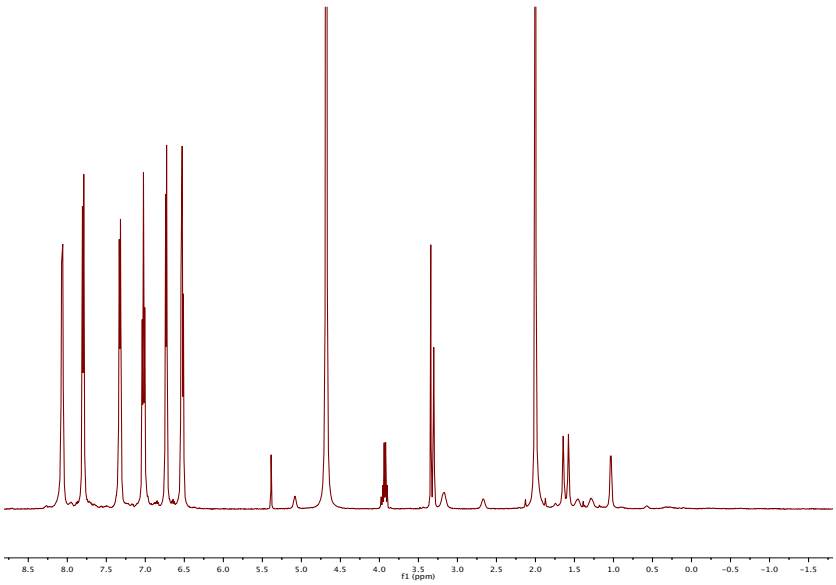

Figure 2.9. ^{1}H-NMR spectrum shows no guest strongly bound to the interior cavity of **1**, by inspection of the upfield "encapsulation region" (0 to -2 ppm).

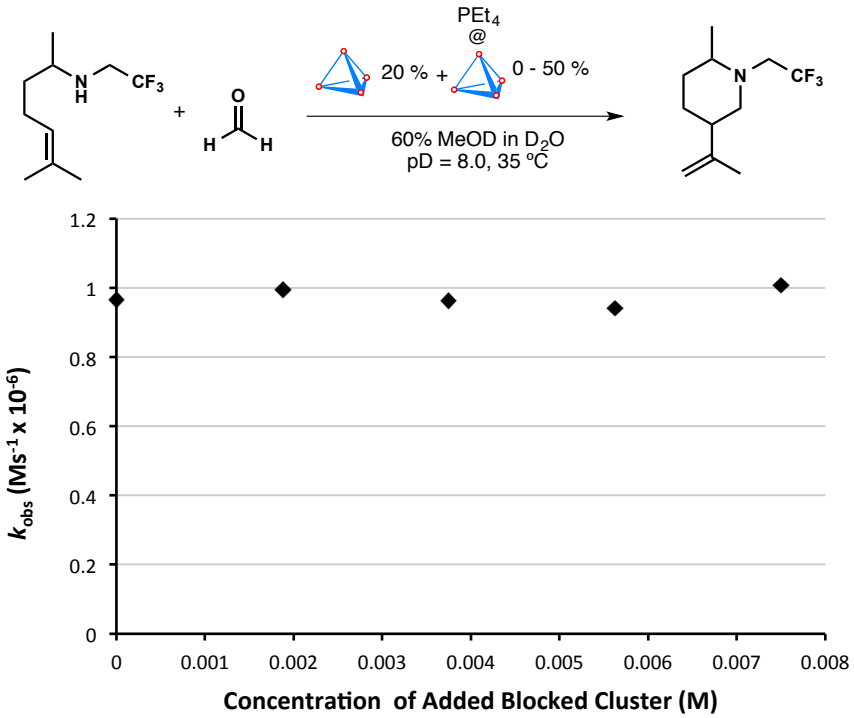

Figure 2.10. Rate dependence on additional blocked cluster showing lack of inhibition.

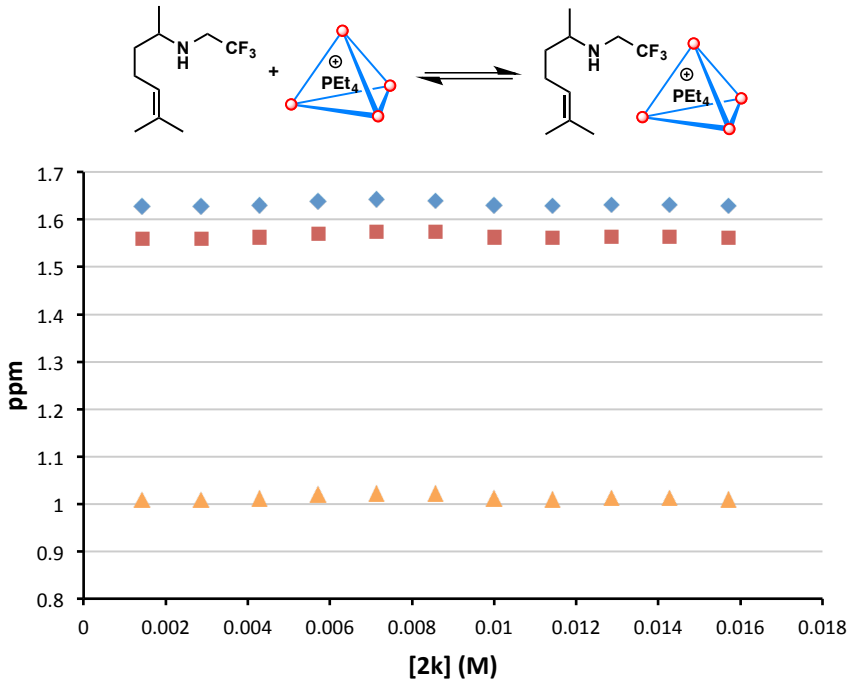

Figure 2.11. Titration of **2k** to a solution of blocked cluster **1**, shows no binding isotherm. Resonances correspond to three methyl groups of **2k**.

2.3.5 Evaluation of the Observed Rate Enhancement

Quantification of the rate acceleration for the cluster catalyzed aza-Prins reaction is complicated by two factors: rate determining encapsulation, as well as product divergence. The typical comparison when determining rate acceleration in supramolecular catalysis is between the uncatalyzed rate and k_{cat}, or the rate of transformation of the catalyst-substrate complex.[2,3] Due to the rate determining encapsulation in the aza-Prins system, no catalyst-substrate complex can be observed. Additionally, since the transannular hydride transfer pathway is too high in energy to be observed in bulk solution, any comparison would be of two diverging reaction pathways, and represents the comparison of two different chemical processes.

Nonetheless, the rate of the disappearance of the starting material in the cluster-catalyzed reaction can be compared to that of the rate of background reaction in order to place a lower bound on the rate acceleration. In order to establish this lower bound, k_{obs} at 20 mol% cluster loading is compared to the uncatalyzed k_{obs} (Table 2.2). Rate accelerations were measured for substrates **2a** and **2k**. The rate of the cluster-catalyzed reaction for both substrates was roughly 1.35 x 10^3 fold greater than that of the background reaction. However, substrate **2a** had a slightly greater rate than **2k** in both the catalyzed reaction (1.21 x 10^{-6} vs 9.73 x 10^{-7} M/s) and the uncatalyzed reaction (8.53 x 10^{-10} vs 7.00 x 10^{-10} M/s). This may be attributed to an inductive destabilization of the transient iminium ion by the trifluoroethyl group in **2k**, which affects the rate of both the cluster-catalyzed and background reactions.

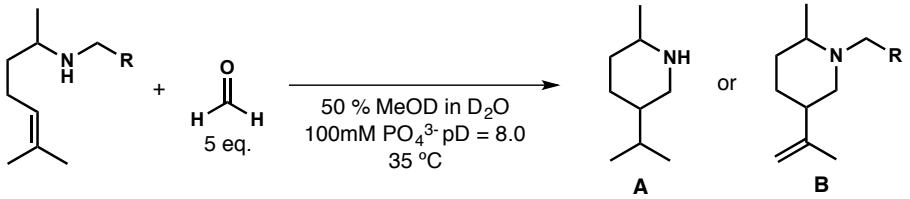

	R	Cluster Pdt.	k_{obs} (Ms^{-1}) Catalyzed[a]	k_{obs} (Ms^{-1}) Uncatalyzed	Observed Acceleration
2a	H	**A**	1.21 x 10^{-6}	9.11 x 10^{-10}	1330
2k	CF_3	**B**	9.73 x 10^{-7}	7.00 x 10^{-10}	1390

[a] 20% cluster loading

Table 2.2. Quantified rate acceleration relative to background decomposition of the substrate under the reaction conditions.

2.4 Conclusions

The ability to completely control, redirect and effect chemical reactivity under mild conditions similar to those of enzymatic catalysis has been a persistent goal of synthetic chemistry since its inception. Constrictive binding through confinement within a molecular cage is one strategy that can be leveraged to this effect. In this work, a supramolecular cluster catalyzed aza-Prins cyclization featuring a 1,5-through space hydride transfer is described. The nature of this transformation was probed by isotopic labeling studies and kinetic analysis, and the effect of nitrogen substitution was assessed. This pathway is uniquely available within the constrictive microenvironment of a supramolecular nanovessel, and is too high in energy to be observed in bulk solution for this class of substrates. The emergent reactivity of 1,5-

hydride transfer in the aza-Prins cyclization represents one of the most pronounced examples of divergent product selectivity enabled by a supramolecular microenvironment catalyst to date.

Furthermore, this work represents a major advance in the reactive intermediates and transition states recognized by cluster **1**. Previous examples of the reactions accelerated by the microenvironment of **1** with developing positive charge in the transition state are dominated by Brønsted acid activation of ethers, alcohols, or aldehydes (orthoformate hydrolysis, Nazarov-like cyclization, and Prins cyclization respectively). The demonstration of catalysis by **1** that proceeds by the stabilization of iminium ion intermediates represents a major step forward in the generality of this phenomenon. Indeed, since the publication of this work the Tiefenbacher group has published an example of iminium ion microenvironment catalysis in hexameric resorcinarene clusters.[18]

2.5 Supporting Information

2.5.1 General Methods

Unless stated otherwise, all reactions were performed in flame-dried glassware sealed with rubber septa under a nitrogen atmosphere and were stirred with Teflon-coated magnetic stir bars. Dry tetrahydrofuran (THF), dimethylformamide (DMF), triethylamine (TEA) and dichloromethane (DCM) were obtained by passing these previously degassed solvents through activated alumina columns. D_2O was used as a buffered solution of 100 mM K_3PO_4 adjusted to pD = 8.0 with DCl. All solvents in cluster-catalyzed reactions were degassed by sparging with nitrogen for 30 minutes prior to use. All reagents were used from commercial sources and were used without further purification unless otherwise noted. The host assembly $K_{12}[Ga_4L_6]$, **1**, and tertiary alcohol **4** were synthesized using previously reported literature procedures.[19,20] All other reagents were used as received. Reactions were monitored by thin layer chromatography (TLC) on Silicycle Siliaplate glass backed TLC plates (250 μm thickness, 60 Å porosity, F-254 indicator) and visualized by UV irradiation and *p*-anisaldehyde stain. Volatile solvents were removed under reduced pressure with a rotary evaporator. All flash column chromatography was performed using Silicycle SiliaFlash® F60, 230-400 mesh silica gel (40-63 μm). NMR spectra were obtained on Bruker Avance AV 300 (300 MHz), AV 400 (400 MHz), AV 500 (500 MHz), or AV 600 (600 MHz) spectrometers as indicated. Chemical shifts are reported as δ in parts per million (ppm) relative to residual protonated solvent resonances. NMR data are reported as follows: chemical shift (multiplicity, coupling constants where applicable, number of hydrogens). Splitting is reported with the following symbols: s = singlet, bs = broad singlet, d = doublet, t = triplet, aq = apparent quartet, ap = apparent pentet, sept = septet, dd = doublet of doublets, m = multiplet. High-resolution mass spectra (HRMS) were performed by the mass spectral facility at the University of California, Berkeley.

2.5.2 Synthesis of Previously Unreported Compounds

Amines **2a-k** and **2a**-d_3 were prepared by one of four general procedures:

(N.B. Many of the amines are volatile, and exposure to vacuum should be minimized.)

Procedure A: Alkyl amine hydrochloride (6 mmol, 1.25 equiv) was added to a 50 mL round bottom flask open to ambient atmosphere and equipped with a magnetic stir bar. MeOH (12.5 mL) was added. Powdered potassium hydroxide (98 mg, 1.75 mmol, 0.35 equiv) was added in one portion. 6-methylhept-5-en-2-one (630 mg, 5 mmol, 1.0 equiv) was added by syringe. $NaBH_3CN$ (134 mg, 2.13 mmol, 0.425 equiv) was added slowly as a solution in MeOH (3 mL). The reaction was allowed to stir overnight, at which point the ketone had been consumed by TLC analysis. KOH (303 mg, 5.4 mmol, 1.35 equiv) was added and the reaction was allowed to stir for ten minutes. The resulting precipitate was removed by filtration and the reaction mixture was concentrated under reduced pressure. The resulting oil was dissolved in diethyl ether (15 mL) and extracted with 1 M aqueous HCl (3 x 10 mL). The combined aqueous layers were cooled in an ice water bath in a 100 mL Erlenmeyer flask and stirred magnetically while 50% aqueous NaOH was added dropwise until the solution had a pH of 13-14 and a white precipitate was observed. The mixture was then extracted with ether (3 x 15 mL). The combined organic layers were dried over sodium sulfate and concentrated under reduced pressure to afford the product.

Procedure B: A 50 mL round bottom flask was charged with 6-methylhept-5-en-2-one (630 mg, 5 mmol, 1.0 equiv), followed by DCM (14 mL), amine (5.5 mmol, 1.1 equiv), sodium triacetoxyborohydride (1.59 g, 7.5 mmol, 1.5 equiv) and acetic acid (510 mg, 8.5 mmol, 1.7 equiv) in that order. The reaction was allowed to stir at room temperature overnight, at which point the ketone was shown to have been consumed by TLC analysis. The reaction was quenched with saturated sodium carbonate (5 mL) and the aqueous layer was extracted with ether (3 x 10 mL). The combined organic phases were dried over sodium sulfate and concentrated under reduced pressure. The resulting oil was dissolved in diethyl ether (15 mL), and extracted with 1 M aqueous HCl (3 x 10 mL). The combined aqueous layers were cooled in an ice water bath in a 100 mL Erlenmeyer flask and stirred magnetically while 50% aqueous NaOH was added dropwise until the solution had a pH of 13-14 and a white precipitate was observed. The mixture was then extracted with ether (3 x 15 mL). The combined organic layers were dried over sodium sulfate and concentrated under reduced pressure to afford the product.

Procedure C: To a suspension of powdered 4Å molecular sieves (300 mg) in methanol (8 mL) in a 25 mL round bottom flask was added 6-methylhept-5-en-2-one (252 mg, 2.00 mmol, 1.00 equiv) followed by amine (3.00 mmol, 1.50 equiv). Pyridine borane (158 mg, 1.70 mmol, 0.85 equiv) was added dropwise. The reaction was allowed to stir at room temperature overnight. 3 M aqueous HCl (10 mL) was added, and then, in an ice bath, the mixture was brought to pH 13-14 with 50% aqueous NaOH. The mixture was extracted with ether (3 x 15 mL) and the combined organic layers were dried over sodium sulfate and concentrated under reduced pressure. The resulting crude oil was chromatographed on silica gel (5% ethyl acetate and 1% triethylamine in hexanes) to afford the product.

Procedure D: To a 50 mL round bottom flask was charged 5-methylhex-4-enal (224 mg, 2.00 mmol, 1.00 equiv), methanol (10 mL), magnesium sulfate (800 mg), and potassium hydroxide (449 mg, 8.00 mmol, 4.00 equiv) in that order. The reaction mixture was stirred for 3 hours, followed by the addition of sodium borohydride (121 mg, 3.20 mmol, 1.6 equiv). After 60 minutes 1 M NaOH (50 mL) was added, and the resulting solution was extracted with diethyl ether (3 x 20 mL). The combined organics were then extracted with 1 M HCl (3 x 20 mL). The combined aqueous layers were cooled in an ice water bath in a 100 mL Erlenmeyer flask and stirred magnetically while 50% aqueous NaOH was added dropwise until the solution had a pH of 13-14 and a white precipitate was observed. The mixture was then extracted with ether (3 x 15 mL). The combined organic layers were dried over sodium sulfate and concentrated under reduced pressure. The resulting oil was distilled with a Kugelrohr apparatus to afford the product.

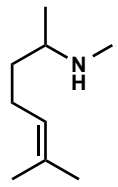

***N*,6-dimethylhept-5-en-2-amine (2a)** – Prepared by method A. Isolated as a colorless oil (368 mg, 52%). ^{1}H NMR (600 MHz, $CDCl_3$) δ 5.09 (t, J = 6.8 Hz, 1H), 2.56 – 2.46 (m, 1H), 2.38 (s, 3H), 2.03 - 1.92 (m, 2H), 1.67 (s, 3H), 1.60 (s, 3H), 1.52 – 1.41 (m, 1H), 1.35 – 1.25 (m, 1H), 1.27 (bs, 1H), 1.02 (d, J = 6.3 Hz, 3H). ^{13}C NMR (126 MHz, $CDCl_3$) δ 131.5, 124.4, 54.6, 36.8, 33.9, 25.7, 24.6, 19.8, 17.7. MS (ESIHR) for $C_9H_{20}N^+$, calcd (found) *m*/*z*: 142.1590 (142.1589).

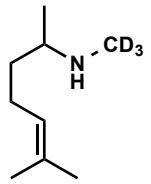

6-methyl-*N*-(methyl-d_3)hept-5-en-2-amine (2a-d_3) – Prepared by method A. Isolated as a colorless oil (541 mg, 75%). ^{1}H NMR (600 MHz, $CDCl_3$) δ 5.09 (t, J = 6.5 Hz, 1H), 2.54 – 2.46 (m, 1H), 2.04 - 1.91 (m, 2H), 1.67 (s, 3H), 1.59 (s, 3H), 1.50 – 1.42 (m, 1H), 1.35 – 1.25 (m, 1H), 1.01 (d, J = 7.3 Hz, 3H), 0.99 (bs, 1H). ^{13}C NMR (126 MHz, $CDCl_3$) δ 131.4, 124.3, 45.4, 36.8, 33.0 (hept, J = 21 Hz), 25.6, 24.5, 19.7, 17.6. MS (ESIHR) for $C_9H_{17}D_3N^+$, calcd (found) *m*/*z*: 145.1779 (145.1777).

***N*,5-dimethylhex-4-en-1-amine (2b)** – Prepared by method D. Isolated as a colorless oil (86 mg, 34%). ^{1}H NMR (300 MHz, $CDCl_3$) δ 5.09 (t, J = 7.3 Hz, 1H), 2.53 (t, J = 7.4 Hz, 2H), 2.39 (s, 3H), 2.04 - 1.91 (m, 2H), 1.93 (bs, 1H), 1.65 (s, 3H), 1.56 (s, 3H), 1.56 – 1.43 (m, 2H). ^{13}C NMR (70 MHz, $CDCl_3$) δ 131.9, 124.4, 52.0, 36.6, 30.2, 26.0, 25.9, 17.9. MS (ESIHR) for $C_8H_{18}N^+$, calcd (found) *m*/*z*: 128.1434 (128.1433).

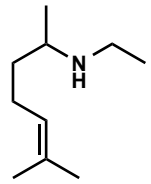

***N*-ethyl-6-methylhept-5-en-2-amine (2c)** – Prepared by method A. Isolated as a colorless oil (437 mg, 56%). ^{1}H NMR (500 MHz, $CDCl_3$) δ 5.19 (t, J = 6.5 Hz, 1H), 2.81 – 2.63 (m, 3H), 2.16 – 2.02 (m, 2H), 1.77 (s, 3H), 1.70 (s, 3H), 1.52 – 1.41 (m, 1H), 1.46 – 1.36 (m, 1H), 1.19 (t, J = 7.1 Hz, 3H), 1.12 (d, J = 6.4 Hz, 3H), 0.88 (bs, 1H). ^{13}C NMR (126 MHz, $CDCl_3$) δ 131.5, 124.4, 52.9, 41.5, 37.2, 25.7, 24.7, 20.4, 17.7, 15.7. MS (ESIHR) for $C_{10}H_{22}N^+$, calcd (found) *m*/*z*: 156.1747 (156.1745).

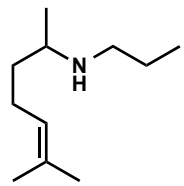

6-methyl-*N*-propylhept-5-en-2-amine (2d) – Prepared by method B. Isolated as a colorless oil (247 mg, 29%). ^{1}H NMR (600 MHz, $CDCl_3$) δ 5.08 (t, J = 8.8, 1H), 2.62 – 2.52 (m, 2H), 2.50 – 2.44 (m, 1H), 2.02 – 1.90 (m, 2H), 1.65 (s, 3H), 1.57 (s, 3H), 1.49 – 1.40 (m, 3H), 1.29 (m, 1H), 1.00 (d, J =

6.3 Hz, 3H), 0.88 (t, *J* = 7.4 Hz, 3H), 0.86 (bs, 1H). ^{13}C NMR (151 MHz, $CDCl_3$) δ 131.3, 124.4, 52.8, 49.3, 37.1, 25.6, 24.6, 23.5, 20.3, 17.6, 11.8. MS (ESIHR) for $C_{11}H_{24}N^+$, calcd (found) *m*/*z*: 170.1903 (170.1902).

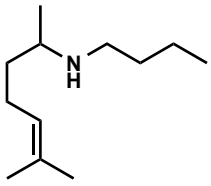

***N*-butyl-6-methylhept-5-en-2-amine (2e)** – Prepared by method B. Isolated as a colorless oil (80 mg, 9%). ^{1}H NMR (600 MHz, $CDCl_3$) δ 5.09 (t, *J* = 6.2, 1H), 2.62 – 2.56 (m, 2H), 2.55 – 2.47 (m, 1H), 2.03 – 1.93 (m, 2H), 1.66 (s, 3H), 1.59 (s, 3H), 1.49 – 1.38 (m, 3H), 1.37 – 1.24 (m, 3H), 1.01 (d, *J* = 6.2 Hz, 3H), 0.89 (t, *J* = 7.3 Hz, 3H). ^{13}C NMR (151 MHz, $CDCl_3$) δ 131.3, 124.3, 52.8, 47.0, 37.0, 32.5, 25.6, 24.6, 20.5, 20.3, 17.5, 13.9. MS (ESIHR) for $C_{12}H_{26}N^+$, calcd (found) *m*/*z*: 184.2060 (184.2059).

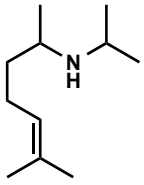

***N*-isopropyl-6-methylhept-5-en-2-amine (2f)** – Prepared by method B. Isolated as a colorless oil (378 mg, 45%). ^{1}H NMR (600 MHz, $CDCl_3$) δ 5.08 (t, *J* = 7.0 Hz, 1H), 2.86 (hept, *J* = 6.3 Hz, 1H), 2.71 – 2.65 (m, 1H), 2.04 – 1.90 (m, 2H), 1.65 (s, 3H), 1.58 (s, 3H), 1.46 – 1.39 (m, 1H), 1.31 – 1.23 (m 1H), 1.03 – 0.94 (m, 9H), 0.60 (bs, 1H). ^{13}C NMR (151 MHz, $CDCl_3$) δ 131.3, 124.4, 49.4, 45.2, 37.4, 25.6, 24.5, 23.7, 23.1, 20.8, 17.6. MS (ESIHR) for $C_{11}H_{24}N^+$, calcd (found) *m*/*z*: 170.1903 (170.1902).

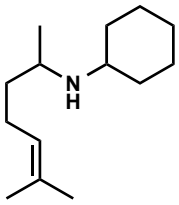

***N*-(6-methylhept-5-en-2-yl)cyclohexanamine (2g)** – Prepared by method B. Isolated as a colorless oil (98 mg, 10%). ^{1}H NMR (600 MHz, $CDCl_3$) δ 5.09 (t, *J* = 7.1, 1H), 2.78 – 2.72 (m, 1H), 2.50 – 2.44 (m, 1H), 2.04 – 1.91 (m, 2H), 1.90 – 1.80 (m, 2H), 1.73 – 1.65 (m, 2H), 1.67 (s, 3H), 1.59 (s, 3H), 1.58 (m, 1H), 1.48 – 1.39 (m, 1H), 1.33 – 0.92 (m, 6H), 1.00 (d, *J* = 5.8 Hz, 3H), 0.75 (bs, 1H). ^{13}C NMR (151 MHz, $CDCl_3$) δ 131.3, 124.4, 53.4, 48.9, 37.5, 34.5, 33.9, 26.1, 25.6, 25.3, 25.2, 24.6, 21.0, 17.6. MS (ESIHR) for $C_{14}H_{28}N^+$, calcd (found) *m*/*z*: 210.2216 (210.2216).

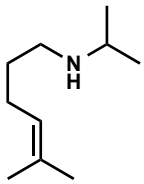

***N*-isopropyl-5-methylhex-4-en-1-amine (2h)** – Prepared by method D. Isolated as a colorless oil (120 mg, 39%). ^{1}H NMR (300 MHz, $CDCl_3$) δ 5.05 (t, *J* = 6.9 Hz, 1H), 2.70 (hept, *J* = 6.3 Hz, 1H), 2.51 (t, *J* = 7.3 Hz, 2H), 1.94 (aq, *J* = 7.3 Hz, 2H), 1.61 (s, 3H), 1.53 (s, 3H), 1.44 (ap, *J* = 7.4 Hz, 2H), 0.97 (d, *J* = 6.3 Hz, 6H), 0.82 (bs, 1H). ^{13}C NMR (75 MHz, $CDCl_3$) δ 131.6, 124.3, 48.7, 47.3, 30.5, 26.0, 25.7, 23.1, 17.7. MS (ESIHR) for $C_{10}H_{22}N^+$, calcd (found) *m*/*z*: 156.1747 (156.1746).

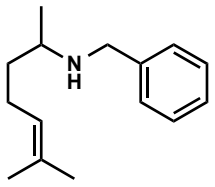

***N*-benzyl-6-methylhept-5-en-2-amine (2i)** – Prepared by method C. Isolated as a colorless oil (310 mg, 71%). ^{1}H NMR (500 MHz, $CDCl_3$) δ 7.38 – 7.34 (m, 4H), 7.33 – 7.25 (m, 1H), 5.15 (t, *J* = 6.7 Hz, 1H), 3.87 (d, *J* = 12.9 Hz, 1H), 3.77 (d, *J* = 12.9 Hz, 1H), 2.78 – 2.70 (m, 1H), 2.15 – 1.99 (m, *J* = 7.3 Hz, 2H), 1.73 (s, 3H), 1.65 (s, 3H), 1.64 – 1.51 (m, 1H), 1.46 – 1.38 (m, 1H), 1.31 (bs, 1H), 1.14 (d, *J* = 6.4 Hz, 3H). ^{13}C NMR (126 MHz, $CDCl_3$) δ 140.9, 131.5, 128.4, 128.2, 126.8, 124.5, 52.2, 51.5, 37.1, 25.8, 24.6, 20.4, 17.7. MS (ESIHR) for $C_{15}H_{24}N^+$, calcd (found) *m*/*z*: 218.1903 (218.1902).

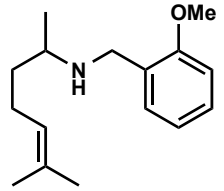

***N*-(2-methoxybenzyl)-6-methylhept-5-en-2-amine (2j)** – Prepared by method C. Isolated as a colorless oil (342 mg, 69%). ^{1}H NMR (500 MHz, $CDCl_3$) δ 7.30 – 7.24 (m, 2H), 6.97 – 6.86 (m, 2H), 5.12 (t, *J* = 6.9 Hz, 1H), 3.86 (s, 3H), 3.85 (d, *J* = 13.1 Hz, 1H), 3.77 (d, *J* = 13.1 Hz, 1H), 2.70 – 2.61 (m, 1H), 2.07 – 1.97 (m, 2H), 1.85 (bs, 1H), 1.71 (s, 3H), 1.63 (s, 3H), 1.61 – 1.49 (m, 1H), 1.43 – 1.34 (m, 1H), 1.11 (d, *J* = 6.2 Hz, 3H). ^{13}C NMR (126 MHz, $CDCl_3$) δ 157. 7, 131.4, 129.9, 128.7, 128.1, 124.5, 120.4, 110.2, 55.2, 51.7, 46.8, 37.0, 25.8, 24.6, 20.3, 17.7. MS (ESIHR) for $C_{16}H_{26}ON^+$, calcd (found) *m*/*z*: 248.2009 (248.2005).

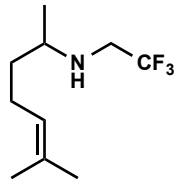

6-methyl-*N*-(2,2,2-trifluoroethyl)hept-5-en-2-amine (2k) – Prepared by method A. Isolated as a colorless oil (560 mg, 54%). ^{1}H NMR (500 MHz, $CDCl_3$) δ 5.09 (t, *J* = 6.8 Hz, 1H), 3.25 – 3.07 (m, 2H), 2.78 – 2.70 (m, 1H), 2.09 – 1.96 (m, 2H), 1.68 (s, 3H), 1.60 (s, 3H), 1.49 – 1.41 (m, 1H), 1.38 – 1.30 (m, 1H), 1.18 (bs, 1H), 1.06 (d, *J* = 6.3 Hz, 3H). ^{13}C NMR (126 MHz, $CDCl_3$) δ 132.1, 125.6 (q, *J* = 281 Hz), 124.1, 52.4, 48.1 (q, *J* = 31 Hz), 37.0, 25.9, 24.6, 20.4, 17.8. ^{19}F NMR (376 MHz, $CDCl_3$) δ -71.2 (t, *J* = 9.4 Hz). MS (ESIHR) for $C_{10}H_{19}NF_3^+$, calcd (found) *m*/*z*: 210.4164 (210.4162).

Synthesis of 2a-d_1:

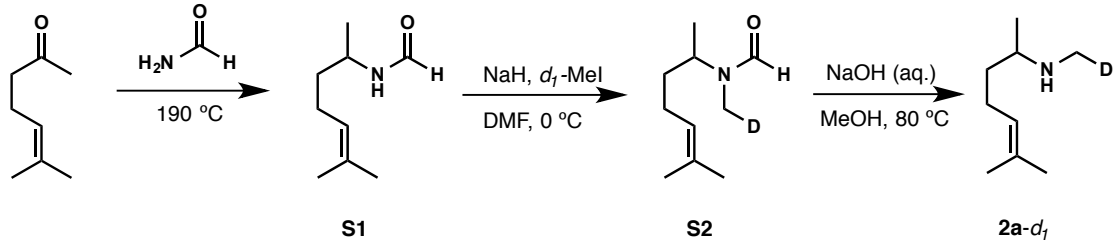

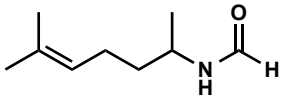

***N*-(6-methylhept-5-en-2-yl)formamide (S1)** – 6-methylhept-5-en-2-one (4.25 g, 33.7 mmol) was charged into a 100 mL round bottom flask equipped with a magnetic stir bar. Formamide (20 mL) was added. A Vigreux column was attached to the flask, and the apparatus was backfilled with nitrogen three times. The reaction mixture was then heated to 140 ºC for 6 hours and then allowed to cool to room temperature. The reaction mixture was then diluted with brine (100 mL) and extracted with ether (30 mL x 3). The combined organic phases were dried over sodium sulfate and volatiles were removed under reduced pressure. The crude oil was purified by silica gel chromatography (20 → 50 % ethyl acetate in hexanes) to afford formamide **S1** (1.60 g, 31 %) as a yellow oil. Major rotamer: ^{1}H NMR (600 MHz, $CDCl_3$) δ 8.10 (s, 1H), 5.64 (bs, 1H), 5.06 (t, *J* = 6.6 Hz, 1H), 4.09 – 4.00 (m, 1H), 2.08 – 1.94 (m, 2H), 1.65 (s, 3H), 1.57 (s, 3H), 1.52 – 1.48 (m, 2H), 1.14 (d, *J* = 6.2 Hz, 3H). Minor rotamer: ^{1}H NMR (600 MHz, $CDCl_3$) δ 8.01 (d, *J* = 12.9 Hz, 1H), 5.83 (bs, 1H), 5.02 (t, *J* = 6.2 Hz, 1H), 3.50 – 3.42 (m, 1H), 2.08 – 1.94 (m, 2H), 1.65 (s, 3H), 1.57 (s, 3H), 1.52 – 1.48 (m, 2H), 1.19 (d, *J* = 6.6 Hz, 3H). Both rotamers: ^{13}C NMR (151 MHz, $CDCl_3$) δ 163.8, 160.5, 132.7, 132.2, 123.3, 122.8, 47.8, 43.9, 37.6, 36.7, 25.6, 24.5, 24.3, 22.6, 20.8, 17.7, 17.6. MS (ESIHR) for $C_9H_{17}ONNa^+$, calcd (found) *m*/*z*: 178.1202 (178.1202).

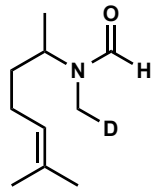

***N*-(methyl-*d*)-*N*-(6-methylhept-5-en-2-yl)formamide (S2) –** To a flame dried 25 mL round bottom flask was added **S1** (456 mg, 2.94 mmol, 1.0 equiv) and DMF (6 mL). The resulting solution was cooled in a water ice bath and NaH (235 mg, 5.87 mmol, 2.0 equiv) was added portionwise. The resulting suspension was allowed to warm to room temperature and then stirred for 20 minutes. d_1-MeI (503 mg, 3.52 mmol, 1.2 equiv) was added dropwise, and the reaction mixture was stirred for six hours. The reaction mixture was then diluted with ether (100 mL) and washed with brine (3 x 30 mL). The ether layer was dried over magnesium sulfate and the volatiles were removed under reduced pressure. The resulting oil was purified by silica gel chromatography (20 → 40 % ethyl acetate in hexanes) to afford **S2** (424 mg, 85 %) as a light yellow oil. Major rotamer: ^{1}H NMR (600 MHz, $CDCl_3$) δ 7.99 (s, 1H), 4.99 (t, J = 6.6 Hz, 1H), 3.55 – 3.47 (m, 1H), 2.67 (t, J = 1.9 Hz, 2H), 1.92 – 1.79 (m, 2H), 1.63 (s, 3H), 1.52 (s, 3H), 1.60 – 1.32 (m, 2H), 1.15 (d, J = 6.5 Hz, 3H). Minor rotamer: ^{1}H NMR (600 MHz, $CDCl_3$) δ 8.04 (s, 1H), 5.04 (t, J = 7.3 Hz, 1H), 4.47 – 4.38 (m, 1H), 2.73 (t, J = 1.9 Hz, 2H), 1.92 – 1.79 (m, 2H), 1.63 (s, 3H), 1.52 (s, 3H), 1.60 – 1.32 (m, 2H), 1.07 (d, J = 6.6 Hz, 3H). Both rotamers: ^{13}C NMR (151 MHz, $CDCl_3$) δ 162.6, 162.6, 132.7, 132.0, 123.3, 122.7, 53.3, 46.4, 33.6, 33.2, 28.7 (t, J = 21 Hz), 25.6, 25.6, 24.9, 24.6, 24.0 (t, J = 22 Hz), 19.3, 17.7, 17.6, 17.4. MS (ESIHR) for $C_{10}H_{18}DONNa^+$, calcd (found) *m*/*z*: 193.1422 (193.1421).

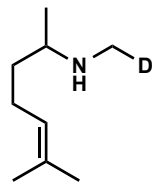

6-methyl-*N*-(methyl-*d*)hept-5-en-2-amine (2-d_1) – To a 25 mL round bottom flask was charged **S2** (340 mg, 2.00 mmol), MeOH (3 mL) and 20 % aqueous NaOH (5 mL). A reflux condenser was attached and the reaction mixture was heated with an oil bath at 80 ºC over night. The reaction mixture was then cooled to room temperature and diluted with ether (30 mL) and water (20 mL). The aqueous layer was extracted with ether (2 x 10 mL) and the combined organic layers were dried over magnesium sulfate and concentrated under reduced pressure. The resulting oil was then distilled to afford **2**-d_1 (160 mg, 56%) as a colorless oil. ^{1}H NMR (300 MHz, $CDCl_3$) δ 5.11 (t, J = 7.1 Hz, 1H), 2.58 – 2.45 (m, 1H), 2.37 (t, J = 1.8 Hz, 2H), 2.08 – 1.92 (m, 2H), 1.69 (s, 3H), 1.61 (s, 3H), 1.54 – 1.41 (m, 1H), 1.37 – 1.23 (m, 1H), 1.03 (d, J = 6.3 Hz, 3H); ^{13}C NMR (126 MHz, $CDCl_3$) δ 131.6, 124.5, 54.7, 37.0, 33.8 (t, J = 20 Hz), 25.8, 25.0, 19.9, 17.8. MS (ESIHR) for $C_9H_{19}DN^+$, calcd (found) *m*/*z*: 143.1653 (143.1652).

Scaled up conditions for the isolation of 5, 5-d_1 and 6:

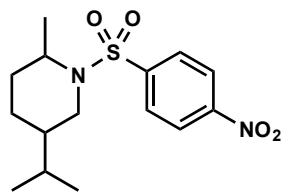

5-isopropyl-2-methyl-1-((4-nitrophenyl)sulfonyl)piperidine (5) – To a 20 mL vial in an N_2 atmosphere wet glove box, was added amine **2a** (8.5 mg, 0.060 mmol, 1.0 equiv), followed by CD_3OD (1.4 mL) and formaldehyde (0.6 mL, 1 M in CD_3OD, 0.60 mmol, 10 equiv). Cluster **1** (40 mg, 0.012 mmol, 0.2 equiv) was added as a solution in D_2O (2.0 mL). The vial was capped and parafilmed, followed by removal from the glove box. After 40 hours, 1 M NaOH (2 mL) was added, and the vial was shaken vigorously. The reaction mixture was then extracted with DCM (3 x 2 mL) and the combined organic layers were dried over Na_2SO_4. HCl(g) was then bubbled

through the DCM solution to protonate the amine and reduce its volatility. The mixture was then concentrated under reduced pressure. To the resulting yellow oil was then added a magnetic stir bar, DCM (1 mL), NEt_3 (25 μL, 0.18 mmol, 3.0 equiv) and NsCl (27 mg, 0.12 mmol, 2.0 equiv). The reaction mixture was stirred at room temperature overnight. 1 M aqueous HCl (2 mL) was added, and the aqueous phase was extracted with DCM (2 x 1 mL). The combined organic phases were dried over Na_2SO_4 and concentrated under reduced pressure. The crude oil was purified by preparative thin layer chromatography (30% ethyl acetate in hexanes) to afford sulfonamide **5** (12.6 mg, 62%) as a white solid. ^{1}H NMR (600 MHz, $CDCl_3$) δ 8.34 (d, J = 8.4 Hz, 2H), 8.99 (d, J = 8.4 Hz, 2H), 4.34 – 4.25 (m, 1H), 3.81 (d, J = 13.3 Hz, 1H), 2.71 (t, J = 12.7 Hz, 1H), 1.65 – 1.51 (m, 2H), 1.48 – 1.38 (m, 1H), 1.35 – 1.18 (m, 2H), 1.15 – 1.05 (m, 1H), 1.06 (d, J = 6.9 Hz, 3H), 0.90 (d, J = 7.6 Hz, 3H), 0.88 (d, J = 7.5 Hz, 3H); ^{13}C NMR (151 MHz, $CDCl_3$) δ 149.7, 147.4, 128.0, 124.3, 48.5, 43.6, 42.2, 30.9, 30.4, 21.7, 19.8, 19.5, 15.7. MS (ESIHR) for $C_{15}H_{23}N_2O_4S^+$, calcd (found) m/z: 327.1373 (327.1384).

2-methyl-1-((4-nitrophenyl)sulfonyl)-5-(propan-2-yl-2-*d*)piperidine (5-*d*$_1$) – Same procedure as **5** except starting with amine **2**-*d*$_3$ (8.7 mg, 0.060 mmol, 1.0 equiv). **5**-*d*$_1$ (14.1 mg, 73%) was isolated as a white solid. ^{1}H NMR (600 MHz, $CDCl_3$) δ 8.34 (d, J = 9.1 Hz, 2H), 7.99 (d, J = 8.3 Hz, 2H), 4.30 – 4.25 (m, 1H), 3.78 (d, J = 13.3 Hz, 1H), 2.71 (t, J = 12.2 Hz, 1H), 1.61 – 1.53 (m, 2H), 1.34 – 1.21 (m, 2H), 1.12 – 1.03 (m, 1H), 1.05 (d, J = 6.5 Hz, 3H), 0.88 (s, 3H), 0.86 (s, 3H). ^{13}C NMR (151 MHz, $CDCl_3$) δ 149.9, 147.6, 128.1, 124.5, 48.6, 43.7, 42.3, 30.6, 30.5 (t, J = 21 Hz), 21.8, 19.8, 19.5, 15.8. MS (ESIHR) for $C_{15}H_{22}DN_2O_4S^+$, calcd (found) m/z: 328.1436 (328.1432).

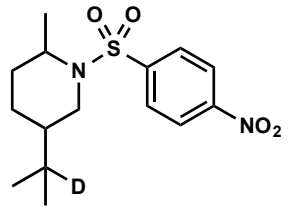

2-methyl-5-(prop-1-en-2-yl)-1-(2,2,2-trifluoroethyl)piperidine (6) – To a 20 mL vial in an N_2 atmosphere wet glove box, was added amine **2k** (20.9 mg, 0.1 mmol, 1.0 equiv), followed by CD_3OD (1.5 mL) and formaldehyde (1 mL, 1 M in CD_3OD, 1.0 mmol, 10 equiv). Cluster **1** (67 mg, 0.02 mmol, 0.2 equiv) was added as a solution in D_2O (2.5 mL). The vial was capped and parafilmed, followed by removal from the glove box. After 40 hours, 1 M NaOH (2 mL) was added, and the vial was shaken vigorously. The reaction mixture was then extracted with DCM (3 x 2 mL) and the combined organic layers were dried over Na_2SO_4 and concentrated under reduced pressure. The resulting oil was purified by silica gel chromatography (0 → 20 % diethyl ether in hexanes) to afford **6** (16.8 mg, 76%) as a clear oil. (**6** was isolated as an inseparable mixture of two diastereomers in a 6.5 : 1 ratio.) Major diastereomer: ^{1}H NMR (600 MHz, $CDCl_3$) δ 4.76 (s, 1H), 4.74 (s, 1H), 3.08 – 2.97 (m, 2H), 2.96 – 2.86 (m, 1H), 2.70 – 2.61 (m, 2H), 2.20 – 2.12 (m, 1H), 1.85 – 1.76 (m, 1H), 1.73 (s, 3H), 1.63 – 1.44 (m, 3H), 1.01 (dd, J = 6.8, 1.7 Hz, 3H). Major diastereomer: ^{13}C NMR (151 MHz, $CDCl_3$) δ 147.9, 126.0 (q, J = 280 Hz), 109.8, 56.2 (q, J = 31 Hz), 53.9, 52.5, 43.0, 30.6, 24.0, 21.8, 12.0. Major diastereomer: ^{19}F NMR (376 MHz, $CDCl_3$) δ -70.3 (t, J = 9.6 Hz). Minor diastereomer: ^{19}F NMR (376 MHz, $CDCl_3$) δ -67.8 (t, J = 10.0 Hz). MS (ESIHR) for $C_{11}H_{19}NF_3^+$, calcd (found) m/z: 222.1464 (222.1461).

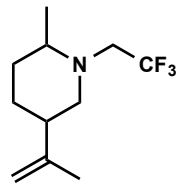

2.5.3 Procedures for Non-preparative Reaction and Supplemental Figures

Standard cyclization conditions to determine conversion:

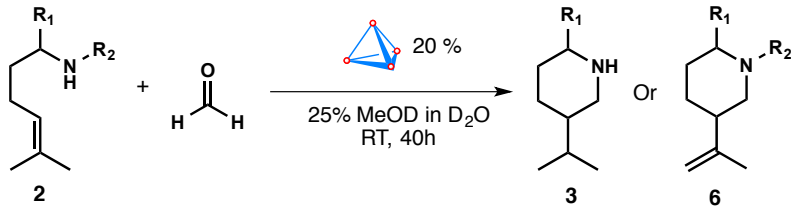

In a nitrogen glove box, an NMR tube was charged amine **2** (0.015 mmol, 1.0 equiv) in MeOD (30 µL) followed by formalin (0.045 mmol, 3.0 equiv) in MeOD (45 µL) and additional MeOD (175 µL). Cluster **1** (10.8 mg, 0.003 mmol, 0.2 equiv) was then added in D_2O (750 µL). After 40 hours, 1M NaOH (1 mL) was added, and the resulting mixture was extracted with CD_2Cl_2 (3 x 0.3 mL). The combined organic layers were dried over sodium sulfate. Conversion was estimated by the ratio of starting material to product in the ^1H NMR of the extracted reaction mixture.

Preequilibrium of trifluoroethylamine 2k with formaldehyde:

Sample procedure for kinetics experiments:

To an NMR tube, in an N_2 atmosphere wet glove box, was added amine **2k** (15 µL, 0.5 M in CD_3OD, 0.0075 mmol, 1 equiv), followed by trifluoroethanol (15 µL, 0.5 M in CD_3OD, 0.0075 mmol, 1 equiv) and CD_3OD (295 µL). Formaldehyde (75 µL, 1 M in CD_3OD, 0.075 mmol, 10 equiv) was then added followed cluster **1** (5.0 mg, 0.0015 mmol, 0.2 equiv) as a solution in D_2O (200 µL). The NMR tube was then capped, parafilmed and shaken vigorously, followed by removal from the glove box and insertion into the NMR spectrometer, which had been previously warmed to 35 ºC (Time between addition of **1** and insertion into the heated NMR probe was minimized, and was generally between 2 and 4 minutes). The sample temperature was allowed to equilibrate and then data points were taken every two minutes (or three minutes for slower reactions).

Sample Kinetic Profile:

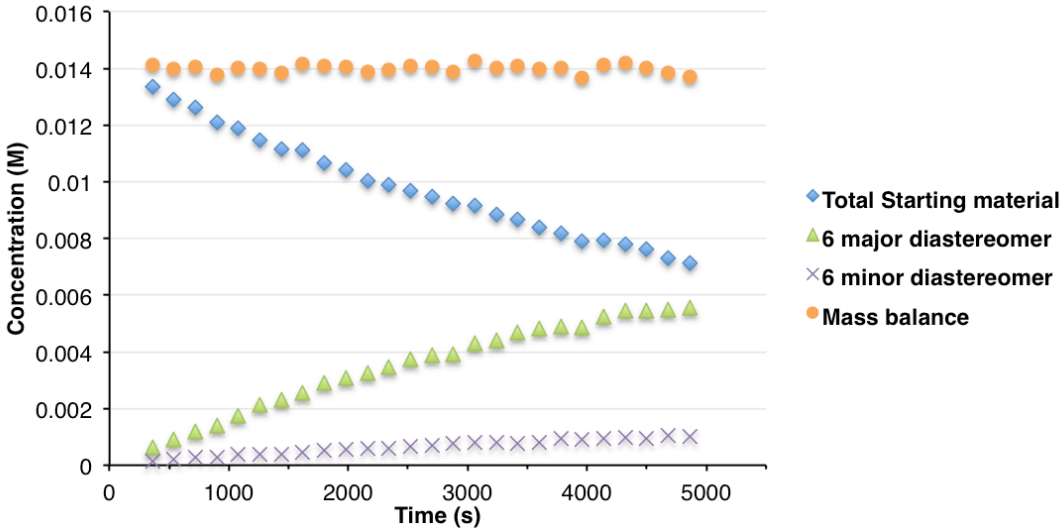

Figure 2.12. Sample kinetic reaction profile

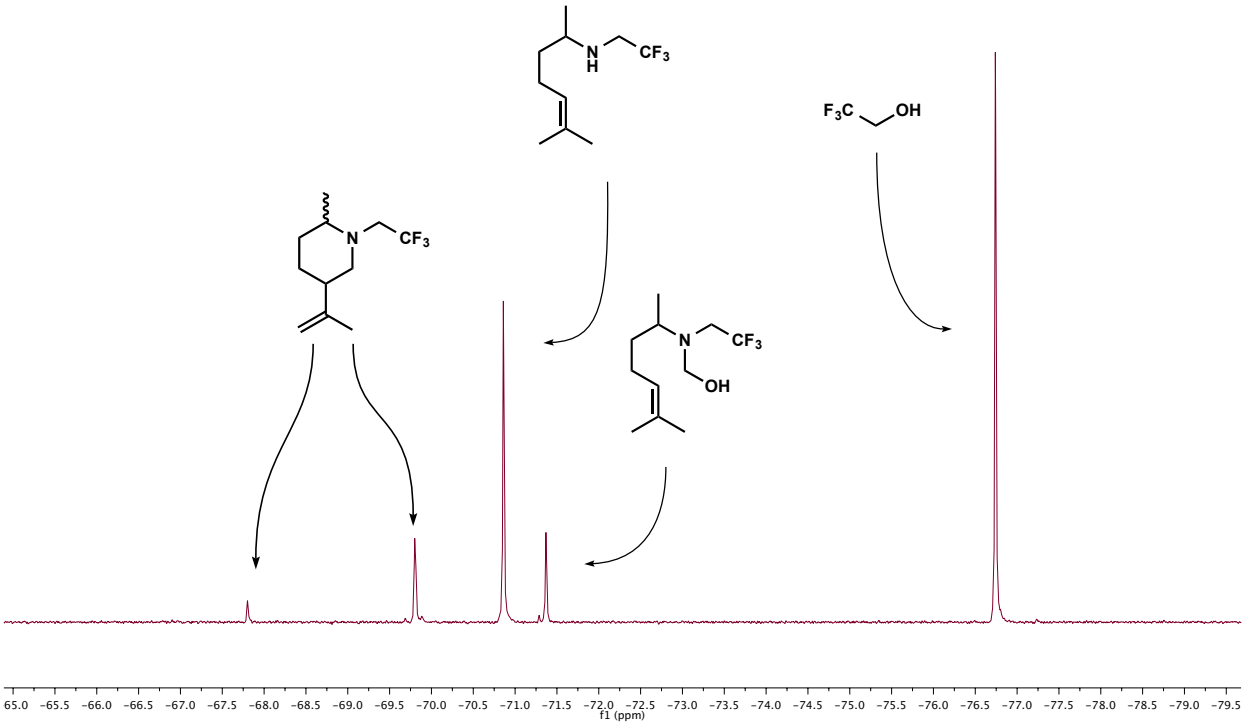

Figure 2.13. ^{19}F NMR at partial conversion

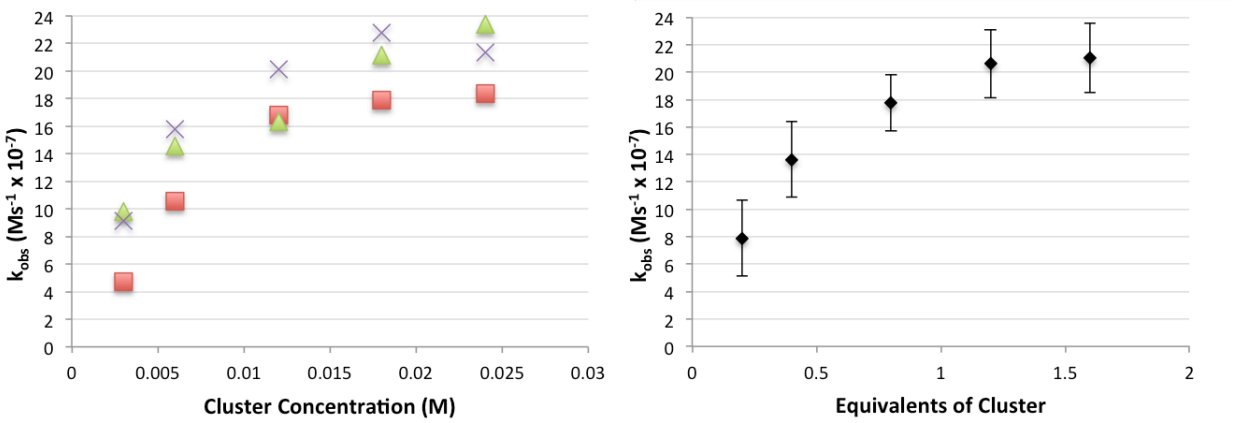

Figure 2.14. Rate dependence on cluster concentration (Error bars are ± 1 standard deviation).

Kinetic isotope experiments:

In order to measure the intermolecular kinetic isotope effect, a mixture of **2a** and **2a**-d_3 were subjected to the cluster-catalyzed aza-Prins cyclization conditions. In order to track both concentrations, resonances at 2.4 ppm, corresponding to the N-methyl group of **2a**, and at 5.1 ppm, corresponding to the olefinic proton of both **2a** and **2a**-d_3. This technique allows for fewer variables to influence the rates, and allows for a more accurate comparison than side-by-side rate comparison. The decay of **2a** and **2a**-d_3 were modeled as first order to negate the influence of differences in initial concentration of **2a** and **2a**-d_3.

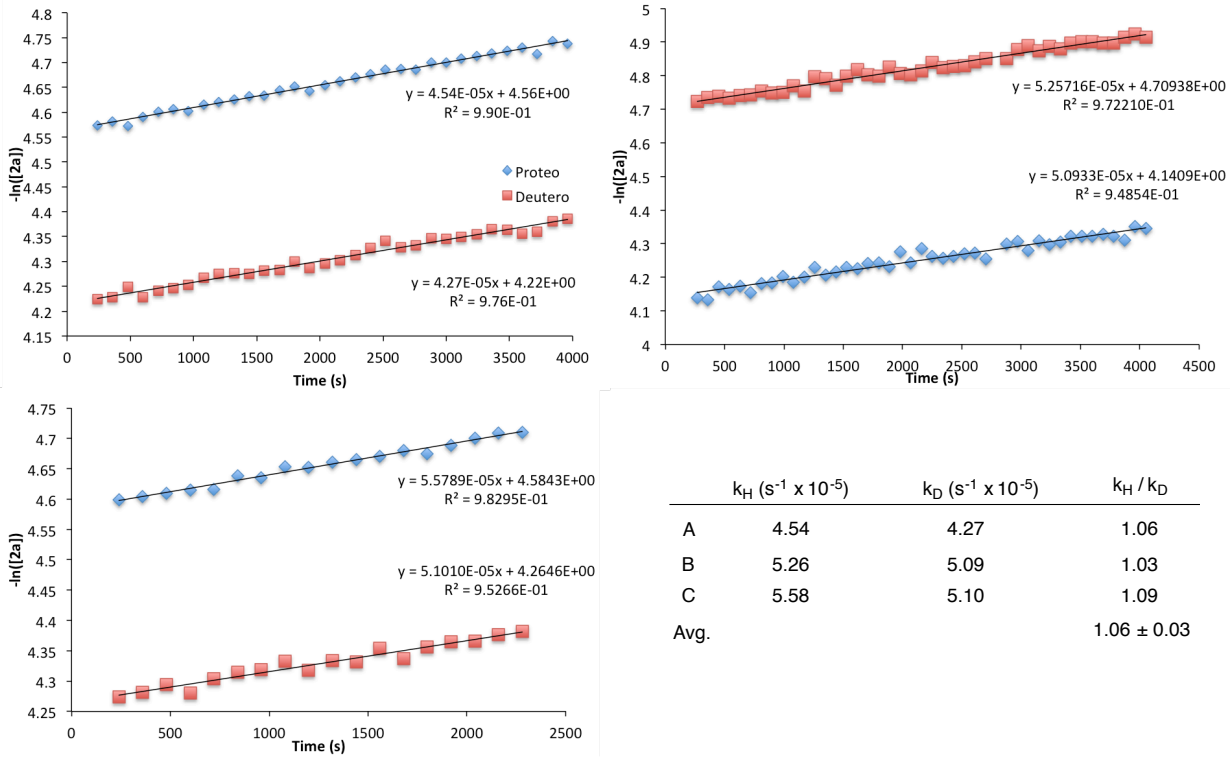

	k_H (s^{-1} x 10^{-5})	k_D (s^{-1} x 10^{-5})	k_H / k_D
A	4.54	4.27	1.06
B	5.26	5.09	1.03
C	5.58	5.10	1.09
Avg.			1.06 ± 0.03

Figure 2.15. Rate of cyclization for **2a** and **2a**-d_3 shows an intermolecular KIE of 1.06 ± 0.03.

Intramolecular isotope effect:

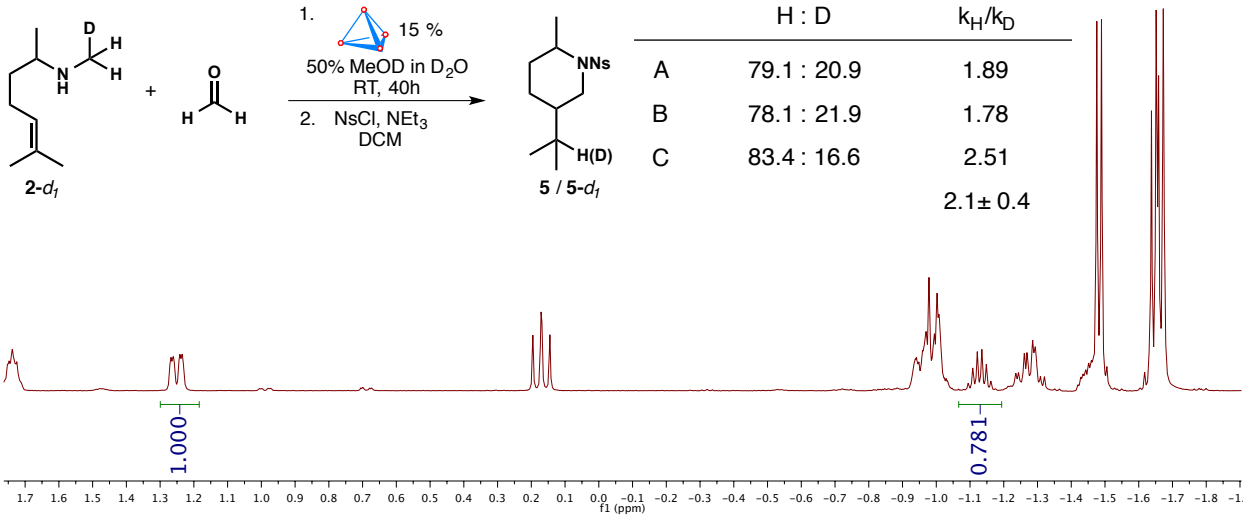

Figure 2.16. Determination of intramolecular kinetic isotope effect with a representative spectrum

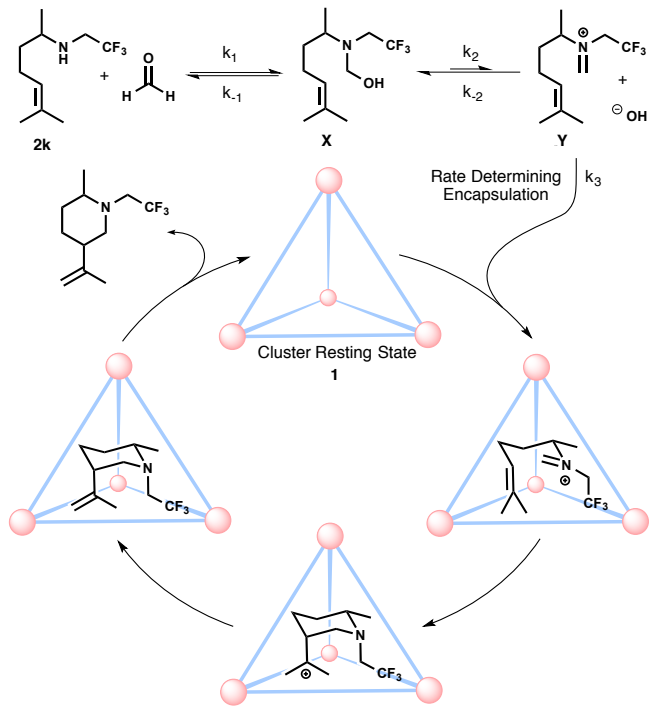

$$\frac{\partial[P]}{\partial t}=k_3[Y][1]$$

$$\frac{\partial[Y]}{\partial t}=0=k_2[X]-k_{-2}[Y]-k_3[Y][1]$$

$$K_1=\frac{[X]}{[2k][CH_2O]}$$

$$[X]=K_1[2k][CH_2O]$$

$$0=K_1k_2[2k][CH_2O]-k_{-2}[Y]-k_3[Y][1]$$

$$[Y]=\frac{K_1k_2[2k][CH_2O]}{k_{-2}+k_3[1]}$$

$$\frac{\partial[P]}{\partial t}=\frac{K_1k_2k_3[2k][CH_2O][1]}{k_{-2}+k_3[1]}$$

Figure 2.17. Derivation of the steady state rate equation for the cluster catalyzed cyclization of **2k**.

Background Rate Measurement:

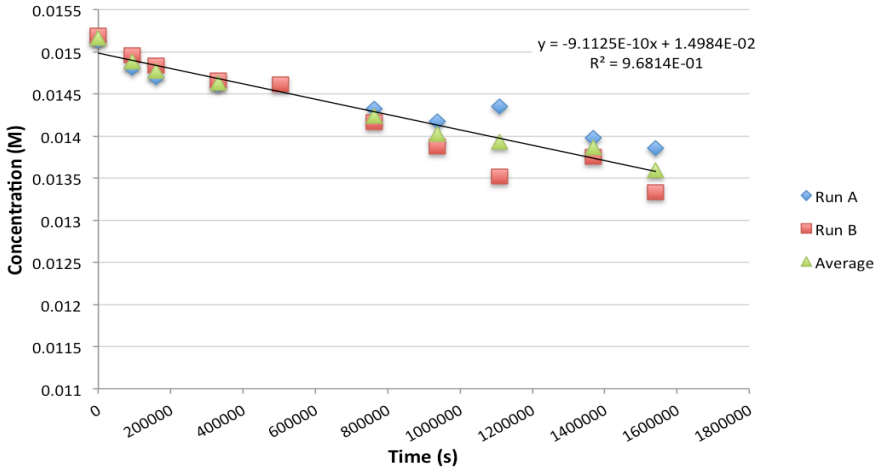

Figure 2.18. Background rate for substrate **2a** (two run average)

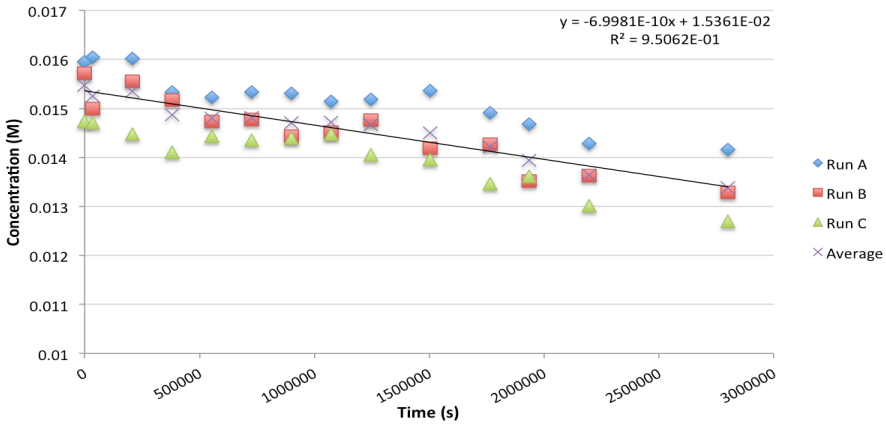

Figure 2.19. Background rate for substrate **2k** (three run average)

2.6 References

(1) (a) Klose, R. J.; Zhang, Y. *Nat. Rev. Mol. Cell Bio.* **2007**, *8*, 308. (b) Cunningham, F. X.; Gantt, E. *Proc. Natl. Acad. Sci.* **2001**, *98*, 2905 (c) Olguin, L. F.; Askew, S. E.; O'Donoghue, A. C.; Hollfelder, F. *J. Am. Chem. Soc.* **2008**, *130*, 16547. (d) Jordan, F.; Li, H.; Brown, A. *Biochemistry*, **1999**, *38*, 6369. (e) Köksal, M.; Hu, H.; Coates, R. M.; Peters, R. J.; Christianson, D.W. *Nat. Chem. Biol.* **2011**, *7*, 431. (f) Christianson, D. W. *Chem. Rev.* **2006**, *106*, 3412. (g) Faraldos, J. A.; Antonczak, A. K.; Gonzalez, V.; Fullerton, R.; Tippmann, E. M.; Allemann, R. K. *J. Am. Chem. Soc.* **2011**, *133*, 13906. (h) Degenhardt, J.; Köllner, T. G.; Gershenzon, J. *Phytochemistry,* **2009**, *70*, 1621.

(2) For reviews, see: (a) Avram, L.; Cohen, Y.; Rebek, J., Jr. *Chem. Commun*. **2011**, *47*, 5368. (b) Purse, B. W.; Rebek, J., Jr. *Proc. Natl. Acad. Sci. U.S.A.* **2005**, *102*, 10777. (c) Yoshizawa, M.; Klosterman, J. K.; Fujita, M. *Angew. Chem., Int. Ed.* **2009**, *48*, 3418. (d) Breiner, B.; Clegg, J. K.; Nitschke, J. R. *Chem. Sci* **2011**, *2*, 51. (e) Weister, M. J.; Ulmann, P. A.; Mirkin, C. A. *Angew. Chem., Int. Ed*. **2010**, *50*, 114.

(3) (a)Kang, J.; Rebek, J. *Nature*, **1997**, *385*, 50. (b) Nishioka, Y.; Yamaguchi, T.; Kawano, M.; Fujita, M. *J. Am. Chem. Soc.* **2008**, *130*, 8160. (c) Yoshizawa, M.; Kusukawa, T.; Fujita, M.; Sakamoto, S.; Yamaguchi, K. *J. Am. Chem. Soc.* **2001**, *123*, 10454. (d) Fiedler, D.; Bergman, R. G.; Raymond, K. N. *Angew. Chem.* **2004**, *116*, 6916. (e) Zhang, Q.; Tiefenbacher, K. *J. Am. Chem. Soc.* **2013**, *135*, 16213.

(4) Hart-Cooper, W. M.; Clary, K.; Toste, F. D.; Bergman, R. G.; Raymond, K. N. *J. Am. Chem. Soc.* **2012**, *134*, 17873.

(5) (a) Yoshizawa, M.; Tamura, M.; Fujita, M. *Science*, **2006**, *312*, 251. (b) J.-L. Hou, D. Ajami, J. Rebek Jr. , *J. Am. Chem. Soc.* **2008**, 130, 7810 – 7811. (c) T. Furusawa, M. Kawano, M. Fujita; *Angew. Chem. Int. Ed.* **2007**, 46, 5717 – 5719. (d) L. S. Kaanumalle, C. L. D. Gibb, B. C. Gibb, V. Ramamurthy, *J. Am. Chem. Soc.* **2004**, 126, 14366 – 14367. (e) Y. Nishioka, T. Yamaguchi, M. Yoshizawa, M. Fujita, *J. Am. Chem. Soc.* **2007**, 129, 7000 – 7001. (f) Zhang, Q.; Tiefenbacher, K. *Nat. Chem.*, **2015**, *7*, 197.

(6) Caulder, D. L.; Powers, R. E.; Parac, T. N.; Raymond, K. N. *Angew. Chem. Int. Ed.* **1998**, *37*, 1840.

(7) Pluth, M. D.; Bergman, R. G.; Raymond, K. N. *J. Am. Chem. Soc.* **2007**, *129*, 11459.

(8) Cram originally coined the term "constrictive binding" to describe the contortions of a host in response to steric repulsions during guest ingress or egress though a host aperture. Here, we expand this definition to include the conformational changes imposed on the guest in order to occupy the cavity of the host. For Cram's definition, see: Cram, D. J.; Tanner, M. E.; Knobler, C. B. *J. Am. Chem. Soc.*, **1991**, *113*, 7717.

(9) Hastings, C. J.; Bergman, R. G.; Raymond, K. N. *J. Am. Chem. Soc.* **2010**, 132, 6938

(10) Dong, V. M.; Fiedler, D.; Carl, B.; Bergman, R.G.; Raymond, K. N. *J. Am. Chem. Soc.* **2006**, *128*, 14464.

(11) For an example of a similar hydride transfer promoted by a rigid carbon framework instead of the constrictive binding of a supramolecular cluster microenvironment, see Heathcock, C. H. *Angew. Chem. Int. Ed.* **1992**, *31*, 665.

(12) **6** was isolated as a mixture of two diastereomers in an 8:1 ratio. Only one diastereomer of amine **3** was observed.

(13) The ratio of **2k** and **X** remains constant over the course of the reaction, suggesting that the two species are in rapid equilibrium.

(14) Pluth, M. D.; Bergman, R. G.; Raymond, K. N. *J. Am. Chem Soc.* **2007,** *129,* 11459-11467
(15) Concentrations of formaldehyde reflect the total amount of formaldehyde added, however, the majority of the reagent likely resides as a complex mixture of adducts and oligomers in solution. The concentration of the active formaldehyde unit is unknown, however, it is assumed that the equilibrium is rapid on the timescale of the reaction.
(16) While the hemiaminal formaldehyde adduct was observed to be in equilibrium with the starting material, this species can not be the steady state intermediate responsible for the saturation behavior, since under the saturation regime, the ratio of the amine and hemiaminal was not perturbed.
(17) It is also possible to derive a rate equation consistent with the experimental observations that involves rate determining cyclization at low cluster concentration if both the free and encapsulated iminium ions are treated as steady state intermediates. However, rate determining encapsulation is more intuitive based on previous studies of this system, as well as similar systems, and so the authors prefer this hypothesis to explain the observed saturation behavior in cluster concentration.
(18) Bräuer, T. M.; Zhang, Q.; Tiefenbacher, K. *Angew. Chem. Int. Ed.* **2016**, *55*, 7698.
(19) Caulder, D. L.; Powers, R. E.; Parac, T. N.; Raymond, K. N. *Angew. Chem. Int. Ed.* **1998**, *37*, 1840.
(20) Cope, A. C.; Burrows, W. D. *J. Org. Chem.*, **1965**, *30*, 2163.

Chapter 3

A Supramolecular Microenvironment Strategy for Organotransition Metal Catalysis

Portions of this chapter have been previously published in:

Kaphan, D. M.*; Levin, M. D.*; Bergman, R. G.; Raymond, K. N.; Toste, F. D. *Science,* **2015**, *350*, 1235-1238.

and

Levin, M. D.*; Kaphan, D. M.*; Hong, C. M.; Bergman, R. G.; Raymond, K. N.; Toste, F. D. *J. Am. Chem. Soc.* **2016**, *138*, 9682-9693.

*denotes equal contribution

3.1 Preface

In this chapter, it is demonstrated that the Raymond supramolecular cluster (**1**) is capable of catalyzing alkyl-alkyl reductive elimination from high-valent gold and platinum complexes. Chapter 2 focused on the expansion of the set of catalytic intermediates recognized by the cluster from oxonium ions to iminium ions; chapter 3 will further expand this set to include cationic organotransition metal complexes. This advance represents a notable departure from the catalysis of simple organotransformations, which are largely biomimetic in nature. The cluster accelerates reductive elimination with enzyme-like rate accelerations of up to 1.9 x 10^7 fold, which represents the largest rate acceleration by a synthetic microenvironment catalyst at the time of this report. Cluster catalyzed reductive elimination was further incorporated into a dual-catalytic cross coupling transformation where both the cluster and an appropriate platinum precatalyst were necessary for efficient turnover to occur.

3.2 Introduction

Organotransition metal catalysis has flourished in recent years as the development of new catalyst systems has enabled methodologies of remarkable activity, selectivity and efficiency.[1,2] In large part, the development of these methodologies can be attributed to the discovery and implementation of novel supporting ligand architectures, which modulate the metal center's local stereoelectronic microenvironment in order to influence the rates of individual elementary steps, control catalyst speciation, and disfavor catalyst deactivation pathways. However, in this traditional approach, the ligand architecture necessarily defines an identical microenvironment to the metal center throughout the course of the catalytic cycle, and modifications necessary in order to facilitate one elementary step may result in deleterious effects on the remaining elementary steps in the catalytic cycle.

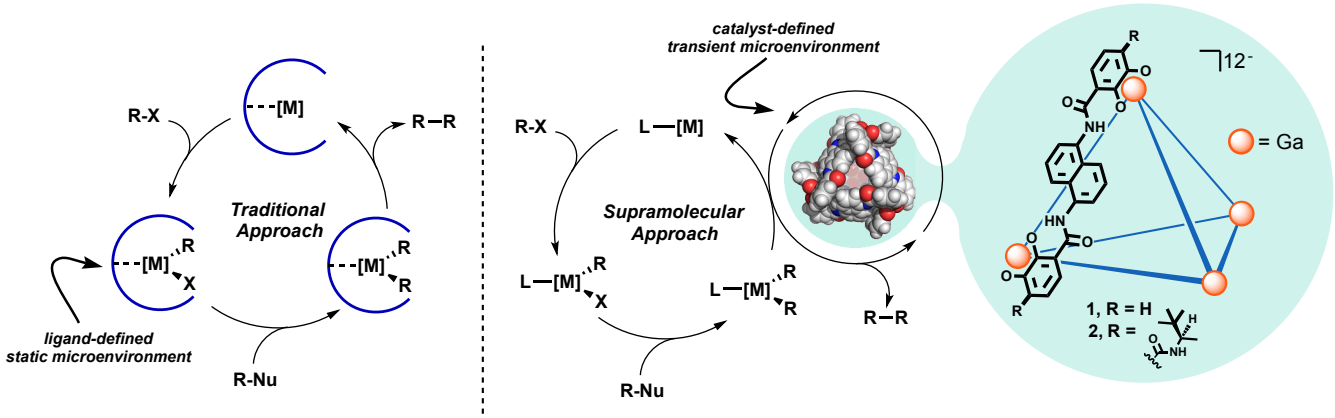

Figure 3.1. A supramolecular approach for transition metal catalyzed cross-coupling.

The necessity for stereoelectronic compromise might be circumvented by the application of a supramolecular microenvironment catalyst (such as tetrahedron **1**), which could engage one elementary step by transient encapsulation and stabilization of the appropriate catalytic intermediate and its subsequent transition state, while leaving the remainder of the catalytic cycle unperturbed (Figure 3.1).[3,4] In such an approach, the microenvironment of the transition metal can be defined for a problematic step by selective

and specific molecular recognition, without complicating deleterious effects on the remainder of the cycle. One might imagine that if this strategy is successful for the acceleration of one kinetically prohibitive elementary step, multiple orthogonal supramolecular microenvironment catalysts could be applied in concert in order to differentially define an optimized microenvironment for each elementary step of the reaction.

Cluster **1** has previously been shown to encapsulate various transition metal complexes, typically with concomitant loss of a halide or other negatively charged ligand, as demonstrated by two representative examples shown in Scheme 3.1. Trimethylphosphine gold(I) bromides and chlorides are strongly encapsulated as their corresponding cation in water.[5,6] By promoting halide dissociation upon encapsulation, the metal center is rendered electron poor and has its coordination number decreased by one. Cluster **1** has also been shown to effect stoichiometric organometallic reactivity upon encapsulation, as exemplified by the retro-cycloisomerization of cyclooctadiene ruthenium cyclopentadienyl chloride upon encapsulation, however, no catalytic turnover could be achieved in this system.[7]

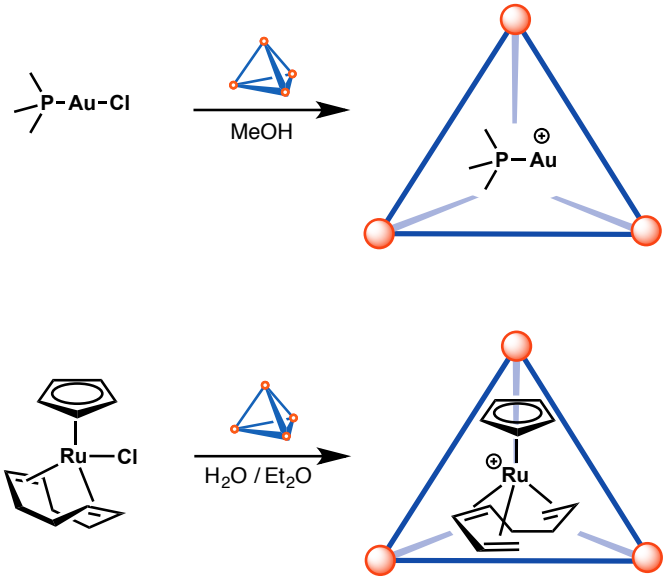

Scheme 3.1. Selected precedent for encapsulation of cationic metal complexes by cluster **1**.

One catalytically relevant, yet particularly sluggish, transformation is the carbon-carbon bond forming reductive elimination of sp^3 fragments from transition metals.[1] As a result, alkyl-alkyl cross-coupling processes are often plagued by slow turnover and undesired side-reactions.[8] This phenomenon is strikingly demonstrated by the difference in the rate of reductive elimination of methyl and aryl substituents from gold(III) complexes (Scheme 3.2).[9,10] The rate of biaryl elimination from gold(III) at cryogenic temperatures (-52 ºC) was at least two orders of magnitude faster than ethane elimination at elevated temperatures (45 ºC), a range of nearly 100 ºC.

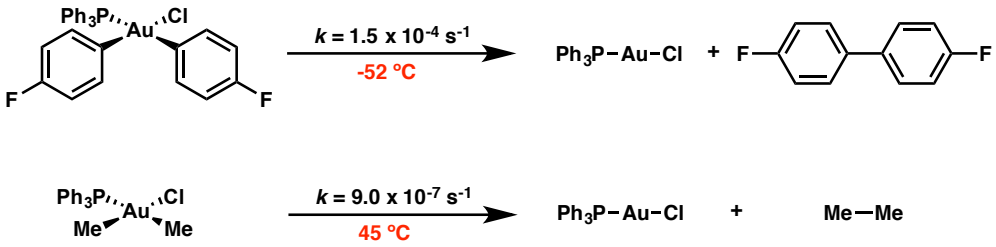

Scheme 3.2. Rates of reductive elimination of sp^2 and sp^3 fragments from Au(III).

The properties of cluster **1** make it particularly amenable to application as a microenvironment catalyst for reductive elimination. A number of factors affect the rate of reductive elimination from a metal center.[1] Generally, electron poor metal centers undergo reductive elimination more rapidly than electron rich metal centers, due fact that reductive elimination intrinsically increases electron density at the metal center. Additionally, odd coordinate metals undergo reductive elimination faster than even coordinate complexes due to orbital symmetry considerations involving the d orbitals on the metal that are populated after the reductive elimination takes place. Finally more sterically congested metal centers undergo faster reductive elimination as a result of steric relief in the transition state, and destabilization of the ground state. Each of these considerations might contribute to an increased rate of reductive elimination upon inclusion within supramolecular cluster **1**, due to the fact that encapsulation generates a constricted cationic species of decreased coordination number.

3.3 Results and Discussion

3.3.1 Cluster Catalysis of Reductive Elimination from Gold(III)

In order to evaluate this hypothesis, cluster **1** was explored as a catalyst for the elimination of ethane from dialkyl Au(III) iodide complex **3-I**[10,11] with dramatic results. The observed half-life for reductive elimination under a 10 mol% loading of **1** decreased from 20 weeks to just 53 minutes, corresponding to a 4,000-fold acceleration in the observed initial rate (Scheme 3.3A). Blocking the cluster's interior cavity with the strongly encapsulated Et_4P cation eliminated the accelerating effect of **1**, suggesting that access to the interior cavity of **1** is essential for efficient catalysis. Additionally, substitution of the compact trimethylphosphine ligand by its more sterically demanding triphenyl congener in complex **5** resulted in no observable acceleration for reductive elimination in the presence of **1**, which is indicative of size-exclusion from the internal cavity of the catalyst (Scheme 3.3B).

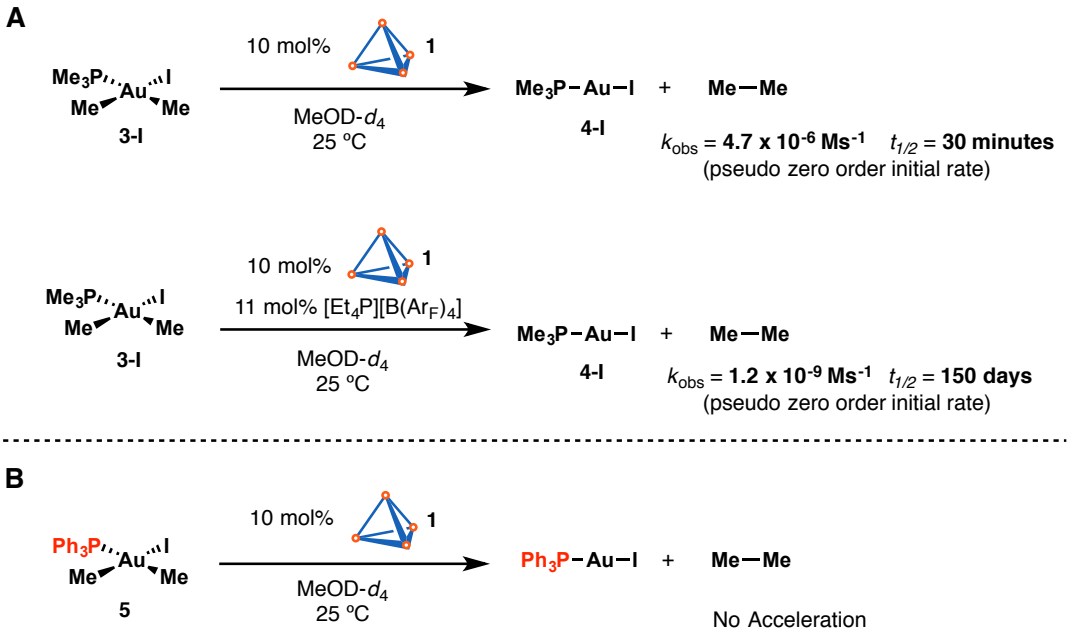

Scheme 3.3. (A) Reductive elimination from **3-I** catalyzed by cluster **1**. (B) Size selection exhibitied by **1**.

Upon inspection of the kinetic profile for the catalyzed reductive elimination from **3-I**, it became clear that a catalyst deactivation pathway was operative at extended reaction times (Figure 3.2A). While product inhibition is commonly observed in supramolecular catalysis, under catalytically relevant conditions, it was shown that product **4-I** did not engage cluster **1**. However, examination of the reaction mixture by ^{1}H-NMR spectroscopy revealed a strongly encapsulated species, which was identified as the cationic bis(phosphine) complex **6** (Figure 3.2B). The identity of inclusion complex **6** ⊂ **1** was verified by independent synthesis and could be characterized single-crystal X-ray diffractometry (Figure 3.2C). Suitable crystals of complex **6** ⊂ **1** were obtained by vapor diffusion of acetone into a solution of the complex in 1:1 water and methanol over two weeks. Due to limited crystal size and a high degree of solvent disorder, synchrotron radiation was required to collect a sufficient data set at 0.88 Å resolution with 1.2276 Å radiation. Complex **6** ⊂ **1** crystallized in the monoclinic space group $P2_1/c$ with 4 formula units per unit cell, and the data are consistent with a molecule of **6** encapsulated within the cavity of **1**.[12,13] Further crystallographic information can be found in the supporting information below.

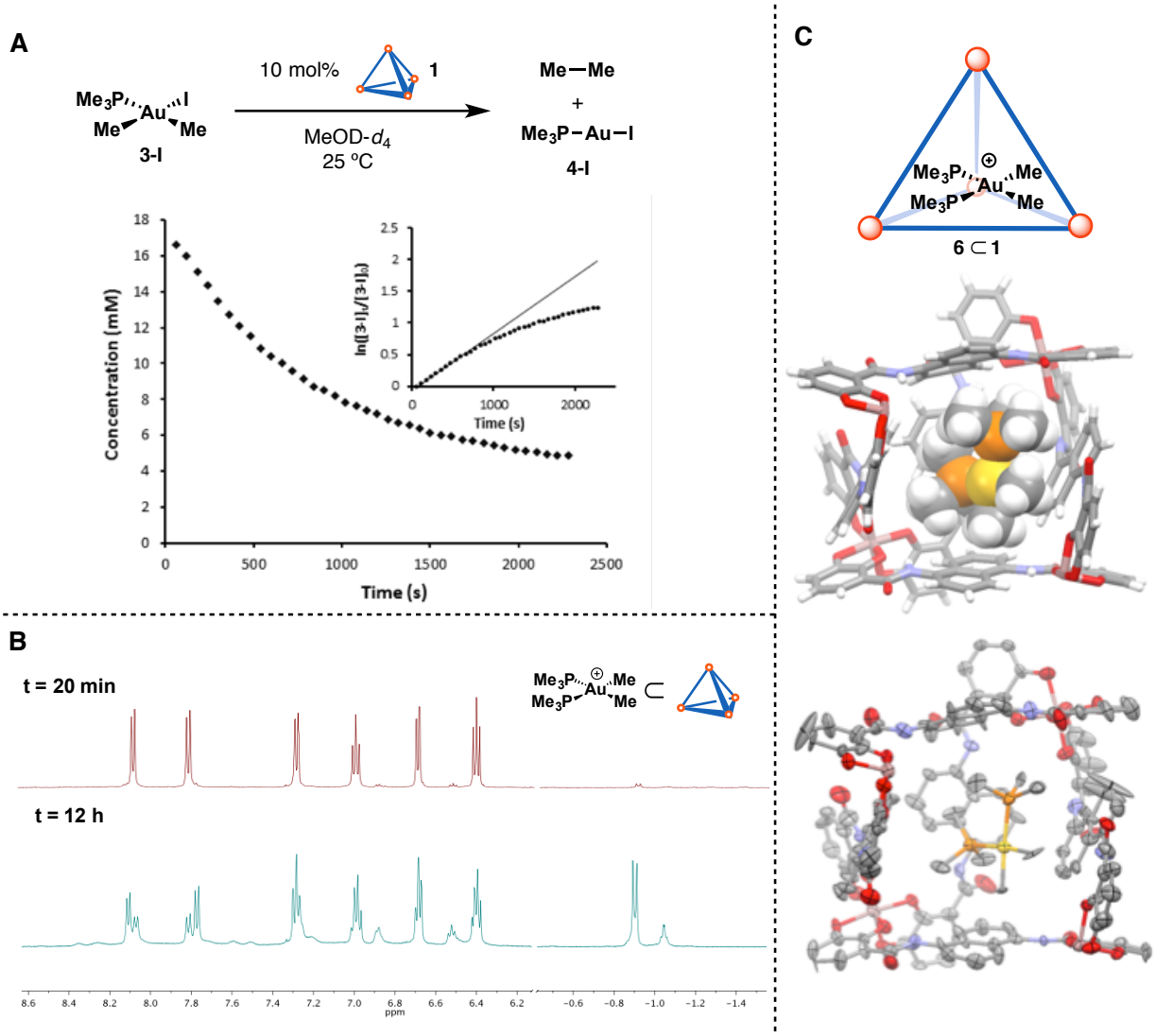

Figure 3.2. (A) Kinetic profile of reductive elimination from **3-I** catalyzed by **1**, showing deviation from first order behavior. (B) ^{1}H-NMR spectrum at early and late reaction times, showing encapsulated **6** ⊂ **1** in the upfield region. (C) Crystal structure of **6** ⊂ **1**, space-filling model (top), and thermal ellipsoids (50% probability, bottom). Potassium ions, solvent, and one ligand of **1** have been removed for clarity.

3.3.2 Mechanistic Investigation of Cluster Catalyzed Reductive Elimination

In order to better understand the catalyzed reductive elimination process, kinetic experiments were conducted to determine the order in each reactant using the method of initial rates. For the reductive elimination of ethane from complex **3-I**, the reaction displayed first order dependence on catalyst **1**, as measured by competitive inhibition with Et_4P^+ (a linear relationship was observed between the rate of reductive elimination and the concentration of unblocked cluster) (Figure 3.3 top). Conversely, the rate of reductive elimination was found to be dramatically attenuated in the presence of exogenous iodide, in the form of potassium iodide added to the reaction mixture (Figure 3.3 middle). The rate dependence on gold concentration showed saturation behavior, which could be linearized by

plotting the double reciprocal of concentration and rate (Figure 3.3 bottom). (Gold complex **3-Br** was employed rather than **3-I** because it was expected to show a higher affinity for the interior of **1** (*vide infra*), however, the calculated value for k_{cat} is necessarily identical for **3-I** and **3-Br** due to the mechanistic convergence in the encapsulated intermediate.) These results are consistent with an overall Michaelis-Menten type mechanism involving pre-equilibrium halide dissociation followed by a transient and reversible encapsulation of the nascent cationic species, and, finally, an irreversible reductive elimination event within the cluster cavity (Scheme 3.4). Accordingly, the aforementioned double reciprocal plot of substrate concentration and rate is directly analogous to a Lineweaver-Burk plot, and from these data the Michaelis-Menten parameter k_{cat} could be assessed. The measured k_{cat} for complex **3-I** was found to be 3.3×10^{-2} s^{-1}, corresponding to an overall acceleration (k_{cat}/k_{uncat}) of 5.0×10^{5}. It should be noted that this mechanistic scenario is kinetically indistinguishable from a mechanism in which the neutral gold(III) complex is encapsulated, followed by halide dissociation inside of the cluster, however, this mechanism is disfavored due to the consideration of microscopic reversibility—this mechanistic pathway in the forward direction would require metal cation egress to occur by a mechanism wherein iodide must approach and enter the undecaanionic inclusion complex, which seems kinetically prohibitive.

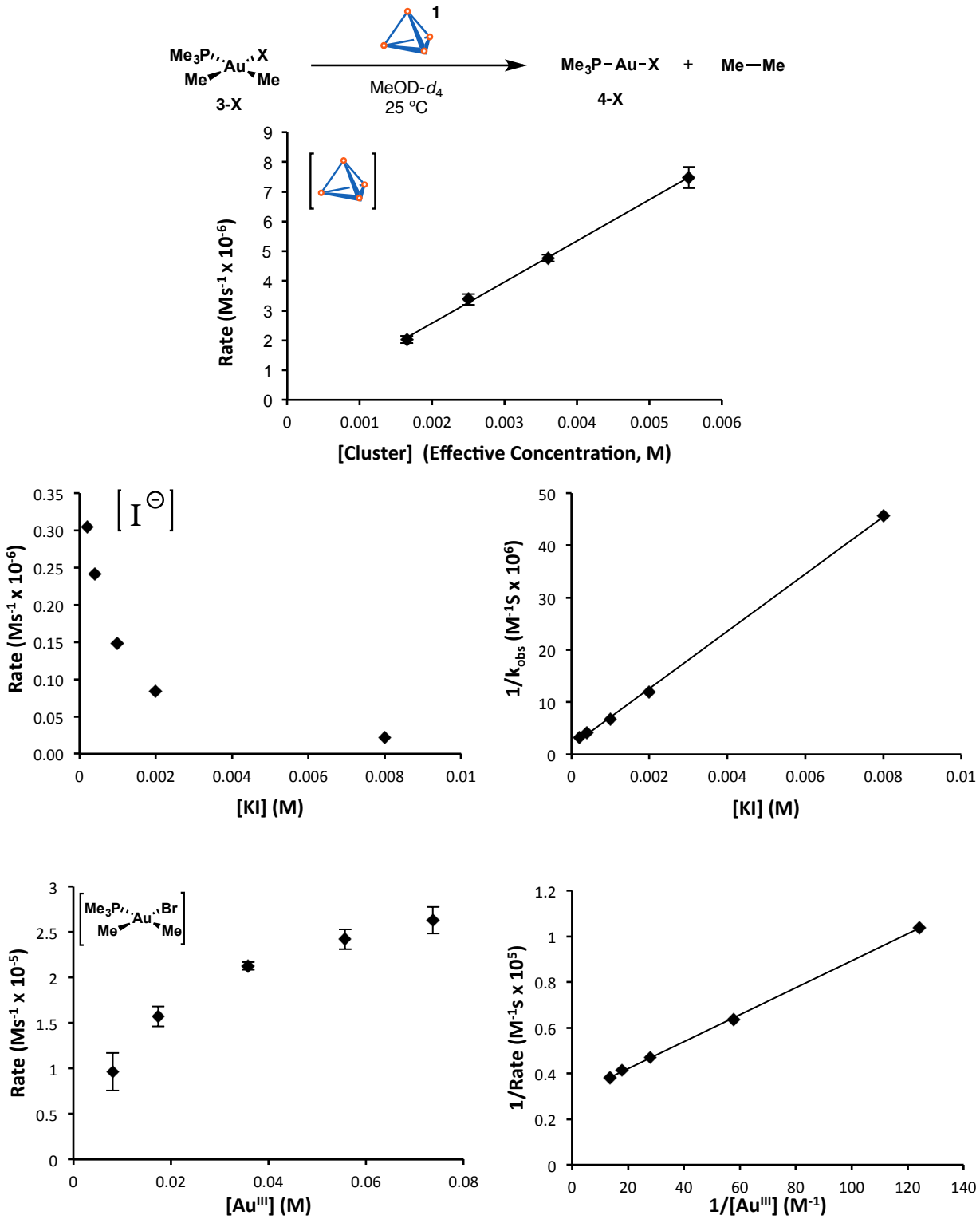

Figure 3.3. Rate dependencies for reductive elimination from **3-I**, catalyzed by cluster **1**. (Top) Cluster open active site dependence, (Middle) Iodide dependence, measured by adding exogenous NaI, (Bottom) Rate dependence on substrate concentration (**3-Br** used in order to accentuate saturation behavior, *vide infra*).

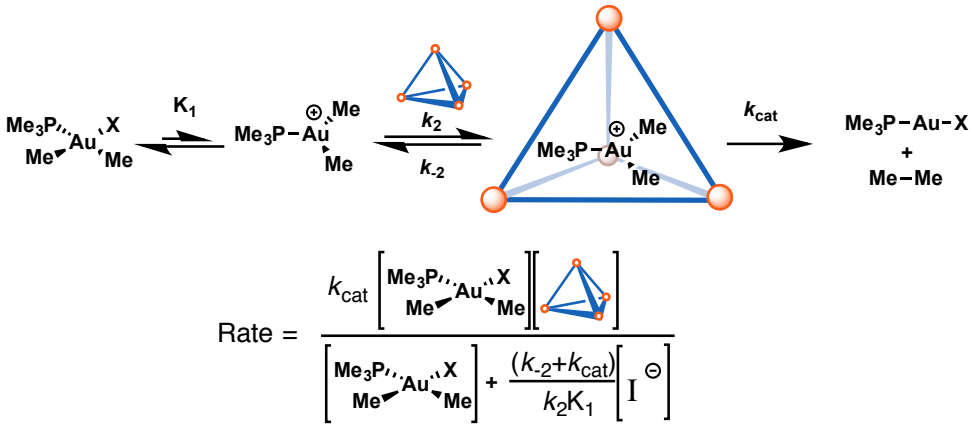

Scheme 3.4. (Top) Michaelis-Menten-like mechanism consistent with kinetic observations. (Bottom) Rate law derived from steady state analysis of Michaelis Menten mechanism with pre-equilibrium halide dissociation.

3.3.3 Influence of Spectator Ligands

Having established a likely mechanism for the catalysis of reductive elimination from **3** by cluster **1**, the effect of substitution on reactivity was investigated. It was hypothesized that it might be possible to disfavor the bisphosphine gold(III) cation catalyst deactivation pathway by increasing the bulk of the supporting phosphine ligand, such that the bisphosphine cation would be sufficiently large to disfavor inclusion within the cavity of **1**. In accordance with this hypothesis, triethylphosphine ligated complex **7-I** exhibited rapid and complete reductive elimination in the presence of **1** (Scheme 3.5). No catalyst deactivation was observed, with the decay of **7-I** following first order kinetics over multiple half-lives, and a turnover number (TON) in excess of 300 could be achieved. The catalyzed reaction of **7-I** exhibits a half-life of just 47 seconds compared to 45 days in the uncatalyzed reaction, corresponding to an observed rate acceleration of 80,000-fold.

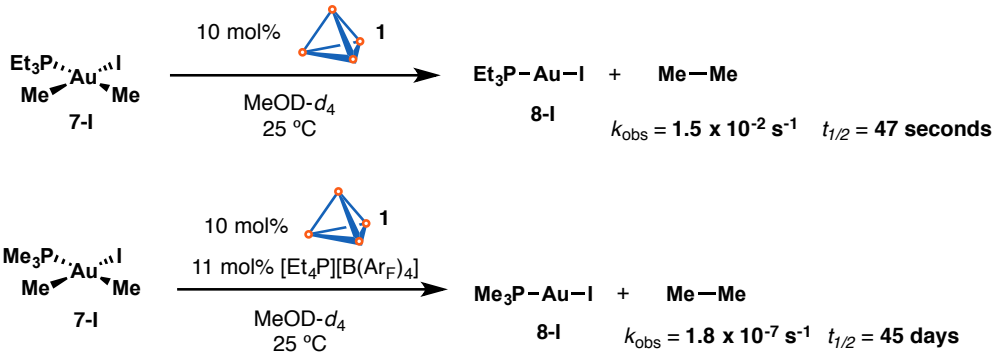

Scheme 3.5. Reductive elimination from **7-I** catalyzed by cluster **1**.

The rate dependence on substrate, cluster, and iodide concentration for reductive elimination from **7-I**, catalyzed by **1**, was consistent with those of **3-I**, indicating that the Michaelis-Menten-like mechanism remains operative (for halide and cluster dependence plots, see supporting information below). However, the rapidity of this reaction introduced substantial error into the estimation of k_{cat} by the method of initial rates (Figure 3.4, left,

orange squares). Instead, since no catalyst deactivation was observed, the technique of Reaction Progress Kinetic Analysis (RPKA) could be applied in order to generate a larger data set (Figure 3.4, left, blue diamonds). The corresponding Lineweaver-Burk plot (Figure 3.4, right) affords an estimate for k_{cat} of 3.4 s^{-1}, corresponding to a rate acceleration (k_{cat}/k_{uncat}) of 1.9 x 10^7.[14] The data obtained by RPKA are consistent with the initial rate data, while providing a more robust measurement due to the expanded data set. This rate acceleration is on par with that of many enzymatic processes; for comparison, chymotrypsin has been shown to accelerate amide bond hydrolysis with rate accelerations of 10^7-fold.[15]

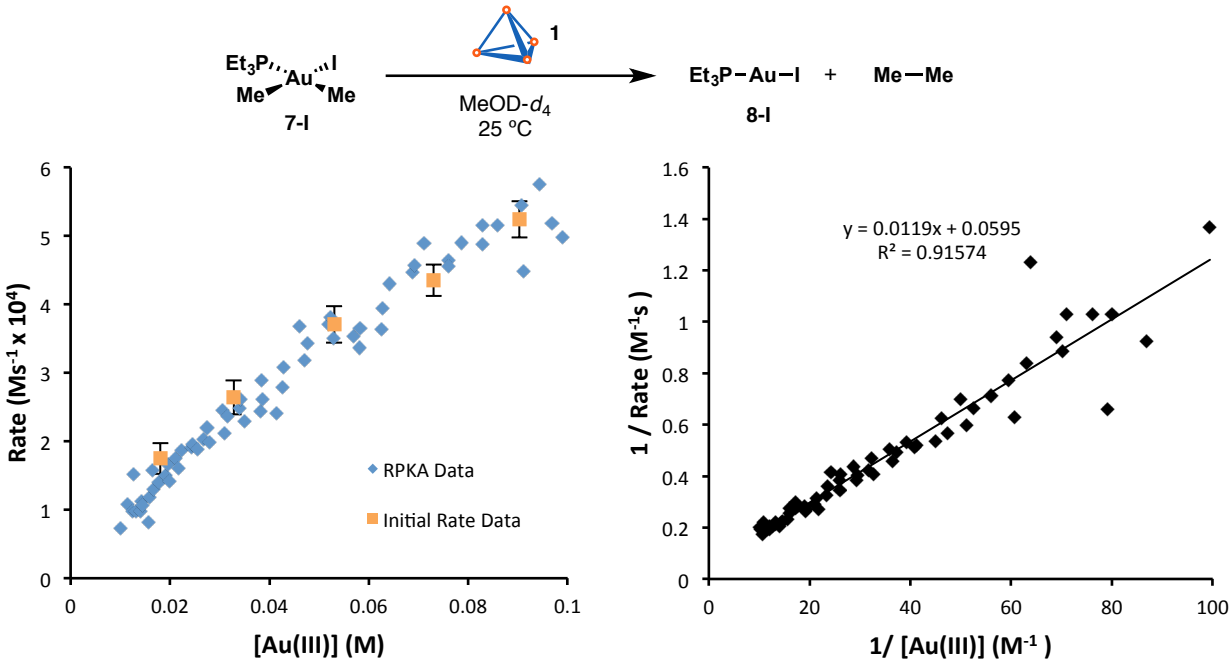

Figure 3.4. (Left) Rate dependence on concentration of **7-I** by initial rates (orange square) and RPKA (blue dots). (Right) Lineweaver-Burk plot from RPKA data used to calculate k_{cat}.

A more detailed comparison of the rates for reductive elimination from trimethylphosphine complex **3-I** and triethylphosphine complex **7-I** catalyzed by cluster **1** provides some additional insights into the influence of the phosphine ligand; namely, **7-I** is bound more tightly than **3-I** by **1** and, after the binding event, the transition state for reductive elimination from **7-I** is more stabilized by **1** than the transition state of reductive elimination from **3-I** (for a graphical depiction of the following analysis, see Figure 3.5). **7-I** undergoes catalyzed reductive elimination with a half-life 68 times shorter than the catalyzed half-life for **3-I** (47 seconds vs. 53 minutes), while the half-lives for uncatalyzed reductive elimination differ by only a factor of four. Additionally, as determined by Michaelis-Menten analysis, the measured rate of reductive elimination within the supramolecular assembly (k_{cat}) is 38 times faster for **7** than for **3**. Comparison of the ratio of catalyzed observed rates (68-fold, corresponding to $\Delta\Delta G^{\ddagger}$ = 2.5 kcal/mol) to the ratio of k_{cat} (38-fold, corresponding to $\Delta\Delta G^{\ddagger}$ = 2.2 kcal/mol) suggests that the triethylphosphine ligated complex shows higher binding affinity for the interior of **1** ($\Delta\Delta G$ = 0.3 kcal/mol). Furthermore, comparison of the ratio of background rates of reductive elimination from **3-I** and **7-I** (3.8-fold, corresponding to $\Delta\Delta G^{\ddagger}$ = 0.79 kcal/mol) to the ratio of the catalyzed rate of reductive elimination suggests that **1**

more effectively stabilizes the transition state for reductive elimination from the triethylphosphine ligated complex ($\Delta\Delta\Delta G^{\ddagger}$ = 1.7 kcal/mmol).

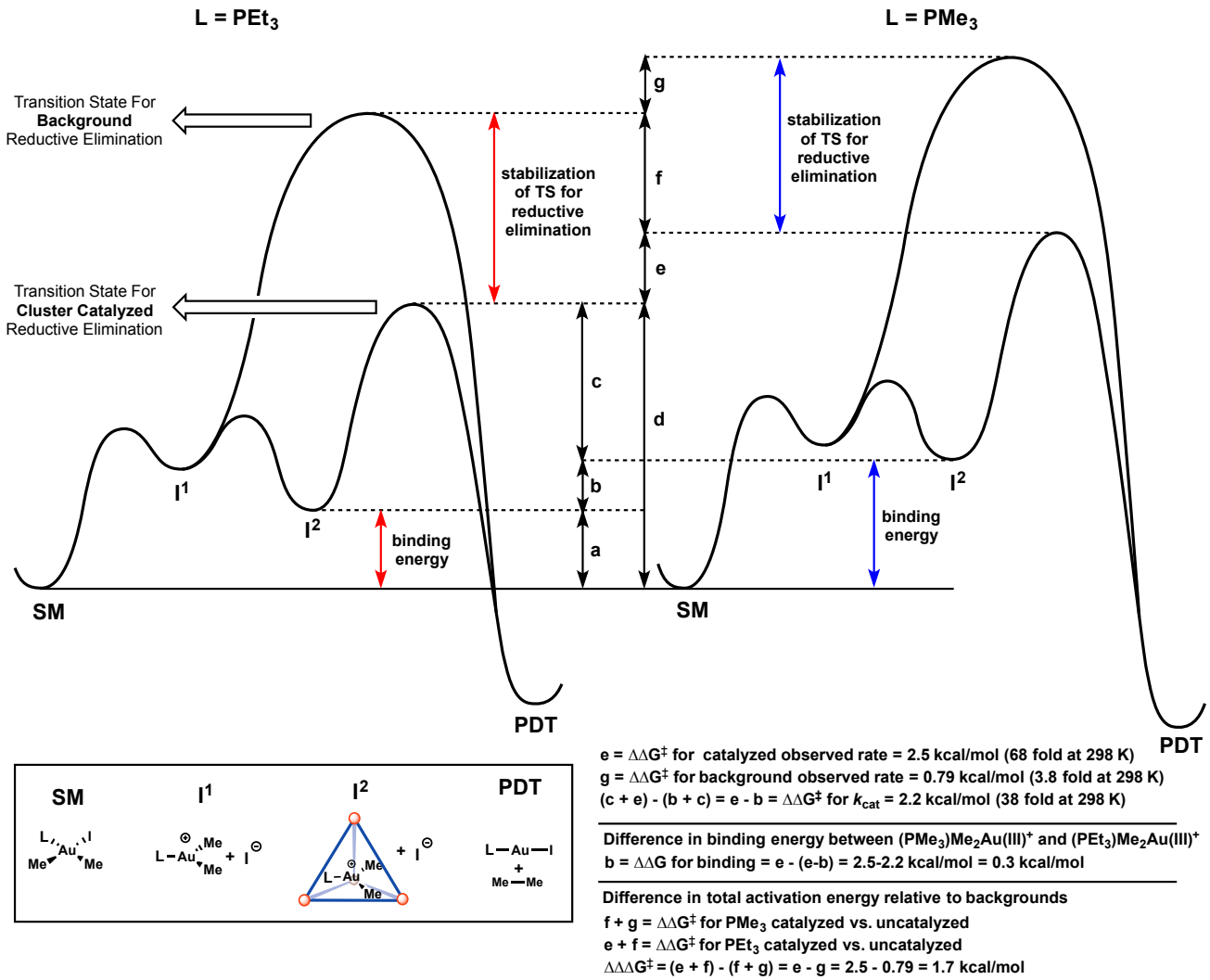

Figure 3.5. Reaction coordinate diagrams for reductive elimination from **7-I** and **3-I**.

Several possible explanations for these phenomena are consistent with the experimental results: (i) increased steric compression of the larger complex within the supramolecular cavity (thus destabilizing the bound ground state relative to the transition state for reductive elimination),[1] (ii) increased hydrophobicity of Et_3P,[16] (iii) better shape complementarity resulting in better solvent exclusion and increased contact surface area,[17] or (iv) higher concentrations of the free cationic Au(III) complex as a result of the stronger electron donation from the triethylphosphine ligand.[2a]

The identity of the halide substituent on **3** also has a dramatic effect on the rate of the reaction, as well as the catalyst deactivation pathways. Examination of the iodide, bromide and chloride congeners **3-I**, **3-Br**, and **3-Cl**, revealed a significant influence on the observed rate of reductive elimination, with the relative rates increasing in the order Cl ~ Br > I (Figure 3.6). Inhibition was also observed from encapsulation of the resulting Au(I) complexes **4-Cl**

and **4-Br** but not for **4-I**. In order to determine the generality of this behavior, the corresponding triethylphosphine ligated analogues **7-Cl** and **7-Br** were prepared and subjected to cluster catalyzed reductive elimination. In this experiment, significant product inhibition by **8-Cl** and **8-Br** was observed, with substantial deviation from first-order decay. In contrast, **7-I** and its product **8-I** followed an uninhibited first order reaction profile past five half-lives (Figure 3.7). The rapid rate of the reaction and sheer extent of product inhibition in the case of **7-Cl** and **7-Br** precluded a quantitative comparison of the initial rate differences between this halide series, however, the qualitative trend for overall reaction rate of Cl ~ Br > I is consistent between the **3-X** and **7-X** series.

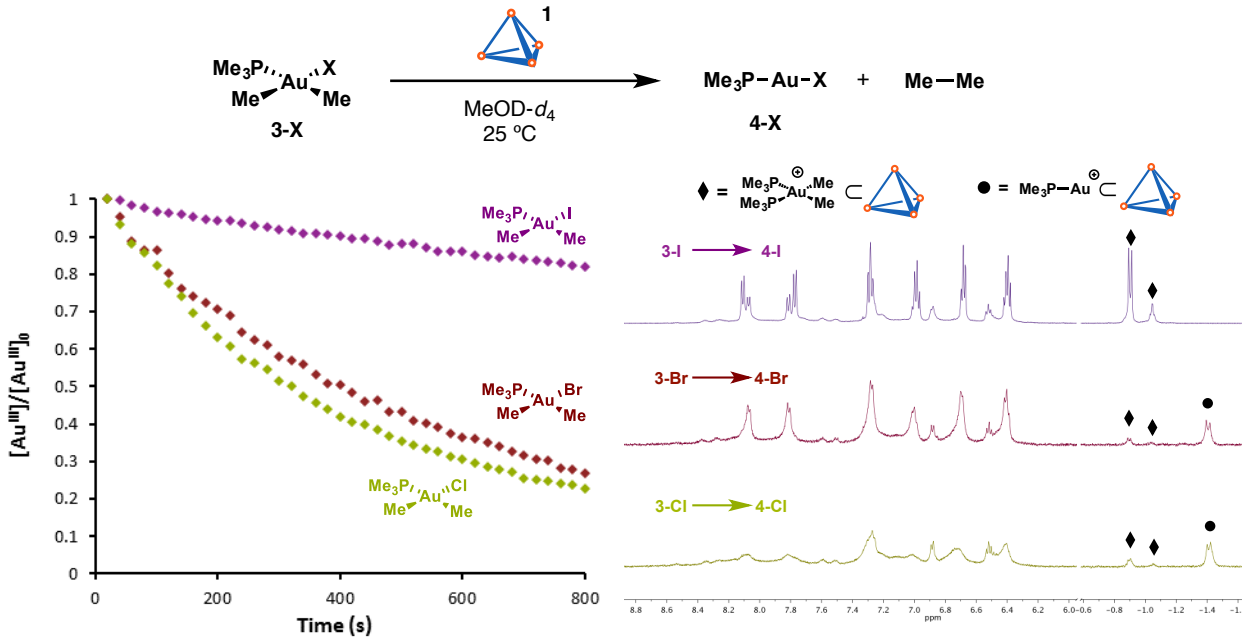

Figure 3.6. Kinetic traces for reductive elimination from **3-I**, **3-Br**, and **3-Cl** catalyzed by 10 mol% **1** (left), and ^{1}H-NMR spectrum showing product inhibition at long reaction times by **4-Br** and **4-Cl** (right)

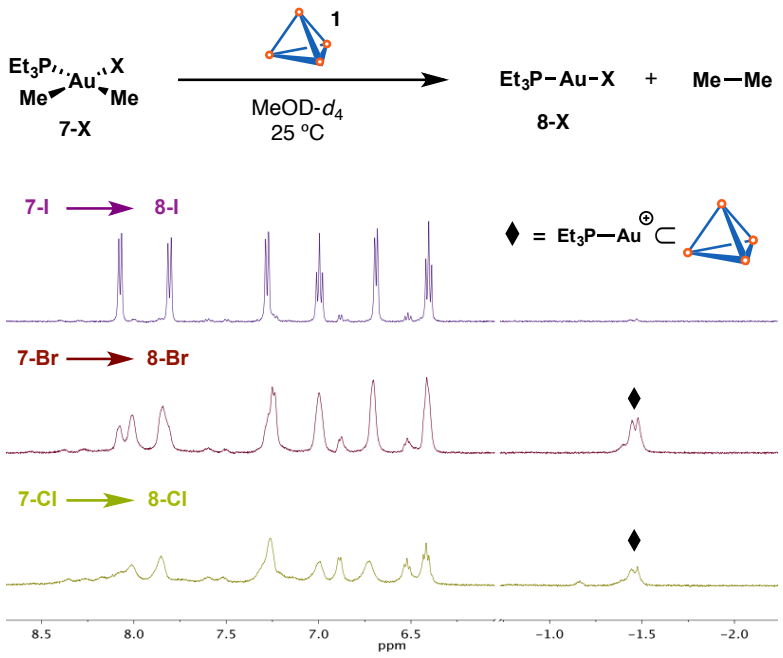

Figure 3.7. [1]H-NMR spectrum showing product inhibition by **8-Br** and **8-Cl**, with no encapsulation observed for **8-I**.

Based on the proposed mechanism for cluster catalyzed reductive elimination, one would expect pre-equilibrium halide dissociation to influence the overall rate. However, *a priori*, the direction of this influence is unclear. Examination of a generalized equilibrium for encapsulation reveals that the empty cluster and encapsulated cation are identical for all members of the series, and as such only the Au–X heterolytic bond dissociation energies and differences in solvation of the dissociated halide anion can influence the position of the equilibrium. For Au(III), the Au–X heterolytic bond strengths trend as Au–I < Au–Br < Au–Cl[18], while solvation enthalpy of the dissociated halides[19] trends as Cl > Br > I. Clearly the observed rates for reductive elimination for **3** (Cl ~ Br > I) correlate more strongly with the halide solvation enthalpy than the relevant Au(III) halide bond strengths (one would expect the gold chloride complexes to undergo slower reductive elimination in that case). For Au(I), the relative influence of solvation and bond strength is less clear. The heterolytic bond strengths trend as Au–Br < Au–Cl < Au–I.[20] Here, the observation of product inhibition in the case of the Au(I) bromide and chloride complexes is consistent with both solvation-dependent and bond strength-dependent equilibrium for encapsulation of **4-X** and **8-X**, but the observation of solvation-dominated behavior for Au(III) suggests that the influence of solvation is likely also the major factor in this trend.

3.3.4 Exploration of Generality with Respect to Metal Center and Eliminating Groups

The phenomenon responsible for the catalytic acceleration of reductive elimination from gold(III) dialkyl halide complexes by cluster **1** should be generalizable to other high valent metal centers, so long they bare an appropriate heterolytically labile X-type ligand to facilitate encapsulation. To test this hypothesis, platinum(IV) complex **9** was prepared, and subjected to catalysis by cluster **1**. The observed half-life for reductive elimination of ethane was just 6 minutes in the presence **1**, as compared to about 9 days when the internal cavity of

cluster **1** was blocked with tetraethylphosphium, corresponding to a 2,300-fold acceleration of the observed rate (Scheme 3.6). The rate dependence on the catalyzed reductive elimination from **9** with respect to substrate, cluster and exogenous iodide concentration were also consistent with a Michaelis-Menten-like mechanism (see supporting information below). Analysis of the Lineweaver-Burk plot for **5** afforded a k_{cat} of 2.3 x 10^{-2} s^{-1}, corresponding to a rate acceleration of 2.6 x 10^4 fold (Figure 3.8).

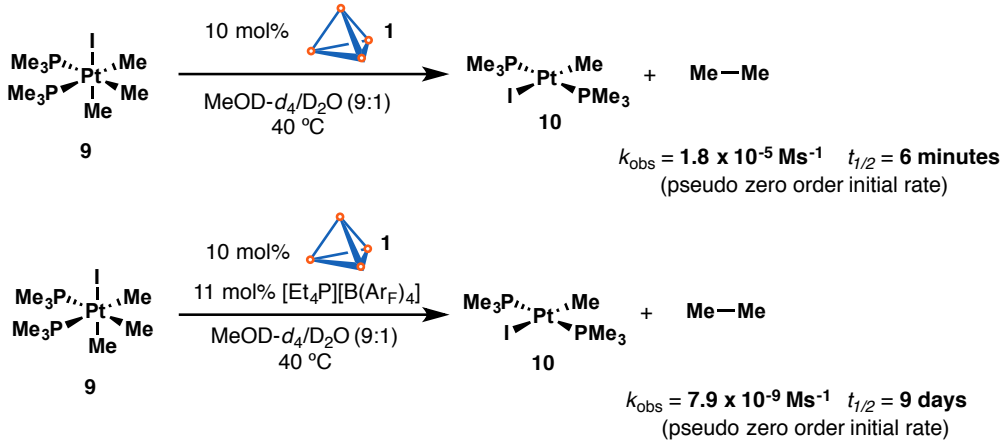

Scheme 3.6. Reductive elimination from **9**, catalyzed by cluster **1**.

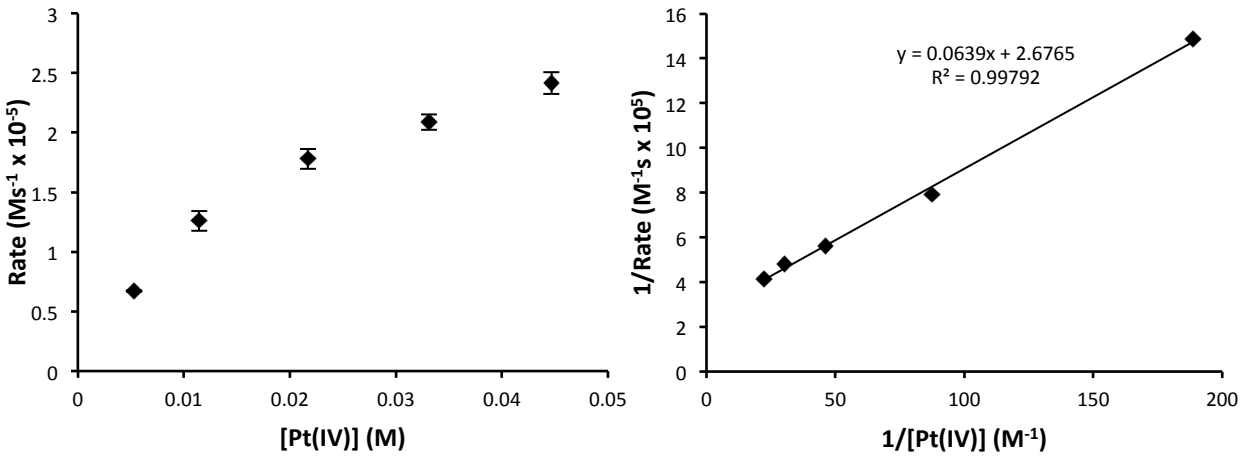

Figure 3.8. (left) Rate dependence on substrate concentration for reductive elimination from **9**, catalyzed by cluster **1**. (right) Lineweaver-Burk plot corresponding for reductive elimination from **9**, catalyzed by cluster **1**.

It should be noted that, while cluster catalyzed reductive elimination from **9** did proceed under the standard conditions developed for gold complexes **3-I** and **7-I**, the reaction proved too sluggish under these conditions for efficient kinetic analysis. It was hypothesized that, given the role of solvation in the relative rates of reductive elimination for the **3-X** and **7-X** halide series, the addition of a small amount of D_2O as co-solvent for the reaction would promote halide dissociation, and thus accelerate the overall catalytic process. In order to evaluate this hypothesis, the rate of reductive elimination from platinum complex **9**, catalyzed by cluster **1**, was evaluated with solvent mixtures ranging from pure methanol to an 85:15

mixture of methanol and water (Figure 3.9). Indeed, as the water content increased, a corresponding increase was observed in the rate of catalyzed reductive elimination. This increase correlates with the strength of solvation for the dissociated halide anions in each solvent, though the effect of the increased binding affinity driven by the greater solventophobic effect for water cannot be disentangled. A water content of 10 percent v/v was selected as a compromise between reaction acceleration and maintaining homogeneity over the course of the reaction, and was employed in all reactions pertaining to the mechanistic analysis of cluster catalyzed reductive elimination from **9** (*vide supra*).

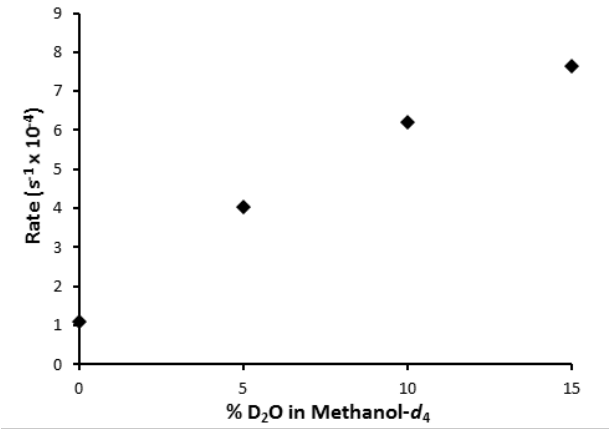

Figure 3.9. Influence of solvent composition on the rate of cluster catalyzed reductive elimination from **9.**

Despite the noted influence of the spectator ligands and reaction conditions, the groups undergoing coupling in the elimination are of greatest interest in the overall process. In order to glean further mechanistic insights as well as to determine the scope of cluster catalyzed reductive elimination, a sampling of functionality was examined. Diethyl gold complex **11**, in the presence of 10 mol % of cluster **1**, underwent catalyzed reductive elimination to form butane with an observed rate constant of 7.6 x 10^{-3} s^{-1}, a relative rate of 29 when compared to catalyzed reductive elimination from dimethyl gold complex **3-I** (k_{obs} = 2.6 x 10^{-4} s^{-1}) (Scheme 3.7).

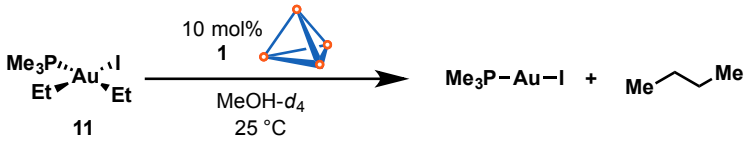

Scheme 3.7. Butane forming reductive elimination from **11** catalyzed by cluster **1**.

The consumption of ethyldimethyl platinium complex **12** was also accelerated dramatically in the presence of cluster **1**, however, instead of observing carbon-carbon bond formation, the exclusive organic products of the reaction were methane and ethylene (Scheme 3.8). These products arise from β-hydride elimination from the pentacoordinate cationic encapsulated species to release ethylene, and subsequent methyl-hydrogen reductive elimination to form methane.[21] The catalyzed process took place with a half-life around one hour, while, in the uncatalyzed reaction, only trace β-hydride elimination was observed after 16 hours. The acceleration of β-hydride elimination from **12** indicates that the intrinsic

reactivity preferences of the metal are not overridden by the cluster; however, it highlights the fact that other elementary transformations are also subject to catalytic acceleration by **1**, so long as they also proceed through cationic transition states.

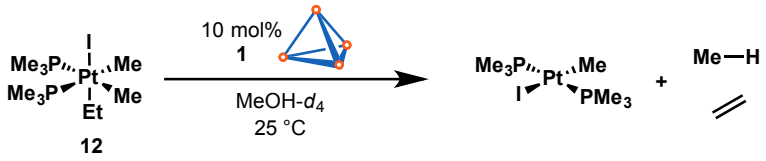

Scheme 3.8. β-hydride elimination for platinum complex **12** catalyzed by cluster **1**.

Acyl dimethyl platinum complex **13** undergoes reductive elimination, catalyzed by cluster **1**, to form acetone. The observed 15-fold acceleration over background in this case is modest relative to the aforementioned $C(sp^3)$–$C(sp^3)$ reductive eliminations, with an initial rate of 2.2 x 10^{-3} s^{-1} in the presence of 10 mol % cluster, and 1.5 x 10^{-4} s^{-1} in the background reaction (Scheme 3.9).[21] This can be explained by the relatively low barrier to reductive elimination in the uncatalyzed reaction for the sp^2-hybridized and electron-deficient acyl group. In this case, the kinetic product is the *cis*-chloroplatinum complex, but undergoes isomerization to the *trans*- isomer after reductive elimination.

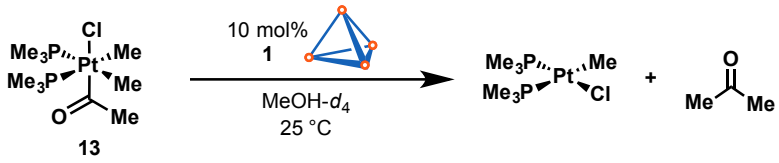

Scheme 3.9. Acetone forming reductive elimination from platinum complex **13** catalyzed by cluster **1**.

3.3.5 The Nature of the Michaelis Complex

While kinetic investigations of the catalytic reductive elimination process reveal a Michaelis-Menten-like mechanism reminiscent of enzymatic catalysis, these data do not provide insight into the nature of the organometallic species undergoing reductive elimination; in the case of reductive elimination from platinum complex **9**, C–C bond formation might occur from a pentacoordinate intermediate, or alternatively from the hexacoordinate solvento complex. Reductive elimination has previously been observed from hexacoordinate d^6 and square planar d^8 metals both with and without prior ancillary ligand dissociation in different cases, suggesting that either pathway might be competent.[22-24] While direct observation of this transient intermediate is precluded, some insight into its nature may be gained from the observation of an inactivated inclusion complex upon the introduction of appropriate non-solvent neutral donors.

Indeed, donor-arrested reductive elimination was first observed as a cluster deactivation pathway in the catalyzed reductive elimination from **3-I** (*vide supra*, Figure 3.2C). In contrast to the transient substrate-host complexes that rapidly undergo reductive elimination, the deactivated inclusion complex **6** ⊂ **1** was persistent enough to allow characterization by single-crystal X-ray diffractometry. Furthermore, when **3-I** is subjected to

6 ⊂ **1** in leu of empty cluster **1**, no catalysis of reductive elimination was observed, supporting the idea that ligand dissociation is essential for efficient catalysis to occur.

Similarly, the addition of exogenous neutral ligands to a solution of **9** and cluster **1** inhibited the catalyzed reductive elimination, and afforded the corresponding high valent cationic inclusion complexes. A small excess of either trimethylphosphine or dimethylsulfide both effected the uptake of the cationic Pt(IV) after displacement of the iodide ligand to form a kinetically stable 1:1 host-guest complex (Figure 3.10). These inclusion complexes were persistent even upon heating over 48 hours, with no detectable reductive elimination observed. In the absence of cluster **1**, no iodide displacement could be detected by ^{1}H-NMR in the presence of dimethylsulfide, and only slow, partial displacement was observed with trimethylphosphine alone. In contrast, added trimethylamine had no effect on **9** or the supramolecular cluster, and the catalyzed reductive elimination proceeded unabated, a phenomenon that likely reflects the low innate affinity of platinum for amine donors.

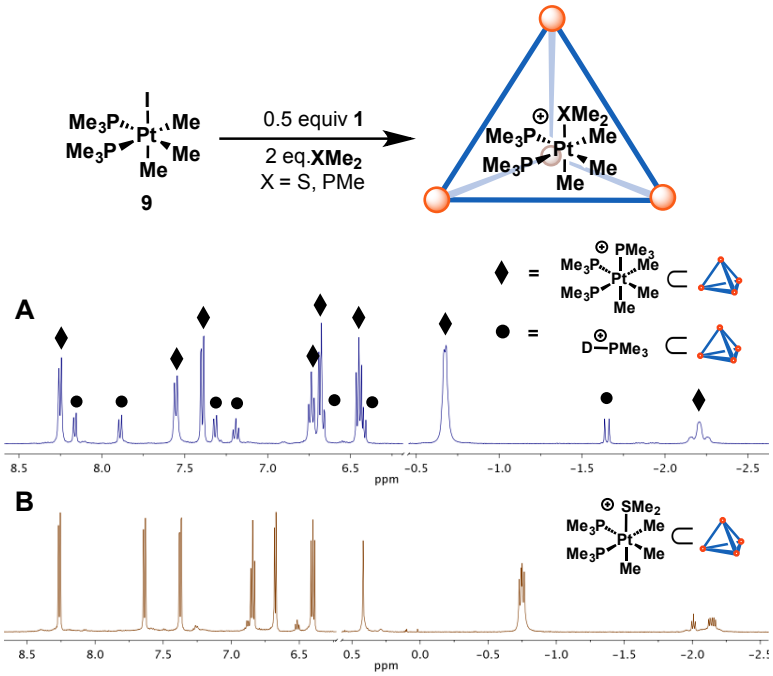

Figure 3.10. Donor-arrested complexes derived from trimethylphosphine and dimethylsulfide. A: MeOD/D_2O 8:2, B: pure MeOD

Surprisingly, carbon monoxide was capable of displacing iodide from **5** to form a hexacoordinate inclusion complex within cluster **2** (albeit with only partial occupancy of **2**, indicating a lower overall association constant). This observation was made quite unexpectedly in the context of an attempted carbonylative coupling (*vide infra*), where no reactivity was observed, due to the encapsulation of the cationic Pt(IV) carbonyl **14** (Figure 3.11). While Pt(IV) carbonyl complexes have been previously observed, their rarity can be attributed to the paucity of electron density available for backdonation to carbonyl antibonding orbitals, underscoring the ability of **2** to perturb otherwise unfavorable equilibria.[25] Indeed, the IR spectrum of **14** ⊂ **2** showed a C=O stretch at ν = 2110 cm^{-1}, indicative of a relatively strong CO bond. Heating **14** ⊂ **2** at 40 ^{o}C effected reductive elimination of ethane with a half-life of about 4 hours to afford the corresponding cationic

Pt(II) carbonyl **15** (ν_{CO} = 2078 cm^{-1}). Clearly, a variety of neutral donors are capable of trapping the high valent cationic platinum intermediate to form a persistent inclusion complex within the cavity of the supramolecular cluster.

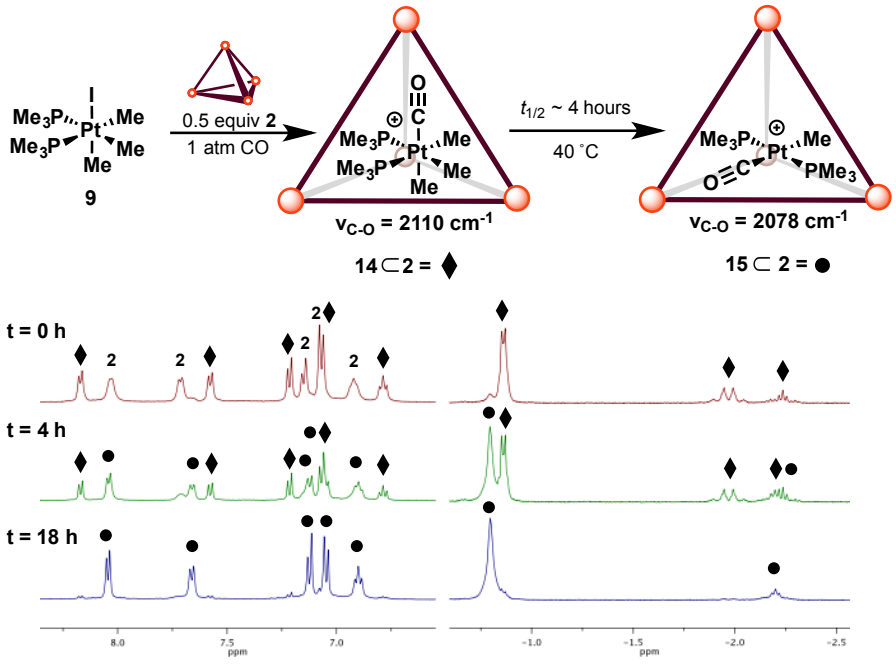

Figure 3.11. Carbon Monoxide trapping of the Michaelis complex and slow reductive elimination.

The fact that these hexacoordinate cationic species, even with donors as weak as carbon monoxide, undergo substantially inhibited reductive elimination compared to the parent catalytic process, provides evidence by analogy that the putative oxygen coordinated solvento complex is unlikely to be the relevant species undergoing carbon-carbon bond formation. A model is therefore favored in which a coordinatively unsaturated cationic metal complex—pentacoordinate for platinum(IV), tricoordinate for gold(III)—undergoes reductive elimination within the cavity of the supramolecular assembly.

The phenomenon of donor arrested reductive elimination was not limited to exogenous neutral donors. Allyl platinum **16** did not undergo catalyzed reductive elimination in the presence of cluster **1**; instead, a platinum species, consistent with the η^3-allyl platinum(IV) complex **17**, was observed as a strongly bound guest in the cluster cavity. The chiral *cis*-dimethyl η^3-allyl platinum cation is kinetically trapped as a diastereomeric mixture within the homochiral *T*-symmetric cluster. However, after 24 hours, the complex isomerizes to favor the achiral *trans*-dimethyl η^3-allyl platinum cation **18** as the thermodynamic product (Figure 3.12). The equilibrium mixture of **17** ⊂ **1** and **18** ⊂ **1** was persistent, with no reductive elimination observed even after heating to 45 ºC for 48 hours. For encapsulated **17**, reductive elimination is decelerated relative to the background reaction, and can be viewed as a case of intramolecular donor arrested reductive elimination, analogous to the previously observed behavior in the presence of exogenous neutral donors. For a similar allyldimethyl complex, Puddephatt and coworkers were unable to observe an η^3-allyl complex by treatment with

$AgPF_6$. Instead, disproportionation products following reductive elimination were observed highlighting the divergent behavior enabled by the microenvironment of **1**.[26]

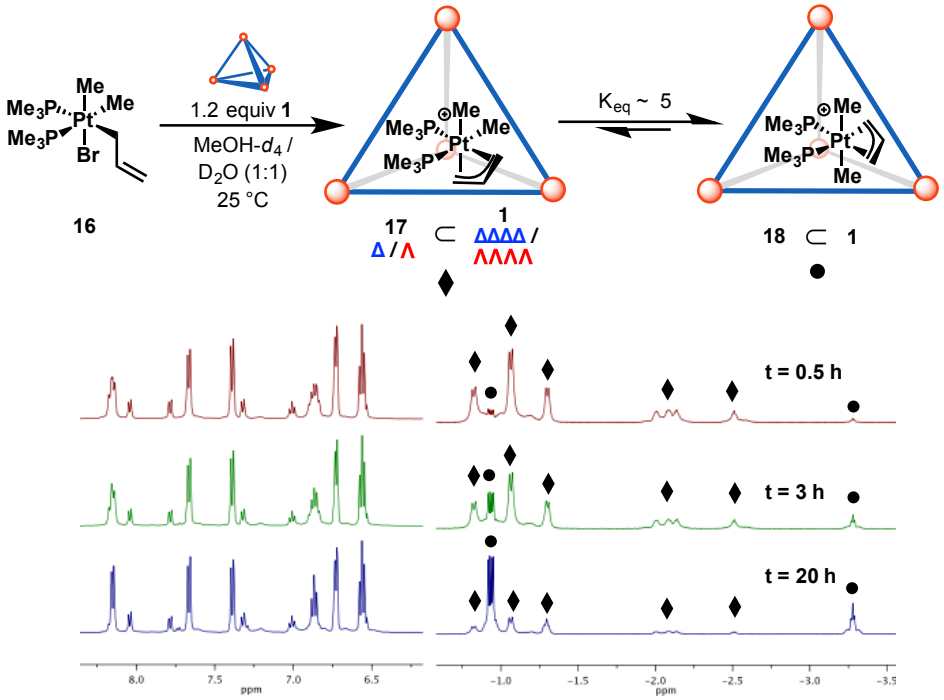

Figure 3.12. η^3-allyl platinum complexes formed upon encapsulation of **16**.

To probe the limits of the intramolecular donor-arrested reductive elimination, the homologated series of butenyl, pentenyl and hexenyl platinum(IV) complexes **19**, **20** and **21** were investigated (Figure 3.13). Unfortunately, the high propensity of these complexes to undergo β-hydride elimination prevented their isolation and purification. To circumvent this, the platinum(IV) complexes were generated in situ, followed by treatment with cluster **1**. The butenyl and pentenyl complexes were strongly encapsulated, and while both inclusion complexes were persistent on the timescale of days, the broadened ^{1}H-NMR resonances in the encapsulation region for pentenyl complex **20** ⊂ **1** suggest that it is less strongly bound than the butenyl analogue. Conversely, only trace encapsulation of hexenyl analogue **21** is observed after 30 minutes at ambient temperature, and no species are encapsulated after 12 hours with background formation of products from β-hydride elimination observed. This trend can potentially be explained as the result of several phenomena, including (i) conformational strain of the expanded ring complexes, (ii) the entropic cost of folding the homologated chains to bring the donor olefin into contact with the Pt cation, and (iii) size exclusion of the less compact complexes. It is additionally relevant to note that platinum complex **9**, under an atmosphere of ethylene, did not form an inclusion complex with cluster **1**.

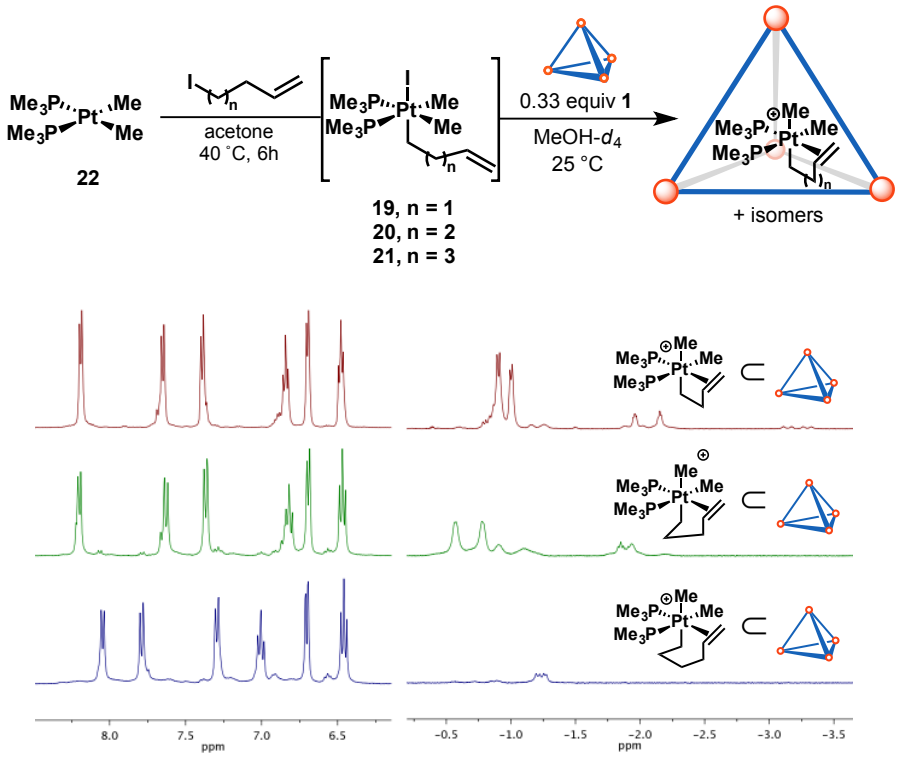

Figure 3.13. Homologous series of cyclic alkene-coordinated encapsulated platinum complexes.

3.3.6 Dual Catalysis – Proof of Principle and Mechanistic Investigation

The initial impetus for the investigation of cluster catalyzed reductive elimination was to demonstrate that the application of a microenvironment catalyst to one problematic organometallic elementary step could facilitate a kinetically prohibitive, but otherwise desirable cross-coupling process.[27] Based on the stoichiometric reactivity (*vide supra*), a co-catalytic cross coupling of a methyl electrophile with a complementary nucleophilic alkyl metal species was targeted as proof of principle. Achieving this goal was impeded by one immediate roadblock: supramolecular assembly **1** was found to decompose in the presence of electrophilic methyl sources, such as methyl iodide.

In order to overcome this difficulty, supramolecular cluster **2** (Figure 3.1), a previously reported analogue of cluster **1**, which bares less electron-rich and more sterically shielded catechol ligands was evaluated as an alternative catalyst for reductive elimination.[28] The rate of reductive elimination of both gold complex **3-I** and platinum complex **9** catalyzed by **2** was measured. In each case, **2** was found to give an observed rate of reductive elimination approximately 1.5 times faster than the rate measured with cluster **1**. Similar relative rates have previously been reported for transformations catalyzed by **1** and **2**.[29]

Interestingly, the reductive elimination of **3-I** catalyzed by **2** does not deviate from first order behavior, with no bis(phosphine)gold(III) inclusion complex (**6** ⊂ **2**) detected (Figure 3.14). One possible explanation for this phenomenon is that **6** is formed from trimethylphosphine liberated upon oxidation of the supramolecular catalyst by **3-I** or **4-I**, and

the decreased electron density of the catecholate ligands on **2** relative to **1** slows this deleterious side reaction. Catalyst **2** was also found to serve as a more robust catalyst in the reductive elimination from **7-I**, with a turnover number (TON) of 947, compared to the measured TON of 312 for complex **1**. Though the catalyst deactivation pathway in this case is unknown, it again seems plausible that **1** and **2** are oxidized by **8-I**, and that the less electron-rich catecholate ligands are less susceptible to oxidation. This is supported by the formation of Au^0 precipitate after a large number of turnovers with **1** but not with **2**.

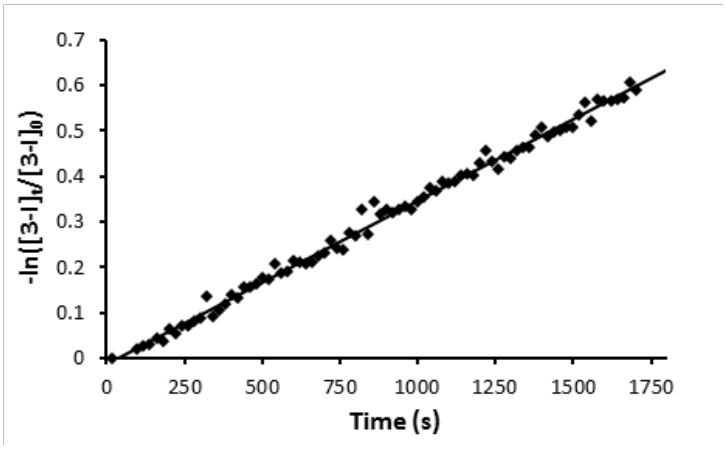

Figure 3.14. Clean exponential behavior for the reductive elimination from **3-I** catalyzed by cluster **2**.

The next major obstacle to overcome was the identification of a nucleophile capable of transmetallating to platinum(II), while remaining tolerant of protic solvent and of the supramolecular catalyst.[30] Stannanes were found to be suitable coupling partners under these criteria, however, the Me_3SnI byproduct formed upon transmetallation from tetramethyltin was a strong guest for **2**, deactivating the supramolecular catalyst after only one turnover. The addition of potassium fluoride, in order to generate the significantly less heterolytically labile Me_3SnF effectively sequestered the trimethyltin cation and prevented catalyst deactivation. Under these conditions, efficient C–C coupling occurred, and the presence of both the platinum and supramolecular catalysts were necessary to achieve turnover (Figure 3.15). The observation of efficient alkyl-alkyl cross coupling dependent on both the transition metal catalyst and the supramolecular microenvironment catalyst represents a proof of principle for the initial motivating hypothesis for this work. However, further questions persisted about the overall mechanism by which this process occurred. Namely, despite the presumed involvement of the stoichiometrically validated supramolecular catalysis of the C–C reductive elimination, the remaining elements of the catalytic cycle remained unclear. For one, limited precedent for transmetallation of alkyl stannanes to phosphine-supported platinum existed, and any additional role of fluoride (originally added to scavenge trimethytin iodide) in this step was unclear.[31] Beyond this, oxidative addition of methyl iodide has been reported to both mono- and di-alkyl Pt(II) complexes, suggesting that either pathway might be relevant.[26]

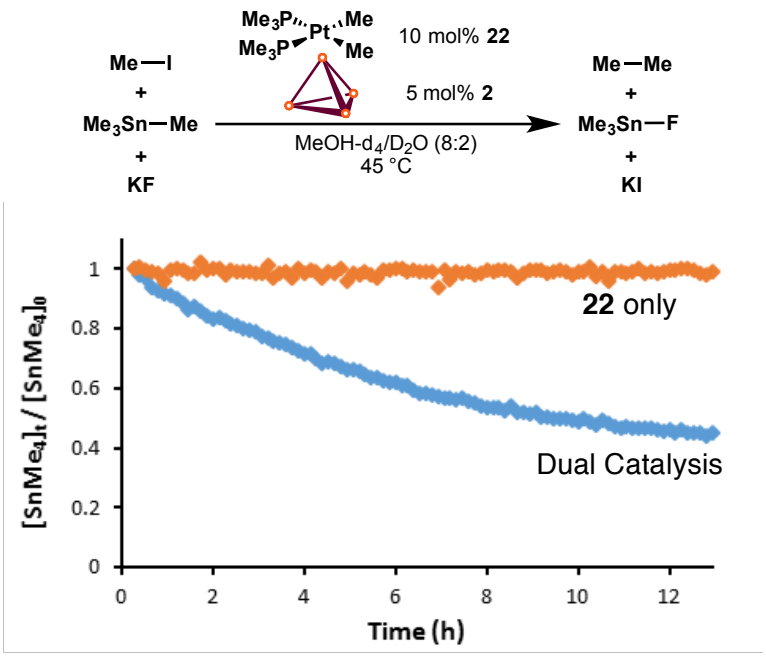

Figure 3.15. Dual Supramolecular and Transition Metal Catalysis in the C–C coupling of tetramethyltin and methyl iodide.

In order to gain further insight into the mechanism of this dual-catalytic process, the platinum speciation over the course of the reaction was interrogated by examination of the reaction mixture by a combination of ^{1}H- and ^{31}P-NMR spectroscopy. Four unique platinum species could be identified and definitely confirmed by independent synthesis. These species were assigned as the platinum(II) complex **10**, and the three platinum(IV) complexes **9**, **23** and **24** (Figure 3.16). While the presence of platinum complexes **9** and **10** was not unexpected considering their role in the previously described stoichiometric reactivity, the involvement of **23** and **24** was less easily accommodated by our initial mechanistic hypothesis. The evolution of the speciation for these complexes over the course of the reaction is depicted in Figure 3.16. While **10** maintains roughly steady concentration, the initial burst and subsequent decay of **23** is accompanied by the growth in concentration of **9**, with **24** growing in gradually at late reaction times. In the absence of the supramolecular catalyst, only **9** and **23** are observed.

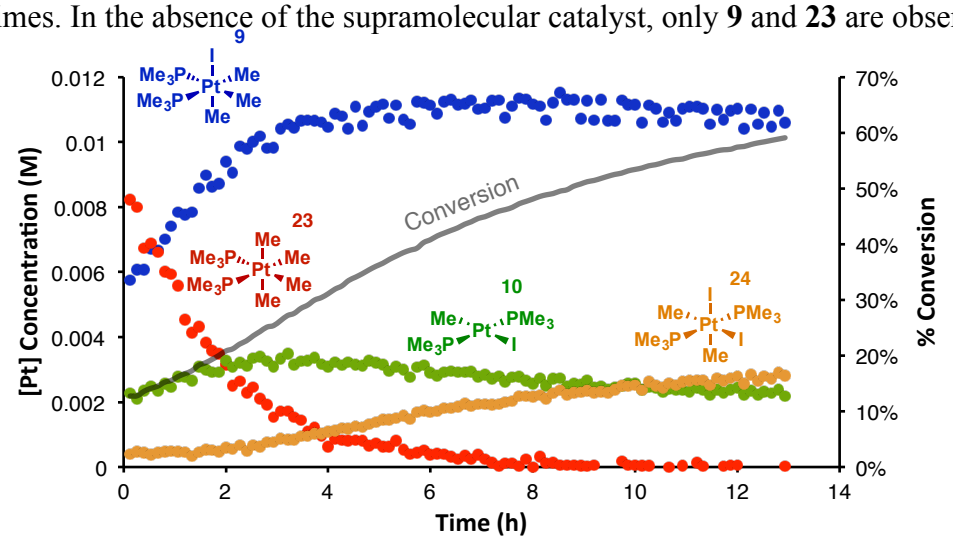

Figure 3.16. Concentration of major platinum species under dual catalytic conditions.

In order to understand the origin of the unexpected platinum complexes **23** and **24**, a series of stoichiometric experiments were performed, beginning with an investigation into the formation of tetramethylplatinum(IV) complex **23**.[32] Treatment of **9** with tetramethyltin under catalytically relevant conditions led to no reaction (Scheme 3.10A). However, addition of potassium fluoride to the same mixture resulted in rapid transmetallation to generate **23** and trimethyltin fluoride (Scheme 3.10B). Surprisingly, this process was found to be reversible, and in the presence of trimethyltin fluoride and potassium iodide, **23** was found to undergo conversion to tetramethyltin and **9** (Scheme 3.10C).[33] These results suggest a dynamic Pt(IV)/Sn transmetallation equilibrium mediated by fluoride, in which the relative concentrations of the four species dictate the overall distribution.

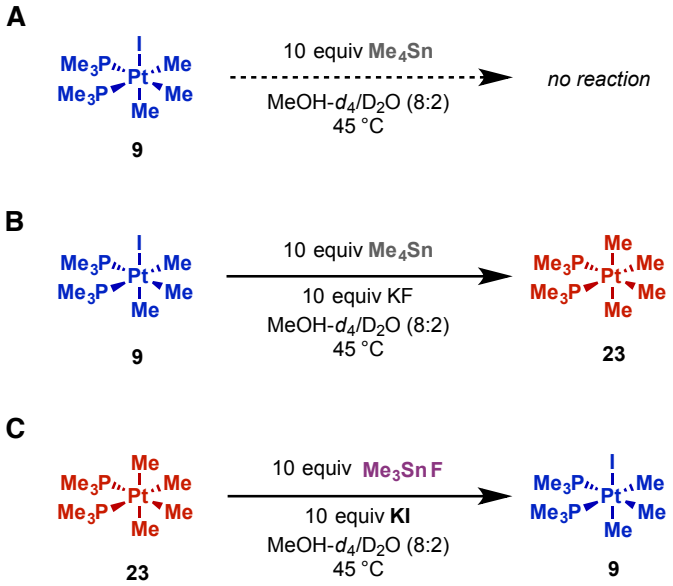

Scheme 3.10. (A) Lack of reactivity between Pt complex **9** and tetramethyl tin. (B) Fluoride promoted transmetalation to **9**. (C) Demonstration of reversibility for transmetallation.

With the likely origin of **23** elucidated, efforts were focused on identifying the pathway by which the putative substrate for cluster catalyzed reductive elimination, **9**, was regenerated from platinum(II) complex **10**. This process requires a transmetallation event and an oxidative addition event, however, their relative order was unclear. Suprisingly, transmetallation experiments similar to those which demonstrated the interconversion of platinum(IV) complexes **9** and **23** indicated that tetramethyltin was unreactive with **10** on catalytically relevant timescales, either the presence or absence of potassium fluoride (Scheme 3.11A). However, it was observed that an equimolar mixture of **10** and **23**, allowed to equilibrate under conditions similar to those used in the dual catalytic reaction, resulted in formation of **9** and **22** (Scheme 3.11B). The kinetic product of transmetallation is the *trans*-dimethylplatinum(II) complex **27** (*vide infra*), but it undergoes isomerization to the *cis*-isomer. The overall process was found to be reversible, suggesting a possible Pt(IV)/Pt(II) transmetallation equilibrium. Furthermore, **22** was shown to undergo exceedingly rapid oxidative addition of methyl iodide under relevant conditions to generate **9**, demonstrating that a mechanism involving transmetallation followed by oxidative addition could potentially be achieved with platinum(IV) complex **23** effectively shuttling a methyl group from tetramethyl tin to complex **10**. However, in a separate experiment, **10** was shown to undergo oxidative addition of methyl iodide directly to afford **24** (Scheme 3.11C). In order to

determine the fate of platinum complex **10**, the rates of transmetallation and oxidative addition under catalytically relevant conditions were measured. Direct comparison of these rates showed that oxidative addition outcompetes transmetallation by a substantial factor (Figure 3.17).

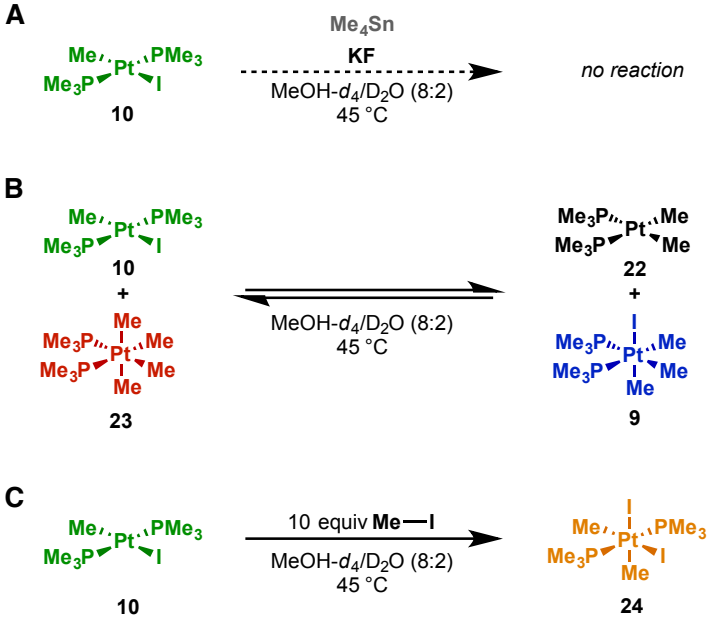

Scheme 3.11. (A) Platinum(II) complex **10** undergoes no reaction with tetramethyl tin and potassium fluoride. (B) Reversible Pt(II)/Pt(IV) transmetallation between **10** and **23**. (C) Oxidative addition of methyl iodide to **10**.

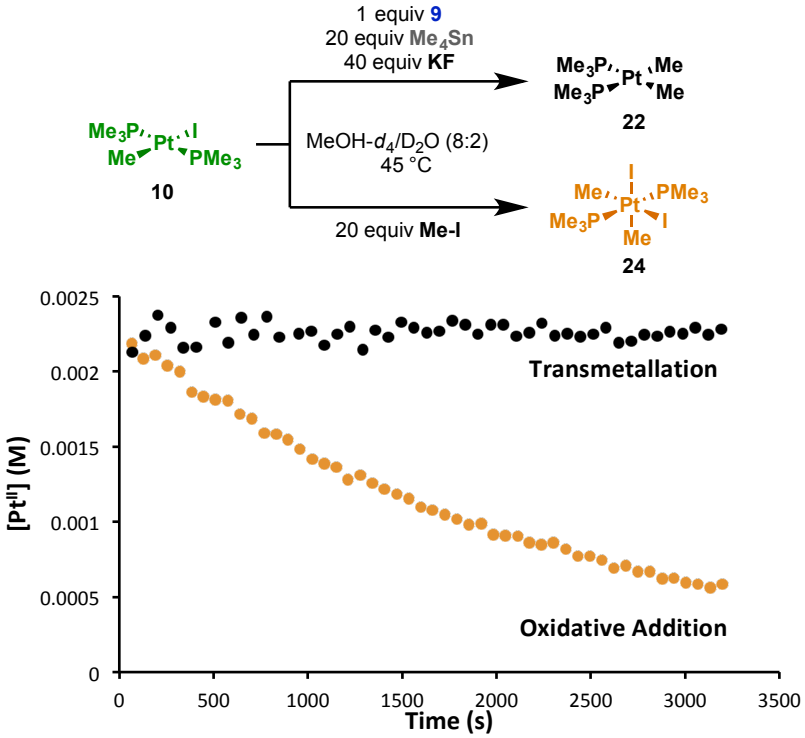

Figure 3.17. Direct rate comparison under catalytically relevant conditions for oxidative addition and transmetallation pathways for the consumption of platinum complex **10**.

With oxidative addition established as the dominant pathway for consumption complex **10**, the behavior of **24** was examined in order to obtain a complete understanding of the closure of the catalytic cycle. No reductive elimination from **24** was observed in the presence or absence of a supramolecular catalyst. However, in a fashion similar to that previously observed with platinum complex **9**, fluoride promoted transmetallation of tetramethyltin to **24** generated a mixture of platinum(IV) complexes **25** and **26**, which could be isolated and fully characterized (Scheme 3.12). Complexes **25** and **26** are the *trans*-phosphine analogues of **9** and **23**, but do not undergo detectable thermal isomerization to the thermodynamically favored *cis*-isomers on catalytically relevant timescales. Moreover, **24** and **26** were observed to conproportionate to afford **25** in the absence of tin, and **25** was observed to disproportionate into **24** and **26** under similar conditions, suggesting that equilibration via platinum(IV)/platinum(IV) methyl transfer is possible under catalytic conditions.

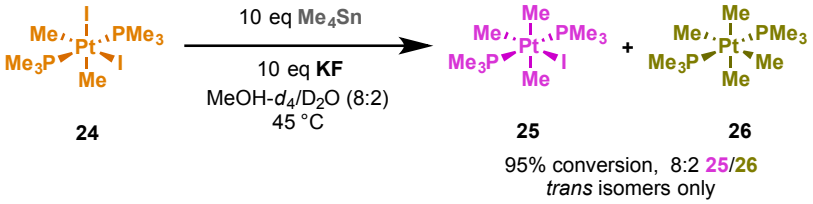

Scheme 3.12. Observation of transmetallation to platinum(IV) complex **24**.

The failure to generate complex **9** from transmetallation to **24** was initially surprising, given that **25** and **26** are not detectable as intermediates in the dual catalytic reaction, and **9** is the dominant platinum species in solution for the majority of the reaction. However, treatment of **25** with the supramolecular catalyst **2** leads to rapid consumption of the *trans*- starting material, affording a mixture of *cis*- isomer **9** and reductive elimination product **10**, along with ethane (Figure 3.18). The reaction at the catalytically relevant temperature of 45 ºC was too rapid to accurately determine a rate constant, explaining the observation that **25** does not build up to detectable levels under catalytic conditions. In the reaction performed at 45 ºC, the initial ratio of isomerized complex **9** to elimination product **10** was about 1:1.15 upon complete consumption of **25**. Monitoring the reaction by ^{1}H-NMR at 25 ^{o}C afforded a rate constant of 2.0 x 10^{-2} s^{-1} for the combined isomerization / reductive elimination process, which could not be deconvoluted, due to overlapping resonances. For comparison, the pseudo-first order rate constant for oxidative addition of methyl iodide to **10** at 45 ^{o}C was measured to be 4.38 x 10^{-4} s^{-1}. This disparity clearly suggests that the failure to detect **25** under catalytic conditions is due to its rapid consumption in the presence of the supramolecular catalyst. The fact that reductive elimination from **25** catalyzed by cluster **2** is significantly more rapid than the catalyzed elimination from **9** (*vide supra*), can be rationalized as a ground state destabilization of **25** relative to **9**, whereas the enthalpic penalty of *trans*-methyl groups for **25** is alleviated as the transition state for reductive elimination is approached. (It is not clear if the Michaelis complexes for **9** and **25** immediately converge, or if there is some significant barrier to isomerization maintained after ionization in the cluster.)

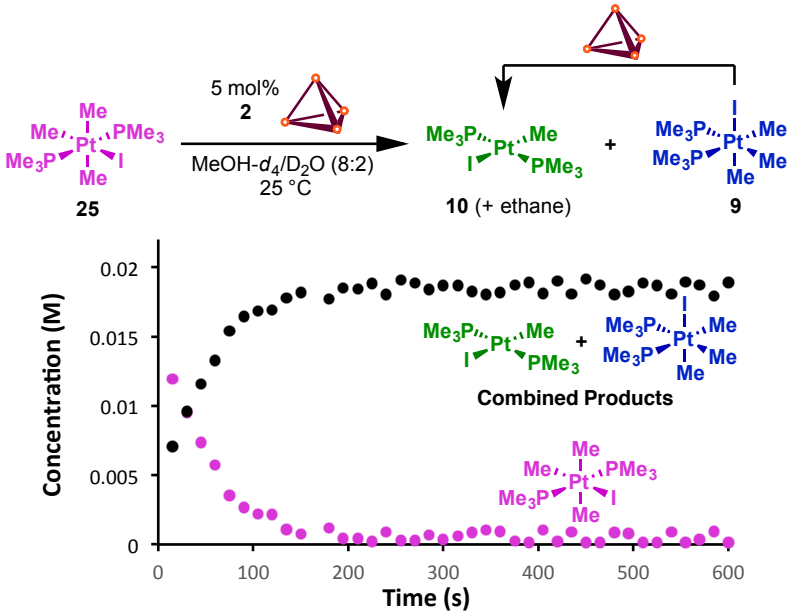

Figure 3.18. rapid consumption of **25** in the presence of cluster **2**.

These observations collectively suggest an overall mechanism for the dual catalytic process in which the *trans*-isomers of the platinum(II) and platinum(IV) complexes lie on cycle, with **9** serving as a readily-engaged off-cycle resting state and reservoir (Figure 3.19). Oxidative addition precedes transmetallation, and **25** is rapidly engaged by the supramolecular catalyst. This mechanism is consistent with the observed platinum speciation, and suggests that as the concentration of tetramethyltin decreases, the reaction undergoes a shift in the turnover-limiting step (from oxidative addition to transmetallation) and concomitant change in the on-cycle resting state (from **10** to **24**). Additionally consistent is the observation that monomethyl platinum(II) complex **10** is a competent precatalyst for this process, although slightly diminished rates are observed (Figure 3.20). This is explained by the fact that oxidative addition product **24** is only marginally soluble in the MeOD/D_2O solvent mixture, and when it rapidly forms under these conditions, it reaches sufficient concentration to crystallize out, lowering the overall catalyst loading. Further support is garnered from flooding experiments; when a 10-fold excess of methyl iodide is introduced, **6** is no longer detectable as a persistent intermediate, whereas introduction of a 10-fold excess of tetramethyltin allows **26** to build to detectable levels under catalytic conditions. Using the modeling program COPASI, this mechanism can be used to fit the observed concentrations of each platinum species, as well as the tin and alkyl halide species observed under the reaction conditions, generating a set of kinetic parameters that accurately reproduces the chemical dynamics of the reaction (see supporting information below for more detail).[34]

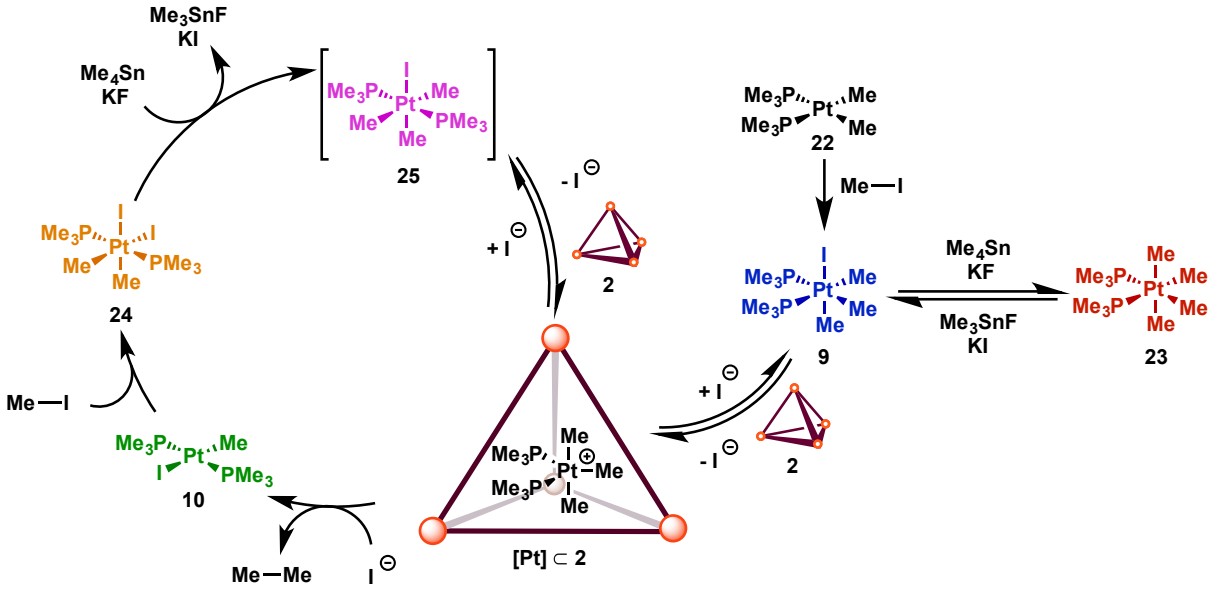

Figure 3.19. Mechanism for the dual catalytic cross-coupling consistent with experimental evidence.

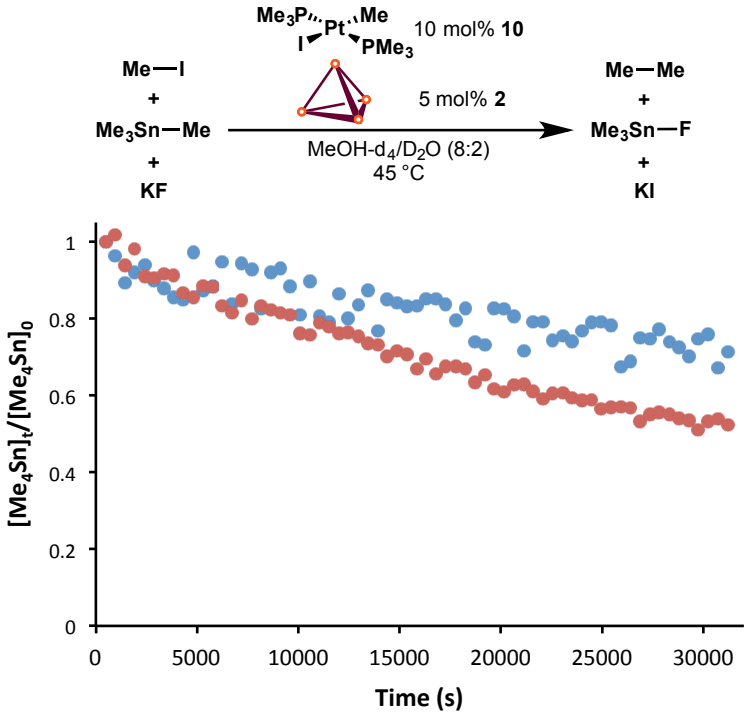

Figure 3.20. Consumption of SnMe4 under dual catalytic conditions, cluster **2** with precatalyst **10** (blue circles) or with **22** (red circles).

3.3.7 Identification of an Acidolysis Side Reaction

In addition to the desired cross-product, ethane, small amounts of methane-d_1 were detected by GC-MS of the reaction headspace. Upon examining several potential sources of this side-product, it was observed that treatment of **23** with supramolecular complex **1** results in the formation of ethane, methane-d_1, and **22** (Scheme 3.13A). Interestingly, the addition of potassium iodide halts the formation of ethane, instead slowly affording a mixture of **9** and methane-d_1 (Scheme 3.13B). In the absence of cluster **1**, no significant protonolysis of **23** was observed.

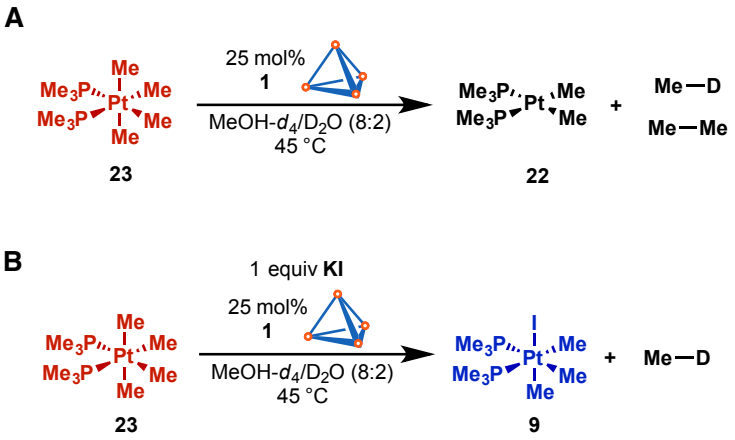

Scheme 3.13. (A) Identification cluster mediated decomposition of **23**, resulting in methane formation. (B) Iodide trapping of apparent intermediate in the acidolysis of **23**.

Monitoring this process by ^{1}H-NMR shows a sigmoidal decay profile for **23**, with formation of **27** as an intermediate *en route* to **22**. The observed reaction mass balance decreases over the course of the reaction, but can be restored upon the addition of potassium iodide to the completed reaction, affording a mixture of **9** and **10** (Figure 3.21). These data are consistent with a mechanism involving cluster-promoted acidolysis of **23**,[35] which generates the corresponding cationic trimethyl Pt(IV) complex. Upon cluster-promoted reductive elimination of ethane, the cationic monomethyl Pt(II) complex can abstract a methyl from **23**, continuing the chain reaction (Figure 3.22). The decrease in mass balance, then, corresponds to the formation of rapidly exchanging unsaturated cationic complexes, either bound within the cluster or free in solution. Similar behavior has previously been observed for Pt(IV) complexes by Puddephatt in the absence of a supramolecular host, wherein initiation occurs by the addition of an extrinsically-prepared coordinatively unsaturated cationic Pt(II) complex.[36] Because the propagation of this pathway is inhibited by iodide, it is unlikely to occur with significant chain-length under catalytic conditions. Furthermore, the substrate for acidolysis (**23**) is present in substantial concentrations only at early reaction times. Nonetheless, this reactivity likely explains some of the observed side-product formation.

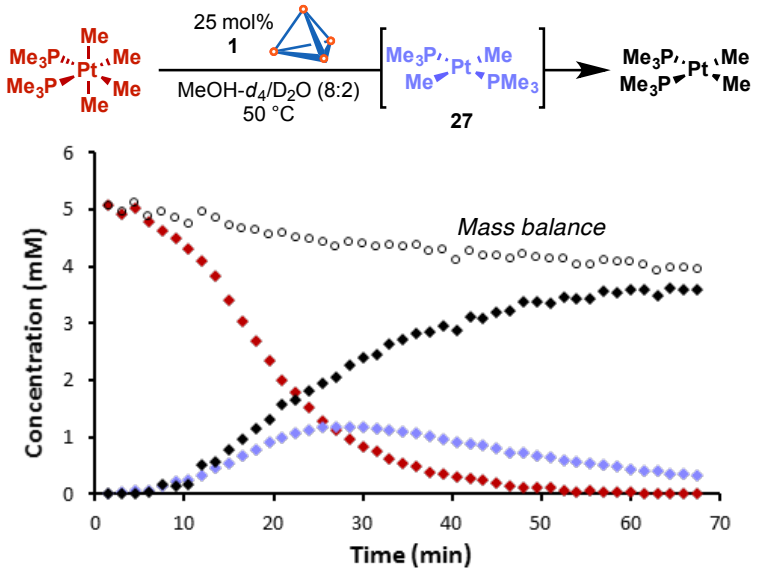

Figure 3.21. Kinetic profile for the cluster catalyzed acidolysis of **23**, displaying sigmoidal kinetics.

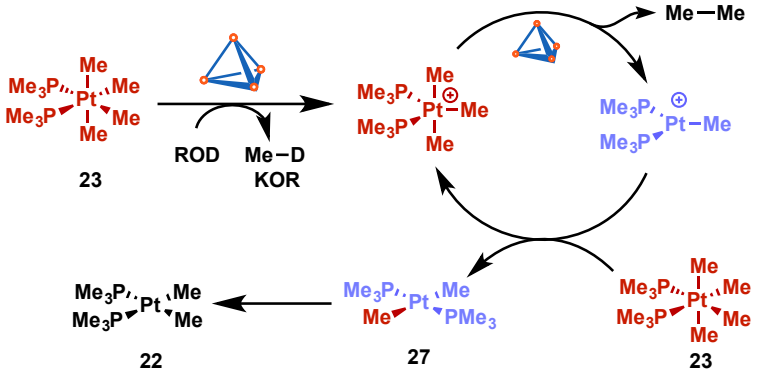

Figure 3.22. Proposed mechanism for protonolysis initiated reductive elimination, involving cluster catalysis of both initiation and reductive elimination.

3.4 Conclusions

Microenvironment catalysis affords a unique opportunity to transiently modulate the stereoelectronic atmosphere of a catalytic intermediate for one step of a cycle, while leaving the remainder of the cycle unperturbed. In this work, the cationic intermediates preceding, and transition states for carbon-carbon bond-forming, reductive elimination that are recognized by a co-catalytic supramolecular cluster were thoroughly examined. The substitutional effects of spectator ligand, halide, reactive group, solvent and catalyst were explored, and insight into the nature of the resultant Michaelis complex was garnered. A full mechanism for the dual catalytic coupling reaction of alkyl tin and alkyl halide was elucidated on the basis of stoichiometric experiments under catalytically relevant conditions, as well as the mechanism of an acidolysis side reaction.

This work represents an important step forward in the field of microenvironment catalysis. Previous examples of microenvironment catalysis are largely biomimetic in nature. While in many ways supramolecular catalysis was born out of the emulation of enzymatic

active sites, it is in no way limited to the simple organic transformations for which enzymes evolved. Catalysis promoted by cluster **1** in particular had predominantly been limited to the stabilization of Brønsted acid generated oxonium ions, and more recently carbenium ions and iminium ions. The extension of these principles to the recognition and stabilization of high-energy organometallic intermediates sheds a new light on the potential power of microenvironment catalysis. Cluster **1** might potentially be relevant to any number of organometallic processes for which the generation of cationic intermediates and transition states is kinetically relevant. Furthermore, microenvironment catalysts with properties orthogonal to **1** (e.g. stabilization of high electron density and negative charge) may be applicable to a number of transformations that would complement the reactivity described herein (such as the catalysis of oxidative addition or transmetallation). Future work in this area will also focus on the development of supramolecular architectures that are capable of influencing the metal's innate reactivity, in order to promote reaction pathways and product selectivity that is inaccessible without complete control of the reactions microenvironment.

3.5 Supporting Information

3.5.1 General Methods

Unless stated otherwise, all reactions were performed in oven-dried glassware sealed with rubber septa under a nitrogen atmosphere and were stirred with Teflon-coated magnetic stir bars. Dry tetrahydrofuran (THF), toluene, dimethylfomamide (DMF), acetonitrile, triethylamine (TEA) and dichloromethane (DCM) were obtained by passing these previously degassed solvents through activated alumina columns. All other reagents were used as received. Reactions were monitored by thin layer chromatography (TLC) on Silicycle Siliaplate^{TM} glass backed TLC plates (250 μm thickness, 60 Å porosity, F-254 indicator) and visualized by UV irradiation and *p*-Anisaldehyde stain. Volatile solvents were removed under reduced pressure with a rotary evaporator and dried on high vacuum on a Schlenk line. ^{1}H-NMR, ^{13}C-NMR, and ^{31}P-NMR spectra were taken with Bruker spectrometers operating at 300, 400, 500, or 600 MHz for ^{1}H (75, 100, 125, and 150 MHz for ^{13}C). Chemical shifts are reported relative to the residual solvent signal. NMR data are reported as follows: chemical shift (multiplicity, coupling constants where applicable, number of hydrogens). Splitting is reported with the following symbols: s = singlet, bs = broad singlet, d = doublet, t = triplet, hept = heptet, dd = doublet of doublets, dt = doublet of triplets, m = multiplet, at = apparent triplet, dq = doublet of quartets. High-resolution mass spectra (HRMS) were performed on a Thermo LTQ-FT-ICR (7T, ESI) by the QB3 mass spectral facility at the University of California, Berkeley. Elemental Analyses were performed by the Microanalytical Facility at the University of California, Berkeley. Previously reported compounds were synthesized according to literature procedures.

3.5.2 Synthesis of Previously Unreported Compounds

General Procedure for preparation of Au(III) complexes
(adapted from the method of Schmidbaur[37])

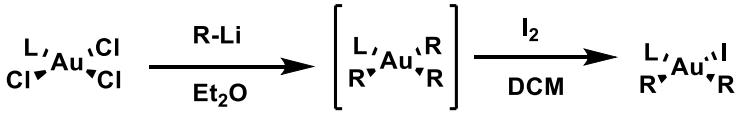

Stage 1: A suspension of the phosphine-supported Au(III) trichloride complex (1 equivalent) in diethyl ether (0.2 M) was placed in a room-temperature water bath, and a solution of R-Li was added dropwise to the suspension (3.0 equivalents). The resulting mixture was stirred at ambient temperature for 2 hours before being quenched with water. The resulting suspension was filtered through Celite into a separatory funnel. The layers were separated and the aqueous layer was extracted twice more with diethyl ether. The combined organic layers were dried over Na_2SO_4, filtered, and concentrated in vacuo to yield a black oil. The oil was dissolved in diethyl ether and filtered through neutral alumina. Upon concentration, a colorless oil was obtained, comprised primarily of the desired Au(III) trialkyl complex, typically contaminated with 5-10% of the corresponding Au(I) alkyl. The mixture discolors upon standing and was used immediately without further purification.

Stage 2: The crude product from the previous step was dissolved in dichloromethane (DCM; 0.1 M) and a saturated solution of iodine (1 equivalent) in DCM was added dropwise to the

suspension causing an immediate color-change to bright yellow. As each drop was added, the purple color fades to golden-yellow. *The addition was monitored colorimetrically and the addition was halted at the endpoint, which is marked by a sharp transition from yellow to orange-brown.* The mixture was stirred for 2 hours at room temperature and then concentrated. Purification was performed as described below for each complex.

cis-iododimethyl(trimethylphosphine)gold(III), 3-I

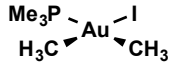

The crude residue was extracted with diethyl ether, filtered and concentrated. The solid product was recrystallized from DCM/n-pentane in the freezer at -20 ºC, and collected in two crops.

Starting from 760 mg (2.0 mmol) of trichlorotrimethylphosphinegold(III), 302 mg (35% over two steps) of **3-I** were obtained as a colorless solid.

^{1}H NMR (600 MHz, Methanol-d_4) δ 1.62 (d, 9H), 1.30 (d, 3H), 1.09 (d, 3H).
^{31}P NMR (243 MHz, Methanol-d_4) δ -7.9.
In accordance with previously recorded spectra.[37]

*General Procedure for halogen exchange reactions from **3-I***

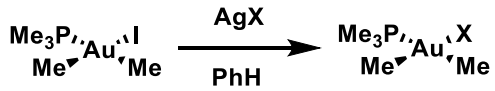

To a solution of **3-I** (100 mg, 0.23 mmol) in benzene (2.5 mL) was added 20 equivalents of AgX (X = Cl, Br). The heterogeneous mixture was stirred vigorously for 20 minutes, and then filtered. The filter cake was washed with additional benzene. An additional 20 equivalents of AgX was added, and the mixture was again stirred vigorously for 20 minutes. The mixture was filtered, the filter cake was washed with benzene and the combined filtrate was concentrated yielding the desired product as a colorless solid.

cis-bromodimethyl(trimethylphosphine)gold(III), 3-Br

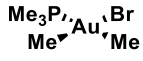

90 mg, 98% yield.

^{1}H NMR (500 MHz, Methanol-d_4) δ 1.62 (d, J = 10.9 Hz, 9 H), 1.23 (d, J = 8.7 Hz, 3H), 0.99 (d, J = 9.6 Hz, 3H).
^{13}C NMR (126 MHz, Methanol-d_4) δ 13.5 (d, J = 125.5 Hz), 10.5 (d, J = 30.6 Hz), 8.1 (d, J = 5.4 Hz).
^{31}P NMR (202 MHz, Methanol-d_4) δ -1.8.
EA: Calculated : C, 15.68; H, 3.95; Found: C, 16.06; H, 3.97;

***cis*-chlorodimethyl(trimethylphosphine)gold(III), 3-Cl**

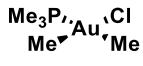 75 mg, 95% yield.

^{1}H NMR (500 MHz, Methanol-d_4) δ 1.58 (d, J = 11.1 Hz, 9H), 1.15 (d, J = 8.8 Hz, 3H), 0.91 (d, J = 9.7 Hz, 3H).
^{13}C NMR (126 MHz, Chloroform-*d*) δ 15.0 (d, J = 124.9 Hz), 9.9 (d, J = 30.2 Hz), 4.3 (d, J = 5.4 Hz).
^{31}P NMR (202 MHz, Chloroform-*d*) δ 1.9.
EA: Calculated : C, 17.74; H, 4.47; Found: C, 17.66; H, 4.39;

***cis*-iododimethyl(triphenylphosphine)gold(III), 5**

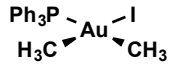 The crude residue was taken up in DCM and layered with hexanes. Upon crystallization of the Ph_3PAuI impurity, the impurity was filtered off and the mother liquor was concentrated. This residue was further purified by dissolution in methanol, filtration, and concentration, yielding the desired product as a colorless solid.

Starting from 292 mg (0.5 mmol) of trichlorotriphenylphosphinegold(III), 140 mg (45% over two steps) of **5** were obtained as a colorless solid.

^{1}H NMR (600 MHz, Methanol-d_4) δ 7.35-7.71 (m, 15H), 1.56 (d, 3H), 1.16 (d, 3H).
^{31}P NMR (243 MHz, Methanol-d_4) δ 29.1.
In accordance with previously recorded spectra.[10]

***cis*-iododimethyl(triethylphosphine)gold(III), 7-I**

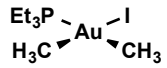 The crude residue was extracted with hexanes, filtered and concentrated. The resulting residue was dissolved in methanol (0.1 M) and KI (2 equivalents) was added. The solution was stirred for 1 hour, concentrated, and extracted with diethyl ether. The ether layer was washed five times with water, dried over Na_2SO_4, filtered, and concentrated. The resulting solid was recrystallized fractionally by cooling a saturated pentane solution to -20°C.

Starting from 1.34 g (3.1 mmol) of trichlorotriethylphosphinegold(III), 950 mg (65% over two steps) of **1b** were obtained as a colorless solid.

^{1}H NMR (600 MHz, Methanol-d_4) δ 2.17 (dt, J = 9.2, 7.6 Hz, 6H), 1.33 (d, J = 7.4 Hz, 3H), 1.23 – 0.95 (m, 12H).
^{13}C NMR (151 MHz, Methanol-d_4) δ 14.1 (d, J = 27.8 Hz), 12.8, 12.3 (d, J = 112.7 Hz), 6.5 (d, J = 1.9 Hz).
^{31}P NMR (243 MHz, Methanol-d_4) δ 18.5.
EA: Calculated : C, 20.35; H, 4.48; Found: C, 20.70; H, 4.44;

*General Procedure for halogen exchange reactions from **7-I***

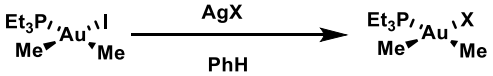

To a solution of **7-I** (80 mg, 0.17 mmol) in benzene (1.5 mL) was added 20 equivalents of AgX (X = Cl: 364 mg, X = Br 478 mg). The heterogeneous mixture was stirred vigorously for 20 minutes, and then filtered. The filter cake was washed with additional benzene. An additional 20 equivalents of AgX was added, and the mixture was again stirred vigorously for 20 minutes. The mixture was filtered, the filter cake was washed with benzene and the combined filtrate was concentrated yielding the desired product as a colorless solid.

cis-bromodimethyl(triethylphosphine)gold(III), 7-Br

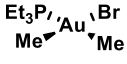

64 mg, 89%

^{1}H-NMR (300 MHz, Methanol-d_4) δ 2.08 (dq, J = 10.1, 7.6 Hz, 6H), 1.21 – 1.05 (m, 12H), 0.98 (d, J = 9.0 Hz, 3H).
^{13}C-NMR (126 MHz, Methanol-d_4) δ 15.90 (d, J = 117.5 Hz), 13.08 (d, J = 27.1 Hz), 7.58 (d, J = 5.6 Hz), 6.57 (d, J = 2.0 Hz).
^{31}P-NMR (202 MHz, Methanol-d_4) δ 24.63.
EA: Calculated: C, 22.60; H, 4.98; Found: C, 22.88; H, 5.14

cis-chlorodimethyl(triethylphosphine)gold(III), 7-Cl

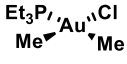

60 mg, 92%

^{1}H-NMR (500 MHz, Methanol-d_4) δ 2.06 (dq, J = 9.9, 7.6 Hz, 1H), 1.29 – 1.07 (m, 2H), 0.93 (d, J = 9.1 Hz, 3H).
^{13}C-NMR (126 MHz, Methanol-d_4) δ 17.47 (d, J = 117.3 Hz), 12.62 (d, J = 26.4 Hz), 6.55 (d, J = 1.9 Hz), 3.98 (d, J = 5.7 Hz).
^{31}P-NMR (202 MHz, Methanol-d_4) δ 27.73
EA: Calculated: C, 25.24; H, 5.56; Found: C, 25.24; H, 5.68

fac-iodotrimethylbis(trimethylphosphino)platinum(IV), 9

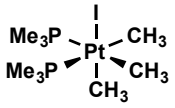

Bis(dimethylphosphino)dimethylplatinum(II) was dissolved in dry, degassed DCM, and 20 equivalents of methyl iodide were added. The solution was stirred at ambient temperature for 6 hours, and then concentrated. The crude product was recrystallized from DCM/pentane at -20°C. Starting from 566 mg (1.5 mmol) of the platinum (II) complex, 533 mg of **9** was obtained (68% yield).

^{1}H NMR (500 MHz, Methanol-d_4) δ 1.57 (dd, J = 8.7, 5.6 Hz, 18H), 1.07 – 0.72 (m, 9H).
^{13}C NMR (126 MHz, Methanol-d_4) δ 13.5 – 12.1 (m), 3.1, 1.9 (dd, J = 127.1, 7.6 Hz).
^{31}P NMR (202 MHz, Methanol-d_4) δ -54.4 (s + d, J_{Pt-P} = 1246 Hz).
EA: Calculated : C, 20.82; H, 5.24; Found: C, 20.67; H, 5.11;

Tetraethylphosphonium tetrakis(3,5-bistrifluoromethylphenyl)borate

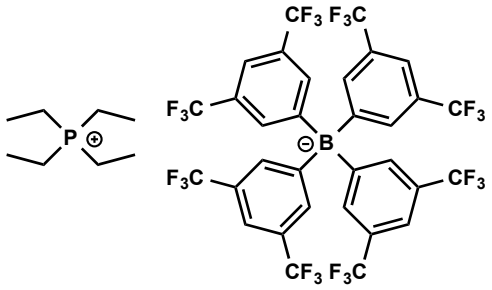

Tetraethylphosphonium bromide (115 mg, 0.5 mmol) was dissolved in minimal acetonitrile. In a separate flask, sodium tetrakis(3,5-bistrifluoromethylphenyl)borate (451 mg, 0.5 mmol) was also dissolved in minimal acetonitrile. The two solutions were combined, resulting in a thick white precipitate (NaBr). The mixture was stirred for 20 minutes, filtered through a glass fiber filter, and concentrated. The solid was extracted with diethyl ether, filtered, and layered with hexanes. The colorless blocks crystallized in this way were dried in vacuo yielding 452 mg of the desired product (86% yield).

^{1}H NMR (500 MHz, Methanol-*d*$_4$) δ 7.62 (s, 12H), 2.26 (dq, *J* = 12.9, 7.7 Hz, 8H), 1.27 (dt, *J* = 18.0, 7.7 Hz, 12H).
^{13}C NMR (126 MHz, Methanol-*d*$_4$) δ 161.5 (m), 134.4, 130.2 – 127.9 (m), 124.4 (q, *J* = 271.5 Hz), 117.1, 10.3 (d, *J* = 49.7 Hz), 4.1 (d, *J* = 5.3 Hz).
^{19}F NMR (470 MHz, Methanol-d$_4$) δ -64.3.
^{31}P NMR (202 MHz, Methanol-*d*$_4$) δ 40.5 .
EA: Calculated : C, 47.55; H, 3.19; Found: C, 47.52; H, 3.12;
HRMS (ESI) m/z calculated for $[C_{32}H_{12}B_1F_{24}]^-$ 863.0654, found 863.0663; m/z calculated for $[C_8H_{20}P_1]^+$ 147.1297, found 147.1295

***Cis*-iododiethyl(trimethylphosphine)gold(III), 11**

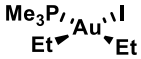

A suspension of the trichlorotrimethylphosphineAu(III) (190 mg, 0.5 mmol, 1 equiv.) in diethyl ether (2.5 mL, 0.2 M) was placed in a room-temperature water bath, and a solution of EtLi was added dropwise to the suspension (3 mL, 0.5M in benzene/cyclohexane, 1.5 mmol, 3 equiv). The resulting mixture was stirred at ambient temperature for 2 hours before being quenched with water. The resulting suspension was filtered through Celite into a separatory funnel. The layers were separated and the aqueous layer was extracted twice more with diethyl ether. The combined organic layers were dried over Na_2SO_4, filtered, and concentrated in vacuo to yield a black oil. The oil was dissolved in diethyl ether and filtered through neutral alumina. Upon concentration, a colorless oil was obtained (120 mg), comprised primarily of the desired Au(III) trialkyl complex, contaminated with a small amount of ethyl(trimethylphosphine)Au(I). The mixture discolors upon standing and was used immediately without further purification. The crude product from the previous step was dissolved in dichloromethane (3.3 mL DCM; ~0.1 M) and a saturated solution of iodine (85 mg, 0.33 mmol, ~1 equiv) in DCM was added dropwise to the suspension causing an immediate color-change to bright yellow. As each drop was added, the purple color fades to golden-yellow. *The addition was monitored colorimetrically and the addition was halted at the endpoint, which is marked by a sharp transition from yellow to orange-brown.* The mixture was stirred for 2 hours at room temperature and then concentrated. The resulting residue was extracted with hexanes, filtered through a glass fiber filter and then concentrated. The crude product was purified by recrystallization from a saturated pentane solution at -20

°C. Two crops of colorless needles were collected, totaling 50 mg (22% yield over 2 steps). The compound was stored in the freezer, as it readily melts near room temperature and is far less stable in the liquid state.

^{1}H-NMR (500 MHz, Methanol-d_4) δ 2.18 (dq, J = 10.6, 7.3 Hz, 2H), 2.04 (dq, J = 7.8, 7.9 Hz, 2H), 1.69 (d, J = 10.4 Hz, 9H), 1.35 (dt, J = 15.0, 7.7 Hz, 3H), 1.22 (t, J = 7.6 Hz, 3H).
^{13}C-NMR (126 MHz, Methanol-d_4) δ 31.52 (d, J = 5.6 Hz), 28.50 (d, J = 119.0 Hz), 14.60 (d, J = 7.0 Hz), 14.46, 12.01 (d, J = 29.1 Hz).
^{31}P-NMR (202 MHz, Methanol-d_4) δ -6.51.
EA: Calculated: C, 18.35; H, 4.18; Found: C, 19.61; H, 4.55 (sample instability prevented a satisfactory analysis)

*General Procedure for Synthesis of **12**, **13**, and **16** by oxidative addition to **22***

Bis(dimethylphosphino)dimethylplatinum(II) was dissolved in dry, degassed DCM, and 20 equivalents of the corresponding electrophile were added. The solution was stirred at ambient temperature for 30 minutes unless otherwise noted, and then concentrated. The crude residue was dissolved in a minimum volume of DCM, followed by layering with pentane. The layered solution was placed in a -20 ºC freezer overnight, and the resulting crystalline solids were isolated by filtration.

Iodobis(trimethylphosphine)dimethyl-ethylplatinum(IV), 12

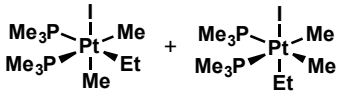

12a **12b**

Starting from 188 mg (0.50 mmol) of platinum (II) complex **22**, 168 mg of **12** were obtained (63% yield). An extended reaction time of 6 hours was required in order to observe consumption of **22**. **12** was isolated as a mixture of two isomers.

^{1}H-NMR (500 MHz, Methylene Chloride-d_2) **12a** + **12b** δ 1.94 – 1.67 (m, CH_2 **a** or **b**), 1.61 – 1.47 (m, 18H, P(CH_3)$_3$ **a** and **b**), 1.40 – 1.16 (m, CH_2 **a** or **b**), 1.07 – 0.57 (m, Pt(CH_3)$_2$ **a** and **b**).
^{13}C-NMR (151 MHz, Methylene Chloride-d_2) **12a** δ 14.9 (dd with ^{195}Pt satellites, J_{PC} = 28.8 Hz, J_{PtC} = 8.2 Hz, J_{PtC} = 1.6 Hz), 14.4 (dd with ^{195}Pt satellites, J_{PC} = 28.2 Hz, J_{PtC} = 9.6 Hz, J_{PtC} = 1.9 Hz), 11.3 (dd with ^{195}Pt satellites, J_{PtC} = 450 Hz, J_{PC} = 122 Hz, J_{PC} = 7.9 Hz), 2.8 (at with ^{195}Pt satellites, J_{PtC} = 652 Hz, J_{PC} = 2.8 Hz), 2.3 (dd with ^{195}Pt satellites, J_{PtC} = 512 Hz, J_{PC} = 121 Hz, J_{PC} = 5.6 Hz), one additional peak could not be located for isomer **a**. It is assumed that this peak overlaps with the phosphine-methyl resonances for **12b**; **12b** δ 18.4 – 18.1 (m), 14.7 – 14.3 (m), 11.9 (s with ^{195}Pt satellites, J_{PtC} = 619 Hz), 3.1 (dd with ^{195}Pt satellites, J_{PtC} = 406 Hz, J_{PC} = 122 Hz, J_{PC} = 7.9 Hz)
^{31}P-NMR (162 MHz, Methylene Chloride-d_2) **12a** δ -51.6 (d with ^{195}Pt satellites, J_{PtP} = 1078.7 Hz , J_{pp} = 11.7 Hz), -52.4 (d with ^{195}Pt satellites, J_{PtP} = 1287.7 Hz , J_{pp} = 13.8 Hz); **12b** δ -53.0 (s with ^{195}Pt satellites, J_{PtP} = 1258.8 Hz).
EA: Calculated: C, 22.52; H, 5.48; Found: C, 22.55; H, 5.48

Chlorobis(trimethylphosphine)dimethylacetylplatinum(IV), 13

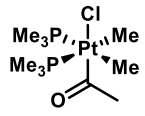

Starting from 76 mg (0.20 mmol) of platinum (II) complex **22**, 64 mg of **13** was obtained (70% yield).

^{1}H-NMR (600 MHz, Methylene Chloride-d_2) δ 2.08 (s with ^{195}Pt satellites, J_{PtH} = 13.0 Hz, 3H), 1.46 (d with ^{195}Pt satellites, J_{PH} = 9.8 Hz, J_{PtH} = 11.6 Hz, 18H), 1.00 (dd with ^{195}Pt satellites, J_{PtH} = 57.4 Hz, J_{PH} = 7.7 Hz, J_{PH} = 6.2 Hz, 6H).
^{13}C-NMR (151 MHz, Methylene Chloride-d_2) δ 194.6 (s with ^{195}Pt satellites, J_{PtC} = 8.0 Hz), 36.6 (s with ^{195}Pt satellites, J_{PtC} = 220 Hz), 13.8 – 13.4 (m), 4.5 (dd with ^{195}Pt satellites, J_{PtC} = 454 Hz, J_{PC} = 113 Hz, J_{PC} = 9.0 Hz)
^{31}P-NMR (162 MHz, Methylene Chloride-d_2) δ -37.4 (s with ^{195}Pt satellites, J_{PtC} = 1413 Hz)
EA: Calculated: C, 26.35; H, 5.97; Found: C, 26.19; H, 5.75

Bromobis(trimethylphosphine)dimethylallylplatinum(IV), 16

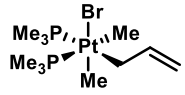

Starting from 200 mg (0.53 mmol) of platinum (II) complex **22**, 148 mg of **16** were obtained (56% yield). **17** was obtained predominantly as the depicted isomer with ~9% of the trans Br-allyl isomer. Spectroscopic characterization is provided only for the major isomer.

^{1}H-NMR (500 MHz, Methylene Chloride-d_2) δ 6.01 – 5.88 (m, 1H), 4.84 – 4.73 (m, 2H), 2.72 – 2.45 (m, 1H), 2.35 – 2.10 (m, 1H), 1.53 – 1.43 (m, 18H), 0.78 (at with ^{195}Pt satellites, J_{PtH} = 55.1 Hz, J_{PH} = 7.8 Hz, 3H), 0.57 (t with ^{195}Pt satellites, J_{PtH} = 71.6 Hz, J_{PH} = 7.3 Hz, 3H).
^{13}C-NMR (151 MHz, Methylene Chloride-d_2) δ 144.7, 109.2, 22.7 (dd, J_{PC} = 116.9 Hz, J_{PC} = 4.4 Hz), 13.5 (dd with ^{195}Pt satellites, J_{PC} = 28.5 Hz, J_{PtC} = 10.1 Hz, J_{PtC} = 1.6 Hz), 13.1 (dd with ^{195}Pt satellites, J_{PC} = 27.7 Hz, J_{PtC} = 12.3 Hz, J_{PtC} = 1.9 Hz), 6.8 (dd, J_{PC} = 120 Hz, J_{PC} = 6.3 Hz), -1.1 (at, J_{PC} = 3.5 Hz).
^{31}P-NMR (162 MHz, Methylene Chloride-d_2) δ -43.2 (d with ^{195}Pt satellites, J_{PtP} = 1260 Hz , J_{pp} = 13.6 Hz), -46.8 (d with ^{195}Pt satellites, J_{PtP} = 1270 Hz , J_{pp} = 13.9 Hz).
EA: Calculated: C, 26.51; H, 5.87; Found: C, 26.59; H, 5.94

Synthesis of cis-bis(trimethyl)phosphinetetramethylplatinum(IV), ***23***

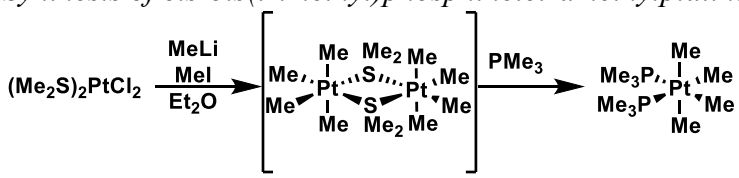

To a solution of bis(dimethylsulfide)dichloroplatinum(II) (390 mg, 1 mmol) in diethyl ether (0.1 M, 10 mL) was added iodomethane (0.4 mL, 6.5 mmol), and the solution was cooled to 0 ^{o}C. Methyllithium (1.9 mL of a 1.6M solution, 3 mmol) was added dropwise, and the mixture was stirred for 30 minutes at 0 ^{o}C, with formation of an orange precipitate. The mixture was

quenched with saturated aqueous ammonium chloride, and the organic layer was separated. The aqueous layer was extracted three more times with diethyl ether and the combined organic layers were dried over sodium sulfate, filtered and concentrated. The resulting product was immediately dissolved in diethyl ether and degassed. Trimethylphosphine (0.2 mL, 2.05 mmol) was added with immediate formation of a precipitate. The mixture was stirred for 30 min, and then filtered. The filtrate was concentrated, and the crude residue was further purified by chromatography on neutral alumina (80:20 benzene/pentane eluent) to afford the desired product as a colorless solid. (271 mg, 66% yield).

^{1}H-NMR (600 MHz, Methylene Chloride-d_2) δ 1.37 – 1.30 (d with ^{195}Pt satellites, J_{PH} = 8.4 Hz, J_{PtH} = 11.6 Hz 18H), 0.35 – 0.18 (dd with ^{195}Pt satellites J_{PH} = 7.9 Hz, 6.8 Hz, J_{PtH} = 56.7 Hz, 6H), -0.28 – -0.46 (t with ^{195}Pt satellites, J_{PH} = 6.6 Hz, J_{PtH} = 44.3 Hz, 6H).
^{13}C-NMR (151 MHz, Methylene Chloride-d_2) δ 12.34 – 11.96 (m), 2.24 (dd with ^{195}Pt satellites, J_{PC} = 134.3, 8.3 Hz, J_{PtC} = 523.0 Hz), -14.22 (t with ^{195}Pt satellites, J_{PC} = 5.0 Hz J_{PtC} = 403.1 Hz).
^{31}P-NMR (243 MHz, Methylene Chloride-d_2) δ -54.61 (s with ^{195}Pt satellites, J_{PPt} = 1292.4 Hz)
EA: Calculated: C, 29.48; H, 7.42; Found: C, 29.83; H, 7.58

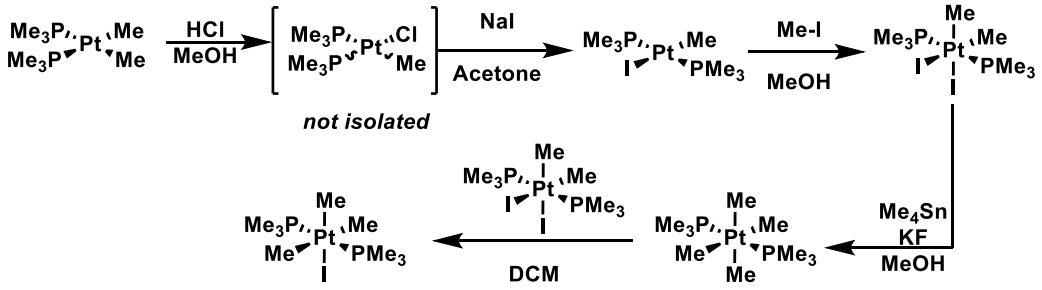

Figure 3.23. *Synthetic Scheme for **10, 24, 25**, and **26***

Trans-iodo(bistrimethylphosphine)methylplatinum(II), 10

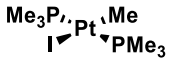

To a solution of bis(trimethylphosphine)dimethylplatinum(II) (2.44 g, 6.5 mmol) in methanol (0.1 M, 65 ml), was added a solution of HCl in methanol (13 mL, 6.5 mmol, 0.5 M, freshly prepared from acetyl chloride). The mixture was stirred for 20 minutes, and the precipitate was filtered off. The filtrate was concentrated, and carried on to the next step without further purification. The crude product (consisting of a mixture of cis- and trans-chloroplatinum complexes) was dissolved in acetone (60 mL) and a saturated solution of sodium iodide (1.84g, 13 mmol, 2 equiv) in acetone was added, with immediate formation of a precipitate. After 30 minutes, the mixture was filtered and the filtrate was concentrated. The mixture was extracted with diethyl ether, filtered through a plug of neutral alumina, and concentrated. This crude product was further purified by recrystallization from diethyl ether/hexanes by the layering method. Three crops of pale yellow crystals were collected, totaling 2.40g (76% yield).

^{1}H-NMR (600 MHz, Methanol-d_4) δ 1.58 (t with ^{195}Pt satellites, J_{PH} = 3.6 Hz J_{PtH} = 28.1 Hz, 18H), 0.62 (t with ^{195}Pt satellites, J_{PH} = 7.1 Hz J_{PtH} = 80.3 Hz, 3H).
^{13}C-NMR (151 MHz, Methanol-d_4) δ 13.57 (t with ^{195}Pt satellites, J_{CP} = 19.3 Hz J_{CPt} = 79.1 Hz), -12.62 (t, J = 6.1 Hz).
^{31}P-NMR (243 MHz, Methanol-d_4) δ -20.19 (s with ^{195}Pt satellites, J_{PPt} = 2660 Hz)
EA: Calculated: C, 17.19; H, 4.33; Found: C, 17.30; H, 4.20

***cis,trans,cis*-diiodobis(trimethylphosphine)dimethylplatinum(IV), 24**

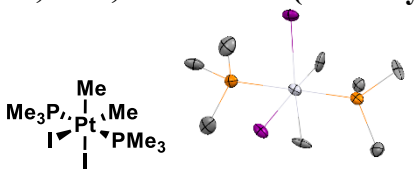

To a solution of **10** (1.22g, 2.5 mmol) in methanol (150 mL, 0.015 M) was added iodomethane (3.1 mL, 50 mmol). The mixture was stirred for 18 hours in the dark and then concentrated. The crude product was recrystallized from DCM/Methanol by the layering method yielding colorless needles (978 mg, 62% yield). X-ray quality crystals were obtained by vapor diffusion of diethyl ether into a saturated DCM solution.

^{1}H-NMR (600 MHz, Methylene Chloride-d_2) δ 1.93 (t with ^{195}Pt satellites, J_{PH} = 4.0 Hz J_{PtH} = 18.9 Hz, 18H), 1.43 (t with ^{195}Pt satellites, J_{PH} = 5.7 Hz, J_{PtH} = 65.9 Hz, 6H).
^{13}C-NMR (151 MHz, Methylene Chloride-d_2) δ 14.44 (t with ^{195}Pt satellites, J_{PC} = 10.1 Hz J_{PtC} = 42.0 Hz) 6.51 (t, J = 2.8 Hz J_{PtC} = 539 Hz).
^{31}P-NMR (243 MHz, Methylene Chloride-d_2) δ -39.67 (s with ^{195}Pt satellites. J_{PtP} = 1950 Hz).
EA: Calculated: C, 15.22; H, 3.83; Found: C, 15.28; H, 3.80

***trans*-bis(trimethylphosphine)tetramethylplatinum(IV), 26**

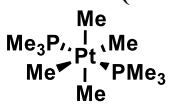

Tetramethyltin (1.67 mL, 12 mmol, 40 equiv.), potassium fluoride dihydrate (1.13 g, 12 mmol, 40 equiv) and **24** (189 mg, 0.3 mmol) were dissolved in methanol (30 mL, 0.01M). The solution was degassed and heated at 40 ^{o}C for 12 hours under N_2. The mixture was concentrated and the residue was extracted with dichloromethane, filtered, and concentrated. The resulting product was dissolved in hexanes and filtered through a short plug of neutral alumina, affording a light yellow solid which discolors upon extended exposure to air (82 mg, 67%).

^{1}H-NMR (500 MHz, Methylene Chloride-d_2) δ 1.33 (t with ^{195}Pt satellites, J_{PH} = 3.5 Hz J_{PtH} = 18.8 Hz, 18H), -0.46 (t with ^{195}Pt satellites, J_{PH} = 5.7 Hz J_{PtH} = 43.3 Hz, 12H).
^{13}C-NMR (126 MHz, Methylene Chloride-d_2) δ 8.98 (t with ^{195}Pt satellites, J_{PC} = 10.0 Hz J_{PtC} = 39.1 Hz), -17.34 (t, J_{PC} = 6.8 Hz).
^{31}P-NMR (202 MHz, Methylene Chloride-d_2) δ -36.68 (s with ^{195}Pt satellites, J_{PtP} = 2120 Hz).
EA: Calculated: C, 29.48; H, 7.42; Found: C, 29.48; H, 7.44

***trans,mer*-iodobis(trimethylphosphine)trimethylplatinum(IV), 25**

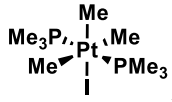

A mixture of **26** (82 mg, 0.2 mmol) and **24** (126 mg, 0.2 mmol) was dissolved in 4 mL of degassed dichloromethane (0.05 M) and heated at 40 °C for 12 hours, affording an equilibrated mixture of **24**, **25**, and **26** (~73% conversion). The mixture was dry loaded onto neutral alumina, and chromatographed, eluting on a gradient from pure hexanes to 20:80 diethyl ether/hexanes. The pure fractions were combined and concentrated, affording 78 mg of a pale yellow solid which discolors upon extended exposure to air (38% yield).

^{1}H-NMR (500 MHz, Methylene Chloride-d_2) δ 1.66 (t with ^{195}Pt satellites, J_{PH} = 3.7 Hz J_{PtH} = 18.4 Hz, 18H), 0.80 (t with ^{195}Pt satellites, J_{PH} = 6.0 Hz J_{PtH} = 68.2 Hz, 3H), 0.13 (t with ^{195}Pt satellites, J_{PH} = 5.6 Hz J_{PtH} = 42.1 Hz, 6H).
^{13}C-NMR (126 MHz, Methylene Chloride-d_2) δ 11.95 (t with ^{195}Pt satellites, J_{PC} = 10.1 Hz J_{PtC} = 41.0 Hz), 3.35 (t J_{PC} = 3.7 Hz), -14.02 (t with ^{195}Pt satellites, J_{PC} = 6.2 Hz J_{PtC} = 374 Hz).
^{31}P-NMR (202 MHz, Methylene Chloride-d_2) δ -38.70 (s with ^{195}Pt satellites, J_{PtP} = 2050 Hz).
EA: Calculated: C, 20.82; H, 5.24; Found: C, 20.93; H, 5.31

3.5.3 Procedures for Non-preparative Reactions

General procedures for kinetics

2-trimethylsilylethanol was used as an internal standard except for dual catalysis reactions, where dimethylacetamide was used in order to avoid overlapping with the tin-methyl resonances, and where otherwise noted. Platinum kinetics on **9** were performed with quantitatively decoupled ^{1}H {^{195}Pt} NMR to eliminate satellites, which was tuned to optimally decouple the starting material resonances. Gold reactions were conducted at 25 °C, platinum reactions at 40 °C, and dual catalysis at 45 °C. Background reactions for **3-I**, **7-I**, and **9** were carried out in sealed NMR tubes and monitored by heating in an oil bath at the specified temperature, and taking time points on a daily basis. One scan was used per time point in order to minimize integration error. All solvents were sparged with nitrogen for 30 minutes prior to use.

General procedure for kinetics analysis for halide dependence

To an NMR tube, in an N_2 atmosphere wet glove box, was added cluster **1** (0.001 mmol, 0.1 eq.) and 2-trimethylsilylethanol (0.01 mmol, 1 eq.) as a solution in CD_3OD (200 μL). The NMR tube was then fitted with a septum top and removed from the glove box, followed immediately by the application of parafilm to seal the edges of the septum. Immediately prior to the kinetics experiment, by microliter syringe the desired amount of potassium iodide was added as a solution in CD_3OD, in addition to excess CD_3OD and finally **3-I**, **7-I**, or **9** (0.01 mmol, 1 eq.) as a solution in CD_3OD, such that the total volume in the tube was equal to 500 μL. The reaction mixture was then placed into the prewarmed, tuned and shimmed NMR spectrometer, and an automatic kinetics program was used to collect regular time points at 15 to 60 second intervals, depending on the rate of the reaction.

General procedure for kinetics analysis for cluster dependence

To an NMR tube, in an N_2 atmosphere wet glove box, was added cluster **1** (0.004 mmol, 0.1 eq.) and 2-trimethylsilylethanol (0.01 mmol, 1 eq.) as a solution in CD_3OD (300 μL). The NMR tube was then fitted with a septum top and removed from the glove box, followed immediately by the application of parafilm to seal the edges of the septum. Immediately prior to the kinetics experiment, by microliter syringe, the desired amounts of $PEt_4BAr^f_4$ and $NaBAr^f_4$ were added as a solution in CD_3OD, and finally **3-I**, **7-I**, or **9** (0.01 mmol, 1 eq.) as a solution in CD_3OD, such that the total volume in the tube was equal to 500 μL. The reaction mixture was then placed into the prewarmed, tuned and shimmed NMR spectrometer, and an automatic kinetics program was used to collect regular time points at 15 to 60 second intervals, depending on the rate of the reaction.

General procedure for kinetics analysis for Substrate dependence

To an NMR tube, in an N_2 atmosphere wet glove box, was added cluster **1** (0.001 mmol, 0.1 eq.) and 2-trimethylsilylethanol (0.01 mmol, 1 eq.) as a solution in CD_3OD (100 μL). The NMR tube was then fitted with a septum top and removed from the glove box, followed immediately by the application of parafilm to seal the edges of the septum. Immediately prior to the kinetics experiment, by microliter syringe, the desired amount of CD_3OD, followed by the desired amount of **3-Br**, **7-I**, or **9** as a solution in CD_3OD, such that the total volume in the tube was equal to 500 μL. The reaction was then placed into the prewarmed, tuned and shimmed NMR spectrometer, and an automatic kinetics program was used to collect regular time points at 15 to 60 second intervals, depending on the rate of the reaction.

General procedure for dual catalysis:

A J. Young tube was charged with bis(trimethylphosphine)dimethylplatinum(II) (**22**) (3.8 mg, 0.01 mmol, 0.1 equiv.) and cluster **2** (24 mg, 0.005 mmol, 0.05 equiv.). The tube was then transferred to an wet-atmosphere N_2 atmosphere glove box, and methyl iodide (28.3 mg, 0.2 mmol, 2 equiv.), tetramethyl tin (17.9 mg, 0.l mmol, 1 equiv.), potassium fluoride (11.6 mg, 0.2 mmol, 2 equiv.) and dimethylacetamide (1.74 mg, 0.02 mmol, 0.2 equiv.) (as an internal standard) were added as a stock solution in methanol-d_4 (0.80 mL) and D2O (0.20 mL). The tube was then sealed, removed from the glove box and placed into a preheated, tuned and shimmed NMR spectrometer at 45 ºC. Scans were collected at 480 second intervals. For the control reaction, cluster **2** was omitted.

<u>General procedure for encapsulation of "donor arrested reductive elimination" complexes:</u>

– *Trimethylphosphine and dimethylsulfide:*

To an NMR tube was added platinum complex **9** (5.2 mg, 0.01 mmol, 1.0 equiv). The NMR tube was brought into an N_2 atmosphere wet glove box, and cluster **1** (0.002 mmol, 0.2 equiv) was added as a solution in CD_3OD (500 μL). Agitation was minimized to keep the dissolution of **5** to a minimum, and thus minimize background reductive elimination prior to the addition of the neutral donor. A septum topped NMR cap was added to the NMR tube, and the tube was removed from the glovebox, followed immediately by the application of parafilm to seal the edges of the septum. Trimethyl phosphine or dimethyl sulfide (0.02 mmol, 2.0 equiv) was

added by microliter syringe through the septum top of the NMR tube. The septum top was further sealed with electrical tape, and the tube was sonicated until homogeneous. Encapsulation was then assessed by ^{1}H-NMR spectroscopy.

– *Platinum allyl:*

To an NMR tube was added platinum complex **16** (2.5 mg, 0.005 mmol, 1.0 equiv). The NMR tube was brought into an N_2 atmosphere wet glove box, and cluster **1** (0.00625 mmol, 1.25 equiv) was added as a solution in CD_3OD (500 μL). The NMR tube was capped, and the tube was removed from the glovebox, followed immediately by the application of parafilm to seal the edges of the cap. Encapsulation was then assessed by ^{1}H-NMR spectroscopy.

– *Platinum butenyl, pentenyl, and hexenyl complexes:*

To an NMR tube was added Pt(II) complex **22** (5.7 mg, 0.015 mmol, 1.0 equiv), followed by acetone-d_6 (0.5 mL) and then the appropriate alkyl iodide (butenyl-, pentenyl or hexenyliodide) (0.225 mmol, 15.0 equiv). The reaction was placed in a oil bath, which was preheated to 40 ºC. After 4 hours, the NMR tube was placed in a vacuum chamber, and volatiles were removed *in vacuo*. The NMR tube, with the crude Pt(IV) residue, was pumped into an N_2 atmosphere wet glove box, and cluster **1** (0.005 mmol, 0.33 equiv) was added as a solution in CD_3OD (500 μL). The NMR tube was capped, and the tube was removed from the glovebox, followed immediately by the application of parafilm to seal the edges of the cap. Encapsulation was then assessed by ^{1}H-NMR spectroscopy.

Kinetics for cluster promoted acidolysis of **23**:

To an NMR tube, in an N_2 atmosphere wet glove box, was added platinum tetramethyl complex **23** (0.005 mmol, 1.0 equiv) and dimethylacetamide (internal standard) (0.005 mmol, 1.0 equiv) as a stock solution in methanol-d_4 (400 µL). Cluster **1** (0.00125 mmol, 0.25 equiv) was added as a stock solution in D_2O (100 µL). The NMR tube was capped and removed from the glove box, followed immediately by the application of parafilm to seal the edges of the cap. The reaction mixture was then placed into the prewarmed, tuned and shimmed NMR spectrometer, and an automatic kinetics program was used to collect regular time points at 60-second intervals. Time between the addition of **1** and first acquisition was minimized, and was generally about 120 seconds.

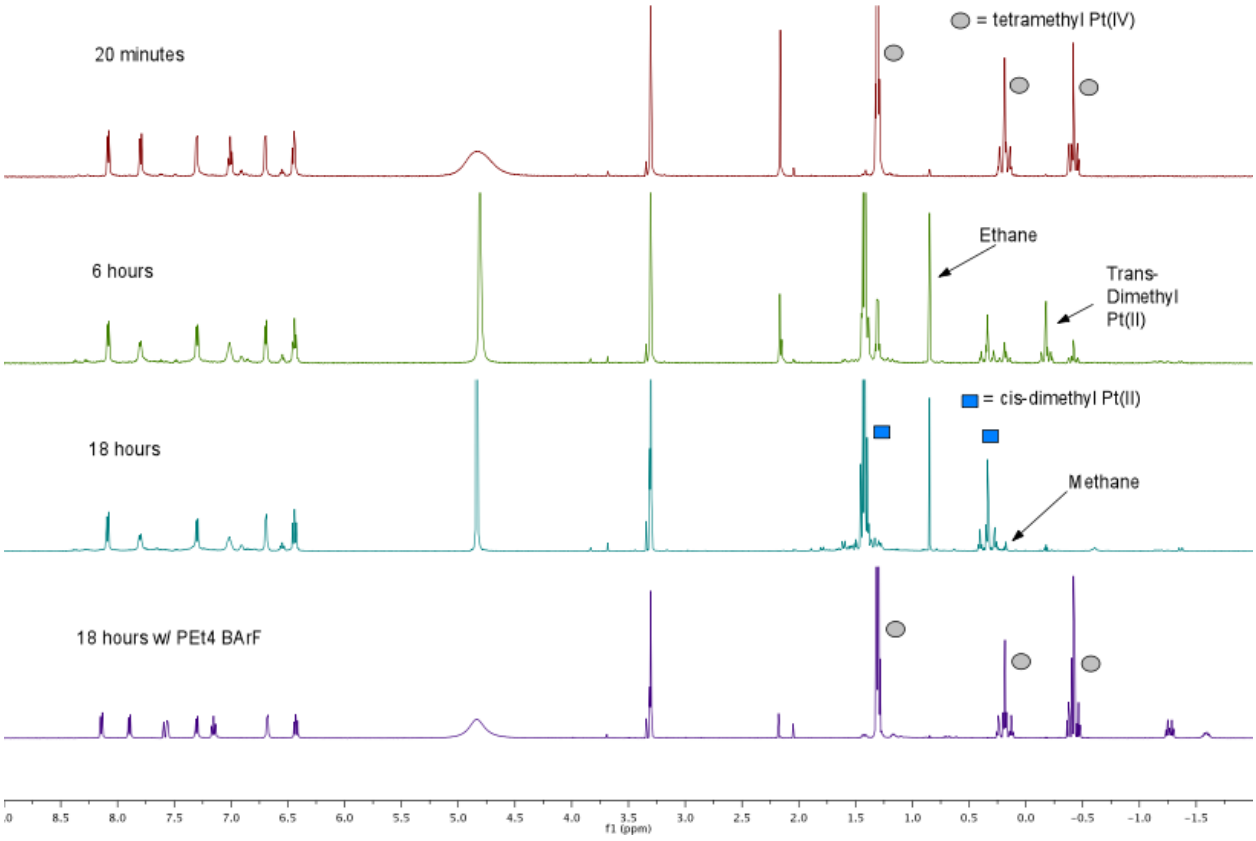

Figure 3.24. Representative ^{1}H-NMR spectra from the cluster promoted acidolysis of **23**.

Competition between transmetallation and oxidative addition to **10**:

– *Transmetallation:*

To an NMR tube, in an N_2 atmosphere wet glove box, was added platinum(II) complex **10** (0.0025 mmol, 1.0 equiv) and platinum(IV) complex **9** (0.0025 mmol, 1.0 equiv) and dimethylacetamide (internal standard) (0.02 mmol, 8.0 equiv) as a stock solution in 8:2 methanol-d_4:D_2O (300 µL). The NMR tube was then fitted with a septum top and removed from the glove box, followed immediately by the application of parafilm to seal the edges of

the septum. Immediately prior to the kinetics experiment, tetramethyl tin (0.05 mmol, 20 equiv) and potassium fluoride (0.1 mmol, 40 equiv) were added by microliter syringe as a solution in 8:2 methanol-d_4:D_2O (200 µL). The reaction mixture was then placed into the prewarmed (45 ºC), tuned and shimmed NMR spectrometer, and an automatic kinetics program was used to collect regular time points at 60 second intervals.

– *Oxidative Addition:*

To an NMR tube, in an N_2 atmosphere wet glove box, was added platinum(II) complex **10** (0.0025 mmol, 1.0 equiv) and dimethylacetamide (internal standard) (0.02 mmol, 8.0 equiv) as a stock solution in 8:2 methanol-d_4:D_2O (300 µL). The NMR tube was then fitted with a septum top and removed from the glove box, followed immediately by the application of parafilm to seal the edges of the septum. Immediately prior to the kinetics experiment, methyl iodide (0.05 mmol, 20 equiv) was added by microliter syringe as a solution in 8:2 methanol-d_4:D_2O (200 µL). The reaction mixture was then placed into the prewarmed (45 ºC), tuned and shimmed NMR spectrometer, and an automatic kinetics program was used to collect regular time points at 60 second intervals.

Kinetic investigation of **25** under kinetically relevant conditions:

To an NMR tube, in an N_2 atmosphere wet glove box, was added cluster **2** (0.001 mmol, 0.1 eq.) and dimethylacetamide (0.01 mmol, 1 eq.) as a solution in CD_3OD (225 µL) and D_2O (75 µL). The NMR tube was then fitted with a septum top and removed from the glove box, followed immediately by the application of parafilm to seal the edges of the septum. Immediately prior to the kinetics experiment, **25** (0.01 mmol, 1 eq.) was added by microliter syringe as a solution in CD_3OD (300µL). The reaction mixture was then placed into the prewarmed, tuned and shimmed NMR spectrometer, and an automatic kinetics program was used to collect regular time points at 15 to 60 second intervals, depending on the rate of the reaction. While the disappearance of **25** could be tracked, overlapping peaks of the isomerized Pt(IV) complex **9**, and the product of reductive elimination, **10**, prevented deconvolution of the two relative rates. However, since the disappearance of **25** is significantly faster than catalyzed reductive elimination from **9**, the ratio of **9** and **10** when **25** is consumed is similar to ratio of the rates for cluster catalyzed isomerization of **25** and reductive elimination from **25**. Note the difference in scale of the x-axes on the plots below for data collected at 25 and 45 degrees Celsius.

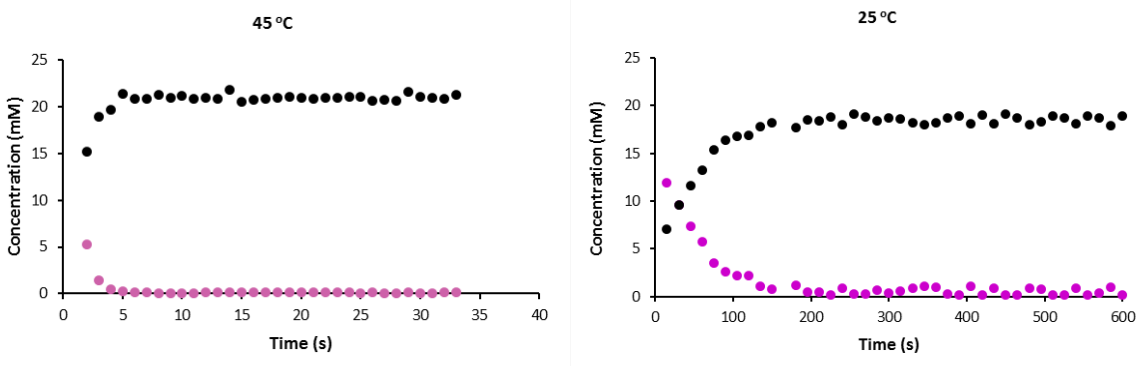

Figure 3.25. Kinetic traces showing rapid consumption of **25** in the presence of **2**. Pink = **25**, black = combined [Pt] products (**9** and **10**)

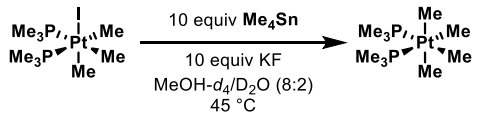

To a solution of **9** (2.6 mg, 0.005 mmol, prepared as a stock solution) in Methanol-d_4/D_2O (4:1, 0.5 mL total) was added 7 μL (0.05 mmol, 10 equiv) of tetramethyl tin, and 5 mg of potassium fluoride dihydrate (0.05 mmol, 10 equiv). After 20 minutes at room temperature, a ^{1}H-NMR spectrum was recorded, showing a 1.5:1 ratio of **9** to **23**, with concomitant formation of Me_3SnF. The mixture was heated at 45 ^{o}C for 3 hours, and a ^{1}H-NMR spectrum was again recorded, showing a 1.2:1 ratio of **9** to **23**.

When this procedure was followed omitting potassium fluoride, the concentration of **23** was below the detection limit for ^{1}H-NMR (>30:1), even after heating.

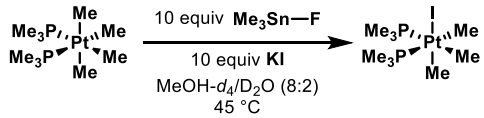

To a solution of **23** (2.0 mg, 0.005 mmol, prepared as a stock solution) in Methanol-d_4/D_2O (4:1, 0.5 mL total) was added 9 mg of trimethyltin fluoride (0.05 mmol, 10 equiv) and 8 mg of potassium iodide (0.05 mmol, 10 equiv). After 15 minutes at room temperature, a ^{1}H-NMR spectrum was recorded, showing complete conversion to **9**.

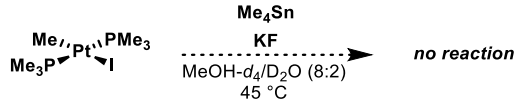

To a solution of **10** (2.5 mg, 0.005 mmol, prepared as a stock solution) in Methanol-d_4/D_2O (4:1, 0.5 mL total) was added 7 μL (0.05 mmol, 10 equiv) of tetramethyl tin, and 5 mg of potassium fluoride dihydrate (0.05 mmol, 10 equiv). After 20 minutes at room temperature, a ^{1}H-NMR spectrum was recorded, showing no reaction. The mixture was heated at 45 ^{o}C for 3 hours, and a ^{1}H-NMR spectrum was again recorded, again showing no reaction.

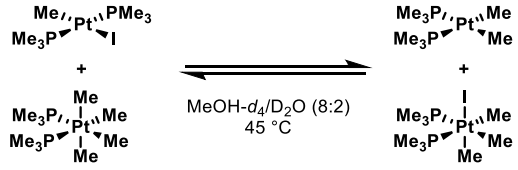

To a solution of **10** (2.5 mg, 0.005 mmol, prepared as a stock solution) in Methanol-d_4/D_2O (4:1, 0.5 mL total) was added 6 mg of **23** (0.015 mmol, 3 equiv). The mixture was heated at 45 ^{o}C for 3 hours, and a ^{1}H-NMR spectrum was recorded, showing the formation of **9** and **22** in approximately equimolar amounts.

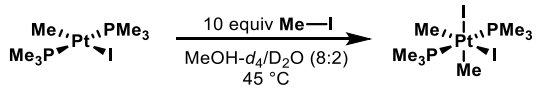

To a solution of **10** (2.5 mg, 0.005 mmol, prepared as a stock solution) in Methanol-d_4/D_2O (4:1, 0.5 mL total) was added 3 μL of iodomethane (0.05 mmol, 10 equiv). The mixture was heated at at 45 ^oC for 30 minutes, and a ^{1}H-NMR spectrum was recorded, showing the formation of **24** (approx. 30% conversion). Heating was continued for an additional four hours, and a ^{1}H-NMR spectrum was again recorded, showing approximately 95% conversion to give **24**.

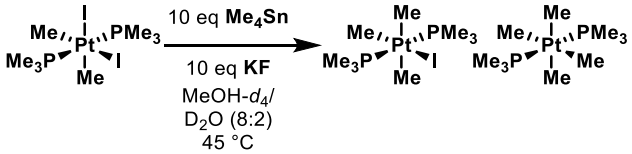

To a solution of **24** (6.3 mg, 0.01 mmol, prepared as a stock solution) in Methanol-d_4/D_2O under N_2 (4:1, 0.5 mL total) was added 13.8 μL of tetramethyl tin (0.1 mmol, 10 equiv) and 9.4 mg of potassium fluoride dehydrate (0.1 mmol, 10 equiv). The mixture was heated at at 45 ^oC for 30 minutes, and a ^{1}H-NMR spectrum was recorded, showing the formation of **25** and **26** (55:42:3 **24**/**25**/**26**). Heating was continued for an additional three hours, and a ^{1}H-NMR spectrum was again recorded, showing complete consumption of **24**, and an 8:2 ratio of **25** to **26**.

Control experiments for acid catalysis of reductive elimination:

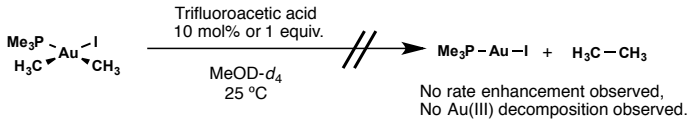

To a solution of **3-I** (0.01 mmol, 4.3 mg) in Methanol-d_4 (0.4 mL) was added a solution of trifluoroacetic acid (0.1 mL, either 0.01 mmol of TFA or 0.001 mmol of TFA, with solutions prepared by serial dilution in volumetric glassware). The reaction mixtures (in NMR tubes) were places in a bath maintained at 25 ^oC sealed with septa, and the mixture was monitored periodically for 4 days via ^{1}H-NMR. No significant deviation from the observed background rate of reductive elimination was observed, and no Au(III) decomposition was observed.

3.5.4 Supporting Figures and Observations

Derivation of the rate law

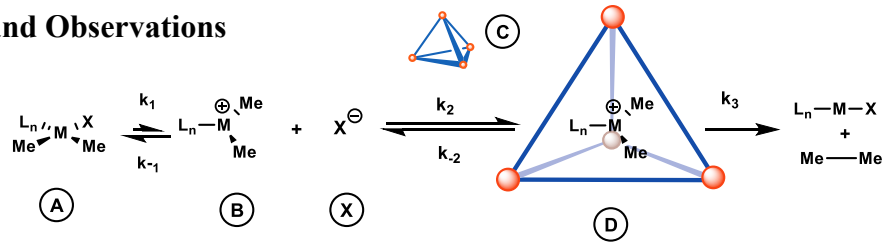

$$\frac{d[D]}{dt} = k_2[B][C] - k_{-2}[D] - k_3[D]$$

$$[C] = [C]_0 - [D]$$

$$\frac{d[D]}{dt} = k_2[B]\left([C]_0 - [D]\right) - k_{-2}[D] - k_3[D] = k_2[B][C]_0 - [D]\left(k_2[B] + k_{-2} + k_3\right)$$

Steady State Approximation: $\frac{d[D]}{dt} = 0$

$$0 = k_2[B][C]_0 - [D]\left(k_2[B] + k_{-2} + k_3\right)$$

$$[D] = \frac{k_2[B][C]_0}{k_2[B] + k_{-2} + k_3} = \frac{[B][C]_0}{[B] + \frac{k_{-2} + k_3}{k_2}}$$

Pre-equilibrium Approximation: $K_1 = \frac{k_1}{k_{-1}} = \frac{[B][X]}{[A]}$

$$[B] = \frac{K_1[A]}{[X]}$$

$$[D] = \frac{\frac{K_1[A]}{[X]}[C]_0}{\frac{K_1[A]}{[X]} + \frac{k_{-2} + k_3}{k_2}} = \frac{[A][C]_0}{[A] + \frac{k_{-2} + k_3}{K_1 k_2}[X]}$$

$$\frac{d[P]}{dt} = k_3[D] = \frac{k_3[A][C]_0}{[A] + \frac{k_{-2} + k_3}{K_1 k_2}[X]}$$

$$k_3 = k_{cat}$$

So,

$$Rate = \frac{k_{cat}[A][C]_0}{[A] + \frac{k_{-2} + k_{cat}}{K_1 k_2}[X]}$$

Alternatively, if you apply a pre-equilibrium approximation to [D] instead of a Steady-State approximation:

$$K_2 = \frac{k_2}{k_{-2}} = \frac{[D]}{[B][C]}$$

$$[D] = K_2[B][C] = K_2[B][C]_0 - K_2[B][D]$$

$$[D](1 + K_2[B]) = K_2[B][C]_0$$

$$[D] = \frac{K_2[B][C]_0}{1 + K_2[B]} = \frac{K_2\left(\frac{K_1[A]}{[X]}\right)[C]_0}{1 + K_2\left(\frac{K_1[A]}{[X]}\right)} = \frac{K_2 K_1[A][C]_0}{[X] + K_2 K_1[A]} = \frac{[A][C]_0}{[A] + \frac{1}{K_1 K_2}[X]}$$

So,

$$Rate = \frac{k_{cat}[A][C]_0}{[A] + \frac{1}{K_1 K_2}[X]}$$

Note, that these are indistinguishable experimentally and that in the limit that $k_{cat} << k_{-2}$

$$\frac{k_{-2} + k_{cat}}{K_1 k_2} \approx \frac{k_{-2}}{K_1 k_2} = \frac{1}{K_1 K_2}$$

We favor the steady state approximation as it is the more general solution.

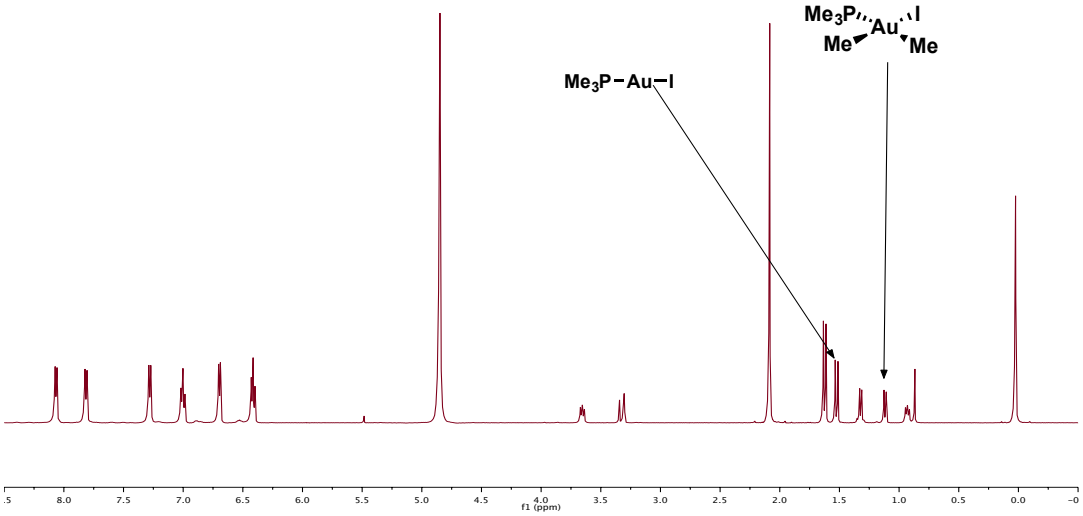

Figure 3.26. A representative spectrum from the kinetics analysis of the cluster catalyzed reductive elimination from **3-I**.

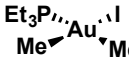

(**7-I**)

Representative trace:

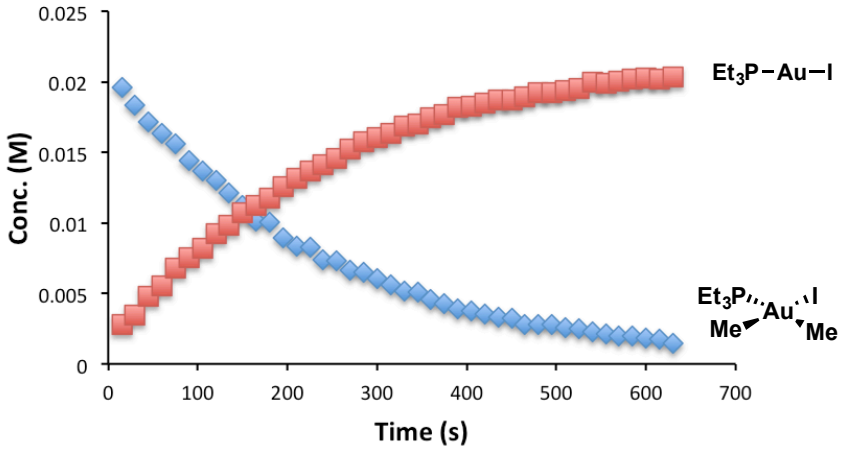

Figure 3.27. A representative kinetic trace of cluster catalyzed reductive elimination from **7-I**.

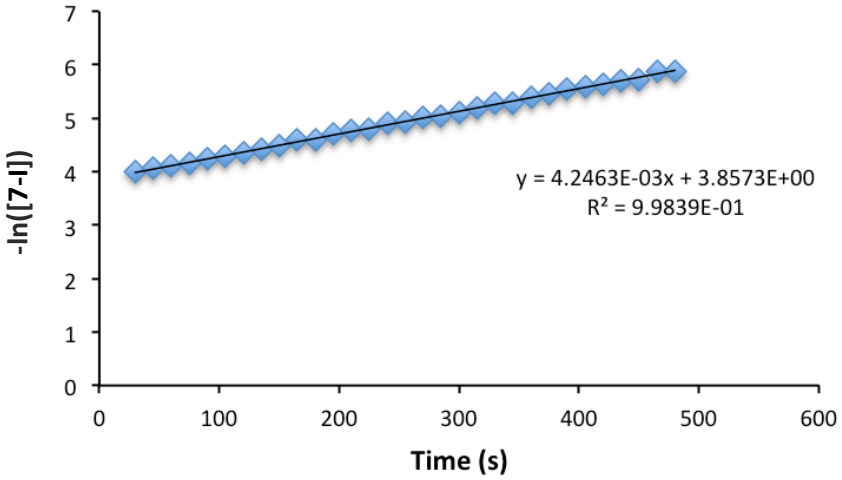

Figure 3.28. Natural log plot affording the first order rate constant for the catalyzed reductive elimination from **7-I**.

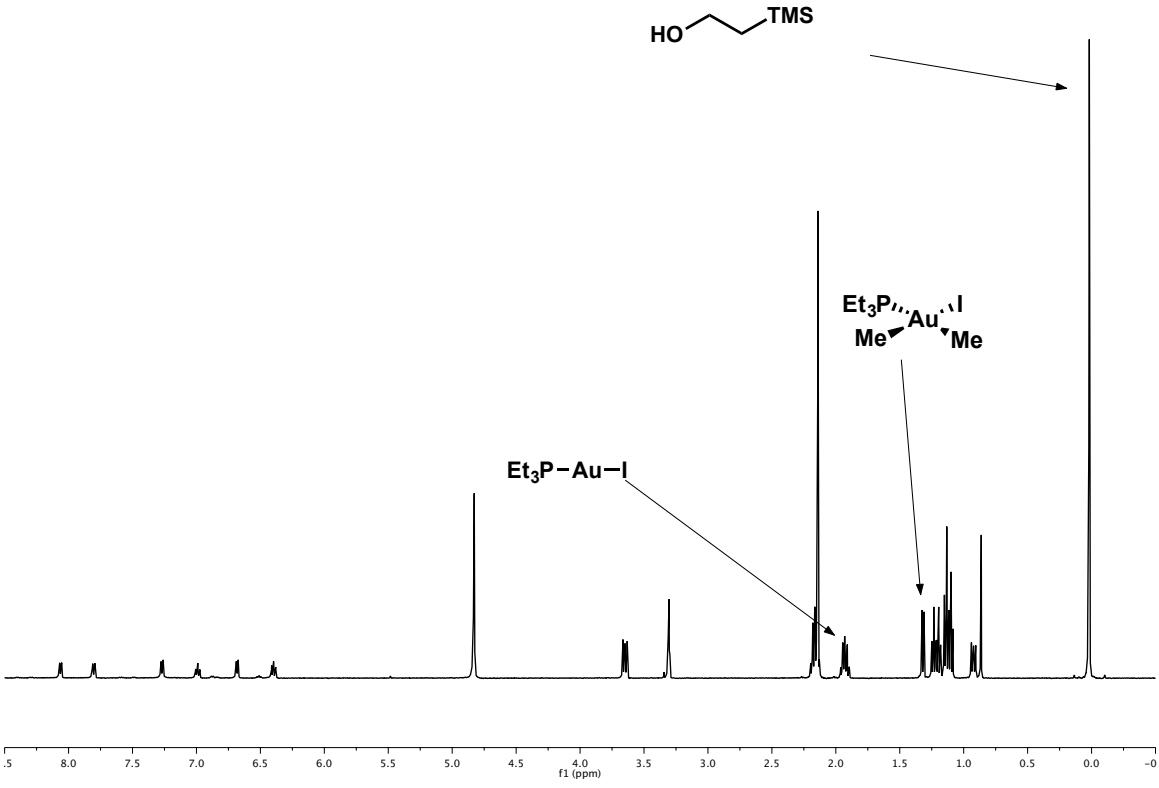

Figure 3.29. A representative spectrum from the kinetics analysis of the catalyzed reductive elimination from **7-I**.

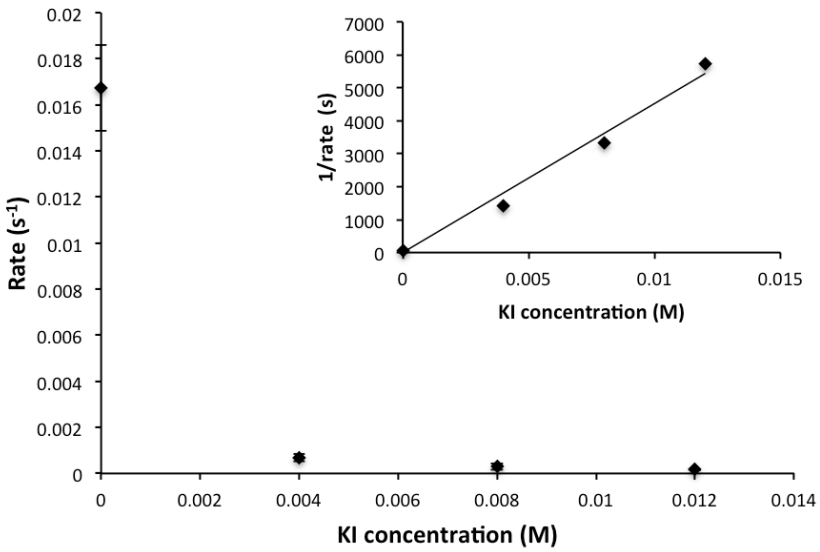

Figure 3.30. Rate dependence of catalyzed reductive elimination from **7-I** on iodide concentration. All error bars represent one standard deviation based on three replicates.

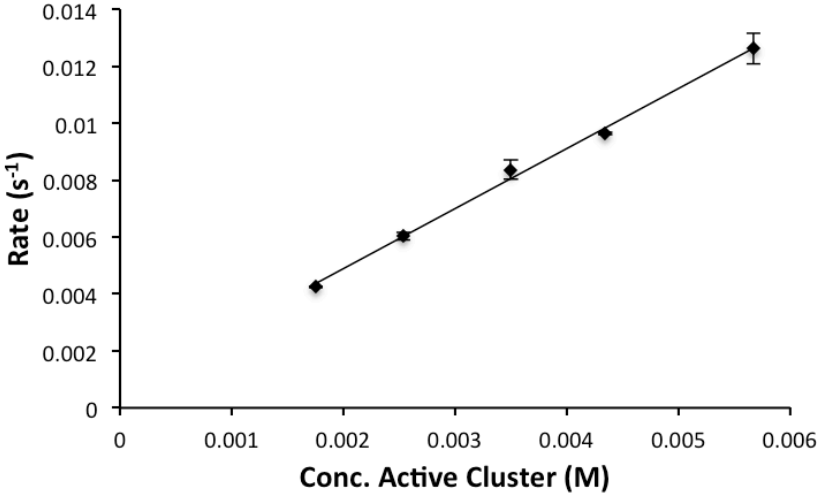

Figure 3.31. Rate dependence of catalyzed reductive elimination from **7-I** on active cluster concentration. All error bars represent one standard deviation based on three replicates.

RPKA Data for Figure 3.4 were generated by application of the Five-Point Stencil method for numerical differentiation

$$\left[f'(t) \approx \frac{-f(t+2h)+8f(t+h)-8f(t-h)+f(t-2h)}{12h} \right],\ h=15\ s$$

*to three independent runs for the reductive elimination of ethane from **4** catalyzed by **1** with a starting concentration for **7-I** of 0.1M. The resulting three data sets for rate vs. concentration were aggregated to give the blue data points shown in Figure 3.4. Similar results were obtained using a polynomial fit method for numerical differentiation. The former method is preferred due to the introduction of artifacts at the high and low concentration ends of the data by the polynomial fit method.*

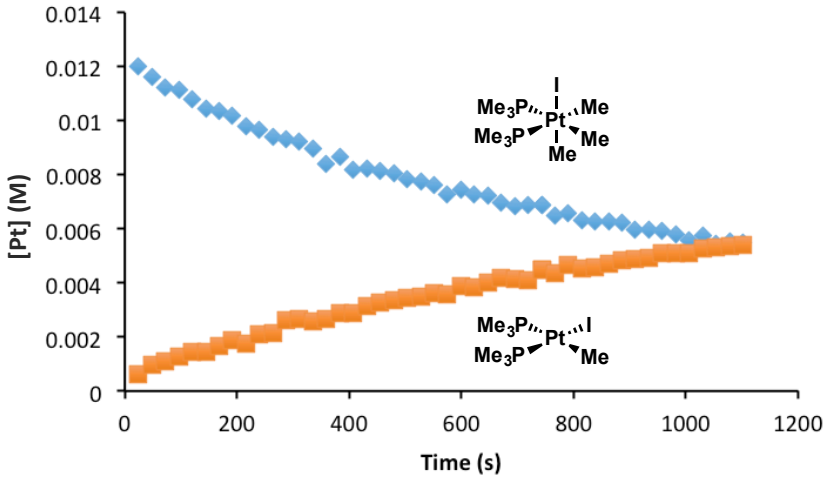

Figure 3.32. A representative kinetic trace of catalyzed reductive elimination from **9**.

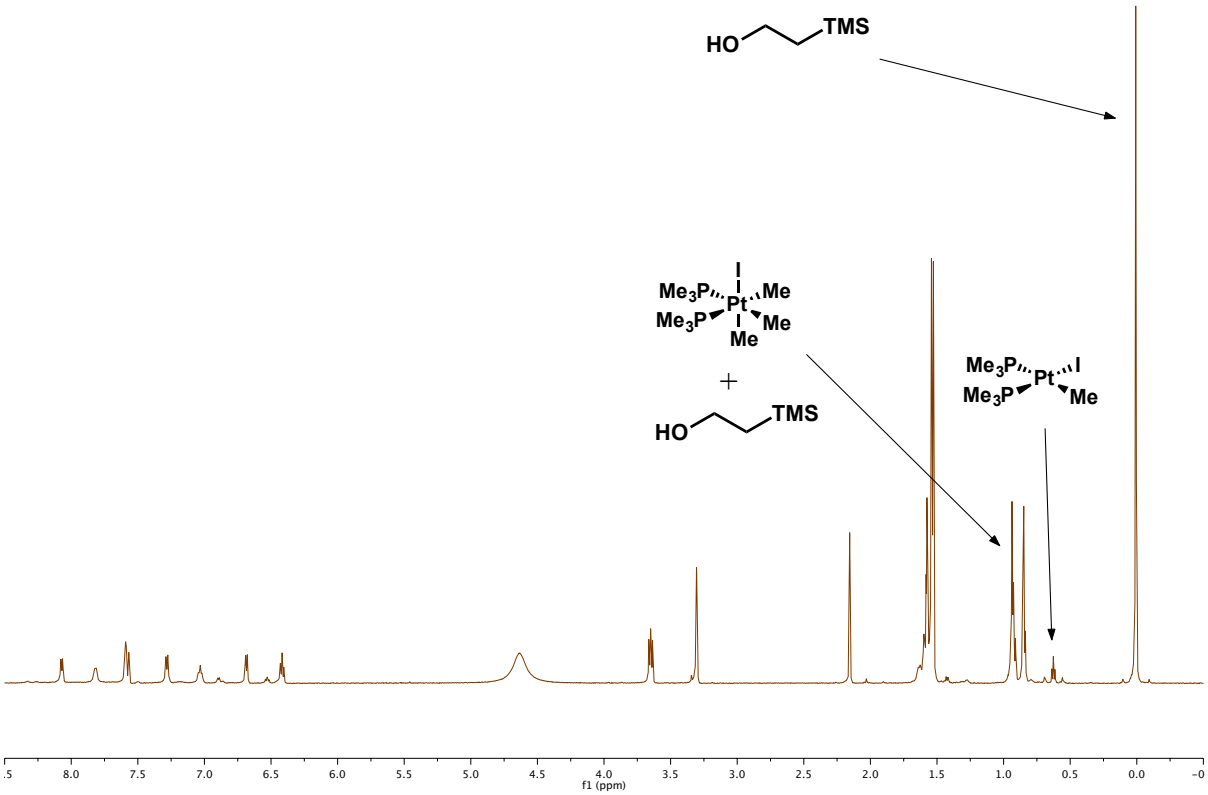

Figure 3.33. A representative spectrum from the kinetics analysis of the catalyzed reductive elimination from **9**.

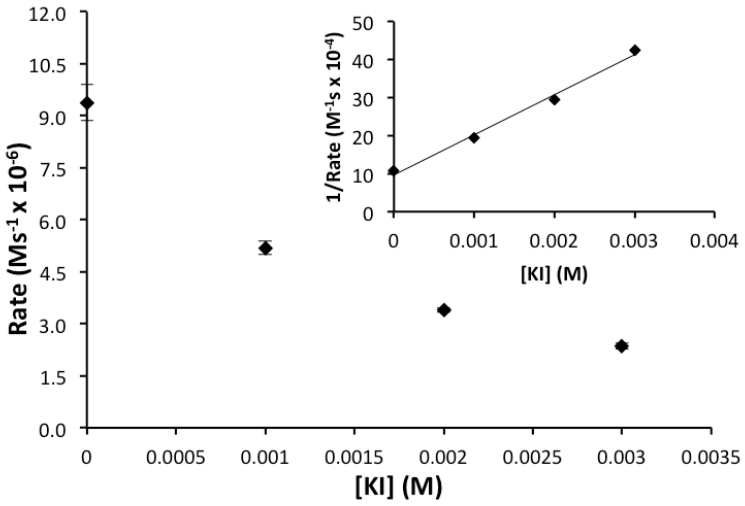

Figure 3.34. Rate dependence of catalyzed reductive elimination from **9** on iodide concentration. All error bars represent one standard deviation based on three replicates.

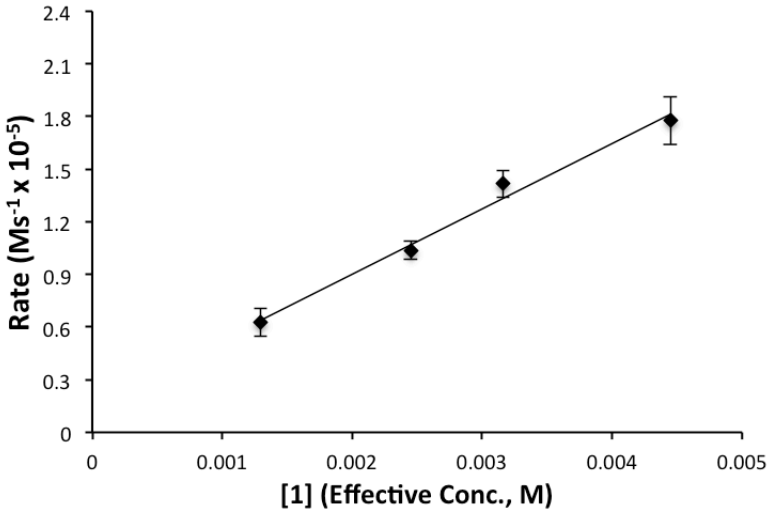

Figure 3.35. Rate dependence of catalyzed reductive elimination from **9** on active cluster concentration. All error bars represent one standard deviation based on three replicates.

Representative Spectra of Platinum Speciation for Dual Catalysis

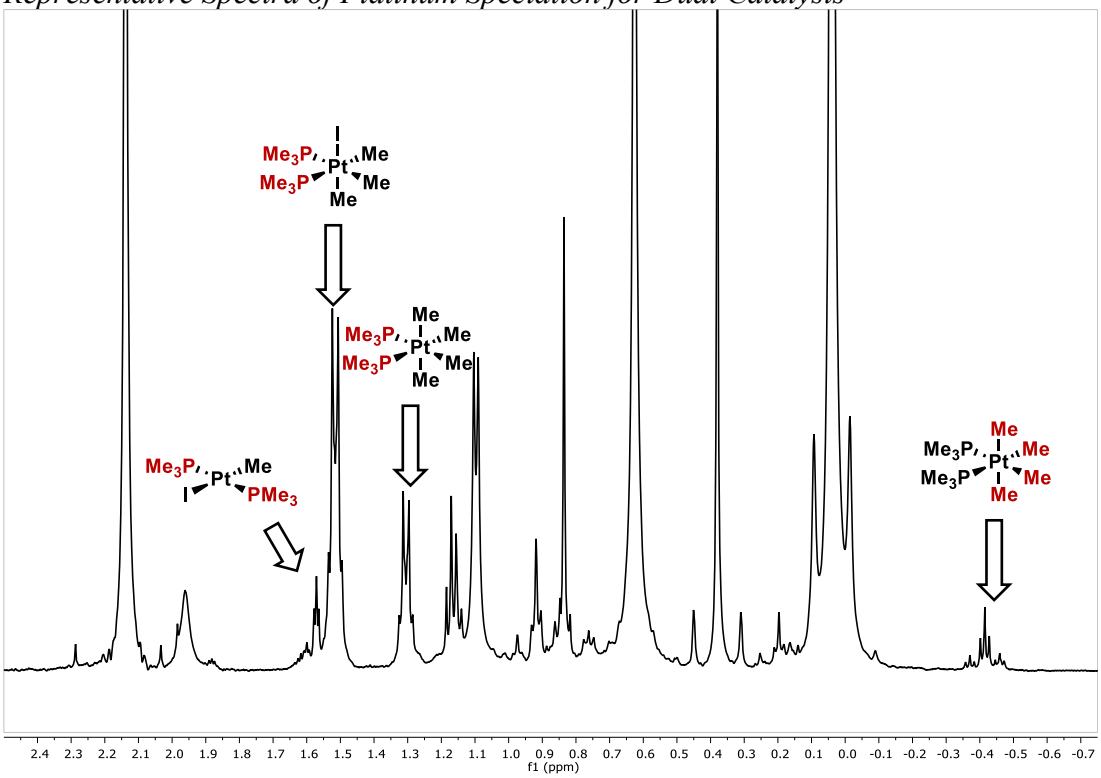

Figure 3.36. Representative spectrum for platinum speciation under dual catalytic conditions at early reaction times.

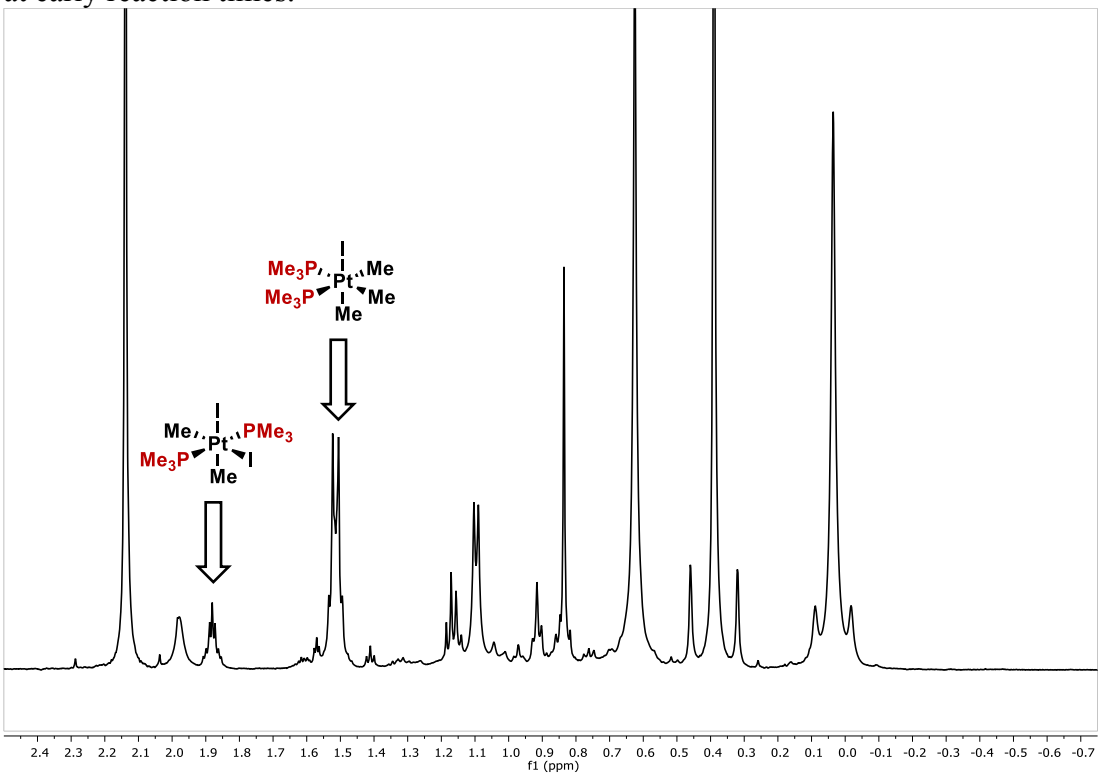

Figure 3.37. Representative spectrum for platinum speciation under dual catalytic conditions at late reaction times.

Precatalyst examination

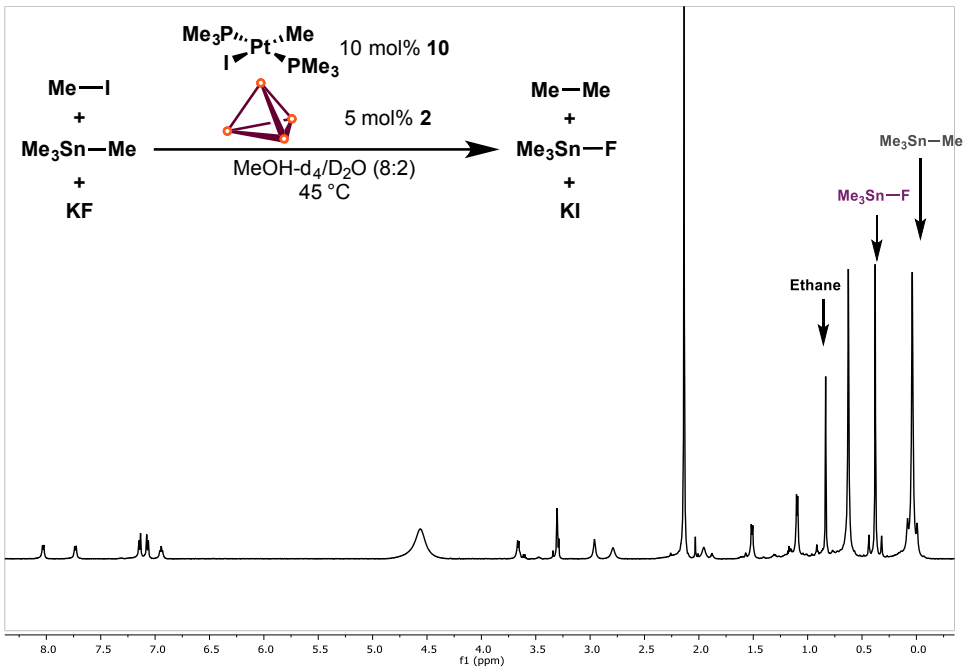

Figure 3.38. Representative NMR spectrum for dual catalysis with **10** and **2**.

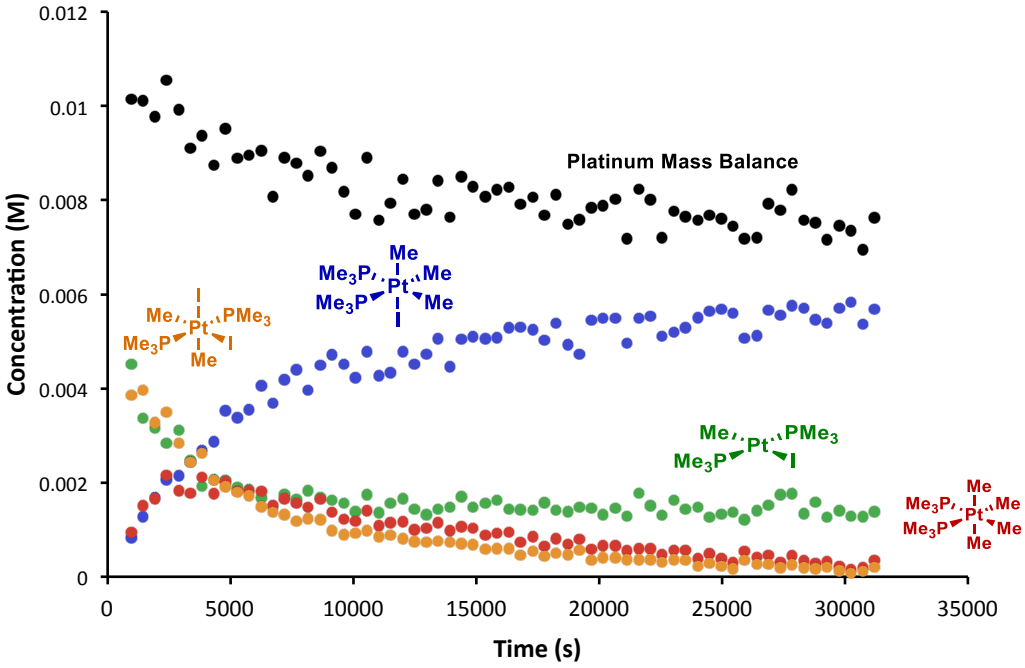

Figure 3.39. Platinum concentrations under dual catalysis with **10** and **2**, showing mass balance decrease due to precipitation of **24** (orange)

In order to probe whether or not methyl groups were incorporated from both iodomethane and tetramethyl tin, a labeling experiment was performed using d_3-iodomethane. It was expected that d_0-, d_3-, and d_6-ethane would be observed due to both inter- and intra-molecular scrambling of alkyl groups on platinum complexes. It is unknown which two of three methyl groups on a given $[Pt^{IV}]Me_3$ complex reductively eliminate.

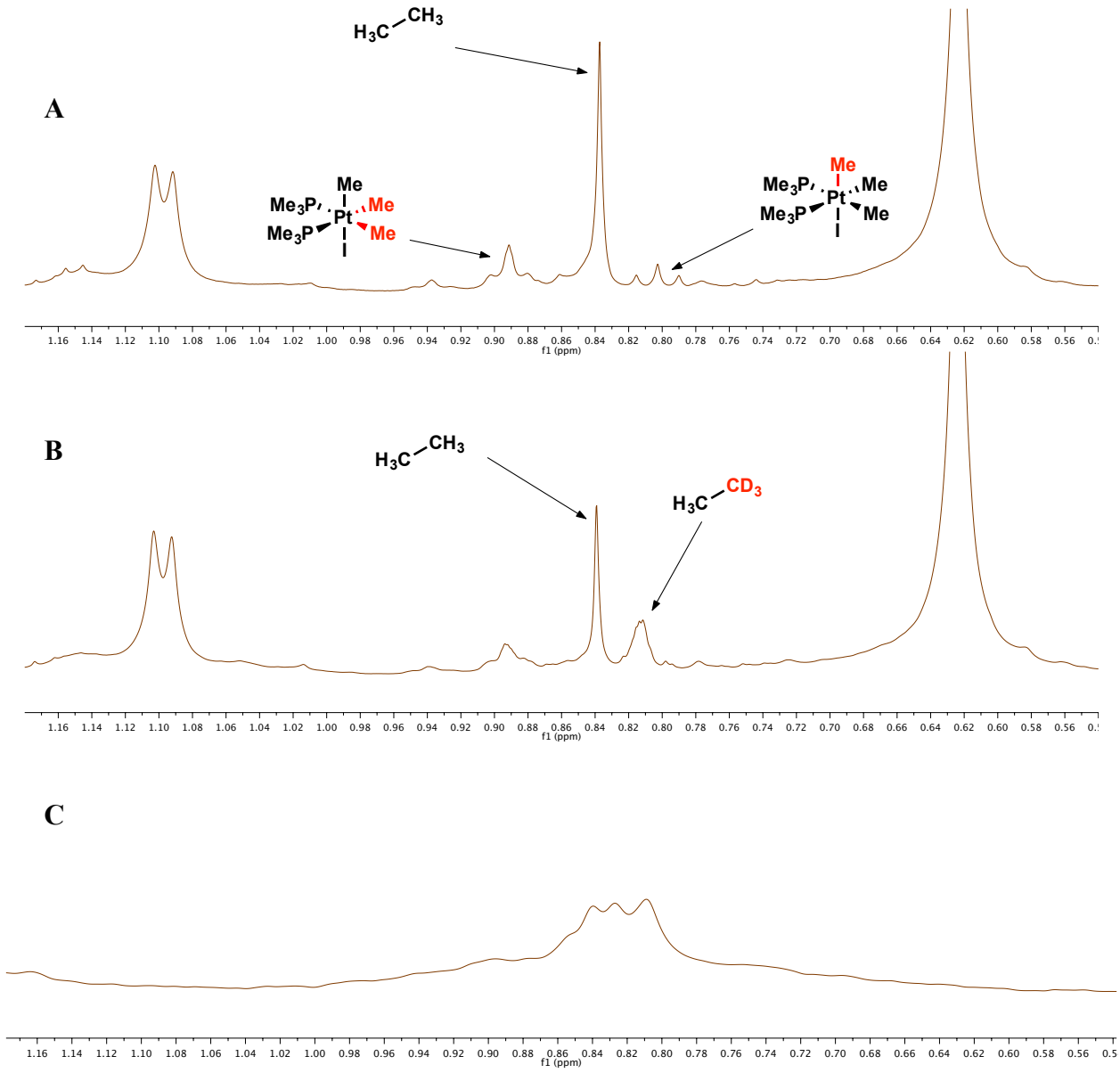

Figure 3.40. Iodomethane labeling experiment. (**A**) Proton NMR spectrum of dual catalytic cross coupling with proteomethyl iodide starting material. Only H_6-ethane is detectable. (**B**) Proton NMR spectrum of coupling with trideuteromethyl iodide starting material. Both H_6-ethane and d_3-ethane are detectable (**C**) Deuterium NMR spectrum of coupling with trideuteromethyl iodide starting material. Peaks at 0.82 ppm are consistent with a mixture of d_3-ethane and d_6-ethane.

Copasi Model:

Global kinetic modeling was performed using COPASI modeling software (http://www.copasi.org). These individual rate constants do not have have any intrinsic significance as the number of kinetic constants being fit results in this model being underdetermined (7 observables and 11 parameters). Rather, this is meant to demonstrate that it is *possible for the proposed mechanism to yield kinetics with the same overall characteristics as those experimentally observed*.

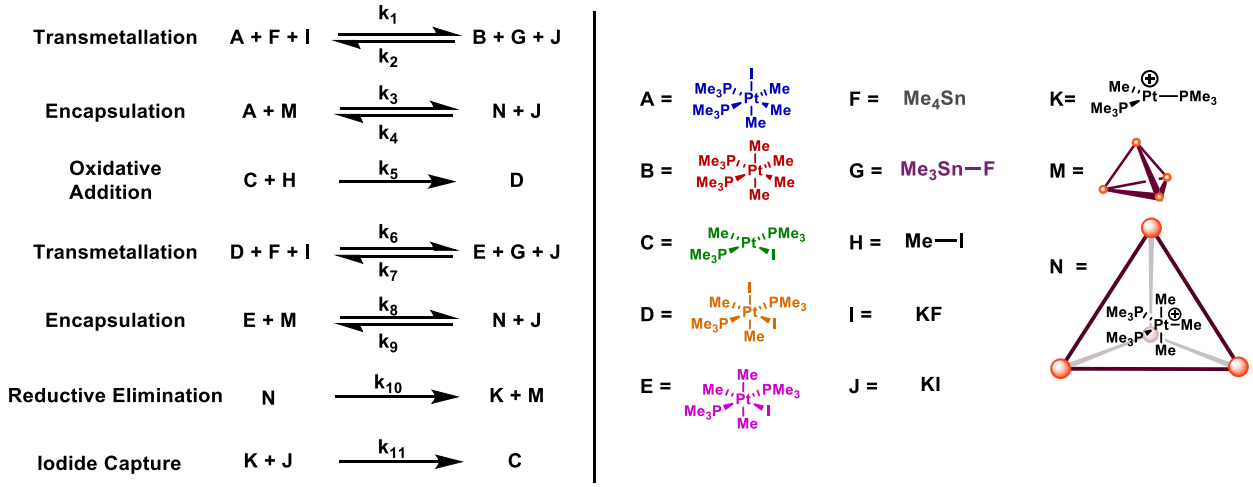

Figure 3.41. Copasi Model

Parameter estimation was performed on k_1- k_{10} with the constraints of $0.001 < k_5 < 0.1$, based on the measured rate for oxidative addition under similar conditions of 0.010 $M^{-1}s^{-1}$ and $0.002 < k_{10} < 0.2$ based on the measured k_{cat} at 40°C with supramolecular catalyst **1** of 0.024 s^{-1}. (In the former case, the supramolecular assembly **2** is expected to exert a salt effect slowing oxidative addition, and in the latter, the higher temperature and different supramolecular assembly were expected to increase k_{10}, though neither of the absolute numbers obtained for the fitted data should be interpreted with particular significance). The model was optimized using the Evolutionary Strategy (SRES) method to yield the kinetic constants in Table S1, and the starting values were randomized several times to counteract false minima. Most repetitions of the simulation converged to the given values after several iterations of optimization. The simulation results for **9**, **10**, **23**, **24**, iodomethane, tetramethyl tin, and trimethyltin fluoride are shown below.

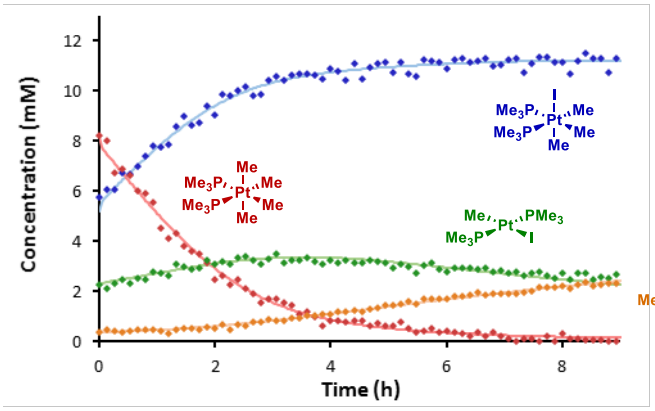

Figure 3.42. COPASI Model of Platinum Speciation. Points represent measured data, lines represent the fitted model.

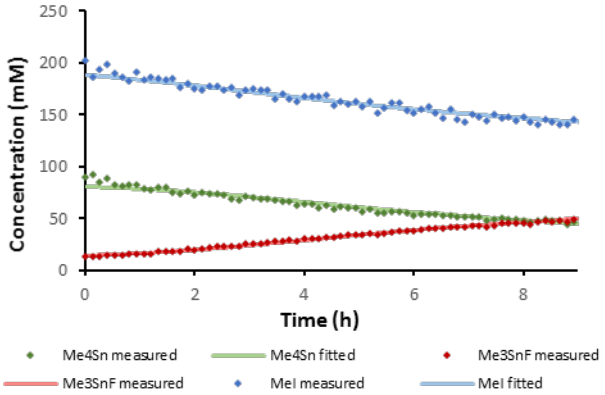

Figure 3.33. [Sn] and MeI concentrations modeled by COPASI compared to measured values

Table 3.1. Fitted parameters from COPASI model of the dual catalytic reaction.

Rate Constant	Fitted Value
9 + **2** → [**Pt**] ⊂ **2** + KI	3.54×10^{-4} $M^{-1}s^{-1}$
[**Pt**] ⊂ **2** + KI → **9** + **2**	2.56 $M^{-1}s^{-1}$
9 + Me_4Sn + KF → **23** + Me_3SnF + KI	13.3 $M^{-2}s^{-1}$
23 + Me_3SnF + KI → **9** + Me_4Sn + KF	5.89×10^{3} $M^{-2}s^{-1}$
10 + MeI → **25**	2.93×10^{-3} $M^{-1}s^{-1}$
[**Pt**] ⊂ **2** → [**K**] + **2** (k_{cat})	0.296 s^{-1}
25 + **2** → [**Pt**] ⊂ **2** + KI	6.16×10^{3} $M^{-1}s^{-1}$
[**Pt**] ⊂ **2** + KI → **25** + **2**	1.00×10^{-4} $M^{-1}s^{-1}$
24 + Me_4Sn + KF → **25** + Me_3SnF + KI	0.154 $M^{-2}s^{-1}$
25 + Me_3SnF + KI → **26** + Me_4Sn + KF	9.54×10^{5} $M^{-2}s^{-1}$
[**K**] + **KI** → **10**	118 $M^{-1}s^{-1}$

In order to account for iodide association to the Pt(II) cation formed upon reductive elimination without introducing a dependence on iodide concentration in k_{cat}, an additional irreversible iodide capture step was incorporated into the model following reductive elimination (not shown above).

Single Crystal X-ray Crystallography of **6** ⊂ **1**

A yellow block crystal with the dimensions of approximately 0.01 x 0.01 x 0.005 mm was grown by slow vapor diffusion of acetone into a solution of the complex in 1:1 water and methanol. The crystal was mounted and single-crystal X-ray data were collected at 100 K on a Bruker D8 with PHOTON 100 detector. Synchrotron radiation at 1.22760 Å was used for data collection and the diffraction measurement method was φ and ω shutterless scans. The structure was solved using direct methods and refined by full-matrix least squares on F^2. Non-hydrogen atoms were refined with anisotropic displacement parameters and hydrogen atoms were placed following a riding model of the attached atom. All refinements were carried out using the SHELXL-2014 software package.

Crystal growth of this complex proved to be challenging and the obtained crystals suffered from high degrees of disorder. Synchrotron radiation was necessary for data collection up to 0.88 Å with 93.8% completeness, however, the model contains irregularities such as large thermal parameters and prolate atoms. Attempts to include complete solvent molecules in the final model yielded unsatisfactory results. Instead, 16 placeholder oxygen atoms were modeled as chelating the 8 potassium ions to represent disordered water and methanol. The final chemical formula has been adjusted with 32 additional hydrogen atoms to represent the 16 placeholder oxygen atoms as water. In addition, the unit cell featured 6106.3 $Å^3$ of disordered solvent channels (25.7% of the total unit cell). This residual electron density could not be further modeled and was treated with the Squeeze algorithm of the PLATON package to correct 1777 unresolved electrons within the void. It should also be noted that the data suggest a small twinned domain from the C-orthorhombic pseudo cell, but accounting for this in the model gave little to no improvements. Therefore, the final model is presented without twinning considerations. Although the model suffers from deficiencies, it is sufficient for the purposes of demonstrating atom connectivity and the encapsulation of **6** in **1**.

Crystal data and structure refinement for **6** $\subset$ **1**.

Identification code	shelx
Empirical formula	C_{152} H_{140} Au Ga_4 K_8 N_{12} O_{52} P_2
Formula weight	3817.37
Temperature	100(2) K
Wavelength	1.2276 Å
Crystal system, space group	Monoclinic, P 21/c
Unit cell dimensions	a = 19.9478(10) Å alpha = 90 deg. b = 60.836(3) Å beta = 118.988(2) deg. c = 19.5518(11) Å gamma = 90 deg.
Volume	20754.5(19) $Å^3$
Z, Calculated density	4, 1.176 Mg/m^3
Absorption coefficient	1.935 mm^{-1}
F(000)	7405
Crystal size	0.010 x 0.010 x 0.005 mm
Theta range for data collection	2.137 to 44.033 deg.
Limiting indices	-22<=h<=18, -68<=k<=68, -19<=l<=21
Reflections collected / unique	63064 / 29588 [R(int) = 0.0486]
Completeness to theta = 44.000	93.8 %
Refinement method	Full-matrix least-squares on F^2
Data / restraints / parameters	29588 / 0 / 2072
Goodness-of-fit on F^2	1.112
Final R indices [I>2sigma(I)]	R1 = 0.1570, wR2 = 0.3706
R indices (all data)	R1 = 0.1739, wR2 = 0.3818
Extinction coefficient	n/a
Largest diff. peak and hole	5.676 and -1.644 e.A^-3

3.6 References

(1) Hartwig, J. F. Organotransition Metal Chemistry: From Bonding to Catalysis; University Science Books, 2010.

(2) For reviews on ligand effects on transition metal catalysis: (a) Tolman, C. A. *Chem. Rev*. **1977**, *77*, 313. (b) Berrisford, D. J.; Bolm, C.; Sharpless, K. B. *Angew. Chem. Int. Ed. Engl.* **1995**, *34*, 1059. (c) van Leeuwen, P. W. N. M.; Kamer, P. C. J.; Reek, J. N. H.; Dierkes, P. *Chem. Rev.* **2000**, *100*, 2741. (d) Surry, D. S.; Buchwald, S. L. *Angew. Chem. Int. Ed.* **2008**, *47*, 6338. (e) Hartwig, J. F. *Acc. Chem. Res.* **2008**, *41*, 1534. (f) Fu, G. C. *Acc. Chem. Res.* **2008**, *41*, 1555.

(3) For reviews on supramolecular microenvironment catalysis: (a) Cram, D. J.; Cram, J. M. *Science* **1974**, *183*, 803. (b) Meeuwissen, J.; Reek, J. N. H. *Nat. Chem*. **2010**, *2*, 615. (c) Brown, C. J.; Toste, F. D.; Bergman, R. G.; Raymond, K. N. *Chem. Rev*. **2015**, *115,* 3012. (d) Yoshizawa, M.; Klosterman, J. K.; Fujita, M. *Angew. Chem. Int. Ed.* **2009**, *48*, 3418. (e) Catti, L.; Zhang, Q.; Tiefenbacher, K. *Synthesis* **2016**, *48*, 3113. For reviews related to non-covalent interaction is catalysis: (f) Zhao, Y.; Cotelle,Y.; Sakai, N.; Matile, S. *J. Am. Chem. Soc.* **2016**, *138*, 4270. (g) Knowles, R. R.; Jacobsen, E. J. *PNAS* **2010**, *107*, 20678. (h) Wheeler, S. E.; Seguin, T. J.; Guan, Y.; Doney, A. C. *Acc. Chem. Res.* **2016**, *49*, 1061.

(4) Selected examples of supramolecular microenvironment catalysis: (a) Salles, A. G.; Zarra, S.; Turner, R. M.; Nitschke, J. R. *J. Am. Chem. Soc*. **2013**, *135,* 19143. (b) Yoshizawa, M.; Tamura, M.; Fujita, M. *Science* **2006**, *312*, 251. (c) Cullen, W.; Misuraca, M. C.; Hunter, C. A.; Williams, N. H.; Ward, M. D. *Nat Chem* **2016**, *8 (3)*, 231. (d) Zhang, Q.; Tiefenbacher, K. *Nat Chem* **2015**, *7*, 197.

(5) Wang, Z. J.; Brown, C. J.; Bergman, R. G.; Raymond, K. N.; Toste, F. D. *J. Am. Chem. Soc.* **2011**, *133*, 7358.

(6) Wang, Z. J.; Clary, K. N.; Bergman, R. G.; Raymond, K. N.; Toste, F. D. *Nat. Chem.* **2013**, *5*, 100.

(7) Fiedler, D.; Bergman, R. G.; Raymond, K. N. *Angew. Chem. Int. Ed.* **2006**, *45*, 745.

(8) Jana, R.; Pathak, T. P.; Sigman, S. *Chem. Rev.* **2011**, *111*, 1417.

(9) Wolf, W. J.; Winston, M. S.; Toste, F. D. *Nat. Chem.* **2014**, *6*, 159.

(10) Komiya, S.; Kochi, J. K. *J. Am. Chem. Soc.* **1976**, *98*, 7599.

(11) Kuch, P. L.; Tobias, R. S. *J. Organomet. Chem.* **1976**, *122*, 429.

(12) Leung, D. H.; Fiedler, D.; Bergman, R. G.; Raymond, K. N. *Angew. Chem. Int. Ed.* **2004**, *43*, 963.

(13) Mecozzi, S.; Rebek, J., Jr. *Chem. – Eur. J.* **1998**, *4*, 1016.

(14) Blackmond, D. G. *Angew. Chem. Int. Ed.* **2005**, *44*, 4302.

(15) R. B. Silverman, *The Organic Chemistry of Enzyme-Catalyzed Reactions* (Academic Press, 2002) 15.

(16) Biros, S. M.; Bergman, R. G.; Raymond, K. N. *J. Am. Chem. Soc*. **2007**, *129*, 12094.

(17) Sgarlata, C.; Mugridge, J. S.; Pluth, M. D.; Tiedemann, B. E. F.; Zito, V.; Arena, G.; Raymond, K. *J. Am. Chem. Soc.* **2010**, *132*, 1005.

(18) For size exclusion in enzymes: (a) Koshland, D. E. *Proc. Natl. Acad. Sci.* **1958**, *44*, 98. (b) Johnson, K. A. *J. Biol. Chem.* **2008**, *283*, 26297.

(19) To calculate the heterolytic bond strengths, the differences in homolytic bond strengths were combined with the differences in electron affinity for the halides, treating the dissociated neutral atoms as isoenergetic. The ionization potential of gold can be omitted

from the calculation because the energies are relative. The results are that in a heterolytic sense, the Au–Cl bond is approximately 9 kcal/mol stronger than the Au–Br bond which is approximately 11 kcal/mol more stable than the Au–I bond. For the Au(III) BDE: (a) Winston, M. S.; Wolf, W. J.; Toste, F. D. *J. Am. Chem. Soc.* **2015**, *137*, 7921. For the electron affinities of Cl, Br, and I: (b) Berzinsh, U.; Gustafsson, M.; Hanstorp, D.; Klinkmueller, A.; Ljungblad, U.; Martensson-Pendrill, A.-M. *Phys Rev A* **1995**, *50*, 231-238. (c) Blondel, C.; Cacciani, P.; Delsart, C.; Trainham, R. *Phys Rev A* **1989**, *40*, 3698-3701. (d) Pelaez, R.J.; Blondel, C.; Delsart, C.; Drag, C. *J. Phys. B: At. Mol. Opt. Phys.* **2009**, *42*, 125001-125007.

(20) (a) Slansky, C. M. *J. Am. Chem. Soc.* **1940**, *62*, 2430. (b) Morris, D. F. C. Structure and Bonding; Springer Berlin Heidelberg: Berlin, Heidelberg, **1968**; pp 63–82.

(21) Brown, M. P.; Puddephatt, R. J.; Upton, C. E. E.; Lavington, S. W. *J. Chem. Soc. Dalton Trans.* **1974**, *15*, 1613.

(22) (a) Komiya, S.; Kochi, J. K. *J. Am. Chem. Soc.* **1976**, *98*, 7599. (b) Komiya, S.; Albright, T. A.; Hoffmann, R.; Kochi, J. K. *J. Am. Chem. Soc.* **1976**, *98*, 7255. (c) Tamaki, A.; Kochi, J. K. *J. Organomet. Chem.* **1974**, *64 (3)*, 411. (d) Tamaki, A.; Kochi, J. K. *J. Organomet. Chem.* **1972**, *40*, C81.

(23) For d^8 metal reductive elimination: (a) Wolf, W. J.; Winston, M. S.; Toste, F. D. *Nat. Chem.* **2014**, *6*, 159. (b) Tatsumi, K.; Hoffmann, R.; Yamamoto, A.; Stille, J. K. *Bull. Chem. Soc. Jpn.* **1981**, *54*, 1857. (c) Gillie, A.; Stille, J. K. *J. Am. Chem. Soc.* **1980**, *102*, 4933. (d) Levin, M. D.; Toste, F. D. *Angew. Chem. Int. Ed.* **2014**, *53*, 6211. (e) Joost, M.; Amgoune, A.; Bourissou, D. *Angew. Chem. Int. Ed.* **2015**, *54*, 15022.

(24) For d^6 metal reductive elimination: (a) Roy, S.; Puddephatt, R. J.; Scott, J. D. *J. Chem. Soc. Dalton Trans.* **1989**, *11*, 2121. (b) Crumpton-Bregel, D. M.; Goldberg, K. I. *J. Am. Chem. Soc.* **2003**, *125*, 9442. (c) Deutsch, P. P.; Eisenberg, R. *J. Am. Chem. Soc.* **1990**, *112*, 714. (d) Buchanan, J. M.; Stryker, J. M.; Bergman, R. G. *J. Am. Chem. Soc.* **1986**, *108*, 1537. (e) Harper, T. G. P.; Desrosiers, P. J.; Flood, T. C. *Organometallics* **1990**, *9*, 2523.

(25) (a) Forniés, J.; Gómez-Saso, M. A.; Martín, A.; Martínez, F.; Menjón, B.; Navarrete, J. *Organometallics* **1997**, *16*, 6024. (b) Scott, J. D.; Puddephatt, R. J. *Organometallics* **1986**, *5*, 1253. (c) Howard, W. A.; Bergman, R. G. *Polyhedron* **1998**, *17*, 803. (d) Martínez-Salvador, S.; Forniés, J.; Martín, A.; Menjón, B. *Chem. – Eur. J.* **2011**, *17*, 8085.

(26) Brown, M. P.; Puddephatt, R. J.; Upton, C. E. E.; Lavington, S. W. *J. Chem. Soc. Dalton Trans.* **1974**, *15*, 1613.

(27) Allen, A. E.; MacMillan, D. W. C *Chem. Sci.* **2012**, *3*, 633.

(28) Zhao, C.; Sun, Q.; Hart-Cooper, W. M.; DiPasquale, A. G.; Toste, F. D.; Bergman, R. G.; Raymond, K. N. *J. Am. Chem. Soc.* **2013**, *135*, 18802.

(29) Hart-Cooper, W. M.; Zhao, C.; Triano, R. M.; Yaghoubi, P.; Ozores, H. L.; Burford, K. N.; Toste, F. D.; Bergman, R. G.; Raymond, K. N. *Chem. Sci.* **2015**, *6*, 1383.

(30) Seechurn, C. C. C. J.; Kitching, M. O.; Colacot, T. J.; Snieckus, V. *Angew. Che. Int. Ed.* **2012**, *51*, 5062.

(31) Examples of alkyl stannane transmetallation to Pt: (a) Romeo, R.; Scolaro, L. M.; Catalano, V.; Achar, S. *Inorganic Syntheses*; John Wiley & Sons, Inc., **2007**; pp 153–158. (b) Clark, H. C.; Goel, A. B.; Jain, V. K.; Tyers, K. G.; Wong, C. S. *J. Organomet. Chem.* **1987**, *321*, 123. (c) Rakowsky, M. H.; Woolcock, J. C.; Rettig, M. F.; Wing, R. M. *Organometallics* **1988**, *7*, 2149. (d) Dekker, G. P. C. M.; Buijs, A.; Elsevier, C. J.; Vrieze,

K.; Van Leeuwen, P. W. N. M.; Smeets, W. J. J.; Spek, A. L.; Wang, Y. F.; Stam, C. H. *Organometallics* **1992**, *11*, 1937. (e) Nilsson, P.; Plamper, F.; Wendt, O. F. *Organometallics* **2003**, *22*, 5235.
(32) (a) Hux, J. E.; Puddephatt, R. J. *Inorganica Chim. Acta* **1985**, *100*, 1. (b) Lashanizadehgan, M.; Rashidi, M.; Hux, J. E.; Puddephatt, R. J.; Ling, S. S. M. *J. Organomet. Chem.* **1984**, *269*, 317.
(33) (a) Herzog, A.; Liu, F.-Q.; Roesky, H. W.; Demsar, A.; Keller, K.; Noltemeyer, M.; Pauer, F. *Organometallics* **1994**, *13*, 1251. (b) Vela, J.; Smith, J. M.; Yu, Y.; Ketterer, N. A.; Flaschenriem, C. J.; Lachicotte, R. J.; Holland, P. L. *J. Am. Chem. Soc.* **2005**, *127*, 7857. (c) Ding, K.; Dugan, T. R.; Brennessel, W. W.; Bill, E.; Holland, P. L. *Organometallics* **2009**, *28*, 6650.
(34) Hoops, S.; Sahle, S.; Gauges, R.; Lee, C.; Pahle, J.; Simus, N.; Singhal, M.; Xu, L.; Mendes, P.; Kummer, U. *Bioinformatics* **2006**, *22*, 3067.
(35) Pluth, M. D.; Bergman, R. G.; Raymond, K. N. *J. Am. Chem. Soc.* **2007**, *129*, 11459.
(36) (a) Hill, G. S.; Puddephatt, R. J. *Organometallics* **1997**, *16*, 4522. (b) Hill, G. S.; Yap, G. P. A.; Puddephatt, R. J. *Organometallics* **1999**, *18*, 1408.
(37) Schuster, O.; Schmidbaur, H. *Naturforschung B.* **2006**, *61*, 1.

Chapter 4

Evidence for the Conformational Selection Mechanism of Guest Binding in a self-assembled M_4L_4 Supramolecular Cluster

4.1 Preface

While chapters 2 and 3 focused on expanding the scope of transition state motifs catalytically recognized by the Raymond supramolecular cluster, chapter 4 will focus on the mechanism of guest encapsulation for a related M_4L_4 assembly. Namely, this work describes evidence supporting the mechanism of conformational selection (as opposed to induced fit) for the binding of guest molecules in a novel class of self-assembled M_4L_4 tetrahedra. The initial motivation of this work was to explore M_4L_4 assemblies as an alternative to the M_4L_6 cluster stoichiometry, which suffers from the tendency to form the entropically-favored M_2L_3 helicate if the ligand geometry is not precisely tuned. A comprehensive study of this simple system provides insight into analogous behavior in biophysics and enzymology, as well as important information to support future efforts in the design of more efficient self-assembled microenvironment catalysts. This work was performed in collaboration with graduate student Cynthia M. Hong.

4.2 Introduction

The understanding of protein–ligand molecular recognition is of paramount importance to the study of enzymatic catalysis and allosteric regulation of cell signaling pathways, as well as to the design of more efficient drug molecules.[1] In 1894, Emil Fischer postulated the lock-and-key model of ligand binding to explain the high levels of specificity observed in enzymatic catalysis.[2] Koshland supplanted the lock-and-key model by introducing the "induced fit" hypothesis of enzyme-substrate interaction in 1958.[3] This theory, also referred to as the Koshland-Nemethy-Filmer model, stipulates that a protein encounters its ligand in an inactive state, and an optimum fit is achieved only after a structural rearrangement is induced by interaction with the ligand. Eight years later, in 1965, Chagneux et al. proposed an alternative mechanism for ligand recognition referred to as "conformational selection", or the Monod-Wyman-Chagneux model.[4] This mechanistic hypothesis suggests that the enzyme exists in solution as a dynamic set of Boltzmann populated conformations, and the ligand selectively interacts with the active conformation of the protein to form the ligated complex (Figure 4.1).

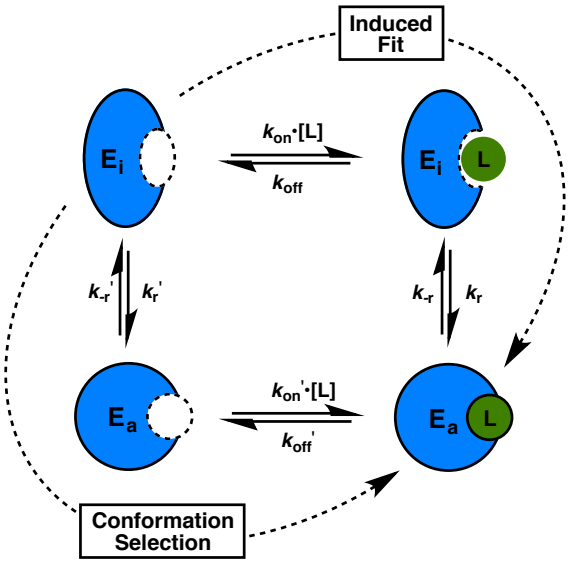

Figure 4.1. Induced fit and conformational selection mechanisms for ligand binding.

As recently as 2008, conformational selection was considered by some to be a fringe mechanism, with very few definitive examples previously reported in the literature.[5] However, recent advances in single molecule fluorescence[6,7] and NMR relaxation[8,9] techniques have resulted in the accumulation of significant evidence in support of conformational selection as a dominant mechanism for protein-ligand interaction.[1,10] While indirect evidence in support of conformational selection can be garnered by techniques including crystallographic analysis, selective mutation of receptors, and *in silico* molecular dynamics, the most compelling evidence to distinguish the induced fit and conformational selection mechanisms comes from the substrate concentration dependence on the relaxation rate as the binding event approaches equilibrium. The general mechanisms and rate constants for approach to equilibrium for the concerted, induced fit, and conformational selection models of ligand binding are depicted in Table 4.1.

The simplest model of the binding, as seen in the lock and key hypothesis, is described by a concerted binding mechanism (Table 4.1, Mechanism A). In this mechanism, the binding of a ligand (L) to its biological target (E) to form ligated complex (EL) occurs in a single-step reversible process, with the association event described by second order rate constant k_{on} and the reverse reaction described by first order rate constant k_{off}. For a reversible, single-step unimolecular reaction the observed rate constant for approach to equilibrium is the sum of the forward and backward rate constants for that process. (The derivation for this potentially counterintuitive result is replicated in the supporting information below.) In the concerted binding mechanism, if the ligand concentration is large compared to protein concentration ([L]>>[E]), then the forward reaction becomes pseudo-first order, and the rate constant for approach to equilibrium is expressed as $k_{obs} = k_{on}[L] + k_{off}$ (Table 4.1, Equation 4.1). A binding event for which the concerted mechanism dominates would display a linear dependence between relaxation rate and ligand concentration (Figure 4.2).

The mechanisms for induced fit and conformational selection (Table 4.1, Mechanisms B and C) each consist of two consecutive reversible reactions, and a complete description of their respective rate laws is beyond simple analysis, and can be found elsewhere.[11] However, if the simplifying assumption is made that ligand binding is fast and reversible on the timescale of the conformational change, an approximate rate constant for the approach to equilibrium can be derived. This "rapid equilibrium approximation" prevails in many cases and is well established in the literature. (Table 4.1, Equations 2 and 3 respectively. See supporting information below for the derivations for equations 2 and 3).[5,12,13]

If ligand binding is fast and reversible compared to isomerization, the two consecutive equilibria can be treated independently. For the induced fit mechanism (Table 4.1, Mechanism B), E_i represents the inactive protein conformation, E_a represents the active conformation, and k_r and k_{-r} represent the forward and reverse rate constants respectively for conformational change. In evaluating the induced fit mechanism, a rate constant for relaxation to equilibrium can be expressed by applying the pseudo-equilibrium approximation to the guest binding step in order to generate an expression for the concentration of intermediate E_iL (in terms of $[E_{i\bullet total}]$ and [L]). This can then be used to express the overall rate constant as the sum of the forward and backward rate constants for conformational change (Table 4.1, Equation 4.2). Notably, the forward reaction shows saturation kinetics in ligand concentration, while the reverse reaction is independent of ligand, resulting in overall saturation behavior in the

relationship between equilibration rate and ligand concentration (Figure 4.2). In contrast, a similar analysis applied to the mechanism for conformational selection reveals that the forward reaction is independent of ligand concentration, while the reverse reaction is inhibited by the ligand. The resulting rate constant (Table 4.1, Equation 4.3) describing the approach to equilibrium under the conformational selection mechanism shows partial inverse order in ligand concentration (Figure 4.2). While surprising, this result has indeed been borne out in the literature.[14–16] It is important to note that not all binding events that proceed *via* conformational selection show ligand inhibition—when the rapid equilibrium approximation does not hold, approximately first order or saturation behavior can be observed. However, if ligand inhibition is observed, the induced fit mechanism can be definitively ruled out in favor of conformational selection. Finally, it is important to note that many biological systems follow a much more complicated mechanism that may incorporate elements of both conformational selection and induced fit.

	Mechanism	Rate Constant (k_{obs})
Concerted Binding	$E \underset{k_{off}}{\overset{k_{on}[L]}{\rightleftharpoons}} EL$ (A)	$k_{on}[L]+k_{off}$ (4.1)
Induced Fit	$E_i \underset{k_{off}}{\overset{k_{on}[L]}{\rightleftharpoons}} E_iL \underset{k_{-r}}{\overset{k_r}{\rightleftharpoons}} E_aL$ (B)	$k_r \frac{[L]}{\frac{k_{off}}{k_{on}}+[L]}+k_{-r}$ (4.2)
Conformational Selection	$E_i \underset{k_{-r}}{\overset{k_r}{\rightleftharpoons}} E_a \underset{k_{off}}{\overset{k_{on}[L]}{\rightleftharpoons}} E_aL$ (C)	$k_r+k_{-r}\frac{1}{1+\frac{k_{on}}{k_{of}}[L]}$ (4.3)

Table 4.1. Mechanism and rate constant for approach to ligand binding equilibrium for concerted binding, induced fit and conformational selection models.

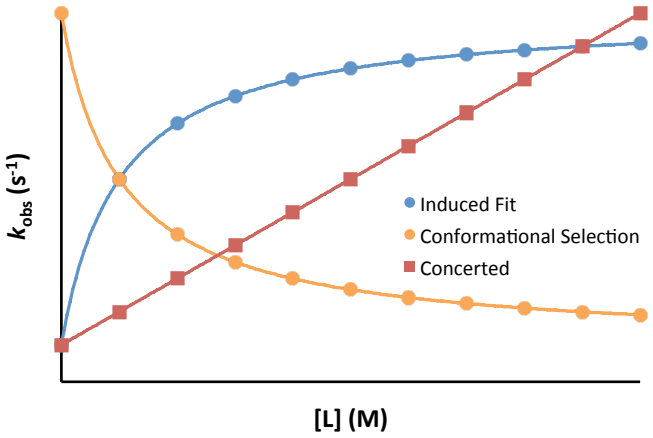

Figure 4.2. Qualitative comparison of observed pseudo-first-order rate constant for approach to ligand binding equilibrium (k_{obs}) as a function of ligand concentration for induced fit (blue dots, ●), conformation selection (orange dots, ●), and concerted binding (red squares, ■).

The field of supramolecular chemistry has grown into a symbiotic relationship with molecular biology. Simple biomimetic supramolecular assemblies act as model systems to provide insight into the underlying stereoelectronic interactions that drive molecular

recognition and enzymatic reactivity in biological systems, and in turn, lessons from biology contribute to the design of synthetic receptors and catalysts. Self-assembled nanovessels including hydrogen bond and metal-ligand based assemblies have been particularly fruitful as a model for the study of molecular recognition and microenvironment catalysis.[17–21]

The Raymond, Toste and Bergman groups have extensively studied the host-guest chemistry and catalytic behavior of $K_{12}Ga_4L_6$ tetrahedral assembly **1** (Figure 4.3A).[22] Assembly **1** is composed of six biscatecholate ligands, bridging four pseudo-octahedral gallium(III) atoms, which display homochirality (ΔΔΔΔ or ΛΛΛΛ), as enforced by mechanical coupling through the ligands. Assembly **1** also shows a range of enzyme-mimetic behaviors including hydrophobic encapsulation of neutral and anionic guests,[23,24] Michaelis-Menten-like mechanisms for a range of catalytic applications with rate accelerations (k_{cat}/k_{uncat}) of up to 1.9 x 10^7 fold,[25–27] unusual product selectivity reminiscent of enzymatic catalysis,[28–30] and even protein-like amide H-D exchange behavior[31]. While cluster **1** has proven especially effective as a supramolecular enzyme mimic, it is inherently limited with respect to the steric and electronic properties of its interior cavity. While some structural analogues of **1** have been reported,[32,33] the synthesis of novel M_4L_6 clusters is hindered by the fact that tetrahedra of M_4L_6 stoichiometry are entropically disfavored relative to the M_2L_3 helicate (Figure 4.3B). Only the carefully tuned geometric offset of the 1,5-substituted naphthalene spacer of the bis-bidentate ligand of **1** prevents fragmentation to the lower stoichiometry helicate. Subtle variation from this structure, such as the substitution of naphthyl to anthracenyl spacer, leads to selective assembly of the helicate.[34]

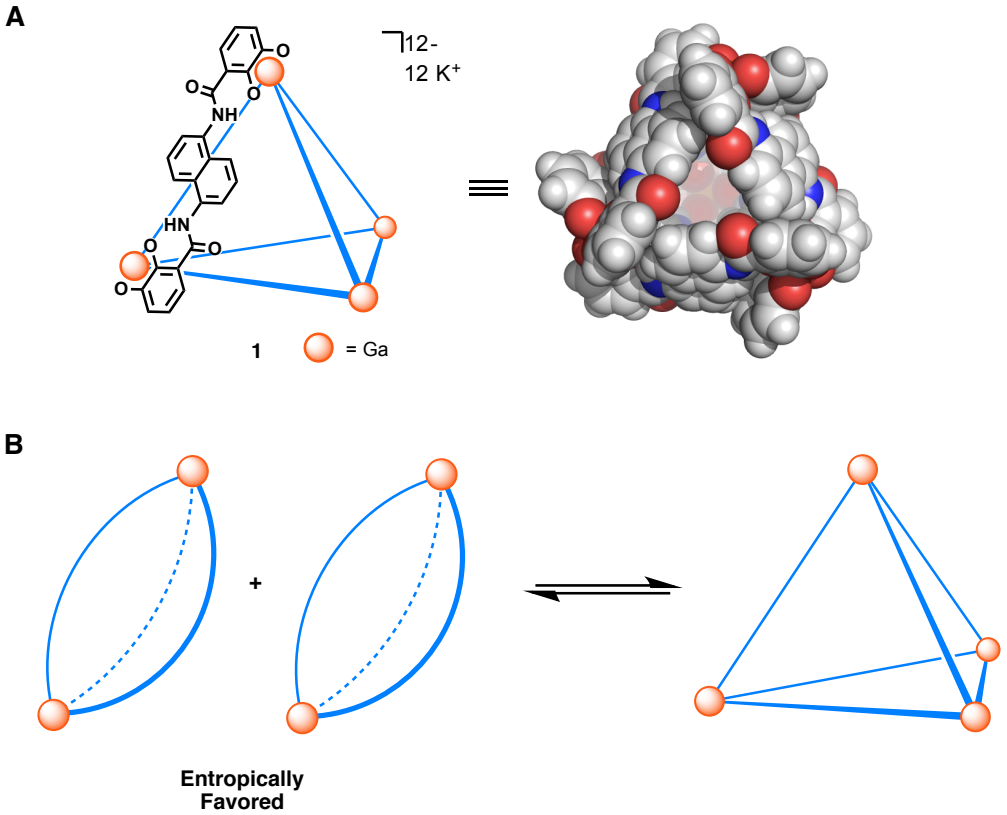

Figure 4.3. (A) M_4L_6 tetrahedral assembly **1**. (B) Helicate / tetrahedron equilibrium.

In contrast, M_4L_4 tetrahedra, assembled from C_3-symmetric tris-bidentate ligands, do not suffer from this entropic complication, so long as they are sufficiently rigid to prevent mononuclear chelation. The Raymond group has previously reported the synthesis of *T*-symmetric M_4L_4 cluster **2** (Figure 4.4); however, the scope of host-guest chemistry observed with **2** was extremely limited in comparison with cluster **1**, despite their similar internal volume.[35] It was hypothesized that the disparity in encapsulation behavior between hosts **1** and **2** might be attributed to a difference in the innate flexibility, or "breathability" of their cavity structures. In much the same way that a protein must undergo a configurational change in order to accommodate and conform to the structure of its ligand (*vide supra*), so too must supramolecular hosts conform to complement their guest molecules in order for optimal binding to occur. The amide substitution on the naphthalene linker for cluster **1** is offset from the center of the ligand, which allows the internal cavity of **1** to expand and contract through rotation of the amide-aryl nitrogen-carbon bond. This is evidenced by the observation that, depending on the nature of the encapsulated guest, the interior cavity volume of **1** ranges from 253 to 435 $Å^3$, as determined by examination of their respective solid-state crystal structures.[36] In contrast, the three amide-aryl bonds for the ligand of cluster **2** are oriented directly toward the center of three-fold symmetry for the ligand. As a result, rotation about the amide-aryl bond cannot contribute to the breathability of cluster **2**, and any structural accommodation of guest molecules must occur predominantly by bond distention, which is enthalpically costly. It was hypothesized that the introduction of rotational flexibility to the M_4L_4 structural manifold might restore the "breathability" required for efficient guest encapsulation, while maintaining the benefits of entropic stability.

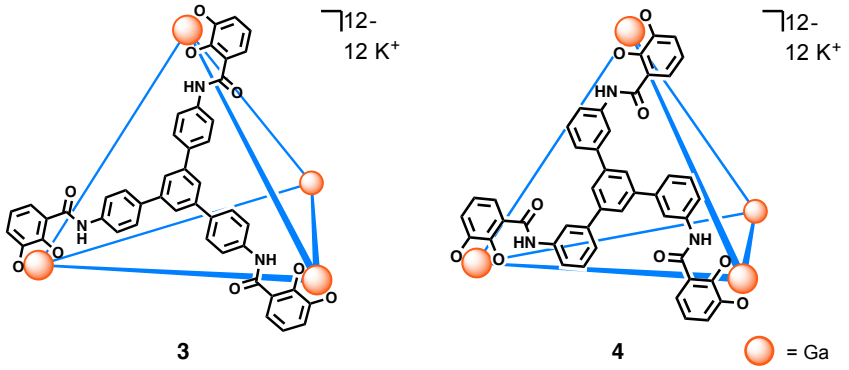

Figure 4.4. M_4L_4 clusters **2** (*para*-substituted) and **3** (*meta*-substituted)

4.3 Results and Discussion

4.3.1 Synthesis of a Flexible M_4L_4 Host

In accordance with the hypothesis that rotational flexibility is essential for efficient guest encapsulation, tetrahedral cluster **3** was selected as a synthetic target (Figure 4.4). Cluster **3** is isomeric to **2**, differing only in the *meta*-substitution of the trianiline linker that generates the three-fold symmetry of the ligand (as opposed to *para*-substitution in **2**). *Meta*-substitution introduces 60 degrees of curvature in each arm of the ligand and offsets the metal binding moiety from the center of the ligand, potentially rendering **3** sufficiently flexible to conform to its guest molecules without incurring a significant enthalpic penalty.

Synthetic access to ligand **4**, the precursor for self-assembly of cluster **3**, was achieved in a manner similar to the ligand precursor to cluster **2** (Scheme 4.1).[35] 3-nitroacetophenone (**5**) underwent dehydrative trimerization by the addition of dry potassium pyrosulfate to molten **5** at 100 ºC, followed by the addition of catalytic sulfuric acid to afford 1,3,5-tris(3'-nitrophenyl)benzene (**6**). Trianiline **7** could be accessed by tin/HCl reduction of **6**, which was then acylated with 3.2 equivalents of 2,3-dimethoxybenzoyl chloride (freshly prepared from the corresponding carboxylic acid) and excess triethylamine, yielding the hexamethyl-protected ligand, **8**. Finally, the deprotected ligand (**4**) was accessed by treatment of **8** with excess boron tribromide at -78 ºC, followed by suspension of the crude product in water at reflux for 12 hours to hydrolyze any boronic esters formed in the deprotection.

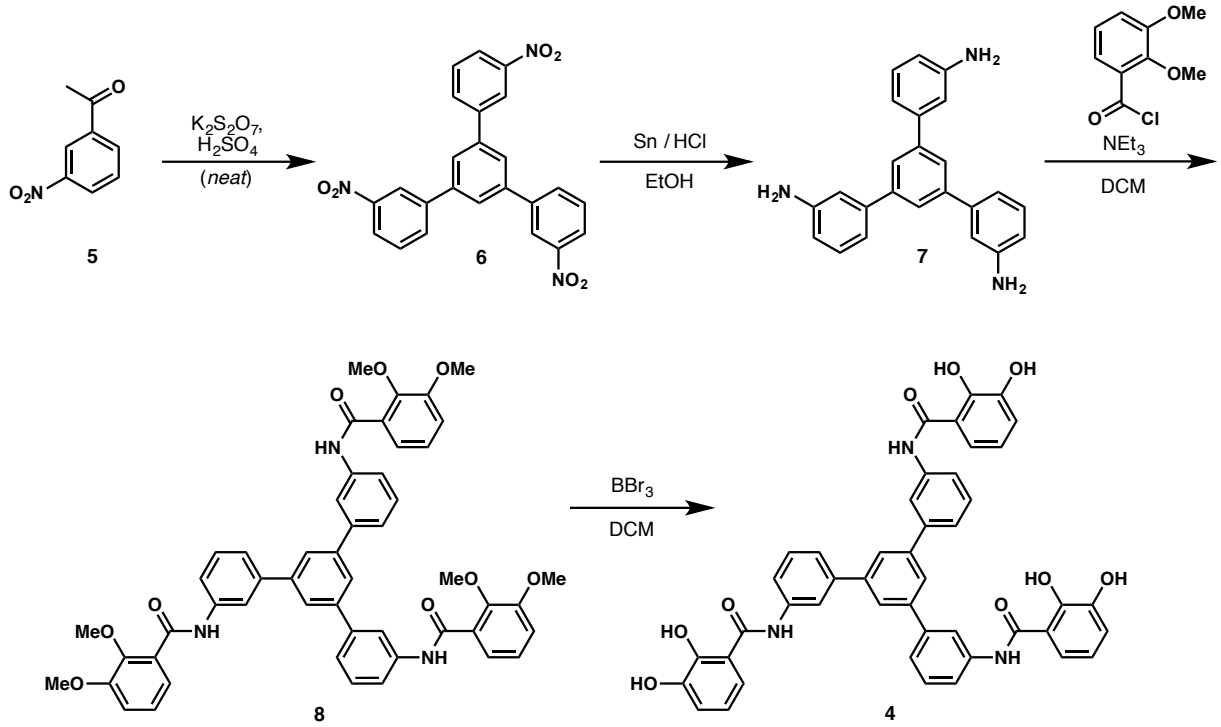

Scheme 4.1. Synthesis of ligand **4**, self-assembly precursor to **3**.

With ligand **4** in hand, the assembly of cluster **3** was attempted under conditions identical to those employed for the formation of **2**. Ligand **4** and $Ga(acac)_3$ in equimolar quantities were suspended in degassed methanol, followed by the addition of three equivalents of potassium hydroxide as a solution in methanol, resulting in spontaneous self-assembly to form a single species, assigned as cluster **3**, which could be isolated by precipitation with acetone. Unexpectedly, inspection of the resulting assembly by ^{1}H-NMR spectroscopy revealed the presence of 24 unique proton resonances, which is inconsistent with the 8 unique chemical environments expected for an M_4L_4 cluster of tetrahedral symmetry (Figure 4.5). This low symmetry species was persistent, even upon heating in methanol for several days. Furthermore, the addition of potential guest molecule tetraethylphosphonium iodide resulted in a rapid reduction in the number of observed proton resonances from 24 to 8, along with the appearance of two new resonances at about -0.5 ppm and -1.5 ppm, consistent with an encapsulated molecule of tetraethylphosphonium shifted upfield by close contact with the aromatic ring currents of the cluster walls. These observations were consistent with the

formation of *T*-symmetric M_4L_4 inclusion complex $PEt_4^+ \subset$ **3** upon the addition of the guest; however, the structure of the initially formed low symmetry species remained unclear.

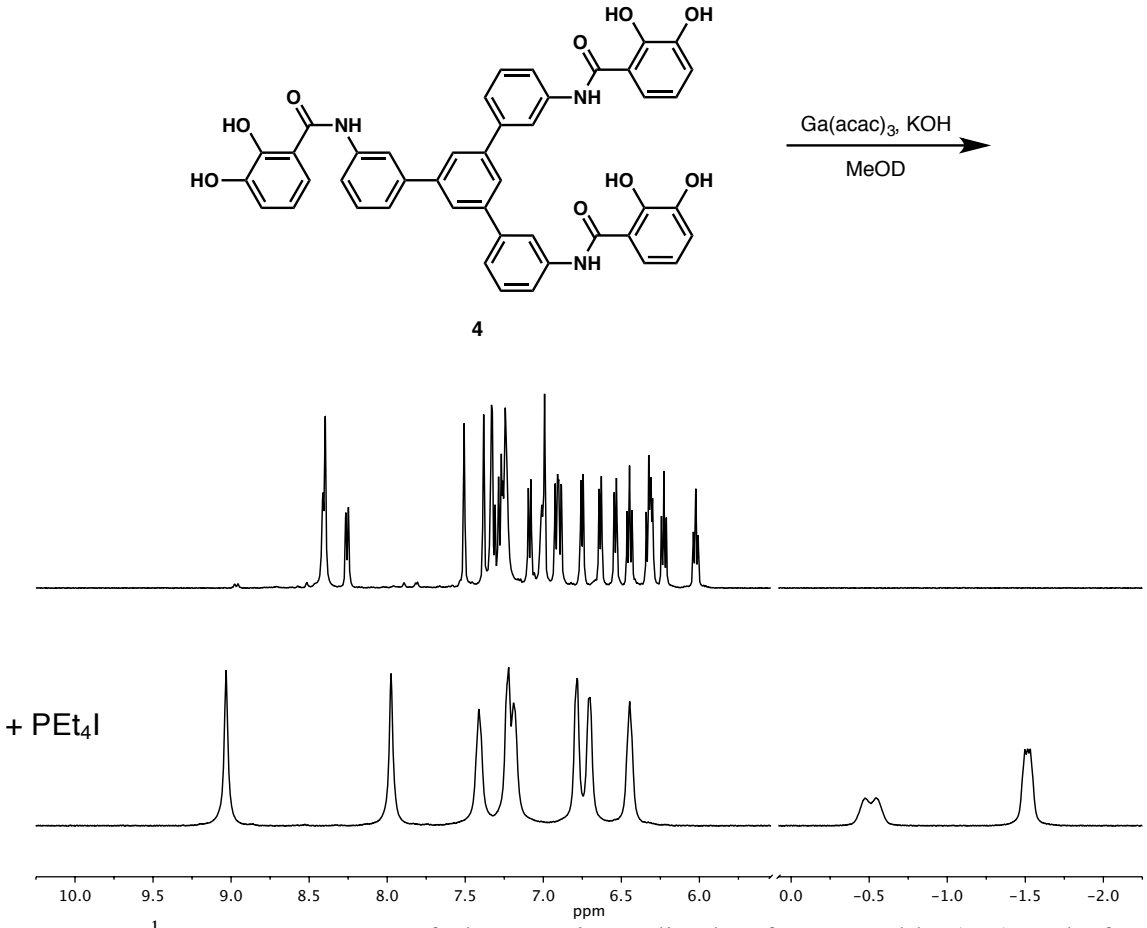

Figure 4.5. ^{1}H-NMR spectrum of cluster **3** immediately after assembly (top) and after the addition of approximately 1.5 equivalents of tetraethylphosphonium iodide (bottom).

4.3.2 Characterization of Host 3 and its Conformational Dynamics

Three potential structures might explain the low symmetry spectrum observed for empty cluster **3**. First, the increased flexibility of ligand **4** might alleviate the mechanical coupling that enforces homochirality of the gallium metal centers in clusters **1** and **2**—if this is the case, then, in the absence of a guest, assembly **3** might prefer the mixed chirality, ΔΔΛΛ isomer. This mixed chirality might be more conducive to a "collapsed" assembly, minimizing the available internal volume and by extension, the number of energetically costly restricted solvent molecules trapped in the empty cluster cavity. Mixed ΔΔΛΛ metal center chirality would desymmetrize the cluster from *T*-symmetry to S_4-symmetry, which would explain the three-fold increase in unique proton chemical environments. While the majority of M_4L_4 and M_4L_6 tetrahedra exhibit *T*-symmetry due to mechanical coupling between the vertices, several examples of M_4L_6 assemblies have been reported to exist as nearly statistical mixtures of *T*-symmetric (ΔΔΔΔ/ΛΛΛΛ), C_3-symmetric (ΛΔΔΔ/ΛΛΛΔ), and S_4-symmetric (ΔΔΛΛ) structures.[37–41] To the best of the author's knowledge, no M_4L_4 or M_4L_6 assembly has been reported for which the S_4-symmetric ΔΔΛΛ-isomer is observed exclusively. In addition to metal center isomerism causing the observed decrease in symmetry, it is also plausible that

the increased number of proton resonances arises from a host of D_2-symmetry. The increased flexibility of **3** may allow the host's walls to collapse while maintaining homochirality of the gallium metal centers. This desymmetrization might also afford a decrease in internal volume by pinching two pairs of vertices together, while increasing the distance between those pairs. If indeed the D_2-symmetry structure were an energetic minimum for homochiral **3**, it seems intuitively improbable that the barrier to interconversion of these structures would be sufficiently high to observe in the NMR timescale; nonetheless, this scenario is possible and worthy of consideration. Finally, it is also conceivable that if ligand **4** is sufficiently flexible, a $Ga_2\mathbf{4}_2$ structure, also of D_2-symmetry could be the initially formed complex. This would require the $Ga_2\mathbf{4}_2$ assembly to rapidly rupture and dimerize upon the addition of a guest to form the M_4L_4 inclusion complex.

In order to differentiate the anticipated M_4L_4 stoichiometry for cluster **3** from a potential $Ga_2\mathbf{4}_2$ structure, the techniques of diffusion ordered NMR spectroscopy (DOSY) and electrospray mass spectrometry (ESI-MS) were employed. If the low symmetry structure for empty assembly **3** is of M_4L_4 stoichiometry, then it would be expected to have a similar hydrodynamic radius to the M_4L_4 inclusion complex $NEt_4^+ \subset \mathbf{3}$. In contrast, if the low symmetry species were of M_2L_2 stoichiometry, then it would have a significantly smaller hydrodynamic radius, and its diffusion rate would be much higher. Low symmetry cluster **3** was found to have a diffusion coefficient of 1.52 x 10^{-5} cm^2/s, while high symmetry $NEt_4^+ \subset \mathbf{3}$ had a diffusion coefficient of 1.97 x 10^{-5} cm^2/s (Figure 4.6). The similarity of these values provides strong evidence that an M_4L_4 stoichiometry is preserved between high and low symmetry **3**. ESI-MS measurements also corroborated this conclusion. Signals consistent with an M_4L_4 stoichiometry for low symmetry **3** were observed between approximately m/z = 1140–1220, corresponding to a 3- charge state (for representative simulated and observed spectra for $\{K_5H_4[Ga_4L_4]\}^{3-}$, see Figure 4.7). These data together support the hypothesis that the low symmetry structure **3** is of M_4L_4 stoichiometry, and must undergo some structural or conformational transition upon encapsulation of a guest. Efforts to confirm these conclusions by single crystal X-ray diffractometry are ongoing.

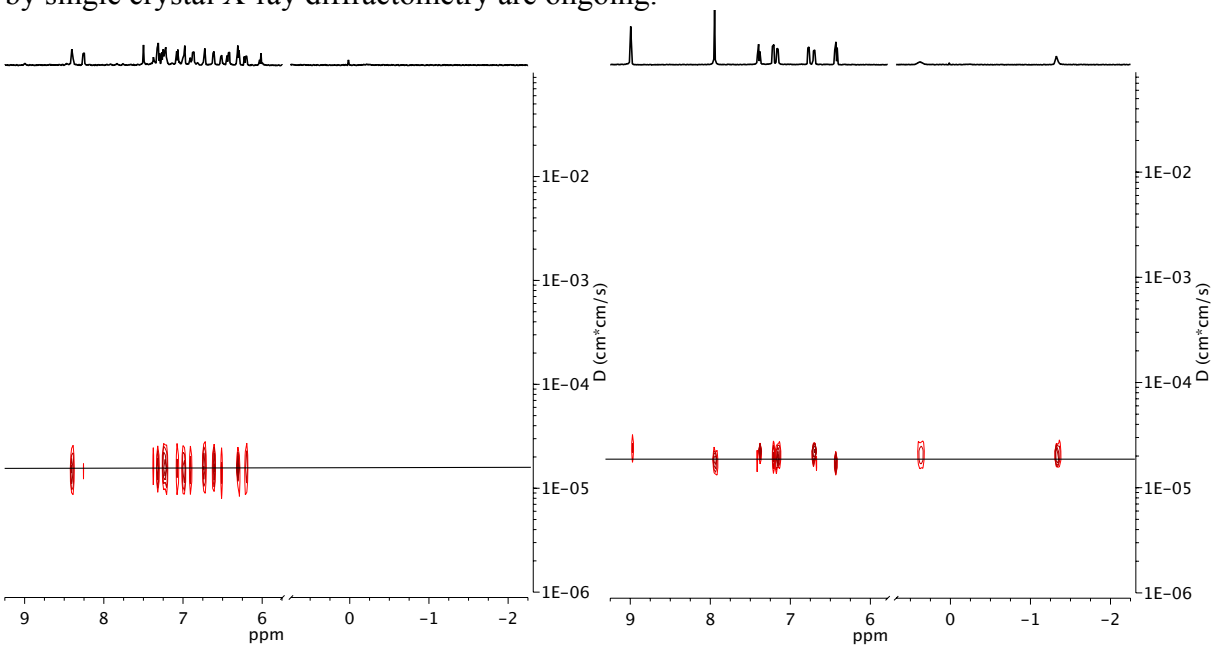

Figure 4.6. DOSY NMR data supporting M_4L_4 stoichiometry for low symmetry cluster **3**.

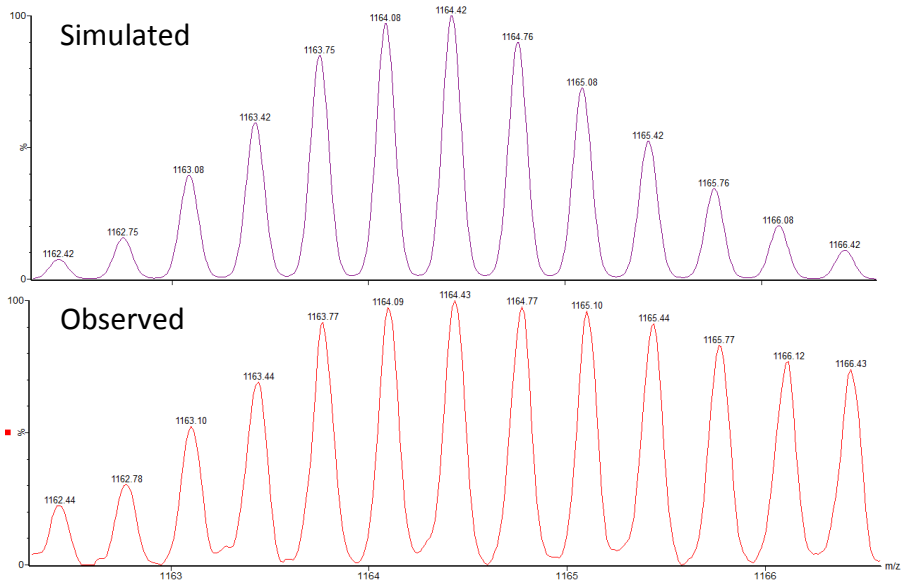

Figure 4.7. ESI-MS signal consistent with $\{K_5H_4[Ga_4L_4]\}^{3-}$.

The dynamics of host isomerization were then investigated in order to gain further insight into the nature of the configurational changes responsible for the increase in symmetry of cluster **3** upon guest binding. While the three-fold symmetry of ligand **4** is broken upon assembly into cluster **3**, the unique chemical environments created by this desymmetrization are expected to be related by chemical exchange in the case of both the S_4 and D_2 symmetry structures for low symmetry cluster **3**. If the low symmetry structure of **3** is the result of mixed ΔΔΛΛ chirality of the pseudo-octahedral gallium metal centers, then the exchange process that interconverts the desymmetrized hydrogen atoms is likely to proceed by stepwise Bailar twists, by analogy to previously conducted studies on the mechanism of gallium triscatecholate isomerization.[42,43] The first Bailar twist from S_4-symmetric **3** (of ΔΔΛΛ-chirality) would generate the C_3-symmetric ΔΔΔΛ/ΔΛΛΛ complex. A second Bailar twist would then provide access to either the T-symmetric ΔΔΔΔ/ΛΛΛΛ complex, or alternatively, a second isomeric S_4-symmetric ΔΔΛΛ-complex (Figure 4.8). Whether or not T-symmetric homochiral empty cluster **3** is an intermediate in the degenerate isomerization of S_4-symmetric ΔΔΛΛ-**3** depends of the relative energetic barrier for the S_4-C_3 Bailar twist, versus the C_3-T Bailar twist. Since the relative magnitude of these barriers is unknown, analysis of the kinetic parameters of self-exchange would not necessarily inform directly on those of the S_4 to T configurational change involved in guest binding; however, as these processes are mechanistically related, it should at least shed a qualitative light on the kinetic parameters of such a process.

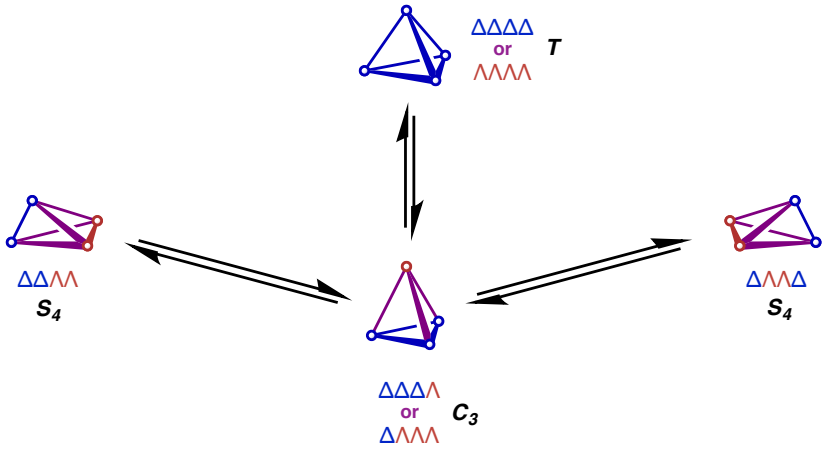

Figure 4.8. Schematic representing the stepwise Bailar twist mechanism for ΔΔΛΛ-**3** degenerate isomerization.

The degenerate isomerization of **3** was first established by the observation of coalescence at elevated temperatures by variable temperature ^{1}H-NMR spectroscopy. In D_2O, the 24 observed resonances of **3** were observed to coalesce into eight broad peaks at around 90 ºC (Figure 4.9). However, proximity to the solvent boiling point and complications involving temperature dependence of isotropic chemical shift prevented accurate determination of kinetic activation parameters from this method. In order to overcome these issues, the technique of Selective Inversion Recovery (SIR) ^{1}H-NMR spectroscopy was used.

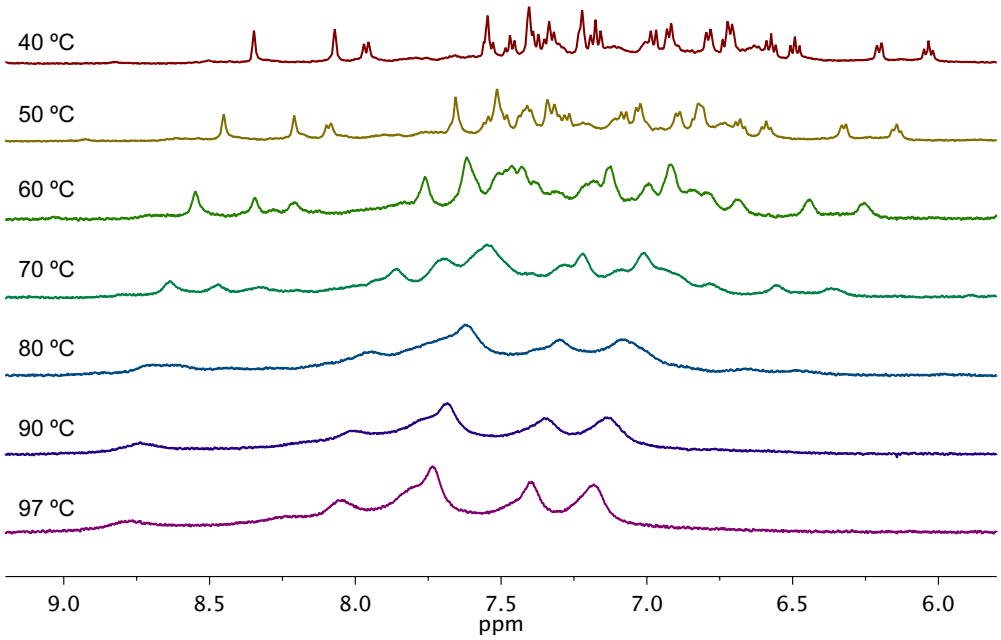

Figure 4.9. Peak coalescence by ^{1}H-NMR spectroscopy of **3** in D_2O at approximately 90 ºC.

SIR experiments are well established as a technique for the measurement of exchange kinetics, when the exchanging populations can be clearly discriminated by NMR. A typical experiment proceeds by selective inversion of the spin population for a unique resonance, effectively labeling those nuclei *via* magnetization. This is followed by a variable delay time, during which the chemical exchange process causes a measurable magnetization transfer of the spin-labeled nuclei between the exchange related chemical environments, after which a 1D spectrum is acquired. This process is repeated for a series of delay times in order to generate a profile of magnetization transfer over time. The rate of chemical exchange between the inverted signal and exchange related, non-inverted signals is correlated to the attenuation of the noninverted signals, as those signals are effectively dampened by the spin-labeled nuclei that exchange into the noninverted chemical environments. By modeling the rate of signal attenuation and relaxation, in conjunction with an independently measured T_1 relaxation rates, the rate of chemical exchange can be evaluated. Although SIR NMR experiments are typically performed on exchange reactions between two chemically distinct environments, the data collection and analysis can be extended to systems of three fold symmetry, as observed in the degenerate rearrangement of host **3**. Gratifyingly, inversion of the singlet appearing in the ^{1}H-NMR spectrum of **3** at 7.50 ppm resulted in the attenuation of the signal intensities of the resonances at 8.38 ppm and 6.97 ppm in a manner characteristic of three-fold chemical exchange (Figure 4.10). Notably, the signals at 8.38 ppm and 6.97 ppm both overlapped with one additional proton resonance, however the overlapping signal could be subtracted without complication in order to model the rate of exchange.

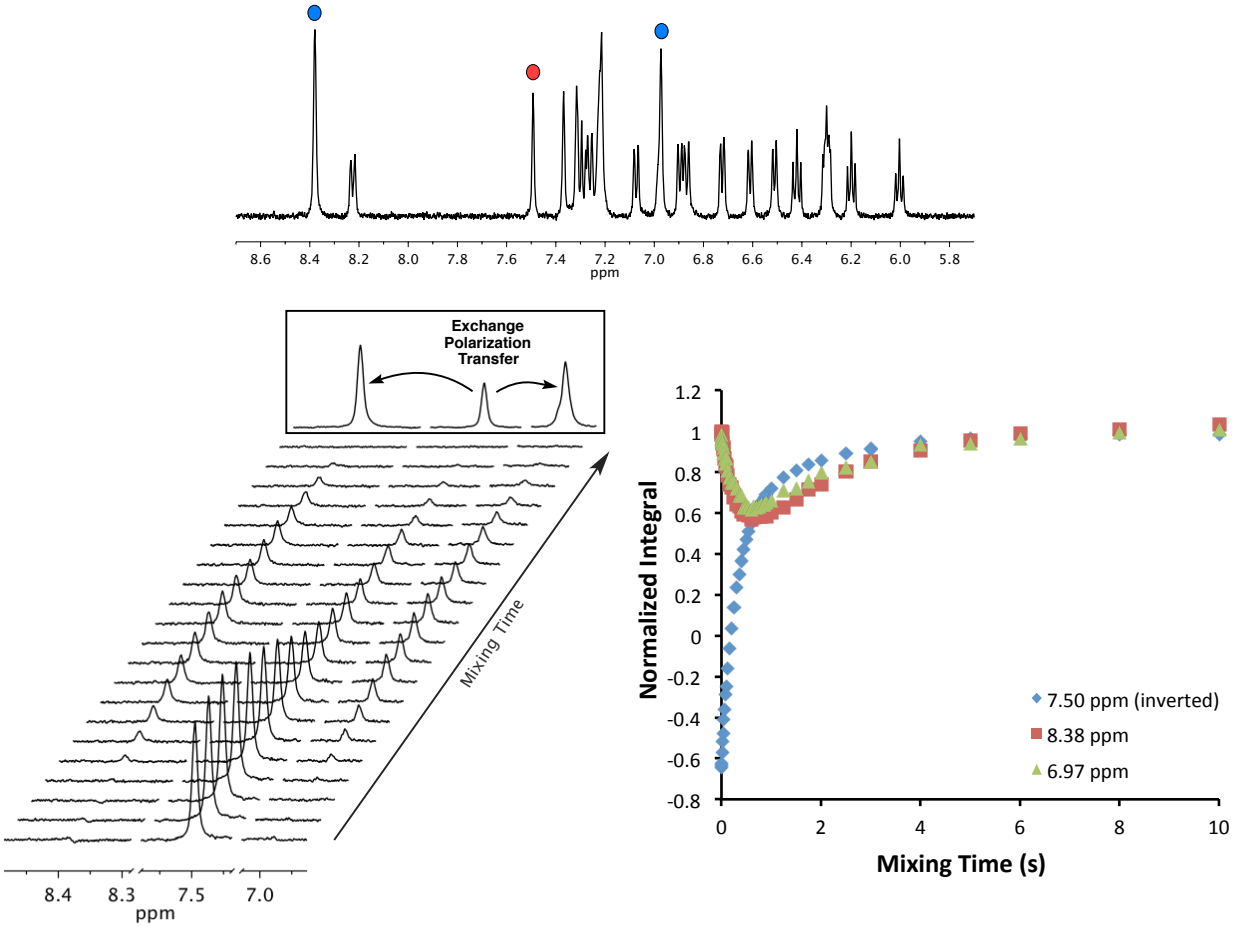

Figure 4.10. (Top) ^{1}H-NMR spectrum of **3** indicating which resonance was selectively inverted (red circle) and which resonances become attenuated as a result of chemical exchange from the inverted resonance (blue circles). (Bottom left) Total magnetization (Difference in integral at equilibrium and integral at various mixing times) for selectively inverted proton resonance (7.50 ppm) and two resonances related by chemical exchange (8.38 and 6.97 ppm respectively). (Bottom right) Normalized Integral for each of the three resonances related by chemical exchange.

The rate of degenerate host isomerization was measured at various temperatures ranging from 33 ºC to 53 ºC in order to extract the kinetic parameters of activation by Eyring analysis (Figure 4.11). This analysis afforded an enthalpy of activation ($\Delta H^{\ddagger}$) of 12.7 kcal/mol, and an entropy of activation ($\Delta S^{\ddagger}$) of -17.4 cal/mol*K, corresponding to a free energy of activation ($\Delta G^{\ddagger}$) of 17.8 kcal/mol at 298 K. Most notably, these data show that the host isomerization even is significantly entropically disfavored, indicating an ordered transition state. These observations are consistent with the expected parameters for a consecutive Bailar twist mechanism for the degenerate isomerization of an S_4-symmetric **3** of ΔΔΛΛ metal center chirality. For comparison, in a previous study, the isomerization of a mononuclear gallium triscatecholate proceeded with an enthalpy of activation of 11.0 kcal/mol, an entropy of activation of -11.4 cal/mol*K, and a free energy of activation of 14.4 kcal/mol at 298 K.[42] The activation parameters for the isomerization of host **3** are qualitatively very similar to those observed for the mononuclear complex. The slight increase in the magnitude of both the

entropy and enthalpy of activation are consistent with the effect of slight mechanical coupling by the polymacrocyclic framework of the cluster. While this data does not definitively rule out a D_2-symmetric homochiral structure for **3**, they are highly consistent with the expected observations for a mixed chirality ΔΔΛΛ system of S_4 symmetry, which is also an intuitively more viable explanation for exchange barriers of this magnitude, and more consistent with previous study of metal ligand self-assemblies of M_4L_4 and M_4L_6 stoichiometry in the literature (*vide supra*).

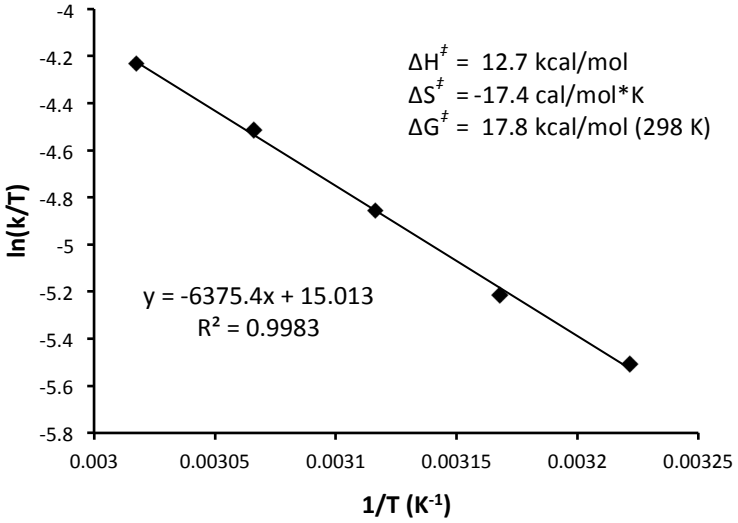

Figure 4.11. Eyring plot for the degenerate isomerization of ΔΔΛΛ-**3**

4.3.3 Generality of Guest-Dependent Host Isomerization

Having established the ΔΔΛΛ-complex of S_4 symmetry as the likely structure of empty cluster **3**, the generality of this phenomenon was interrogated by the synthesis of a novel cluster, baring similar design features, but differing in the chemical building blocks used to achieve at those features. Potential M_4L_4 cluster **9** was targeted, which would be assembled from a C_3-symmetric triscatecholate ligand, **10**, bearing curvature in each of the three metal-binding arms. Ligand **10** features a triazine core in order to generate the appropriate C_3-symmetry of the ligand, and *m*-phenylenediamine spacers to provide flexibility and angle offset analogus to the *meta*-substituted arenes of ligand **4**. The core of ligand **10** was assembled through a triple S_NAr reaction between cyanuric chloride (**11**) and excess 3-nitroaniline, affording tris(3-nitroaryl)melamine complex **12**. The remaining steps of the ligand synthesis were carried out in analogy to the synthesis of ligand **4**. Nitro group reduction of **12** with tin metal and hydrochloric acid afforded trianiline **13**, which was followed by acylation with 2,3-dimethoxybenzoyl chloride, providing hexamethyl protected ligand **14**. Global dimethylation with boron tribromide yielded ligand (**10**) (Figure 4.12). The self-assembly of **9**, similar to that of **3**, was conducted by combining equimolar quantities of ligand **10** and $Ga(acac)_3$ in water, followed by four equivalents of potassium hydroxide. Similar to previous observations, self-assembly with ligand **10** revealed the appearance of a low symmetry species assigned as ΔΔΛΛ-**9**. Additionally, just as was observed for cluster **3**, the addition of excess tetraethylphosphium iodide induced an increase in symmetry, which is attributed to the formation of homochiral ΔΔΔΔ/ΛΛΛΛ-**9** (Figure 4.13). Unlike cluster **3**,

however, no upfield shifted resonances corresponding to encapsulated phosphonium ion were observed in the high symmetry ^{1}H-NMR spectrum of **9**. This observation is likely explained by fast guest exchange on the NMR time scale, due to the increase pore size for cluster **9**. M_4L_4 stoichiometry for assembly **9** is also supported by ESI-MS and DOSY NMR spectroscopy (see supporting information below). Despite the comparatively large changes in ligand structure between clusters **3** and **9**, it appears that the self-assembly behavior is conserved for this bent C_3-Symmetric motif.

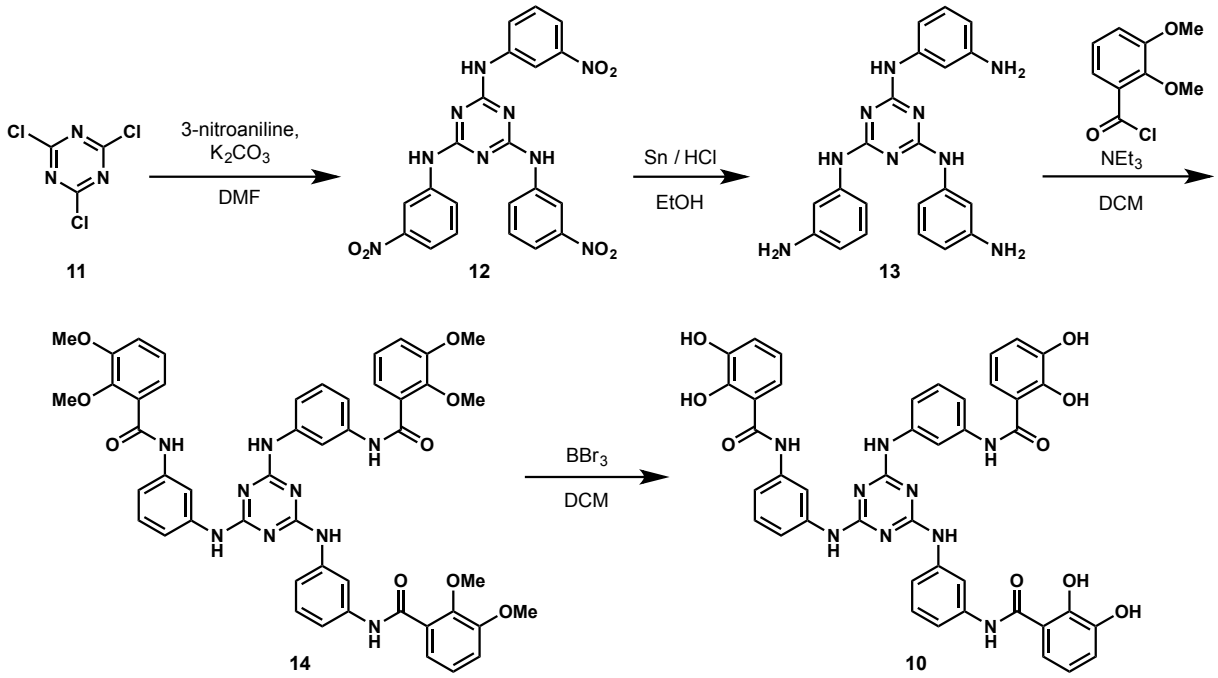

Scheme 4.12. Synthesis of ligand **10**, self-assembly precursor to **9**.

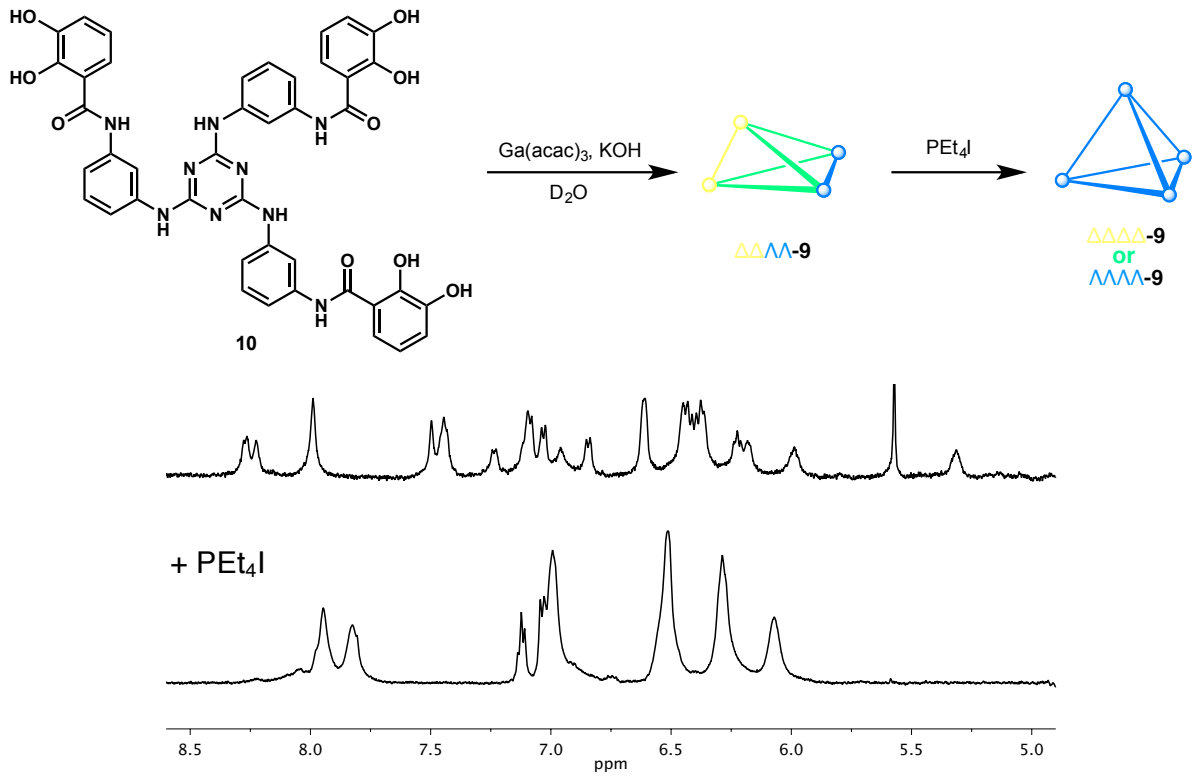

Figure 4.13. ^{1}H-NMR spectrum of cluster ΔΔΛΛ-**9** immediately after assembly (top) and ΔΔΔΔ/ΛΛΛΛ-**9** after the addition of excess tetraethylphosphonium iodide (bottom).

4.3.4 Evaluation of the Mechanism for Guest Dependent Host Isomerization

In order to further understand the mechanism by which the addition of a guest molecule effects the isomerization of cluster **3** from ΔΔΛΛ S_4-symmetry to homochiral T-symmetry, the rate dependence of the approach to the encapsulation equilibrium with respect to ammonium guest concentration was studied. A number of supramolecular systems have been shown to undergo configurational changes in order to accommodate and conform to their respective guest molecules.[44–52] This phenomenon is often referred to imprecisely as "induced-fit" binding, although to the best of the author's knowledge, no mechanistic study has been performed in order to differentiate the induced fit and conformational selection binding mechanism in a synthetic supramolecular host. As described above, the two basic mechanisms for non-concerted guest binding, conformational selection and induced fit, are differentiated by the relative order of host isomerization and guest binding, with isomerization preceding guest binding for conformational selection, and guest binding preceding isomerization in the induced fit mechanism (Figure 4.14).

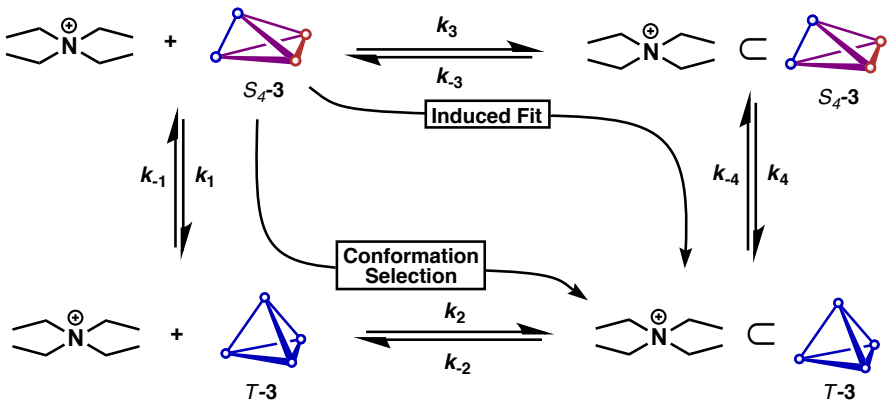

Figure 4.14. Induced fit and conformational selection mechanism for encapsulation of ammonium guests by cluster **3**.

It was possible to observe the approach to encapsulation equilibrium by cooling a methanolic solution of empty host **3** in an NMR tube to -78 ºC, followed by the addition of the guest at low temperature and then allowing the resulting mixture to warm in a pre-cooled NMR spectrometer. The observation of the approach to equilibrium was possible for the binding of both tetraethylammonium (Figure 4.15) and tetrapropylammonium ion guests (Figure 4.16). When data were collected at 8 ºC, the approach to equilibrium occurred on a reasonable timescale for kinetic study, and the approach to equilibrium followed pseudo-first order kinetics (the plot of $\ln([NR_4^+\subset\mathbf{3}]_e - [NR_4^+\subset\mathbf{3}]_t)$ vs. time is linear).

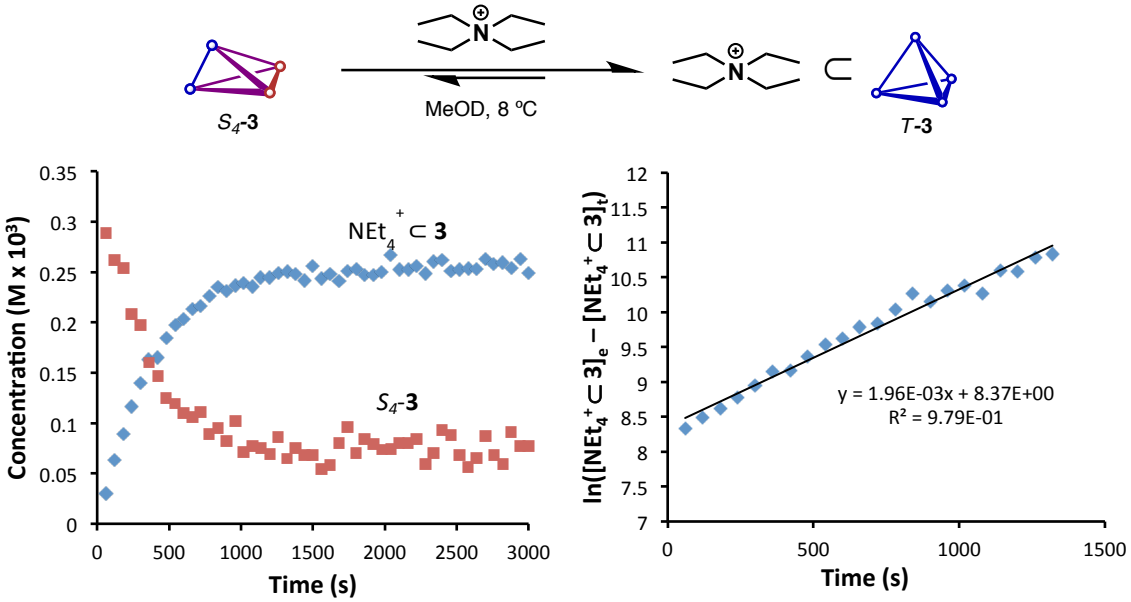

Figure 4.16. (Left) Kinetic profile for approach to equilibrium of tetraethylammonium encapsulation. (Right) Natural log plot displaying first order kinetics for approach to equilibrium.

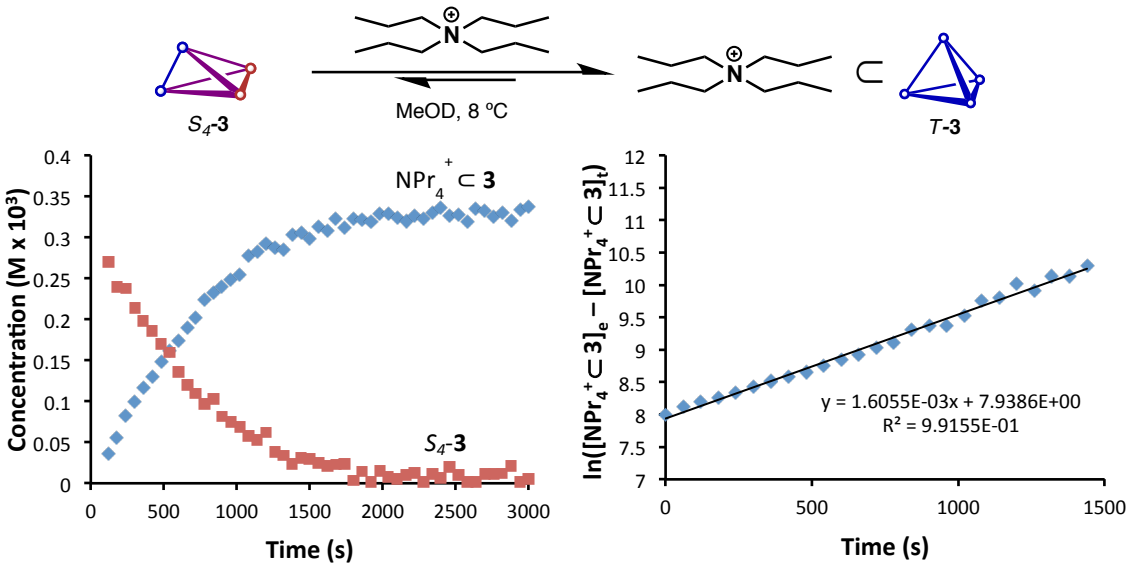

Figure 4.17. (Left) Kinetic profile for approach to equilibrium of tetraproylammonium encapsulation. (Right) Natural log plot displaying first order kinetics for approach to equilibrium.

The rate of approach to encapsulation equilibrium (k_{obs}) for both tetraethylammonium and tetrapropylammonium guests and cluster **3** was found to be inhibited by the guest molecule, with a decrease in rate associated with increasing guest concentration (Figures 4.18 and 4.19 respectively). Inhibition of the rate of approach to encapsulation equilibrium by guest concentration is the classic kinetic signature of a conformational selection mechanism of guest encapsulation (*vide supra*). If the rapid equilibrium approximation—guest exchange is rapid compared to host isomerization—holds true for this kinetic scenario, then the rate constant for approach to equilibrium, based on the mechanism depicted in Figure 4.14, is shown in equation 4.4.

$$k_{obs} = k_1 + k_{-1}\frac{1}{1+\frac{k_2}{k_{-2}}[NR_4^+]} \qquad (4.4)$$

This rate constant, by analogy to the established analysis of conformational selection in enzymatic substrate binding, is composed of the sum of the forward and reverse rate constants for the encapsulation equilibrium. Since, under the rapid equilibrium approximation, the forward rate constant is independent of guest and the reverse reaction is inhibited by guest, the overall observed rate becomes partial inverse order in ammonium ion concentration.

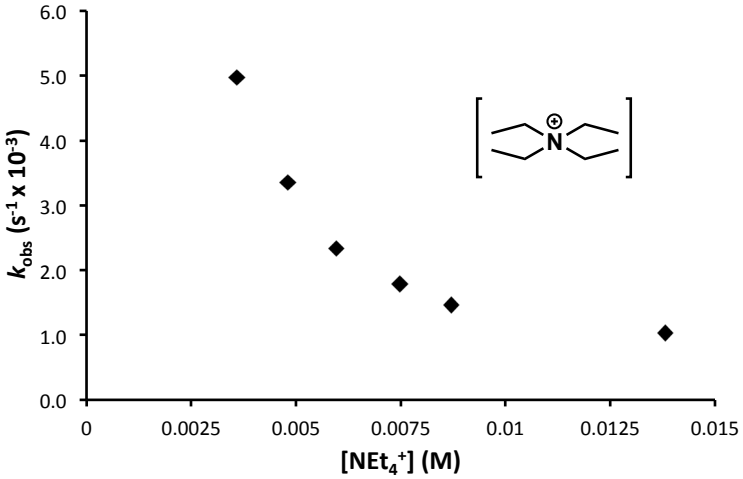

Figure 4.18. Rate dependence of the approach to encapsulation equilibrium on the concentration of tetraethylammonium ion concentration for cluster **3**.

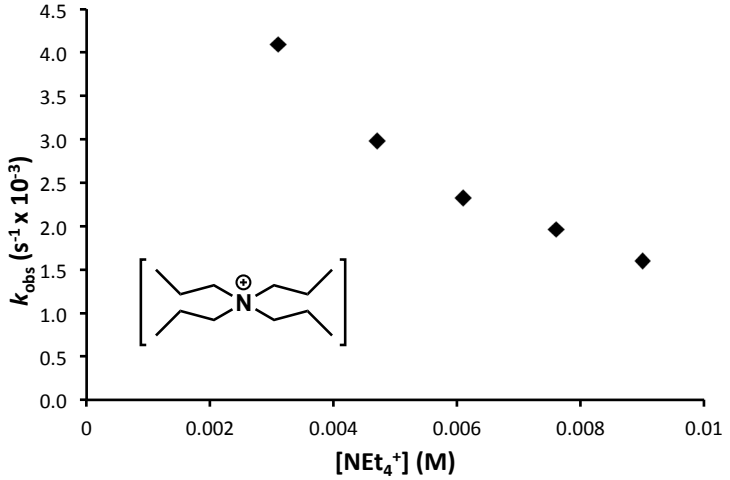

Figure 4.19. Rate dependence of the approach to encapsulation equilibrium on the concentration of tetraproylammonium ion concentration for cluster **3**.

In order to evaluate the applicability of the rapid equilibrium approximation for this system, the rate of guest self-exchange for tetraethylammonium inclusion complex $NEt_4^+ \subset$ **3** was examined by SIR NMR spectroscopy. Eyring analysis of this system revealed that the barrier to guest self-exchange ($\Delta G^{\ddagger}$ = 16.2 kcal/mol at 298 K) is dominated by entropic considerations ($\Delta S^{\ddagger}$ = -46.3 cal/mol*k), with only a modest enthalpic component ($\Delta H^{\ddagger}$ = 2.3 kcal/mol) (Figure 4.20). These observations are consistent with previous analyses of guest self-exchange in cluster **1**, where a significant entropic contribution to the barrier was observed.[53] To assess the applicability of the rapid equilibrium approximation, the kinetic parameters for guest self-exchange and degenerate host isomerization were extrapolated to 8 ºC (the temperature at which the encapsulation kinetic measurements were performed). At this temperature, guest self-exchange occurs with a barrier of 15.3 kcal/mol, as compared to 17.6 kcal/mol for degenerate guest rearrangement, implying that guest self-exchange occurs at a rate greater than 60 fold faster than degenerate host rearrangement. It is important to note, as discussed above, the rate degenerate host rearrangement is only an approximation for the isomerization process involved in guest binding; however, this process is mechanistically

related, and expected to proceed with a similar barrier. This analysis indicates that the rapid equilibrium approximation should be applicable to this system.

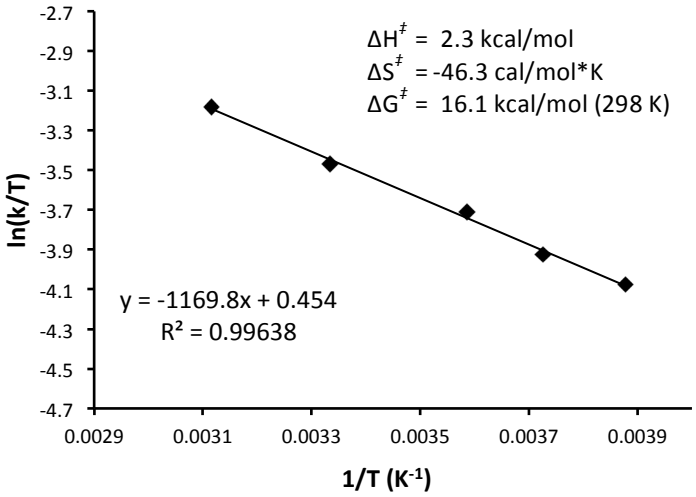

Figure 4.20. Eyring plot for tetraethylammonium guest self-exchange with cluster **3**.

However, while the observed guest-inhibited relaxation rates provide strong support for a conformational selection mechanism for guest binding, this does not preclude the possibility of fast, reversible guest association to the low symmetry host before the equilibrium is reached. It is possible that the first step of the induced fit pathway is kinetically viable, while the guest molecule acts as an inhibitor to the Bailar twist host isomerization mechanism, preventing the second step (isomerization) of the induced fit mechanism from occurring. Indeed, some support for the idea that there is encapsulation of the guest by the low symmetry host is provided by the observation that there is a large shift in the ^{1}H-NMR chemical shift of the ammonium ion in the presence of *S*$_4$-**3**. As the low symmetry host disappears, a concomitant decrease in the magnitude of the ammonium ion chemical shift is observed (Figure 4.21). This is consistent with ammonium encapsulation by *S*$_4$-**3** that is fast and reversible on the NMR timescale.

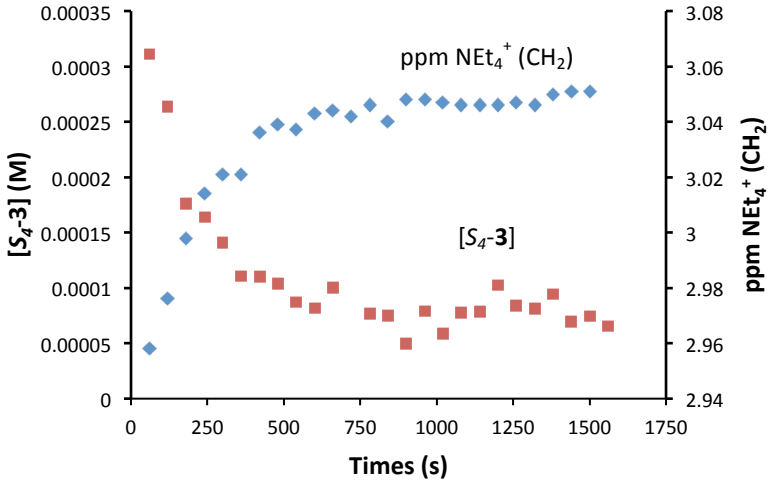

Figure 4.21. Observation of strong ^{1}H-NMR chemical shift dependence of NEt_4^+ methylene on the concentration of low symmetry **3**, supporting transient encapsulation.

The mechanistic scenario involving pre-equilibrium association of the guest molecule to the low symmetry cluster **3** can be easily evaluated by assessing the respective contributions of the forward and backward rates to the overall observed rate constant for approach to equilibrium. As previously mentioned, the observed rate constant for a reversible reaction is the sum of the forward and backward rate constants. Inspection of equation 4.4 reveals that the forward rate constant contribution is independent of guest concentration, while the reverse rate constant contributes the guest inhibition to the overall rate constant. If the conformational selection mechanism (Figure 4.14) is amended to include reversible guest binding for the low symmetry host (K_3), a new expression for k_{obs} is derived, as shown in equation 4.5.

$$k_{\text{obs}} = k_1 \frac{1}{1 + \frac{k_3}{k_{-3}}[\text{NR}_4^+]} + k_{-1} \frac{1}{1 + \frac{k_2}{k_{-2}}[\text{NR}_4^+]} \tag{4.5}$$

In this alternative expression of the observed rate constant, both the forward and reverse reaction display inhibition with respect to the concentration of the guest. It is possible to differentiate these mechanistic scenarios—simple conformational selection vs. conformational selection with fast low symmetry encapsulation equilibrium—by observing the guest dependence on the initial rate for the approach to equilibrium. While the observed overall rate constant displayed guest inhibition in both scenarios, only fast and reversible encapsulation by low symmetry **3** would display inhibition in the initial rates, where the reverse reaction has a negligible impact on the instantaneous rate. Indeed, a plot of initial rates versus guest concentration for the approach to equilibrium between tetraethylammonium ion and cluster **3** shows clear guest inhibition, supporting the modified conformational selection with low symmetry pre-equilibrium mechanism (Figure 4.22). This observation suggests that a complete mechanistic picture for the relaxation to guest binding equilibrium for host **3** involves guest dissociation from *S*$_4$-symmetric ΔΔΛΛ-**3**, followed by host isomerization, and guest binding to *T*-symmetric homochiral **3**.

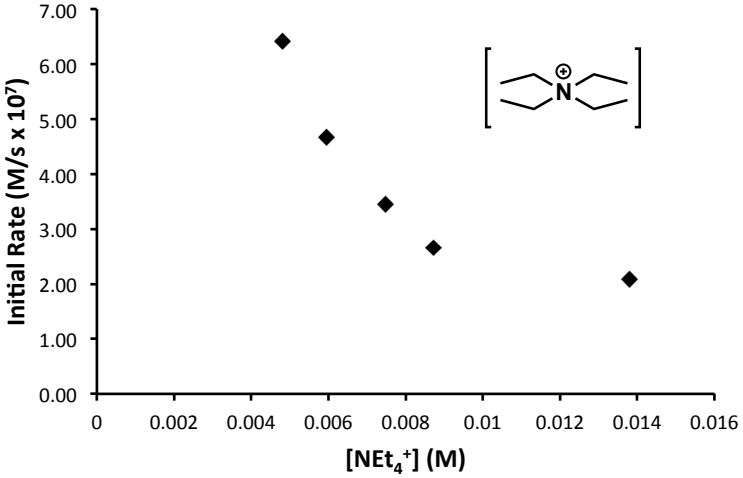

Figure 4.22. Initial rates for the increase in symmetry of host **3** as a function of tetraethylammonium ion concentration

4.4 Conclusion

In this chapter, a novel motif in supramolecular metal-ligand self-assembly has been identified and explored. The incorporation of an appropriate element of flexibility into the *C*$_3$-

symmetric ligand of an M_4L_4 metal ligand cluster enables the emergent property of dynamic configurational states. The empty cluster is most stable in the ΔΔΛΛ-mixted chirality state of S_4-symmetry. However, in order to efficiently encapsulate a guest molecule, a dual metal center isomerizaion event occurs in order to generate the homochiral *T*-symmetric cluster-guest inclusion complex, which bears an internal cavity that is more sterically compatible with the guest. The mechanism of this configurational change was studied, and found recapitulate the conformational selection model of ligand binding in a biological context. The guest molecule effectively traps the high symmetry cluster out of a dynamic equilibrium in solution. Additionally, evidence is presented that suggests that the guest molecule is initially encapsulated by the low symmetry cluster; however, the guest acts as an inhibitor for the double Bailar twist mechanism by which the host transitions from S_4 to *T* symmetry, and only after guest dissociation can the isomerization occur. While the debate between the induced fit and conformational selection models for substrate binding by large biomolecules is an ongoing and lively area of research, this work represents the first investigation in this area for biomimetic supramolecular host-guest systems.

4.5 Supporting Information

4.5.1 General Methods

Unless otherwise stated, all reactions were performed in flame-dried or oven-dried glassware sealed with rubber septa under a nitrogen atmosphere. Reaction solutions were stirred by Teflon-coated magnetic stir bars with the exception of those performed in NMR tubes. Dry dichloromethane (DCM) and triethylamine (TEA) were obtained by passing these previously degassed solvents through activated alumina columns. All other solvents were degassed by thoroughly sparging with nitrogen. All other reagents were used as received from Acros, Sigma Aldrich, or Fisher. Deuterated solvents were purchased from Cambridge Isotope Laboratories and used without further purification. Reactions were monitored by thin layer chromatography (TLC) on Silicycle Siliaplate^{TM} glass backed TLC plates (250 μm thickness, 60 Å porosity, F-254 indicator) and visualized by UV irradiation and *p*-anisaldehyde stain. Volatile solvents were removed under reduced pressure with a rotary evaporator and dried on high vacuum on a Schlenk line. ^{1}H-NMR and ^{13}C-NMR spectra were taken with Bruker spectrometers operating at 300, 400, 500, or 600 MHz for ^{1}H (75, 100, 125, and 150 MHz for ^{13}C). Chemical shifts are reported relative to the residual solvent signal. NMR data are reported as follows: chemical shift (multiplicity, coupling constants where applicable, number of hydrogens). Splitting is reported with the following symbols: s = singlet, bs = broad singlet, d = doublet, t = triplet, dd = doublet of doublets, dt = doublet of triplets, m = multiplet. High-resolution mass spectrometry (HRMS) was performed on a Thermo LTQ-FT-ICE (7T, ESI) by the QB3 mass spectral facility at the University of California, Berkeley and on a PerkinElmer AxION 2 (ESI, positive mode) at the Catalysis Center at the University of California, Berkeley.

4.5.2 Synthesis of Previously Unreported Compounds

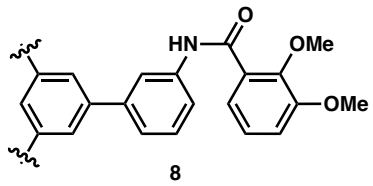

8

Hexamethyl protected ligand **8**, precursor to cluster **3** –

2,3-dimethoxybenzoic acid (2.33 g, 12.8 mmol, 3.2 equiv.) was dissolved in dry DCM (96 mL) in a 250 mL Schlenk flask. Thionyl chloride (1.88 mL, 25.6 mmol, 6.4 equiv.) was added dropwise, followed by 6 drops of DMF. The reaction mixture was stirred overnight, and then volatiles were removed *in vacuo*. The resulting residue was redissolved in dry DCM (96 mL), and previously reported trianiline **7**[54] (1.41 g, 4.00 mmol, 1 equiv.) was added in one portion, followed by the dropwise addition of triethylamine (3.6 mL). The resulting reaction mixture was stirred overnight. DCM (100 mL) was added, and then the solution was washed with 1M NaOH (50 mL), and 1M HCl (50 mL). The organic layer was dried over magnesium sulfate and concentrated under reduced pressure. The residue was purified by silica gel chromatography (30 → 50% ethyl acetate in hexanes) to afford **8** (1.94 g, 57% yield) as an off white solid.

^{1}H-NMR (600 MHz, Chloroform-*d*) δ 10.15 (s, 1H), 8.02 (s, 1H), 7.87 (s, 1H), 7.81 (t, *J* = 8.4 Hz, 2H), 7.52 (app. s, 2H), 7.22 (t, *J* = 7.9 Hz, 1H), 7.11 (d, *J* = 7.9 Hz, 1H), 4.04 (s, 3H), 3.93 (s, 3H).
^{13}C-NMR (151 MHz, Chloroform-*d*) δ 163.24, 152.77, 147.49, 142.19, 139.04, 129.70, 127.03, 125.65, 124.82, 123.53, 123.15, 119.50, 119.23, 116.00, 61.91, 56.31.
HRMS (*m/z*): calculated for $[C_{51}H_{45}N_3O_9Na]^+$, 866.3054; observed, 866.3482.

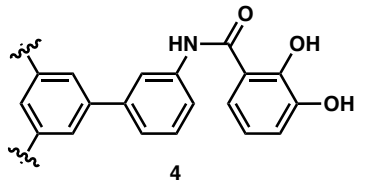

4

Ligand **4**, precursor to cluster **3** –

To a 100 mL round bottom flask was added **8** (1.94 g, 2.30 mmol, 1.0 equiv.) and dry DCM (50 mL). The resulting solution was cooled to -78 ºC, and boron tribromide (5.18 g, 20.7 mmol, 9 equiv.) was added slowly. The reaction mixture was allowed to warm to room temperature overnight, and then poured over ice (~50 g). Upon reaching room temperature, the resulting biphasic mixture was filtered. The solid was suspended in water (50 mL) and then the resulting suspension was heated to reflux for 12 hours. The reaction mixture was allowed to cool to room temperature, and the solid was filtered and washed with copious amounts of water, to afford ligand **4** (1.53 g, 83%) as a beige solid.

^{1}H NMR (600 MHz, DMSO-d_6) δ 11.66 (s, 1H), 10.46 (s, 1H), 9.42 (s, 1H), 8.14 (s, 1H), 7.93 (s, 1H), 7.85 (d, *J* = 7.4 Hz, 1H), 7.67 (d, *J* = 7.1 Hz, 1H), 7.55 (t, *J* = 7.5 Hz, 1H), 7.48 (d, *J* = 7.6 Hz, 1H), 7.00 (d, *J* = 7.3 Hz, 1H), 6.80 (t, *J* = 7.6 Hz, 1H).
^{13}C NMR (151 MHz, DMSO) δ 167.91, 148.40, 146.20, 141.54, 140.49, 138.66, 129.40, 124.48, 123.09, 120.68, 119.92, 119.06, 118.43, 118.31, 117.02.
HRMS (*m/z*): calculated for $[C_{45}H_{32}N_3O_9]^-$, 758.2139; observed, 758.2120.

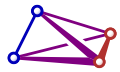

ΔΔΛΛ

S_4 - 3

Cluster **3** – To a 1000 mL 3-neck flask was added ligand **4** (942 mg, 1.24 mmol, 4.00 equiv.) and $Ga(acac)_3$ (455.2 mg, 1.24 mmol, 4.00 equiv.). Degassed methanol (38 mL) was added, and the resulting milky suspension was stirred for 10 minutes. KOH (209 mg, 3.72 mmol, 12.0 equiv.) was added in methanol (2 mL). The mixture became homogeneous and was stirred for 20 minutes. Degassed acetone (400 mL) was added dropwise over the course of about three hours. The resulting suspension was filtered, affording **16** (946 mg, 81%) as a beige solid.

^{1}H-NMR (500 MHz, Methanol-d_4) δ 8.45 – 8.34 (m, 8H), 8.25 (d, J = 7.8 Hz, 4H), 7.50 (s, 4H), 7.38 (s, 4H), 7.35 – 7.18 (m, 24H), 7.08 (d, J = 8.5 Hz, 4H), 7.03 – 6.96 (m, 8H), 6.93 – 6.87 (m, 8H), 6.75 (d, J = 7.3 Hz, 4H), 6.63 (d, J = 7.3 Hz, 4H), 6.53 (d, J = 6.9 Hz, 4H), 6.44 (t, J = 7.9 Hz, 4H), 6.35 – 6.28 (m, 8H), 6.22 (t, J = 7.5 Hz, 4H), 6.22 (t, J = 7.5 Hz, 4H), 6.02 (t, J = 7.6 Hz, 4H).

For ESI-MS and DOSY NMR data, see Figure 4.6 and 4.7.

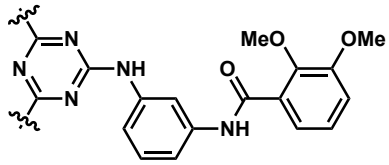

14

Hexamethyl protected ligand **14**, precursor to cluster **9** –

In a 50 mL round bottom flask, previously reported trinitroaryl compound **12**[55] (1.9 g, 3.88 mmol, 1 eq.) was suspended in ethanol (15 mL) and subsequently treated dropwise with a solution of $SnCl_2$ dihydrate (8.0 g, 35.5 mmol, 9.15 eq.), 11.65 M HCl (18 mL), and ethanol (18 mL) *via* an addition funnel. The resulting reaction mixture was heated to reflux for 18 h, allowed to cool to ambient temperature, then filtered. The resulting solids were dissolved in boiling water then filtered. The aqueous filtrate was neutralized with 1 M KOH until pH > 11, and the resulting precipitate was filtered, washed with water, and washed with cold methanol to afford trianiline **13** as an off-white solid (1.4 g, 3.51 mmol) in 90.3% yield, which was then carried on without further purification.

A 100 mL flask was charged with 2,3-dimethoxybenzoic acid (1.52 g, 8.34 mmol, 3.3 equiv.) under a nitrogen atmosphere. Thionyl chloride (4 mL, 32.90 mmol, 13 equiv.) was added dropwise, followed by the addition of 3 drops of DMF. The reaction mixture was stirred overnight, and then the volatiles removed *in vacuo*. The resulting residue was redissolved in dry DCM (25 mL) and treated with the freshly prepared trianiline **13** (1.01 g, 2.53 mmol, 1 equiv.) in one portion. The resulting orange suspension was treated dropwise with triethylamine (4 mL) and the reaction was stirred overnight. The reaction mixture was then diluted with DCM (25 mL), washed with 1M HCl (30 mL) followed by 1M NaOH (30 mL), and brine (40 mL). The organic layer was dried over Na_2SO_4 and concentrated *in vacuo*. The resulting off-white material was dissolved in hot methylene chloride (~50 mL) and precipitated by layering with ether (~75 mL), and the resulting solid was collected by filtration, affording protected ligand **14** (1.47 g, 65%) as the resulting off-white solid.

^{1}H-NMR (500 MHz, Chloroform-*d*) δ 9.86 (s, 1H), 7.94 (s, 1H), 7.68 (d, J = 8.4 Hz, 1H), 7.59 (s, 1H), 7.39 (d, J = 7.9 Hz, 1H), 7.23 (d, J = 6.6 Hz, 1H), 7.17 (t, J = 7.9 Hz, 1H), 7.12 (t, J = 8.0 Hz, 1H), 7.01 (dd, J = 8.0, 1.5 Hz, 1H), 3.87 (s, 3H), 3.84 (s, 3H).

^{13}C-NMR (126 MHz, Chloroform-*d*) δ 163.17, 152.60, 147.23, 138.81, 138.68, 129.22, 126.96, 124.67, 122.92, 116.99, 115.69, 115.44, 112.82, 61.69, 56.14.
HRMS (*m/z*): calculated for $[C_{48}H_{45}N_9O_9Na]^+$, 914.3248; observed, 914.3295.

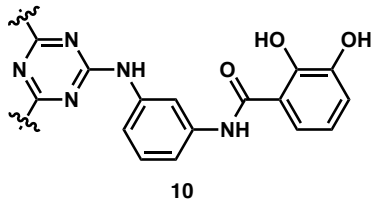

10

Ligand **10**, precursor to cluster **9** –

In a 25 mL flask, **14** (115 mg, 0.14 mmol, 1 equiv.) was dissolved in dry DCM (5 mL). The resulting solution was cooled to -78 °C and treated dropwise with boron tribromide (0.3 mL, 2.84 mmol, 20 equiv.). The resulting yellow mixture was stirred for 1 hour at -78 °C, and then slowly warmed to ambient temperature and stirred for 8 additional hours. The reaction mixture was then poured slowly into a large beaker of ice (~25 g). Upon reaching ambient temperature, the biphasic slurry was then filtered and washed with water (3 x 100 mL) to give ligand **10** (100 mg, 88%) as an off-white powder.

^{1}H-NMR (500 MHz, Chloroform-*d*) δ 11.70 (br. s, 1H), 10.35 (s, 1H), 9.71 (s, 1H), 7.90 (s, 1H), 7.73 (s, 1H), 7.45 (d, *J* = 8.5 Hz, 1H), 7.28 (br. s, 2H), 6.99 (d, *J* = 7.5 Hz, 1H), 6.78 (t, *J* = 7.8 Hz, 1H).
HRMS (*m/z*): calculated $[C_{42}H_{34}N_9O_9]^+$, 808.2474; found, 808.2464.

4.5.3 Procedures for Non-preparative Reactions

Kinetics for relaxation to encapsulation equilibrium –

In a wet N_2 atmosphere glove box, to an NMR tube was added cluster **3** (0.25 μmol, 1.0 equiv) and 2-TMS-ethanol (5.0 μmol) as a stock solution in methanol-d_4 (400 μL). The NMR tube was sealed with a septum-topped cap, removed from the glove box, and the cap was sealed with parafilm. The NMR tubes were stored at -78 ºC in a dry ice / acetone bath. Immediately prior to use, the appropriate ammonium salt was added as a stock solution in methanol-d_4 (100 μL) while submerged in the dry ice / acetone bath. The reaction mixture was then placed into the precooled, tuned and shimmed NMR spectrometer, and an automatic kinetics program was used to collect regular time points.

In situ generation of cluster **9** –

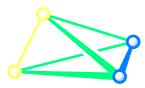
ΔΔΛΛ-**9**

To a 10 mL flask was added ligand **10** (20 mg, 0.02 mmol, 1 equiv.) and $Ga(acac)_3$ (7.3 mg, 0.02 mmol, 1 equiv.) and degassed water (1.5 mL) under a nitrogen atmosphere. The resulting suspension was sonicated for 10 minutes, then treated dropwise with KOH (3.4 mg, 0.06 mmol, 3 equiv.) in water (0.5 mL) until the reaction mixture became homogeneous. This solution was then heated at 60 °C for 1 hour. An aliquot of the resulting reaction mixture was then analyzed by no-deuterium ^{1}H-NMR spectroscopy.

4.5.4 Supplemental Figures

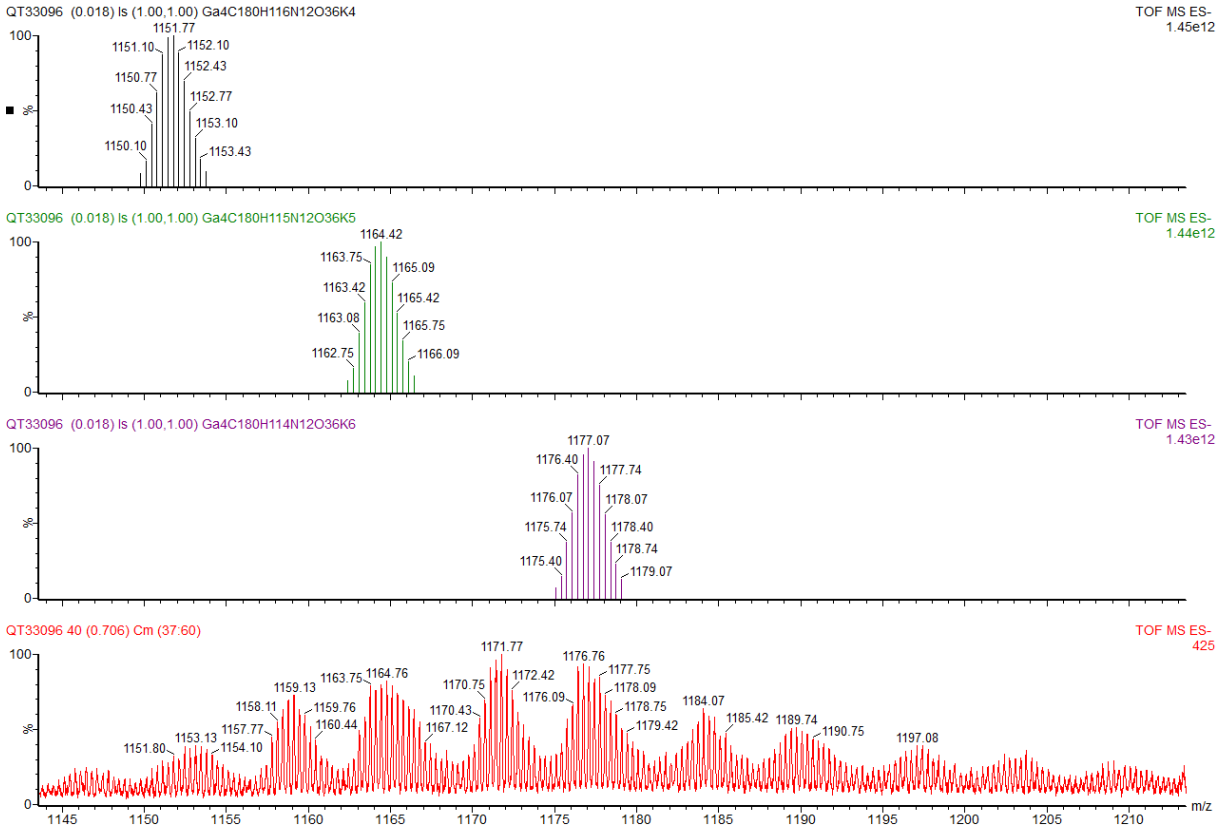

Figure 4.23. Cluster of ESI-MS peaks consistent with $X_9M_4L_4^{3-}$ (bottom) with simulated spectra for $\{K_4H_5[Ga_4L_4]\}^{3-}$, $\{K_5H_4[Ga_4L_4]\}^{3-}$, and $\{K_6H_3[Ga_4L_4]\}^{3-}$ matching observed peaks (top to bottom)

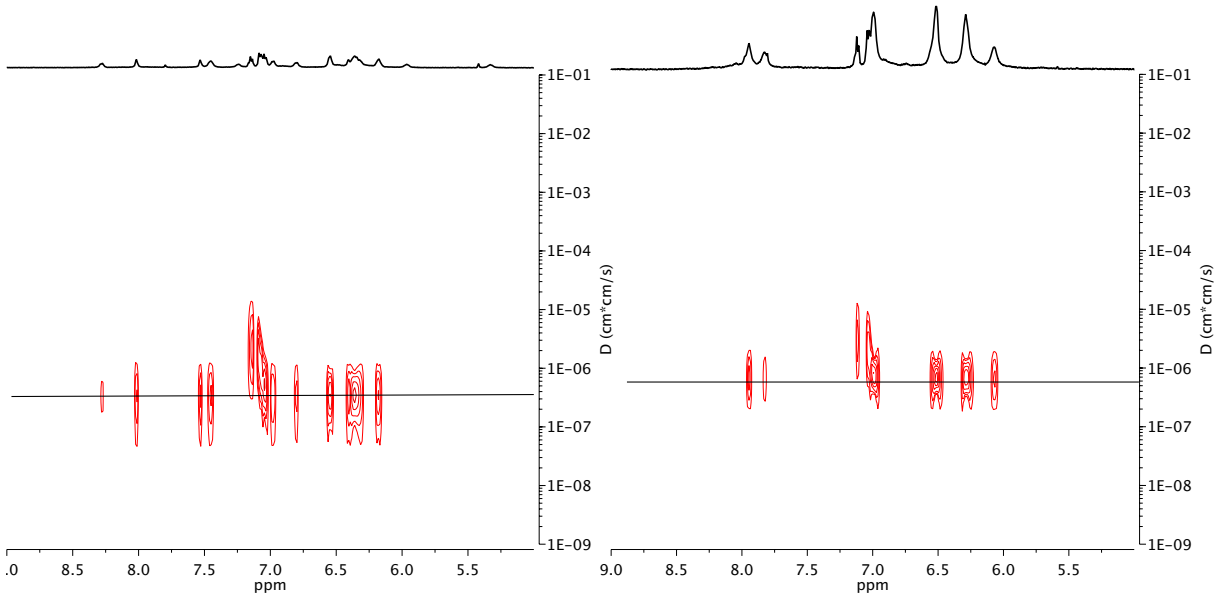

Figure 4.24. DOSY NMR for cluster **9** (left) and **9** + PEt_4I (right).

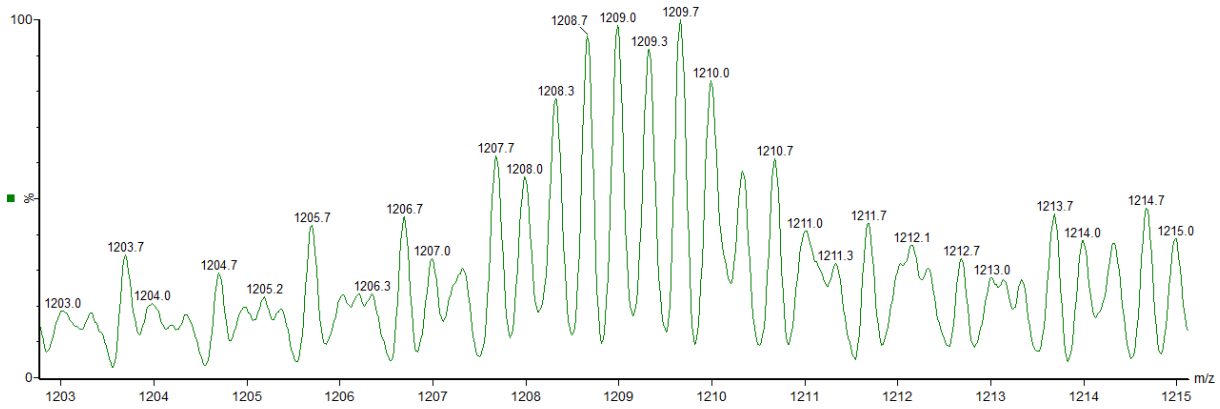

Figure 4.25. ESI-MS signal consistent with an cluster **9** in the -3 charge state, although further modeling is required in order to determine the counterion distribution.

4.5.5 Derivation of Observed Rate Constants

The first order rate constant for approach to equilibrium in a reversible reaction is the sum of the forward and backward rate constants.

$$\mathrm{A} \underset{k_{-1}}{\overset{k_1}{\rightleftharpoons}} \mathrm{B} \qquad k_{obs} = k_1 + k_{-1}$$

$$-\frac{\partial[\mathrm{A}]}{\partial t} = k_1[\mathrm{A}]_t - k_{-1}[\mathrm{B}]_t$$

$$[\mathrm{A}]_0 + [\mathrm{B}]_0 = [\mathrm{A}]_e + [\mathrm{B}]_e = [\mathrm{A}]_t + [\mathrm{B}]_t$$

$$k_1[\mathrm{A}]_e = k_{-1}[\mathrm{B}]_e$$

$$[\mathrm{B}]_t = [\mathrm{A}]_e + \frac{k_1}{k_{-1}}[\mathrm{A}]_e - [\mathrm{A}]_t$$

$$-\frac{\partial[\mathrm{A}]}{\partial t} = k_1[\mathrm{A}]_t - k_{-1}\left([\mathrm{A}]_e + \frac{k_1}{k_{-1}}[\mathrm{A}]_e - [\mathrm{A}]_t\right)$$

$$-\frac{\partial[\mathrm{A}]}{\partial t} = k_1[\mathrm{A}]_t - k_{-1}[\mathrm{A}]_e - k_1[\mathrm{A}]_e + k_{-1}[\mathrm{A}]_t$$

$$-\frac{\partial[\mathrm{A}]}{\partial t} = (k_1 + k_{-1}) \times ([\mathrm{A}]_t - [\mathrm{A}]_e)$$

For a bimolecular reaction that is reversible, one component is significantly greater in concentrations (i.e. [L] >>[E]), then the forward reaction becomes pseudo-first order, with the reagent of larger concentration absorbed into the rate constant, as in the one step binding event:

$$\mathrm{E} \underset{k_{off}}{\overset{k_{on}[\mathrm{L}]}{\rightleftharpoons}} \mathrm{EL} \qquad k_{obs} = k_{on}[\mathrm{L}] + k_{off}$$

For the analysis of the conformational selection mechanism, and the induced fit mechanism, two assumptions are made: (1) ligand exchange is fast compared to host isomerization, and (2) the ligand concentration is large compared to host concentration. Since the isomerization step is significantly slower than guest binding, the two reactions can be treated independently.

Induced Fit:

$$\mathrm{E_i} \underset{k_{off}}{\overset{k_{on}[\mathrm{L}]}{\rightleftharpoons}} \mathrm{E_iL} \underset{k_{-r}}{\overset{k_r}{\rightleftharpoons}} \mathrm{E_aL} \qquad k_{obs} = k_r \frac{[\mathrm{L}]}{\frac{k_{off}}{k_{on}} + [\mathrm{L}]} + k_{-r}$$

$$\frac{\partial[\mathrm{E_aL}]}{\partial t} = k_{\mathrm{r}}[\mathrm{E_iL}] - k_{\text{-r}}[\mathrm{E_aL}]$$

$$k_{\mathrm{on}}[\mathrm{L}][\mathrm{E_i}] = k_{\mathrm{off}}[\mathrm{E_iL}]$$

$$[\mathrm{E_{i\text{-}total}}]=[\mathrm{E_i}]+[\mathrm{E_iL}]$$

$$k_{\mathrm{on}}[\mathrm{L}]([\mathrm{E_{i\text{-}total}}]-[\mathrm{E_iL}]) = k_{\mathrm{off}}[\mathrm{E_iL}]$$

$$k_{\mathrm{on}}[\mathrm{L}][\mathrm{E_{i\text{-}total}}] = k_{\mathrm{off}}[\mathrm{E_iL}] + k_{\mathrm{on}}[\mathrm{L}][\mathrm{E_iL}]$$

$$[\mathrm{E_iL}]=\frac{k_{\mathrm{on}}[\mathrm{L}][\mathrm{E_{i\text{-}total}}]}{k_{\mathrm{off}} + k_{\mathrm{on}}[\mathrm{L}]} = \frac{[\mathrm{L}][\mathrm{E_{i\text{-}total}}]}{\frac{k_{\mathrm{off}}}{k_{\mathrm{on}}} + [\mathrm{L}]}$$

$$\frac{\partial[\mathrm{E_aL}]}{\partial t} = k_{\mathrm{r}} \frac{[\mathrm{L}]}{\frac{k_{\mathrm{off}}}{k_{\mathrm{on}}} + [\mathrm{L}]}[\mathrm{E_{i\text{-}total}}] - k_{\text{-r}}[\mathrm{E_aL}]$$

$$k_{\mathrm{obs}} = k_{\mathrm{r}} \frac{[\mathrm{L}]}{\frac{k_{\mathrm{off}}}{k_{\mathrm{on}}} + [\mathrm{L}]} + k_{\text{-r}}$$

Conformational Selection

$$\mathrm{E_i} \underset{k_{\text{-r}}}{\overset{k_{\mathrm{r}}}{\rightleftharpoons}} \mathrm{E_a} \underset{k_{\mathrm{off}}}{\overset{k_{\mathrm{on}}[\mathrm{L}]}{\rightleftharpoons}} \mathrm{E_aL} \qquad k_{\mathrm{obs}} = k_{\mathrm{r}} + k_{\text{-r}} \frac{1}{1 + \frac{k_{\mathrm{on}}}{k_{\mathrm{of}}}[\mathrm{L}]}$$

$$-\frac{\partial[\mathrm{E_i}]}{\partial t} = k_{\mathrm{r}}[\mathrm{E_i}] - k_{\text{-r}}[\mathrm{E_a}]$$

$$k_{\mathrm{on}}[\mathrm{L}][\mathrm{E_a}] = k_{\mathrm{off}}[\mathrm{E_aL}]$$

$$[\mathrm{E_{a\text{-}total}}]=[\mathrm{E_a}]+[\mathrm{E_aL}]$$

$$k_{\mathrm{on}}[\mathrm{L}][\mathrm{E_a}] = k_{\mathrm{off}}([\mathrm{E_{a\text{-}total}}]-[\mathrm{E_a}])$$

$$k_{\mathrm{on}}[\mathrm{L}][\mathrm{E_a}] + k_{\mathrm{off}}[\mathrm{E_a}] = k_{\mathrm{off}}[\mathrm{E_{a\text{-}total}}]$$

$$[\mathrm{E_a}]=\frac{k_{\mathrm{off}}[\mathrm{E_{a\text{-}total}}]}{k_{\mathrm{off}} + k_{on}[\mathrm{L}]} = \frac{[\mathrm{E_{a\text{-}total}}]}{1 + \frac{k_{\mathrm{on}}}{k_{\mathrm{off}}}[\mathrm{L}]}$$

$$\frac{\partial[\mathrm{E_aL}]}{\partial t} = k_{\mathrm{r}}[\mathrm{E_i}] - k_{\text{-r}} \frac{1}{1 + \frac{k_{\mathrm{on}}}{k_{\mathrm{off}}}[\mathrm{L}]}[\mathrm{E_{a\text{-}total}}]$$

$$k_{\mathrm{obs}} = k_{\mathrm{r}} + k_{\text{-r}} \frac{1}{1 + \frac{k_{\mathrm{on}}}{k_{\mathrm{off}}}[\mathrm{L}]}$$

4.6 References

(1) Changeux, J.-P.; Edelstein, S. *F1000 Biol. Rep.* **2011**, *3*.
(2) Fischer, E. *Berichte Dtsch. Chem. Ges.* **1894**, *27* (3), 2985.
(3) Koshland, D. E. *Proc. Natl. Acad. Sci.* **1958**, *44* (2), 98.
(4) Monod, J.; Wyman, J.; Changeux, J.-P. *J. Mol. Biol.* **1965**, *12* (1), 88.
(5) Tummino, P. J.; Copeland, R. A. *Biochemistry (Mosc.)* **2008**, *47* (20), 5481.
(6) Antikainen, N. M.; Smiley, R. D.; Benkovic, S. J.; Hammes, G. G. *Biochemistry (Mosc.)* **2005**, *44* (51), 16835.
(7) Ha, T.; Ting, A. Y.; Liang, J.; Caldwell, W. B.; Deniz, A. A.; Chemla, D. S.; Schultz, P. G.; Weiss, S. *Proc. Natl. Acad. Sci.* **1999**, *96* (3), 893.
(8) Eisenmesser, E. Z.; Bosco, D. A.; Akke, M.; Kern, D. *Science* **2002**, *295* (5559), 1520.
(9) Boehr, D. D.; Nussinov, R.; Wright, P. E. *Nat. Chem. Biol.* **2009**, *5* (11), 789.
(10) Vogt, A. D.; Di Cera, E. *Biochemistry (Mosc.)* **2013**, *52* (34), 5723.
(11) Vogt, A. D.; Di Cera, E. *Biochemistry (Mosc.)* **2012**, *51* (30), 5894.
(12) Fersht, A. *Enzyme Structure and Mechanism*; W. H. Freeman, 1977.
(13) Hammes, G. *Enzyme Catalysis and Regulation*; Elsevier, 1982.
(14) Halford, S. E. *Biochem. J.* **1971**, *125* (1), 319.
(15) Fersht, A. *Structure and Mechanism in Protein Science: A Guide to Enzyme Catalysis and Protein Folding*; Macmillan, 1999.
(16) Pozzi, N.; Vogt, A. D.; Gohara, D. W.; Di Cera, E. *Curr. Opin. Struct. Biol.* **2012**, *22* (4), 421.
(17) Yoshizawa, M.; Klosterman, J. K.; Fujita, M. *Angew. Chem. Int. Ed.* **2009**, *48* (19), 3418.
(18) Brown, C. J.; Toste, F. D.; Bergman, R. G.; Raymond, K. N. *Chem. Rev.* **2015**, *115* (9), 3012.
(19) Catti, L.; Zhang, Q.; Tiefenbacher, K. *Synthesis* **2015**, *48* (03), 313.
(20) Wiester, M. J.; Ulmann, P. A.; Mirkin, C. A. *Angew. Chem. Int. Ed.* **2011**, *50* (1), 114.
(21) Raynal, M.; Ballester, P.; Vidal-Ferran, A.; Leeuwen, P. W. N. M. van. *Chem. Soc. Rev.* **2014**, *43* (5), 1734.
(22) Caulder, D. L.; Powers, R. E.; Parac, T. N.; Raymond, K. N. *Angew. Chem. Int. Ed.* **1998**, *37* (13-14), 1840.
(23) Brumaghim, J. L.; Michels, M.; Raymond, K. N. *Eur. J. Org. Chem.* **2004**, *2004* (22), 4552.
(24) Pluth, M. D.; Bergman, R. G.; Raymond, K. N. *J. Am. Chem. Soc.* **2007**, *129* (37), 11459.
(25) Pluth, M. D.; Bergman, R. G.; Raymond, K. N. *Science* **2007**, *316* (5821), 85.
(26) Hart-Cooper, W. M.; Clary, K. N.; Toste, F. D.; Bergman, R. G.; Raymond, K. N. *J. Am. Chem. Soc.* **2012**, *134* (43), 17873.
(27) Kaphan, D. M.; Levin, M. D.; Bergman, R. G.; Raymond, K. N.; Toste, F. D. *Science* **2015**, *350* (6265), 1235.
(28) Hastings, C. J.; Backlund, M. P.; Bergman, R. G.; Raymond, K. N. *Angew. Chem.* **2011**, *123* (45), 10758.
(29) Zhao, C.; Toste, F. D.; Raymond, K. N.; Bergman, R. G. *J. Am. Chem. Soc.* **2014**, *136* (41), 14409.
(30) Kaphan, D. M.; Toste, F. D.; Bergman, R. G.; Raymond, K. N. *J. Am. Chem. Soc.* **2015**, *137* (29), 9202.
(31) Hart-Cooper, W. M.; Sgarlata, C.; Perrin, C. L.; Toste, F. D.; Bergman, R. G.; Raymond, K. N. *Proc. Natl. Acad. Sci.* **2015**, *112* (50), 15303.

(32) Zhao, C.; Sun, Q.-F.; Hart-Cooper, W. M.; DiPasquale, A. G.; Toste, F. D.; Bergman, R. G.; Raymond, K. N. *J. Am. Chem. Soc.* **2013**, *135* (50), 18802.
(33) Hart-Cooper, W.; Zhao, C.; Triano, R.; Yaghoubi, P.; Ozores, H. L.; Burford, K.; Toste, F. D.; Bergman, R. G.; Raymond, K. *Chem. Sci.* **2014**.
(34) Scherer, M.; Caulder, D. L.; Johnson, D. W.; Raymond, K. N. *Angew. Chem. Int. Ed.* **1999**, *38* (11), 1587.
(35) Yeh, R. M.; Xu, J.; Seeber, G.; Raymond, K. N. *Inorg. Chem.* **2005**, *44* (18), 6228.
(36) Pluth, M. D.; Johnson, D. W.; Szigethy, G.; Davis, A. V.; Teat, S. J.; Oliver, A. G.; Bergman, R. G.; Raymond, K. N. *Inorg. Chem.* **2009**, *48* (1), 111.
(37) Black, S. P.; Wood, D. M.; Schwarz, F. B.; Ronson, T. K.; Holstein, J. J.; Stefankiewicz, A. R.; Schalley, C. A.; Sanders, J. K. M.; Nitschke, J. R. *Chem. Sci.* **2016**, *7* (4), 2614.
(38) Meng, W.; Clegg, J. K.; Thoburn, J. D.; Nitschke, J. R. *J. Am. Chem. Soc.* **2011**, *133* (34), 13652.
(39) Saalfrank, R. W.; Demleitner, B.; Glaser, H.; Maid, H.; Bathelt, D.; Hampel, F.; Bauer, W.; Teichert, M. *Chem. – Eur. J.* **2002**, *8* (12), 2679.
(40) Beissel, T.; Powers, R. E.; Parac, T. N.; Raymond, K. N. *J. Am. Chem. Soc.* **1999**, *121* (17), 4200.
(41) Mahata, K.; Frischmann, P. D.; Würthner, F. *J. Am. Chem. Soc.* **2013**, *135* (41), 15656.
(42) Kersting, B.; Telford, J. R.; Meyer, M.; Raymond, K. N. *J. Am. Chem. Soc.* **1996**, *118* (24), 5712.
(43) Kersting, B.; Meyer, M.; Powers, R. E.; Raymond, K. N. *J. Am. Chem. Soc.* **1996**, *118* (30), 7221.
(44) Anderson, H. L.; Hunter, C. A.; Meah, M. N.; Sanders, J. K. M. *J. Am. Chem. Soc.* **1990**, *112* (15), 5780.
(45) Fujita, K.; Chen, W.-H.; Yuan, D.-Q.; Nogami, Y.; Koga, T.; Fujioka, T.; Mihashi, K.; Immel, S.; Lichtenthaler, F. W. *Tetrahedron Asymmetry* **1999**, *10* (9), 1689.
(46) Liu, Y.; Han, B.-H.; Sun, S.-X.; Wada, T.; Inoue, Y. *J. Org. Chem.* **1999**, *64* (5), 1487.
(47) Haino, T.; Rudkevich, D. M.; Shivanyuk, A.; Rissanen, K.; Rebek, Jr., J. *Chem. - Eur. J.* **2000**, *6* (20), 3797.
(48) Le Gac, S.; Marrot, J.; Reinaud, O.; Jabin, I. *Angew. Chem. Int. Ed.* **2006**, *45* (19), 3123.
(49) Hiraoka, S.; Harano, K.; Nakamura, T.; Shiro, M.; Shionoya, M. *Angew. Chem. Int. Ed.* **2009**, *48* (38), 7006.
(50) Swinburne, A. N.; Paterson, M. J.; Beeby, A.; Steed, J. W. *Chem. - Eur. J.* **2010**, *16* (9), 2714.
(51) Albrecht, M.; Isaak, E.; Baumert, M.; Gossen, V.; Raabe, G.; Fröhlich, R. *Angew. Chem. Int. Ed.* **2011**, *50* (12), 2850.
(52) Sawada, T.; Hisada, H.; Fujita, M. *J. Am. Chem. Soc.* **2014**, *136* (12), 4449.
(53) Davis, A.; Fiedler, D.; Seeber, G.; Zahl, A.; van Eldik, R.; Raymond, K. N. *J. Am. Chem. Soc.* **2006**, *128*, 1324.
(54) Horiuchi, N.; Huff, J.; Rebek, J. *Tetrahedron Lett.* **1990**, *31* (36), 5121.
(55) Strukov, O. G.; Emel'yanova, A. D.; Dubov, S. S.; Kozlova, N. V. *J. Struct. Chem.* **1965**, *6* (2), 201.